Modeling the anisotropic shear-wave velocity structure in the Earth's mantle on global and regional scales

A thesis presented

by

Bogdan Kustowski

to

The Department of Earth and Planetary Sciences

in partial fulfillment of the requirements

for the degree of

Doctor of Philosophy

in the subject of

Geophysics

Harvard University

Cambridge, Massachusetts

January, 2007

Modeling the anisotropic shear-wave velocity structure in the Earth's mantle on global and regional scales

Bogdan Kustowski

Advisor: Adam M. Dziewoński

Co-advisor: Göran Ekström

Abstract

We combine large data sets of surface-wave phase anomalies, long-period waveforms, and body-wave travel times in order to provide new constraints on the anisotropic shear-wave velocity structure of the Earth's mantle. The waveform inversion is performed using a new and more accurate method developed to correct seismograms for non-linear crustal effects. Starting with an isotropic spherically symmetric earth model, we build a new one-dimensional, transversely isotropic reference model by independently constraining variations in five elastic parameters and density. Using this new reference model, we invert the data for a whole-mantle model of shear-wave velocity and investigate lateral anisotropic variations at all depths in the mantle. Finally, we develop a technique that allows us to calculate a high-resolution tomographic model of a specific region as a perturbation with respect to the low-resolution global model, and implement this technique to study the structure beneath Eurasia.

Our new reference model fits the data as well as PREM, although it does not contain the 220-km discontinuity present in PREM. We find the average shear-wave anisotropy to be strongest at a depth of about 125 km and the parameter η to be very similar to that in PREM. The strong fast-velocity anomalies beneath stable parts of continents, which may represent the continental lithosphere, extend down to a depth of about 200 km if waveform data are corrected for crustal effects using the

new non-linear method. In contrast, if the standard, less accurate, linear approach is used, significantly thicker fast-velocity anomalies beneath continents are observed. With the non-linear crustal corrections, the strongest decrease in the absolute shear-wave velocity appears within depths between 150 and 250 km beneath cratons in northern Eurasia. Allowing for radial anisotropy in the transition zone does not improve data fit. The depth of about 650 km is characterized by a significant change in the power spectrum of heterogeneity, which suggests a change in the flow pattern between the upper and lower mantle. We find that allowing for anisotropic variations at the bottom of the mantle improves the data fit. However, constraining such variations is difficult since they strongly trade off with the isotropic variations.

Contents

1 Introduction **1**

2 Inversion for a transversely isotropic model **10**

2.1 Theoretical approximations and simplifying assumptions 11

2.2 Body-wave travel times 15

2.2.1 Plane waves in a transversely isotropic medium 16

2.2.2 New method for calculating sensitivity kernels 21

2.2.3 Joint inversion for velocity and topography 23

2.2.4 Linearized equations 26

2.2.5 Travel-time corrections 27

2.3 Surface-wave phase velocities 30

2.3.1 Phase anomalies, normal modes, and Fréchet kernels 31

2.3.2 Linearized equations 34

2.3.3 Crustal corrections 36

2.4 Waveforms 37

2.4.1 Path-average approximation 37

2.4.2 Waveform inversion 42

2.4.3 Crustal corrections: a new method 48

2.5 The inverse problem 58

2.5.1 Solution to the inverse problem 59

2.5.2 Geometrical parameterization 61

2.5.3 Regularization 63

3 Data **67**

3.1 Body-wave travel times 68

3.2 Surface-wave dispersion 75

3.3 Mantle and body waveforms 77

4 Modeling velocity structure on a global scale **83**

4.1 New one-dimensional reference model 84

4.1.1 Starting model 85

4.1.2 Parameterization and inversion 86

4.1.3 New reference model 89

4.2 Global three-dimensional shear-wave velocity model 90

4.2.1 Parameterization 91

4.2.2 Sensitivity and weighting of different data sets 94

4.2.3 Inversion 95

4.2.4 Isotropic velocity structure 96

4.2.5 Where is the mantle anisotropic? 111

4.2.6 Anisotropic velocity structure 118

4.2.7 Comment on laterally varying sensitivity kernels and depth of the Moho . . 126

4.2.8 Effect of the reference model 130

4.2.9 Effect of anisotropy 133

4.2.10 Effect of crustal corrections 135

4.2.11 Comparison with the CMT solutions for SH8/U4L8 138

5 Regional model of the upper mantle beneath Eurasia 142

5.1 Parameterization 144

5.2 Inversion 149

5.3 Isotropic velocity variations 153

5.3.1 Comparison with CU_SRT1.0 154

5.3.2 Structure of the stable part of the continent 158

5.3.3 Structure in regions of recent tectonic activity 163

5.3.4 Boundary at the base of the continental lithosphere 169

5.4 Effect of crustal corrections 176

5.5 Anisotropic variations 178

6 Discussion and future directions 184

6.1 The continental lithosphere 185

6.2 Anisotropy in the uppermost mantle 188

6.3 Style of convection in the mantle 189

6.4 Anisotropy in the transition zone and lower mantle 193

6.5 Robustness of the CMT solutions 195

6.6 Progress in seismic tomography 196

A Model availability **200**

References **201**

Acknowledgements

I am grateful to Adam M. Dziewoński and Göran Ekström for giving me an opportunity to address fundamental problems in earth sciences, helping me to focus on the critical questions, making their data and computational resources available to me, and for their patience. I thank the members of my committee, Miaki Ishii, Richard J. O'Connell, and John Shaw, for reading the manuscript, their advice, and being available with their vast knowledge.

I owe a great deal to Lapo Boschi, who was my mentor during my first year at Harvard, and to Colleen Dalton, Karen Felzer, Jeffrey Yu Gu, Vedran Lekic, Meredith Nettles, Jianfeng Pan, and Victor Tsai, who made the Seismology Laboratory a fun and stimulating place to work. Without Chenoweth Moffatt's guidance through the bureaucratic maze and Bim Toth's efforts to maintain our computer system, I would have never completed this dissertation.

Many thanks to Thorsten Becker, Mathieu Dumberry, Chris Guzofski, Kevin Halverson, Pippa Halverson, Eleanor Hennessey, Kaushik Katari, and Jamie Kellogg for their friendship, which has been keeping me sane for the past six years. Special thanks to Renata Dmowska and Stanisław Lasocki, who have been an inexhaustible source of encouragement. I am immensely grateful to Matylda for looking after me and putting up with me for years, and my Parents and Brother for their moral support and sharing with me their healthy, common sense attitude towards the challenges I was facing.

Chapter 1

Introduction

The determination of the Earth's composition and explanation of the dynamics of its interior are primary goals of solid Earth sciences. In this thesis, we focus on the Earth's mantle; a region not as accessible for direct sampling as the crust, but equally important for understanding processes responsible for plate tectonics, occurrence of earthquakes, volcano eruptions, and processes operating at larger depths such as the sinking of lithospheric slabs or heat transport away from the Earth's core.

Understanding the Earth's mantle requires an interdisciplinary approach. Geochemists study rocks that provide constraints on the composition and history of the mantle; mineral and rock physicists estimate properties of the rocks at large depths; geodynamicists model deformation processes in order to cast a light on the evolution of the mantle. In particular, the most uniform constraints on the structure of the mantle are provided by seismic waves. Seismologists develop tools for converting these data into three-dimensional models of physical properties in the mantle. In this thesis, we image the distribution of seismic wave velocities in the mantle using the technique known as seismic

tomography, which was pioneered by Dziewoński *et al.* (1977). Tomographic velocity models can be interpreted in terms of thermal, compositional, and density heterogeneities based on the study of mantle rocks at high pressures and temperatures, and used to constrain geodynamic models of the mantle.

Initially, seismologists focused on the determination of velocity variations only in the radial direction. The early models (*e.g.*, Jeffreys and Bullen, 1940) explained only travel times of short-period body waves, but more recent studies incorporate the measurements of longer-period waves. The Preliminary Reference Earth Model (PREM) of Dziewoński and Anderson (1981) was obtained by inverting the observed body-wave travel times, surface-wave dispersion, and periods of free oscillations of the Earth for radial variations in compressional- and shear-wave velocity and attenuation, density, and radial anisotropy. PREM is still used as a reference model in many tomographic studies; however, it has some undesirable features, as it will be shown in this thesis. For example, we eliminate the 220-km discontinuity from PREM and develop a better reference model, which should be useful in future studies of the structure of the mantle.

Although spherically symmetric models fit seismic data fairly well, it has been known for a long time (Dorman *et al.*, 1960; Toksöz and Anderson, 1966) that there must be significant lateral velocity variations in the Earth's mantle. Woodhouse and Dziewoński (1984) showed that the global pattern of lateral variations in the uppermost mantle obtained by inverting seismic waves without any *a priori* regionalization is well-correlated with surface tectonics; velocities are low along the mid-ocean ridges and high within the continental lithosphere. At larger depths, however, the mantle heterogeneity is dominated by a spherical-harmonic degree-2 component, which is correlated with the geoid (Masters *et al.*, 1982) but not with the distribution of oceans and continents. The degree-2

pattern below the lithospheric depths was also observed in the model of Woodhouse and Dziewoński (1984) and it has become clear that seismic waves provide constraints on the deep mantle heterogeneity that could not be inferred from surface observables or from tomographic inversions with an *a priori* regionalization based on surface observables.

In the pioneering work, Dziewoński *et al.* (1977) inverted short-period travel times of compressional waves collected by the International Seismological Centre (ISC). Henceforth tomographic images obtained from the ISC data have often shaped opinions of the scientific community about the structure of the mantle. Most notably, models of compressional- (*e.g.*, van der Hilst *et al.*, 1997) and shear-wave (*e.g.*, Grand *et al.*, 1997) velocity showed fast-velocity anomalies extending below major subduction zones into the lower mantle, which convinced many scientists that the upper–lower mantle boundary is permeable and that the convective flow that drives plate tectonics involves the whole mantle.

However, the broad-band seismograms recorded on the stations of the Global Seismologic Network (GSN) provide more diverse constraints on the structure of the mantle than the hand-picked arrivals collected by the ISC. When seismograms are available, arrivals of body waves can be accurately measured and reliably identified using cross-correlation techniques. Even more importantly, while the ISC data constrain fairly well only the structure of the lower mantle, the GSN data allow for measuring various types of waves that altogether have peak sensitivities in all depth ranges in the mantle. The GSN seismograms have been used in tomography by inverting full waveforms based on the path-average approximation (*e.g.*, Woodhouse and Dziewoński, 1984), partitioned waveform inversion (*e.g.*, Nolet, 1995), non-linear asymptotic coupling theory (NACT; *e.g.*, Li and Romanowicz, 1996); and by inverting measurements of phase (*e.g.*, Montagner and Tanimoto 1990; Trampert

and Woodhouse, 1995; Laske and Masters, 1996; Ekström *et al.*, 1997) and group (*e.g.*, Levshin *et al.*, 1989) velocities of short- and intermediate-period fundamental-mode surface waves, overtones (*e.g.*, van Heijst and Woodhouse, 1997), normal-mode splitting functions (*e.g.*, Resovsky and Ritzwoller, 1998; Masters *et al.*, 2000), as well as body-wave travel times (*e.g.*, Liu and Dziewoński, 1998; Bolton and Masters, 2001). Several tomographic models have been obtained from combined, diverse data sets that allowed for retrieving spectral properties of the heterogeneity in the whole mantle. Su and Dziewoński (1991) reported that the heterogeneity is dominated by the long-wavelength patterns. Models of Gu *et al.* (2001a) and Ritsema *et al.* (2004) revealed a significant change in the heterogeneity power spectrum at the upper–lower mantle boundary, which suggests a change in the flow pattern. This result is dramatically different from the conclusions of van der Hilst *et al.* (1997) and Grand *et al.* (1997). The sub-horizontal deflection of the flow at the bottom of the upper mantle has been suggested by several tomographic models (for review, see Fukao *et al.*, 2001), the topography of the transition zone discontinuities (Shearer and Masters, 1992; Flanagan and Shearer, 1998; Gu *et al.*, 1998, 2003), and by the location and mechanism of deep earthquakes (Giardini and Woodhouse, 1984, 1986; Lekic, 2004). Since the style of convection is a fundamental question in solid earth sciences and is still a subject of debate, we address this issue by re-examining the power spectrum of velocity heterogeneity and topography of the transition zone discontinuities using new data and improved modeling techniques.

Another important problem addressed by seismic tomography is the determination of the thickness of the continental lithosphere. Early studies suggested that phase-velocity variations could be explained by models with significant continent-ocean contrast confined to the region above 200 km depth (*e.g.*, Dziewoński, 1971). However, Jordan (1975) found indications that this contrast may

extend down to at least 400 km and proposed that the continental lithosphere be underlain by the neutrally buoyant roots depleted in heavy basalt-like elements, which translate coherently with the moving lithospheric plates (Jordan, 1978). While some recent tomographic models obtained by waveform inversion suggest that the continental roots my indeed extend below 300 km (Megnin and Romanowicz, 2000; Gu *et al.*, 2001a), models derived from the measurements of surface waves, but not through the waveform inversion (Ritsema *et al.*, 2004; Nettles, 2005), indicate that significant differences between the continental and oceanic regions are confined to the uppermost 200 km of the mantle. The shallower differences can be explained in terms of primarily thermal anomalies, whereas the deep continental roots extending down to about 400 km require more complicated explanation in terms of compositional heterogeneity (Jordan, 1978) or high viscosity (Shapiro *et al.*, 1999), protecting the roots from the convective disruption. Evidently, the thickness of the continental lithosphere and the depth extent of the continent-ocean contrast have profound geodynamical and geochemical implications, hence it is important to understand the discrepancy between different tomographic models. In this work, we argue that the discrepancy may be caused by the inaccuracy of the standard linear crustal corrections implemented in the waveform inversion. By developing a new non-linear method, we correct seismograms more accurately for crustal effects and obtain models with strong continental signatures confined to the uppermost 200 km of the mantle, which is consistent with the surface-wave tomography.

Seismologists have demonstrated that the Earth's mantle is not only heterogeneous but also anisotropic. They found evidence for the discrepancy between the dispersion of Rayleigh and Love waves (*e.g.*, Anderson, 1961; Harkrider and Anderson, 1962), azimuthal dependence of P_n velocities (Hess, 1964; Raitt *et al.*, 1969), and for the splitting of the SKS arrivals (*e.g.*, Kind *et al.*,

1985; Silver and Chan, 1991). Accounting for seismic anisotropy in tomographic inversions is important owing to its effect on the modeled isotropic velocity variations, but also because modeling anisotropy helps us to understand deformation processes in the mantle. Anisotropy in the asthenosphere is thought to be caused by the lattice-preferred orientation (LPO; for review see Nicolas and Christensen, 1987) of crystals of anisotropic minerals such as olivine. The correlation of the modeled direction of fast axes in the sub-oceanic mantle with the direction of plate motion observed in some tomographic models (*e.g.*, Montagner and Tanimoto, 1990; Ekström, 2000; Maggi *et al.*, 2006) can be explained in terms of LPO anisotropy in the convecting mantle. Besides modeling azimuthal velocity variations, seismologists attempt to resolve radial anisotropy, which represents the difference between azimuthally averaged velocities of horizontally polarized waves and velocities of vertically polarized waves. Unfortunately, significantly different anisotropic patterns are observed in models obtained by different researchers. Ekström and Dziewoński (1998) found that lateral anisotropic variations are strong only beneath the Pacific, and that the $v_{SH} > v_{SV}$ anomalies change from lower-than-average at the 50-km depth to higher-than-average at 150 km. Megnin and Romanowicz (2000) found strong anisotropic anomaly in the Pacific, whose pattern, however, does not change significantly with depth. Gung *et al.* (2003) reported a strong $v_{SH} > v_{SV}$ trend not only in the sub-oceanic mantle but also beneath the continental lithosphere. Significant variations within the continental plates were observed by Nettles (2005).

In addition to the difficulties in modeling lateral anisotropic heterogeneity, it is also not clear how global average anisotropy varies with depth. The shear-wave anisotropy in PREM is strongest at the Mohorovičić discontinuity (hereafter Moho) and vanishes at the 220-km discontinuity. This discontinuity has been proposed to mark the base of the anisotropic layer beneath continents (*e.g.*,

Gaherty and Jordan, 1995), perhaps associated with the transition from dislocation to diffusion creep (Karato, 1992). A recent survey of the $S_{220}S$ reflectors (Gu *et al.*, 2001b) demonstrated that this boundary does not have a global extent. Modeling anisotropy on a global scale should therefore be performed independently of PREM. In this thesis, we build a new spherically symmetric reference Earth model, which is smooth at 220-km depth, and use it as a reference model in three-dimensional tomography. Our new models show depth variations in both, strength of average anisotropy and root-mean-square lateral anisotropic variations, consistent with the flow model of Becker (personal communication). Such agreement, on the other hand, is not observed for PREM. In this thesis we also discuss lateral anisotropic variations in different tomographic models and technical challenges of modeling the anisotropy in continental regions.

Anisotropy has also been reported to be significant in the deep mantle (for review see Kendall, 2000). The proposed mechanisms responsible for the presence of anisotropy include the LPO (*e.g.*, Karato, 1998) and the shape-preferred orientation (SPO, *e.g.*, Kendall and Silver, 1996). Recently, an evidence for the anisotropic post-perovskite phase, which may be abundant at the bottom of the mantle, has been reported in the high-pressure laboratory measurements (Murakami *et al.*, 2004; Oganov and Ono, 2004; Shim *et al.*, 2004). Panning and Romanowicz (2004) and Panning (2006) have found significant global anisotropic variations in the D'' region and mantle transition zone using the NACT waveform inversion. In this thesis, we investigate whether robust anisotropic patterns in these depth ranges can be obtained by inverting body-wave travel times analyzed using ray theory and seismograms inverted using the path-average approximation.

Another goal of seismic tomography is the determination of regional-scale velocity anomalies. Tomographic models elucidating such anomalies have been obtained either by inverting for a model

confined to a region of interest and sufficient data coverage (*e.g.*, van der Lee and Nolet, 1997; Priestley and Debayle, 2003; Maggi and Priestley, 2005) or by inverting a global data set for a global model with finer parameterization in regions of good data coverage (*e.g.*, Bijwaard *et al.*, 1998; Boschi *et al.*, 2004; Nettles, 2005). In this thesis, we implement the latter approach to obtain a continental-scale (hereafter regional-scale) model of Eurasia. Despite very dense ray-path coverage in Eurasia, the only fine-scale resolution model of the entire continent obtained so far is that of Shapiro and Ritzwoller (2002). This model, however, lacks constraints on structures below a depth of 250 km. In this thesis, we combine large and diverse data sets to determine the structure of the entire upper mantle beneath Eurasia with nominal horizontal resolution of about 300 km.

Another interesting question that seismologists are facing is that of the resolution limits of mantle tomography. A vigorous debate about the importance of scattering effects has first convinced many scientists that small-scale velocity anomalies can be resolved properly only if finite-frequency effects are taken into account (Nolet and Dahlen, 2000; Spetzler *et al.*, 2002; Baig *et al.*, 2003). However, several recent papers indicate the insignificance of these effects (van der Hilst and de Hoop, 2005; de Hoop and van der Hilst, 2005; Trampert and Spetzler, 2006). In the light of this debate, it should be important to establish an empirical limit on seismic tomography based on ray theory by comparing our regional model of Eurasia with the detailed geological maps, geodynamic models, and tomographic models obtained from high-frequency seismic data. Our preliminary interpretation demonstrates that surface waves at period of 35 seconds can resolve the upper mantle structures of diameters significantly smaller than 1000 km.

In Chapter 2, we present the technical background of the inversion for the three-dimensional anisotropic velocity model. We also describe a new method developed to account for non-linear

crustal effects on normal-mode seismograms, and a new method for the anisotropic inversion of body-wave travel-time anomalies based on ray theory. In Chapter 3, we present the diverse data sets that we combine to constrain the structure of the whole mantle. In Chapter 4, we develop a new spherically symmetric reference Earth model and a new three-dimensional anisotropic model of shear-wave velocity in the mantle. In Chapter 5, we invert for a new regional-scale model of shear-wave velocity in the upper mantle beneath Eurasia. In Chapter 6, we discuss our results and future directions.

Chapter 2

Inversion for a transversely isotropic model

Seismologists attempt to determine the elastic, anelastic, and density structure of the Earth from entire seismograms or major arrivals recorded at seismic stations. Imaging of the Earth's interior always involves simplifying assumptions about the material properties, propagation of seismic waves, and solution of the inverse problem. In the first section of this chapter, we discuss the choices of the most appropriate approximations for our tomographic inversions. In the following sections, we explain how different types of data can be used to constrain three-dimensional transversely isotropic structure of the mantle and how to correct the data for crustal effects. In the last section, we show how we define, regularize, and solve the inverse problem.

Special attention is given to two methods that have been developed in the course of this study. Normal-mode seismograms are corrected for crustal effects using a more accurate method than the standard linear approximation of Woodhouse and Dziewoński (1984). Sensitivity kernels for body-

wave travel times are calculated using a new method based on ray theory, which is simpler and more versatile than the technique of Woodhouse and Girnius (1982) derived from equations governing the free oscillations of the Earth.

2.1 Theoretical approximations and simplifying assumptions

The dominating part of the signal in our data can be explained by the effects of wave propagation in the heterogeneous elastic velocity field. Seismic waves are also affected by anelastic attenuation (*e.g.*, Romanowicz, 1990), but variations in attenuation are difficult to constrain and usually neglected in tomographic inversions. In this work, we invert only for variations in the elastic parameters and density in the Earth's mantle.

Early tomographic studies focused only on the determination of isotropic velocities (Dziewoński *et al.*, 1977; Woodhouse and Dziewoński, 1984). However, some minerals abundant in the mantle exhibit strong anisotropic properties. Convection in the asthenosphere and deformation processes in the upper and lower mechanical boundary layers of the mantle may lead to nonrandom orientations of these minerals leading to anisotropic velocities in such layers. Different types of seismic data are sensitive to the anisotropy in the mantle. Anisotropy in the upper mantle has been proposed to explain the splitting of SKS waves, azimuthal variations in P_n velocity, and discrepancy between Rayleigh and Love waves (for review, see Anderson, 1990). Ekström and Dziewoński (1998) showed that not only vertical but also lateral variations in anisotropy in the uppermost mantle are required by surface-wave data. Many researchers have investigated anisotropy in the lowermost mantle (*e.g.*, Lay, 1998; Kendall 2000). Panning (2004) also suggested the presence of anisotropy in the transition zone. Some of recent global (Boschi and Ekström, 2002; Shapiro and Ritzwoller,

2002; Panning and Romanowicz, 2004) and regional (Boschi *et al.*, 2004; Nettles, 2005) models account for anisotropy. The work presented here is an attempt to investigate the distribution and strength of the anisotropic structure of the mantle using an unprecedentedly large and diverse data set.

Currently available seismic data are insufficient to resolve three-dimensional variations of all 21 independent elements of the elastic tensor. To reduce the number of unknowns, it is necessary to assume certain symmetry of the material. The simplest system with one axis of symmetry is called transverse isotropy. Transversely isotropic models, in which the axis of symmetry coincides with the radial direction, are often referred to as radially anisotropic. More complex models account for the tilt of the symmetry axis or azimuthal dependence of velocity. Since the strongest anisotropic signal in our data can be associated with the predominantly horizontal alignment of crystals, it is reasonable to reduce the number of unknowns in the inversion by assuming that the axis of symmetry is vertical. Determination of azimuthally anisotropic velocities introduces additional unknowns compared to the radially anisotropic velocities. Azimuthal variations may trade off with the laterally heterogeneous structure (Larson, 1998) and are therefore difficult to constrain. With good azimuthal data coverage, however, the azimuthal variations are averaged out and can be represented in terms of the transversely isotropic model (Ekström, 2000). We achieve relatively good azimuthal data coverage by building large data sets of surface-wave and waveform data and choose the transversely isotropic parameterization with the symmetry axis in the radial direction.

We analyze our data using ray theory, as well as the great-circle and path-average approximations (Woodhouse and Dziewoński, 1984). These approximations allow us to calculate sensitivity kernels very efficiently and to combine large data sets. Montelli *et al.* (2004a,b) and Li and

Romanowicz (1996) have used more complex approaches to build the sensitivity kernels, which, however, are not suitable for using diverse data sets and constraining the structure of the mantle as uniformly as our approach. Similarity of models obtained using ray theory and finite-frequency (FF) theory presented in Montelli *et al.* (2004b) suggests that the choice of theory affects tomographic models less than the data coverage and choices of parameterization and regularization schemes, as pointed out by van der Hilst and de Hoop (2005). The differences between the two models are significantly smaller than those among models compared by Boschi and Dziewoński (1999) using the same theory and data but different parameterization and damping. So far, there is little evidence that methods more complex than ray theory lead to more reliable tomographic models. On the contrary, certain shortcomings of the FF kernels are yet to be investigated. While travel-time measurements are always averaged out over certain range of frequencies, the FF kernels are designed to analyze observations at a single frequency, and using such kernels may lead to erroneous interpretation of the data. The FF kernels are designed to account for scattering of seismic waves assuming that rays travel along the paths predicted by a spherically symmetric Earth model. It is not known, however, whether there is any benefit of including scattering effects while neglecting ray bending in the heterogeneous Earth. While employing more sophisticated theories may prove useful in the future, we believe that, at this point, significant progress in seismic tomography can be achieved by combining data that sample the mantle as uniformly as possible, improving the methods used to account for crustal effects, experimenting with the model parameterization, and regularization of the inverse problem.

In the analysis of surface waves and waveforms, we simplify ray theory by integrating along minimum-distance paths rather than minimum-travel-time paths. Nettles (2005) showed that the

largest errors of phase-velocity maps obtained using the great-circle approximation are in the most heterogeneous regions and that such maps are systematically too fast. The errors are, however, very small. The low computational cost required to find great-circle paths makes it possible to analyze an extended surface-wave and waveform data sets. We believe that our new data reveal more details of the Earth's structure than using a slightly more accurate and computationally expensive method and fewer measurements.

To analyze body-wave travel times, we calculate ray paths in a spherically symmetric Earth model. Rays traveling through the laterally heterogeneous Earth deviate from such paths but this deviation has little effect on travel times at teleseismic distances (Kustowski *et al.*, 2003). Results of Widiyantoro *et al.* (2000) and Gorbatov *et al.* (2001) suggest that accounting for the ray deviation may somewhat affect the amplitude of the anomalies but does not appreciably change the pattern of heterogeneity within the mantle. Considering the high computational cost of three-dimensional ray tracing and its small effect on tomographic images, we prefer to trace rays in a spherically symmetric model using a very efficient algorithm of Woodhouse (1981).

We use the data by inverting only for the structure of the Earth's mantle. Surface waves and most of our body-wave data are practically insensitive to the core structure. Vigorously convecting outer core is unlikely to produce significant heterogeneity that would affect our data (Stevenson, 1987), and none of the rays used in this study sample the inner core. The SKS and SKKS residuals may, however, be affected by slightly inaccurate compressional-wave velocities in the outermost part of the core in PREM (Lay and Young, 1990). Consequently, the observed systematic baseline shift between the SKS and SKKS residuals may reflect the core structure rather than the properties of the lowermost mantle (Liu, 1997).

Although all recorded seismic waves sample the crust, our surface-wave data, whose periods are longer than 30 seconds, cannot resolve details of the crustal structure. We assume that crustal effects can be best accounted for by correcting all data using a detailed global crustal model CRUST2.0 of Bassin *et al.* (2000).

2.2 Body-wave travel times

In this section, we present theoretical background necessary to find velocities of body waves in the transversely isotropic model. We define the linear relationship between the observed travel-time anomalies and perturbations in model parameters and explain how to calculate sensitivity kernels for the inversion of travel times. This theory is further extended to include the effects of discontinuity topography on travel times.

A variety of simple methods can be applied to trace rays in isotropic models. Including anisotropy, however, complicates ray theory. Woodhouse (1981) derived formulas for travel times and ray paths in spherically symmetric, transversely isotropic models from the equations governing the free oscillations of the Earth. Woodhouse and Girnius (1982) extended this theory to find partial derivatives, which have been used in the inversions for laterally heterogeneous anisotropic Earth models (*e.g.*, Boschi and Dziewoński, 2000). In this work, we adopt the formulas of Woodhouse (1981) to find the ray paths in the transversely isotropic model and refer the reader to the original paper for more details. We focus on the problem of finding partial derivatives, which we have solved without using the asymptotic properties of free oscillations. Our method, as opposed to that of Woodhouse and Girnius (1982), does not require the reference model to be spherically symmetric, and therefore may find a wider range of applications. In this work, however, we use only spherically symmetric

reference Earth models. Demonstrating the applications of the new method in solving nonlinear inverse problems would require tracing rays through a three-dimensional anisotropic model, which is beyond the scope of this thesis. Our new algorithm is also simpler than that of Woodhouse and Girnius (1982) since is does not involve a singularity at the turning point.

2.2.1 Plane waves in a transversely isotropic medium

The equation of motion for a continuum, which relates the body forces f_i and spatial derivatives of the stress tensor τ_{ij} in the elastic medium to the acceleration can be written as

$$\frac{\partial \tau_{ij}}{\partial x_j} + f_i = \rho \frac{\partial^2 u_i}{\partial t^2}, \tag{2.1}$$

where u_i is the displacement vector, ρ is the density, and t is the time. The effects of body forces, such as gravity, can be neglected for body waves at typically observed frequencies. Away from the source region, the stress-strain relationship is assumed to be linear, and by inserting the Hooke's law $\tau_{ij} = c_{ijkl} \partial u_k / \partial x_l$ into equation 2.1, we obtain

$$c_{ijkl} \frac{\partial^2 u_k}{\partial x_j \partial x_l} = \rho \frac{\partial^2 u_i}{\partial t^2}, \tag{2.2}$$

where the elastic tensor c_{ijkl} is constant within a small homogeneous region. In ray theory, we seek a solution of equation 2.2 in terms of a plane wave $u_i = U_i e^{i\omega(p n_k x_k - t)}$ of frequency ω propagating in the direction of a unit vector n_k with the slowness p. The polarization vector U_i indicates the direction of particle motion. Differentiation of the displacement in time and space leads to an

eigenvalue problem

$$\left[c_{ijkl}n_j n_l - \frac{\rho}{p^2}\delta_{ik}\right] U_k = 0, \tag{2.3}$$

whose solutions can be identified with three types of body waves known as quasi-SH, quasi-SV, and quasi-P (or qSH, qSV, and qP, respectively). The orthogonal eigenvectors U_1, U_2, and U_3 indicate the polarizations of these three waves. The eigenvalues $\frac{\rho}{p^2_{qSH}}$, $\frac{\rho}{p^2_{qSV}}$, and $\frac{\rho}{p^2_{qP}}$ divided by the density are related to the propagation velocities of the wavefronts by $v^{phase}_{qSH} = \frac{1}{p_{qSH}}$, $v^{phase}_{qSV} = \frac{1}{p_{qSV}}$, and $v^{phase}_{qP} = \frac{1}{p_{qP}}$. In the transversely isotropic model, equation 2.3 can be solved analytically. In that case, the elastic tensor has only five independent elastic muduli A, C, N, L, and F defined by Love (1927). If the axis of symmetry is vertical, the vector $\hat{\mathbf{n}}$ normal to the wavefront can be expressed in terms of the angle of inclination θ between $\hat{\mathbf{n}}$ and the vertical by setting, for example, $n_1 = sin\,\theta$, $n_2 = 0$, and $n_3 = cos\,\theta$. The first term of equation 2.3 can be then written explicitly as

$$c_{ijkl}n_j n_l = \begin{pmatrix} A\sin^2\theta + L\cos^2\theta & 0 & (F+L)\sin\theta\cos\theta \\ 0 & N\sin^2\theta + L\cos^2\theta & 0 \\ (F+L)\sin\theta\cos\theta & 0 & L\sin^2\theta + C\cos^2\theta \end{pmatrix}, \tag{2.4}$$

and the wavefronts of the three body waves propagate with velocities (Kennett, 2001)

$$v^{phase}_{qSH} = \sqrt{v^2_{SV}\cos^2\theta + v^2_{SH}\sin^2\theta}, \tag{2.5}$$

$$v^{phase}_{qSV} = \sqrt{\frac{Z_1 - Z_4}{2}}, \tag{2.6}$$

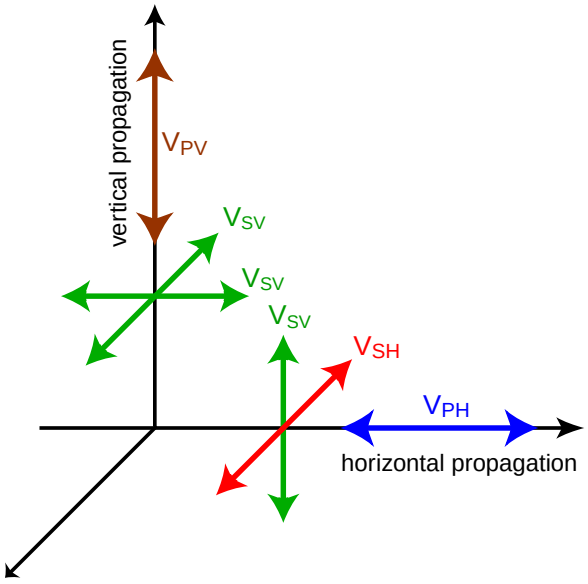

Figure 2.1: Velocities of the horizontally and vertically traveling compressional and shear waves in the transversely isotropic medium with a vertical axis of symmetry. For the vertical propagation, the solution of equation 2.3 is degenerate and the shear-wave velocity is v_{SV} regardless of polarization. In other directions, horizontally- and vertically-polarized shear waves travel at different velocities.

$$v_{qP}^{phase} = \sqrt{\frac{Z_1 + Z_4}{2}}, \tag{2.7}$$

where $Z_1 = v_{PV}^2 \cos^2\theta + v_{PH}^2 \sin^2\theta + v_{SV}^2$, $Z_2 = v_{PH}^2 \sin^2\theta - v_{PV}^2 \cos^2\theta + v_{SV}^2 \cos 2\theta$, $Z_3 = (\gamma^2 + v_{SV}^2) \sin 2\theta$, $Z_4 = \sqrt{Z_2^2 + Z_3^2}$, and $\gamma = \sqrt{\frac{F}{\rho}}$. Four of the elastic moduli are often identified with velocities $v_{PH} = \sqrt{\frac{A}{\rho}}$, $v_{PV} = \sqrt{\frac{C}{\rho}}$, $v_{SH} = \sqrt{\frac{N}{\rho}}$, and $v_{SV} = \sqrt{\frac{L}{\rho}}$, which must not be confused with the phase velocities. By inserting $\theta = 0$ and $\theta = \pi/2$ into equations 2.5 - 2.7, we can verify that these four velocities have interpretation illustrated in Figure 2.1. Horizontally and vertically traveling compressional waves propagate with velocities v_{PH} and v_{PV}, respectively. Horizontally polarized shear waves travel horizontally at v_{SH}. Velocity of both vertically traveling shear waves and horizontally traveling vertically polarized shear waves is equal to v_{SV}. When body waves travel vertically or horizontally, their velocities are independent of the fifth parameter

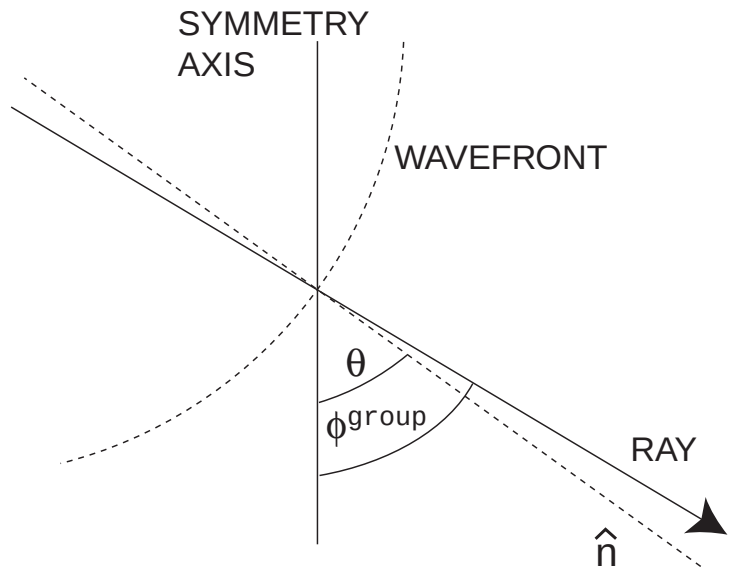

Figure 2.2: In the anisotropic medium, the ray deviates from the direction normal to the wavefront **n**. The angle θ between **n** and the axis of symmetry is called the phase angle. The angle ϕ^{group} between the ray and the axis of symmetry is called the group angle. The energy of a seismic wave propagates along the ray and the measured travel time is determined by the group velocity along the ray.

γ. At intermediate angles, the velocities differ from v_{SH}, v_{SV}, v_{PH}, and v_{PV}, and depend on γ. In PREM, the parameter $\eta = \frac{F}{A-2L}$ is defined instead of γ.

In the isotropic medium $A = C$, $N = L$, and $\eta = 1$, and solutions to equation 2.3 are independent of the propagation direction. In that case, the eigenvalue problem is degenerate and the velocities of qSH and qSV are identical. In an anisotropic medium, phase velocities vary with the propagation direction. Consequently, the energy propagates along the ray with a different velocity than the phase velocity and the ray deviates from the direction normal to the wavefront, **n**, as illustrated in Figure 2.2. The angle ϕ^{group} between the ray path and the axis of symmetry is related to the phase velocity and the inclination θ (or a phase angle) by (Berryman, 1979; Thomsen, 1986)

$$\phi^{group} - \theta = \text{atan}\left(\frac{1}{v^{phase}}\frac{dv^{phase}}{d\theta}\right). \tag{2.8}$$

Velocity at which the energy propagates along the ray is given by

$$v^{group} = \frac{v^{phase}}{\cos(\phi^{group} - \theta)}. \tag{2.9}$$

In order to find partial derivatives (Section 2.2.2), it is necessary to calculate the group velocity along a known ray path, which we find using the method of Woodhouse and Girnius (1982). The group velocity depends on the unknown phase angle θ, which has to be calculated numerically. We employ the following approximation to find the phase angle. We assume that the ray path is known and therefore the group angle ϕ^{group} is known. We use ϕ^{group} as a first guess on the phase angle and insert it into the right hand side of equation 2.8. In this way, we obtain the approximate deviation angle $\phi^{group} - \theta$. In a weakly anisotropic model, such as PREM, the deviation of the group angle ϕ^{group} from the phase angle θ is less than 3 degrees (Figure 2.3), and so is the error of our first guess on θ. The deviation $\phi^{group} - \theta$ changes slowly with θ, and is therefore almost insensitive to the small error in θ. In other words, even if the first guess on θ is not perfect, the approximation of the deviation $\phi^{group} - \theta$ obtained from equation 2.8 will be nearly exact. Knowing the deviation angle, as well as the ray path and hence ϕ^{group}, we can find the phase angle, and ultimately the group velocity v^{group}. Travel times calculated by integrating v^{group} obtained using this method agree with those predicted by the method of Woodhouse (1981) up to 0.001 seconds at teleseismic distances. In contrast, when we insert the group angle ϕ^{group} instead of θ into equations 2.5 - 2.7, and integrate v^{phase} instead of v^{group} along the path, the travel times show errors of 0.02-0.05 seconds. This travel-time error is small compared to the measurement accuracy and neglecting the difference between ϕ^{group} and θ does not significantly affect the partial derivatives calculated

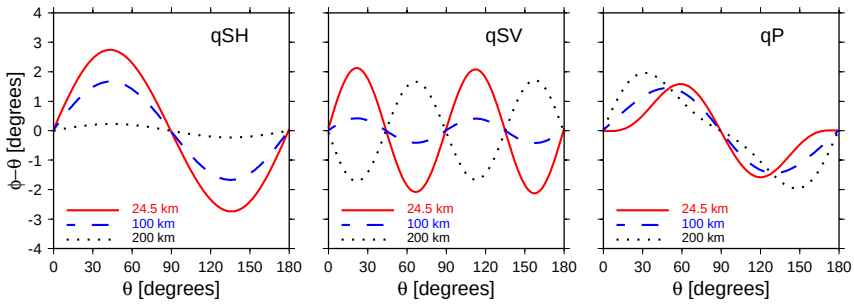

Figure 2.3: Deviations of the group angle ϕ^{group} from the inclination θ (phase angle) in PREM at three different depths for qSH, qSV, and qP waves. In the isotropic model, rays are normal to the wavefronts and $\phi = \theta$.

for PREM. Accounting for these differences, however, does not increase the computational time appreciably and can be easily implemented.

2.2.2 New method for calculating sensitivity kernels

Let us consider the time t necessary for a body wave to travel from an earthquake to a seismic station. Assuming that the wave of infinite frequency propagates along an infinitely thin ray, we can write

$$t = \int_{path} \frac{1}{v^{group}} \, ds, \tag{2.10}$$

where v^{group} indicates the group velocity and the integral is taken along the ray path. Given a number of travel-time observations, seismologists attempt to determine velocity variations in the interior of the Earth. This is a nonlinear problem because the path of each ray depends on the velocity. The classic analytic Herglotz-Wiechert formulas allow for the inversion of a travel-time curve into the velocity model as a function of depth. In modern seismology, however, much more

versatile discrete inverse methods are used. The discrete inversions usually involve the linearization of the problem based on the assumption that the true ray path does not deviate significantly from the path predicted by the reference model. The deviation is indeed small for teleseismic rays. If we integrate along the path predicted by the reference model, the difference δt between the observed and predicted travel time will be approximately linearly related to the unknown perturbation in velocity by

$$\delta t = - \int\limits_{path} \frac{\delta v^{group}}{(v_0^{group})^2}\, ds, \tag{2.11}$$

where $\delta v^{group} = v^{group} - v_0^{group}$, and v_0^{group} is the group velocity in the reference model. The first-order Taylor series approximation to v^{group} is given by

$$\delta v^{group} = \frac{\partial v^{group}}{\partial v^{PH}}\delta v^{PH} + \frac{\partial v^{group}}{\partial v^{PV}}\delta v^{PV} + \frac{\partial v^{group}}{\partial v^{SH}}\delta v^{SH} + \frac{\partial v^{group}}{\partial v^{SV}}\delta v^{SV} + \frac{\partial v^{group}}{\partial \eta}\delta \eta. \tag{2.12}$$

We find group velocities from equation 2.9 and calculate the partial derivatives numerically. Upon inserting equation 2.12 into 2.11 we find the linear relationship between the observed travel-time anomalies and the unknown perturbations in the transversely isotropic model

$$\delta t = - \int\limits_{path} \frac{\left[\delta v^{PH} T_{v^{PH}} + \delta v^{PV} T_{v^{PV}} + \delta v^{SH} T_{v^{SH}} + \delta v^{SV} T_{v^{SV}} + \delta \eta T_{\eta}\right]}{(v_0^{group})^2}\, ds, \tag{2.13}$$

where the partial derivatives of the group velocity are indicated by T. The integral is taken along the ray path and, as opposed to the method of Woodhouse and Girnius (1982), does not encounter a

singularity at the turning point.

Figure 2.4 shows sensitivities of different types of body waves to anisotropic velocities and η in PREM. A large majority of our travel-time data are measured on the transverse component of a seismogram, which records qSH waves. Such data are primarily sensitive to the variations in v_{SH} near the turning point and to the variations in v_{SV} in case of the nearly vertical propagation. Measurements of the qSV waves, such as SKS or SKKS, recorded on the vertical or longitudinal component, are insensitive to δv_{SH} and very sensitive to δv_{SV} regardless of the propagation direction. Since we use only teleseismic travel times, which have rays that do not bottom in the upper mantle, even a combination of measurements recorded on all components cannot resolve variations in v_{SH} in the upper mantle. In the lower mantle, δv_{SH} and δv_{SV} could be determined if both qSH and qSV data were available. It should be noted, however, that variations in v_{PH}, v_{PV}, and η also affect the qSV velocity and would be interpreted as variations in v_{SV} if we inverted only for shear-wave velocities. Another interesting observation is that $\partial v_{qSV}/\partial v_{PH}$ is almost a mirror image of $\partial v_{qSV}/\partial v_{PV}$. Assuming that the isotropic perturbation in P-wave velocity is the arithmetic or Voigt average of δv_{PH} and δv_{PV}, the two partial derivatives, when added, will cancel out each other. Consequently, the qSV wave will be more sensitive to the variations in the P-wave anisotropy than variations in the P-wave velocity.

2.2.3 Joint inversion for velocity and topography

Topographies of the transition zone discontinuities are constrained in this study by inversion of differential travel times SS-S_{400}S, SS-S_{670}S, and S_{400}S-S_{670}S. In attempt to isolate the sensitivity of the SS precursors to the discontinuity topography, some researchers (*e.g.*, Flanagan and Shearer,

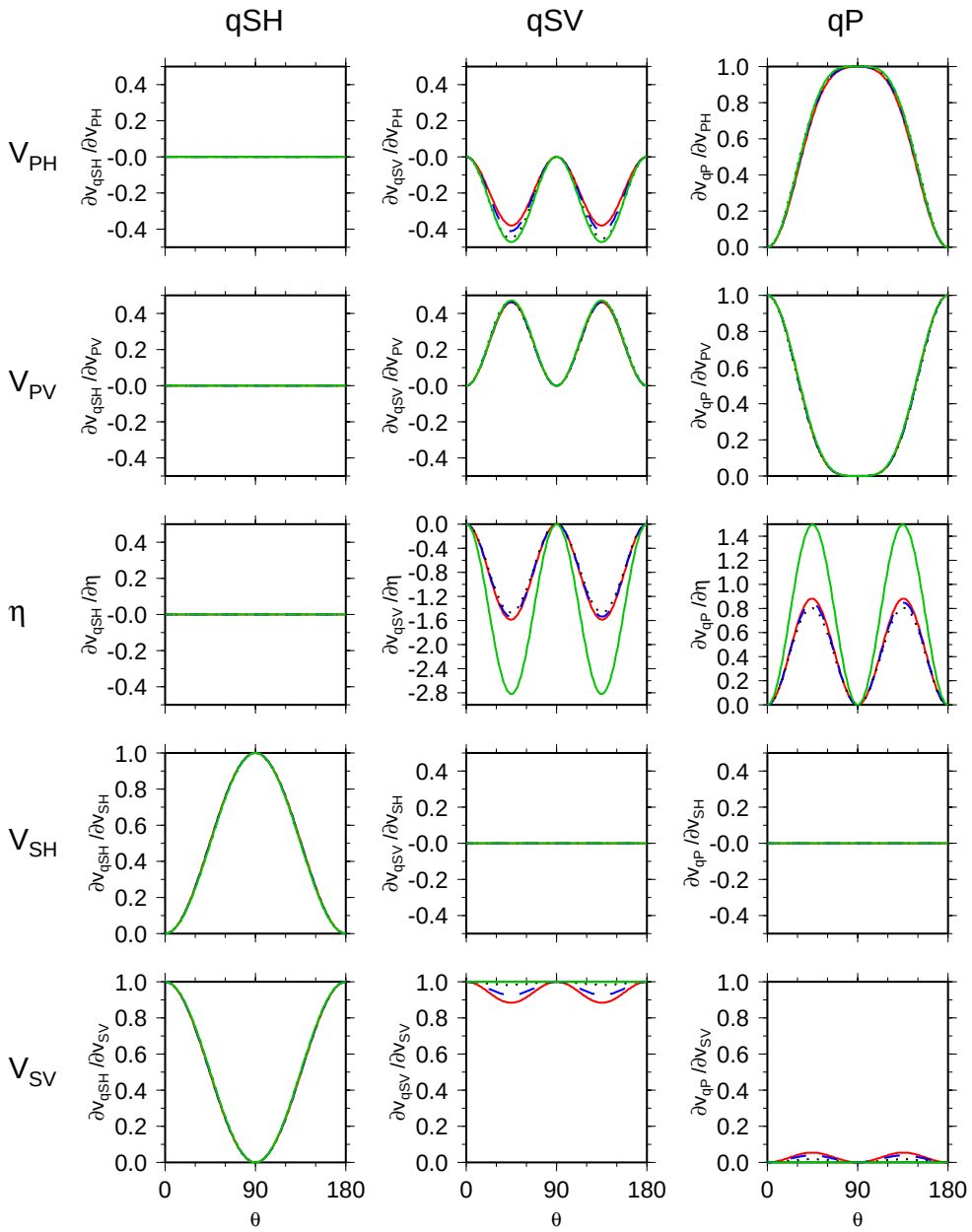

Figure 2.4: Partial derivatives of travel times for PREM at 25 km (solid red line), 100 km (dashed blue line), 200 km (black dotted line), and 2800 km (solid green line) as a function of the phase angle θ. The measurements of qSH waves, such as S travel times recorded on the transverse component, are sensitive primarily to the variations in v_{SH} near the turning point of the ray, and variations in v_{SV} in case of nearly vertical propagation. The measurements of qSV waves, such as SKS travel times recorded on the radial component, are sensitive primarily to the variations in v_{SV}.

1998) subtract travel-time anomalies predicted by a preferred three-dimensional velocity model from the observed residuals. This approach, however, may lead to significant artifacts, as shown by Gu *et al.* (2003), because the effect of velocity heterogeneity on travel times cannot be perfectly represented by the *a priori* constrained velocity model with constant discontinuity depths. To avoid velocity-topography trade-offs, we prefer to invert simultaneously for mantle velocities and topography of the discontinuities following Gu *et al.* (2003). The generalized form of equation 2.13 can be written as

$$\delta t = - \int\limits_{path} \frac{\left[\delta v^{PH} T_{v^{PH}} + \delta v^{PV} T_{v^{PV}} + \delta v^{SH} T_{v^{SH}} + \delta v^{SV} T_{v^{SV}} + \delta \eta T_{\eta}\right]}{(v_0^{group})^2} \, ds + \sum_{d_{400}} T_{400} \delta h_{400} + \sum_{d_{670}} T_{670} \delta h_{670}, \qquad (2.14)$$

where d_{400} and d_{670} indicate all interactions of the ray with the discontinuities. Sensitivities at points of bottom-side reflections are given by Dziewoński and Gilbert (1976) as

$$T = -\frac{2}{r}\sqrt{\eta_-^2 - p^2}, \qquad (2.15)$$

and at piercing points as

$$T = \frac{1}{r}\left(\sqrt{\eta_+^2 - p^2} - \sqrt{\eta_-^2 - p^2}\right), \qquad (2.16)$$

where p is the ray parameter, r is the radius at the discontinuity, $\eta = r/v$ (not to be confused with the elastic parameter η), v is the velocity, and subscripts '+' and '-' indicate the top and bottom of the discontinuity, respectively.

2.2.4 Linearized equations

Equation 2.14 establishes the linear relationship between the observed travel-time anomaly and the unknown perturbations in model parameters. Using this relationship, we wish to build a tomographic model that is defined at every point in the mantle. Given a finite number of observations, we can determine only a finite number of unknowns. Therefore, we expand the unknown parameters at every radius r, co-latitude θ, and longitude ϕ over the finite set of basis functions $f_j(r, \theta, \phi)$

$$\begin{aligned}
\frac{\delta v^{PH}}{v_0^{PH}} &= \sum_{j^{PH}=1}^{n^{PH}} c_j^{PH} f_j^{PH} \quad ; \quad \frac{\delta v^{PV}}{v_0^{PV}} = \sum_{j^{PV}=1}^{n^{PV}} c_j^{PV} f_j^{PV} \\
\frac{\delta v^{SH}}{v_0^{SH}} &= \sum_{j^{SH}=1}^{n^{SH}} c_j^{SH} f_j^{SH} \quad ; \quad \frac{\delta v^{SV}}{v_0^{SV}} = \sum_{j^{SV}=1}^{n^{SV}} c_j^{SV} f_j^{SV} \\
\frac{\delta \eta}{\eta_0} &= \sum_{j^{\eta}=1}^{n^{\eta}} c_j^{\eta} f_j^{\eta} \quad ; \quad \frac{\delta \rho}{\rho_0} = \sum_{j^{\rho}=1}^{n^{\rho}} c_j^{\rho} f_j^{\rho} \\
\delta h_{400} &= \sum_{j^{h_{400}}=1}^{n^{h_{400}}} c_j^{h_{400}} f_j^{h_{400}} \quad ; \quad \delta h_{670} = \sum_{j^{h_{670}}=1}^{n_{h_{670}}} c_j^{h_{670}} f_j^{h_{670}},
\end{aligned} \tag{2.17}$$

where the subscript '0' indicates value from the reference model. To accommodate surface waves, we introduce a perturbation in the density ρ, although the partial derivative is zero for body-wave travel times. In some inversions (Chapter 4), we will expand shear-wave velocities using different basis functions compared to other parameters, therefore the distinction between different basis functions for different parameters in equations 2.17 is necessary. For simplicity, let m^k, where k=1,2,...6, denote v_{PV}, v_{PH}, v_{SV}, v_{SH}, η and ρ, respectively. Upon inserting equation 2.17 into 2.14, we obtain

$$\delta t = \sum_j c_j \left[- \int_{path} \frac{\sum_{k=1}^{6} m_0^k \, T_k \, f_j}{(v_0^{group})^2} \, ds + \sum_{d_{400}} T_{400} f_j + \sum_{d_{670}} T_{670} f_j \right] \tag{2.18}$$

where f_j, m_0^k, T_k, and v_0^{group} are functions of position, and v_0^{group} also depends on the angle between the ray path and the vertical axis of symmetry. Writing the term in brackets as A_j, we obtain

$$\delta t_i = \sum_j c_j A_{ij}, \tag{2.19}$$

for the i-th travel-time anomaly. For a number of observations δt_i, formula 2.19 defines a system of linear equations with unknowns c_j, which can be solved using discrete inverse theory discussed in Section 2.5.

2.2.5 Travel-time corrections

Effects of crustal heterogeneity and ellipticity of the Earth on body-wave travel times can be as large as several seconds and therefore are significant. We use the most recent and detailed global crustal model CRUST2.0 (Bassin *et al.*, 2000) to find corrections beneath seismic stations, points of surface reflection, and hypocenters of shallow earthquakes. Finding exact crustal corrections would require tracing rays through the reference model and CRUST2.0. We prefer to use a more efficient and very accurate approximation, which is outlined below.

Let us consider two rays traveling through CRUST2.0 and PREM shown in Figure 2.5. Our goal is to find the difference $t^{CRUST2.0} - t^{PREM}$ between times necessary for the two rays to travel from an earthquake or a bounce point to their bottoming points, or from the bottoming points to the bounce point or a station. Let us define the reference radius at 6291 km, which is deeper than the Moho everywhere around the Earth according to CRUST2.0, and the reference ray REF, which reaches this depth exactly beneath the source, receiver, or a bounce point. Assuming that wavefronts traveling through PREM, PREM overlain by CRUST2.0, and REF take the same time

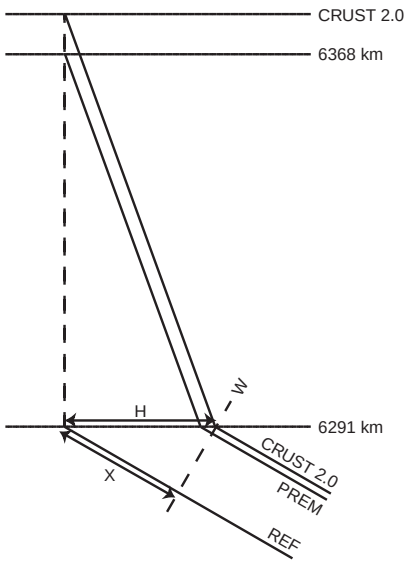

Figure 2.5: Paths of rays traveling through PREM, CRUST2.0, and the reference ray REF, which reaches 6291 km exactly beneath the source, station, or a bounce point. Rays traveling through PREM, PREM overlain by CRUST2.0, and REF are assumed to take the same time to travel between the bottoming points and the wavefront W.

to travel between the bottoming points and W we can write

$$t^{CRUST2.0} - t^{PREM} = (t^{CRUST2.0}_{above\ W} - t^{REF}_{above\ W}) - (t^{PREM}_{above\ W} - t^{REF}_{above\ W}), \tag{2.20}$$

where the subscript '$aboveW$' indicates the travel time between W and the source, station, or a bounce point. The first term can be calculated as

$$t^{CRUST2.0}_{above\ W} - t^{REF}_{above\ W} = t^{CRUST2.0}_{above\ 6291} - \frac{X}{v_{6291}} = t^{CRUST2.0}_{above\ 6291} - H \cdot p, \tag{2.21}$$

where H is the horizontal distance traveled by the ray in the crust, X is the distance traveled by the reference ray between W and the 6291 km radius, p is the ray parameter, and v_{6291} is the velocity in

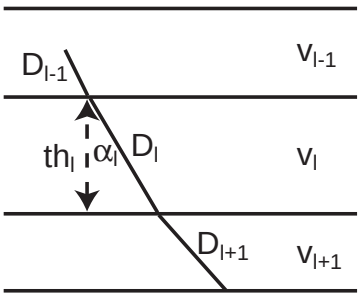

Figure 2.6: Three layers of CRUST2.0. D_l is the distance traveled by the ray within the layer l with the velocity v_l, th_l is the thickness of the l-th layer, and α_l is the incidence angle of the ray in the l-th layer.

the mantle at 6291 km radius. By summing up contributions from all crustal layers l and the portion of the mantle above the radius of 6291 km (Figure 2.6), we can find the travel time

$$t^{CRUST2.0}_{above\ 6291} = \sum_l \frac{D_l}{v_l} \tag{2.22}$$

and the horizontal distance

$$H = \sum_l D_l \cdot \sin(\alpha_l) = \sum_l D_l \cdot p \cdot v_l, \tag{2.23}$$

where $D_l = \frac{th_l}{\cos(\alpha_l)} = \frac{th_l}{\cos(\arcsin(p \cdot v_l))}$, v_l is the velocity, and th_l is the thickness of the l-th layer. The same method can be used to find $t^{PREM}_{above\ W} - t^{REF}_{above\ W}$. If travel-time residuals were measured with respect to PREM, such as data of Liu and Dziewoński (1998), $t^{PREM}_{above\ W}$ has to be calculated up to the bottom of the ocean layer at radius of 6368 km. If absolute or differential travel times were measured (*e.g.*, Bolton, 1996), travel times in the reference model and residuals have to be found using PREM without the ocean layer, and $t^{PREM}_{above\ W}$ should be calculated up to 6371 km. After applying the crustal corrections, all data are referenced to PREM with the shallow structure defined by CRUST2.0, and can be inverted jointly. This method allows for very efficient calculation of

crustal corrections, which nearly perfectly approximate differences $t^{CRUST2.0} - t^{PREM}$, as shown by our experiments with tracing rays though PREM and through PREM overlain by CRUST2.0.

We find ellipticity corrections as the travel-time difference in the aspherical and spherical earth models. Rays are traced in the spherical model and travel times are calculated after the ray paths have been perturbed into the elliptical geometry (Ekström, 2005, personal communication). Our ellipticity corrections calculated for PREM are very similar to those found by the standard method of Dziewoński and Gilbert (1976). In this work, we prefer to use the new method since it can be readily implemented for models other than PREM, while the application of the older method to a new reference would involve additional programming effort.

2.3 Surface-wave phase velocities

The sensitivity of a surface wave to the structure of the mantle is nearly constant along the entire ray path. Consequently, surface waves provide much more uniform constraints on the upper mantle structure than body waves. The sensitivity of a monochromatic surface wave to the lateral variations in velocity can be found, as in case of body waves, by integration of the slowness along the ray path. To constrain three-dimensional velocity variations from phase measurements of dispersive surface waves at different frequencies, we introduce normal-mode theory. In this section, we discuss the relationship between the measured phase of the surface wave, normal-mode eigenfrequency, and parameters characterizing a transversely isotropic Earth model.

2.3.1 Phase anomalies, normal modes, and Fréchet kernels

The phase Φ of the surface wave is given by

$$\Phi = \int\limits_{path} \frac{\omega}{c(\omega)}\, ds, \tag{2.24}$$

where the phase velocity c is a function of the frequency ω and the integral is taken along the ray path. The phase is affected by the lateral heterogeneity in the phase velocity as the wave travels along the path. Following Ekström *et al.* (1997) and Ekström (2000), we write the linear relationship between the observed phase anomaly $\delta\Phi$ and the local phase-velocity anomaly δc as

$$\delta\Phi = -\frac{\omega}{c_0} \int\limits_{path} \frac{\delta c}{c_0}\, ds, \tag{2.25}$$

where c_0 is the phase velocity of the reference model. Note that this equation is equivalent to the formula 2.11 for a travel-time anomaly given $\delta\Phi = \omega\delta t$. The phase-velocity perturbation at a fixed frequency ω is related to the frequency perturbation at a fixed wavenumber k (Dahlen and Tromp, 1998) by

$$\left(\frac{\delta c}{c}\right)_{\omega} = \frac{c}{U}\left(\frac{\delta\omega}{\omega}\right)_{k}, \tag{2.26}$$

where U is the group velocity. In order to relate the frequency perturbation to the variations in the Earth structure, we use normal-mode theory. Surface waves are free oscillations, or normal modes of the Earth; Rayleigh waves correspond to spheroidal modes and Love waves correspond to toroidal modes. Our phase anomalies are measured using the method of Ekström *et al.* (1997),

which separates out the fundamental-mode signal from that of overtones. We can therefore describe the sensitivity of Rayleigh and Love waves to the structure using properties of fundamental modes. Following equation 9.39 of Dahlen and Tromp (1998), we define the perturbation in normal-mode eigenfrequency as

$$\delta\omega = \int_0^a \left[\delta v^{PH} K_{v^{PH}} + \delta v^{PV} K_{v^{PV}} + \delta v^{SH} K_{v^{SH}} + \delta v^{SV} K_{v^{SV}} + \delta\rho K_\rho + \delta\eta K_\eta\right] dr + K_{400}\delta h_{400} + K_{670}\delta h_{670}, \tag{2.27}$$

where the integral is taken over the radius r from the Earth's center to the free surface at a=6371 km. Fréchet kernels, or partial derivatives of the angular frequency ω with respect to v^{PH}, v^{PV}, v^{SH}, v^{SV}, η, and ρ are indicated by $K_{v^{PH}}$, $K_{v^{PV}}$, $K_{v^{SH}}$, $K_{v^{SV}}$, K_η, and K_ρ respectively; and partial derivatives with respect to the changes in depths of the discontinuities are indicated by K_{400} and K_{670}. All partial derivatives are calculated from eigenfunctions of normal modes in the spherically symmetric reference model (Takeuchi and Saito, 1972; Dahlen and Tromp, 1998). Equations 2.25 -2.27 define the linear relationship between the observed phase anomaly and the perturbations in elastic parameters, density, and discontinuity depths.

Figure 2.7 shows the sensitivity of 35-, 75-, and 150-second fundamental-mode surface waves to the Earth's structure calculated with PREM. Long-period waves sample deeper structures than short-period waves, and Rayleigh waves sample deeper structures than Love waves at the same period. Changes in the normal-mode eigenfrequency depend strongly on the variations in shear-wave velocities, but sensitivities to variations in compressional-wave velocities, η, and density are

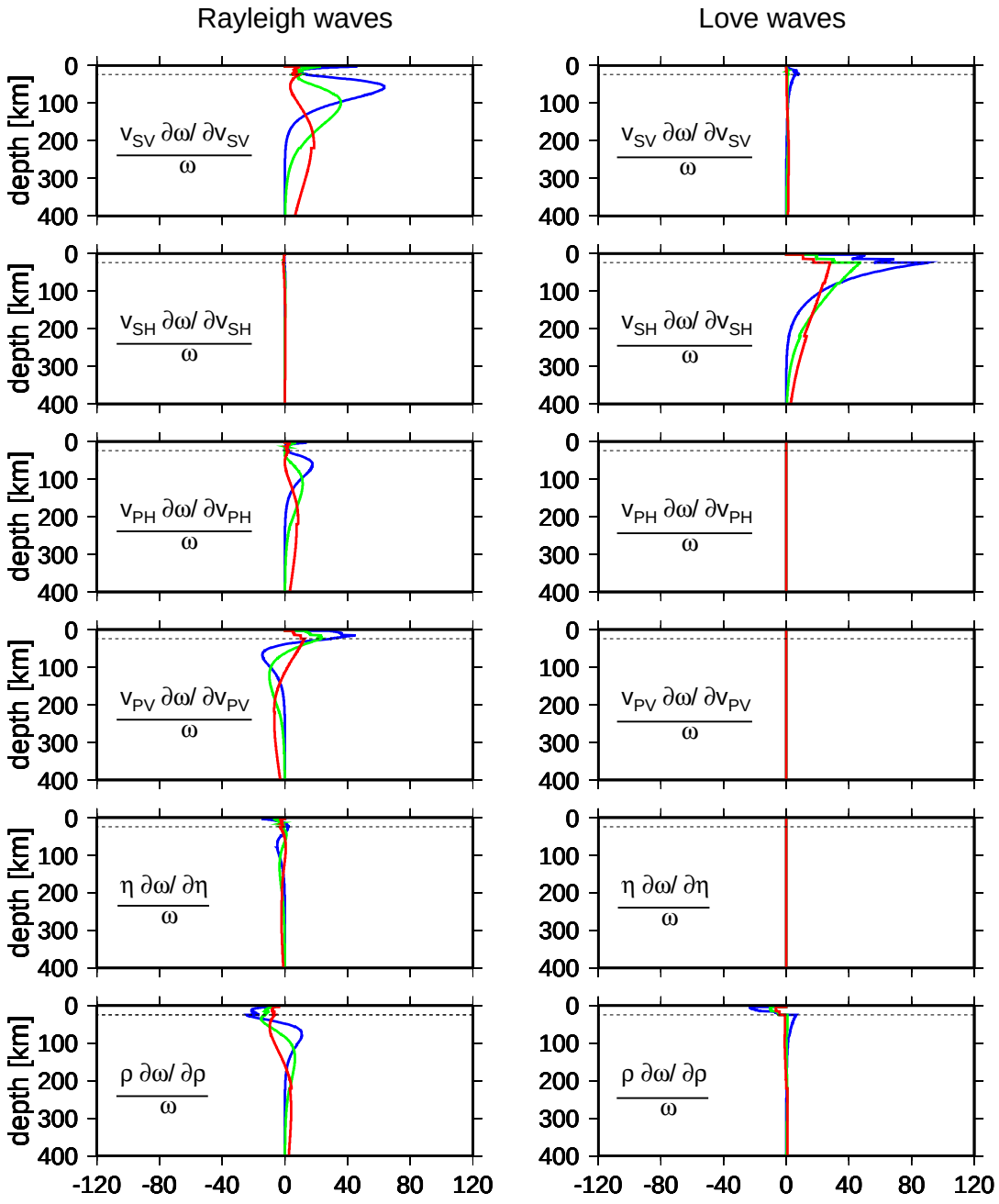

Figure 2.7: Sensitivity of the 35- (blue), 75- (green), and 150-second (red) fundamental-mode Rayleigh and Love waves to the Earth's structure in PREM. Partial derivatives are multiplied by model parameters as in the inversion for relative, rather than absolute, perturbations in model parameters. The derivatives are also nondimensionalized by dividing by ω. The derivatives are normalized in such a way that they describe a relative change $\delta\omega/\omega$ due to the perturbation of a given parameter by 100% at a given depth within a 6371-km-thick shell. The black dashed line indicates the depth of the Moho in PREM.

also significant. Measurements of Rayleigh waves primarily constrain δv_{SV}, whereas velocity of Love waves are controlled by δv_{SH}. Combined Rayleigh- and Love-wave data should therefore be able to resolve variations in anisotropic shear-wave velocities in the uppermost mantle, if this region is anisotropic. Our surface-wave data, however, provide little constraints on the structure at depths larger than 250 km. While 150-s Rayleigh waves have the maximum sensitivity to δv_{SV} at about 220 km, the sensitivity of Love waves decreases monotonically with depth. This means that anisotropic variations are constrained to even smaller depths than variations in velocity. To determine the Earth structure at 200 km and deeper, we need to use overtones and long-period mantle waves discussed in Section 2.4.

2.3.2 Linearized equations

As in Section 2.2.4, let m_k, where k=1,2,...6, indicate v_{PV}, v_{PH}, v_{SV}, v_{SH}, η, and ρ, respectively. This allows us to write equation 2.27 in a more compact form

$$\delta\omega = \int_0^a \sum_{k=1}^{6} \delta m^k K_k \, dr + K_{400}\delta h_{400} + K_{670}\delta h_{670}. \tag{2.28}$$

Let us also expand the unknown perturbations in model parameters according to 2.17. It is convenient to define basis functions f_j as a product

$$f_j(r,\theta,\phi) = B_b(r)S_s(\theta,\phi), \tag{2.29}$$

where the radial basis functions $B(r)$ and spherical basis functions $S(\theta,\phi)$ are further discussed in Section 2.5. Upon inserting 2.17 and 2.29 into 2.28 and interchanging the order of summation and

integration, we obtain

$$\delta\omega = \sum_{s=1}^{N_s} \sum_{b=1}^{N_b} S_s c_{bs} \left[\int_0^a B_b \sum_{k=1}^{6} m_0^k K_k \, dr + K_{400} + K_{670} \right], \tag{2.30}$$

where we set the radial basis functions B_b corresponding to the topography of the discontinuities to be equal to one. Let us define the radially integrated kernels as

$$V_b = \int_0^a B_b \sum_{k=1}^{6} m_0^k K_k \, dr + K_{400} + K_{670}. \tag{2.31}$$

Once the kernels V_b are calculated for each mode in a given reference model, they can be used in the inversion of both surface-wave phase anomalies and waveforms (Section 2.4). Combining 2.25, 2.26, 2.30, and 2.31, we obtain

$$\delta\Phi = \sum_s \sum_b c_{bs} \left[-\frac{V_b}{U_0} \int_0^a S_s \, ds \right], \tag{2.32}$$

where U_0 is the group velocity in the reference model. Using the correspondence between indices j, and b, s defined in 2.29, we write the term in brackets as A_j and obtain

$$\delta\Phi_i = \sum_j c_j A_{ij} \tag{2.33}$$

for the i-th phase anomaly. Formula 2.33 defines a system of linear equations with unknowns c_j, whose solution will be discussed in Section 2.5.

2.3.3 Crustal corrections

Measurements of surface waves, which we use to constrain the structure of the mantle, are also sensitive to the lateral heterogeneity in the crust, as shown in Figure 2.7. Instead of inverting for the crustal structure, we subtract predictions of CRUST2.0 (Bassin *et al.*, 2000) from the observations.

The phase anomalies $\delta\Phi$, which have been measured with respect to PREM, are related to the local perturbations in phase velocity $\delta c = c^{observed} - c^{PREM}$ by equation 2.25. We account for crustal effects on surface waves by referencing the local δc to the new reference model REF (Chapter 4) overlain by the laterally heterogeneous CRUST2.0. The corrected phase can be written as

$$\delta c^{corrected} = \left(c^{observed} - c^{PREM}\right) - \left(c^{REF+CRUST2.0} - c^{REF}\right). \qquad (2.34)$$

In order to find $c^{REF+CRUST2.0}$ at every surface point on the Earth, we build a number of one-dimensional, local, whole-earth models, with the core and mantle of REF, and the shallow structure defined by CRUST2.0 at a given latitude and longitude. CRUST2.0 is specified on a 2-by-2-degree grid with topography and bathymetry defined in ETOPO5 database. By rounding the topography and bathymetry to an integer number of kilometers, we reduce the number of distinct local models from over 16,000 to 812. For all such models we calculate normal-mode eigenfrequencies and phase-velocities of all Rayleigh and Love waves used in the inversion. Knowing $c^{REF+CRUST2.0}$ at every latitude and longitude, we correct the observed phase velocities while integrating along each path.

2.4 Waveforms

Seismologists often measure arrivals or body waves or surface-wave dispersion and use them to study the Earth's structure. Finding the relationship between travel times of body or surface waves and the structure is rather straightforward, and tomographic inversions take reasonable amount of computer time. It is more difficult to use the entire seismogram, instead of selected phases in tomographic inversions. If every sample of a digitally recorded seismogram were to be related to every coefficient of the mantle model, the inverse problem would be too large to be solved even on a modern computer. In 1984, Woodhouse and Dziewoński (hereafter WD84) developed a method, which made the waveform inversion computationally feasible, by employing the path-average approximation. We use this technique to build synthetic seismograms for three-dimensional models of the mantle and improve it by accounting for crustal effects using a new method outlined in Section 2.4.3.

2.4.1 Path-average approximation

In this section, we closely follow the theory presented in Woodhouse and Dziewoński (1984). A seismogram recorded at station r at location $\mathbf{x}_r$ for the s-th earthquake is a function of time t, and can be expressed as

$$U_i(t) = u_i(\mathbf{x}_r, t, \mathbf{i}_r, \mathbf{x}_s, t_s, \mathbf{f}_s, \oplus) + \varepsilon_i(t), \tag{2.35}$$

where the i-th observed seismogram U_i and the synthetic seismogram u_i are recorded and calculated for the s-th source and r-th receiver, and ε_i is the misfit. We assume that $\mathbf{x}_r$ and the instrumental

response $\mathbf{i}_r$ are known. The earthquake is characterized by a point source at location $\mathbf{x}_s$, origin time t_s, and the moment tensor $\mathbf{f}_s$. The synthetic seismogram is calculated for the three-dimensional model $\oplus$ of elastic parameters, attenuation, and density. We write the model as a sum

$$\oplus = \oplus_0 + \delta\oplus, \tag{2.36}$$

where $\oplus_0$ is a spherically symmetric reference Earth model, and $\delta\oplus$ is the three-dimensional perturbation to this model. We express $\delta\oplus$ in terms of coefficients c_{bs} of radial functions $B_b(r)$ and spherical functions $S_s(\theta, \phi)$

$$\delta\oplus = \sum_{b=1}^{N_b} \sum_{s=1}^{N_s} c_{bs} B_b(r) S_s(\theta, \phi). \tag{2.37}$$

The goal of the waveform inversion is to find the source parameters and the perturbation $\delta\oplus$ that minimize the misfit

$$\varepsilon^2 = \sum_i \int_{time} \varepsilon_i^2(t)\, dt = \sum_i \int_{time} \left[U_i(t) - u_i(t)\right]^2\, dt \tag{2.38}$$

between observed seismograms U_i and seismograms u_i predicted by the model $\oplus$. For simplicity, in equation 2.38, we omitted weights used to normalize the seismograms to the same mean-square value.

The synthetic seismogram is calculated by summation of normal modes and the assumption that the misfit ε_i is solely a result of the phase shift that accumulates as the waves sample the heterogeneous structure of the Earth. We use the path-average approximation and write the phase

perturbation for each mode as

$$\delta\psi = \int_0^t \delta\omega_{local}\, dt, \tag{2.39}$$

where the integral is taken with respect to the group travel time t along the great-circle path. The local perturbation in frequency ω_{local} is related to the local perturbation in phase velocity (equation 2.26), and represents laterally heterogeneous structure of the Earth. Equation 2.39 can be written in a more explicit form for odd and even orbits

$$\delta\psi = \begin{cases} \int_0^{t_1} \delta\omega_{local}\, dt + n\int_0^T \delta\omega_{local}\, dt & \text{odd orbits} \\ \int_0^{\bar{t}_1} \delta\omega_{local}\, dt + n\int_0^T \delta\omega_{local}\, dt & \text{even orbits,} \end{cases} \tag{2.40}$$

where n is the number of complete great circles traveled by the wave, and the group travel times T, t_1, and $\bar{t}_1 = T - t_1$ correspond to the time taken to traverse the great-circle, minor-arc, and major-arc paths, respectively. The phase perturbations can be mimicked by fictitious shifts in the frequency $\delta\widehat{\omega}$ and epicentral distance $\delta\Delta$, and written as

$$\delta\psi = \begin{cases} -(l+\frac{1}{2})\delta\Delta + \delta\widehat{\omega}(t_1 + nT) & \text{odd orbits} \\ (l+\frac{1}{2})\delta\Delta + \delta\widehat{\omega}(\bar{t}_1 + nT) & \text{even orbits,} \end{cases} \tag{2.41}$$

where l is the angular order of the mode. Upon equating 2.40 and 2.41, we obtain formulae for the

great-circle average of $\delta\omega_{local}$

$$\delta\widehat{\omega} = \frac{1}{T}\int_0^T \delta\omega_{local}\, dt, \tag{2.42}$$

and the distance perturbation

$$\delta\Delta = \frac{t_1}{(l+\frac{1}{2})}(\delta\widehat{\omega} - \delta\tilde{\omega}), \tag{2.43}$$

where the minor-arc average of $\delta\omega_{local}$ is given by

$$\delta\tilde{\omega} = \frac{1}{t_1}\int_0^{t_1} \delta\omega_{local}\, dt. \tag{2.44}$$

The frequency and distance shifts are used to calculate the synthetic seismogram u_i, which can be written as

$$u_i = \sum_j e^{i(\omega_j + \delta\widehat{\omega}^e + \delta\widehat{\omega}^a)t} \cdot \mathbf{a}_j(\Delta + \delta\Delta^e + \delta\Delta^a) \cdot \mathbf{f}, \tag{2.45}$$

where the excitation amplitude $\mathbf{a}_j$ and the hydrostatic ellipticity corrections $\delta\widehat{\omega}^e$ and $\delta\Delta^e$ are given by Gilbert and Dziewoński (1975) and WD84. The epicentral distance is indicated by Δ and ω_j is the eigenfrequency of the j-th mode in the spherically symmetric model. The frequency shift $\delta\widehat{\omega}^a$ due to aspherical structure is the great-circle average of $\delta\omega_{local}$, and for a given perturbation $\delta\oplus$, it

can be written as

$$\delta\widehat{\omega}_j^a = \sum_b V_{bj}\widehat{H}_b, \tag{2.46}$$

where V_{bj} are the radially integrated kernels for the j-th mode (equation 2.31), and

$$\widehat{H}_b = \sum_s c_{bs}\widehat{S}_s \quad \text{and} \quad \tilde{H}_b = \sum_s c_{bs}\tilde{S}_s. \tag{2.47}$$

Symbols '$\wedge$' and '$\sim$' on the right-hand side represent the great-circle and minor-arc averages of the amplitudes of the spherical functions S. The fictitious shift in epicentral distance is given by

$$\delta\Delta^a = \sum_b \frac{a\Delta}{(l+\frac{1}{2})U_j} V_{bj}(\widehat{H}_b - \tilde{H}_b), \tag{2.48}$$

where a=6371 km and U_j is the group velocity of the j-th mode. Equations 2.47 represent the concept of the path-average approximation (PAVA); the seismogram u_i depends on the average structure along the path rather than on all coefficients c_{bs}. This approximation allows for a very efficient calculation of synthetic seismograms in aspherical Earth models.

Li and Romanowicz (1995) compared the waveform inversions based on the PAVA and the nonlinear asymptotic coupling theory (NACT). The NACT takes into account cross-branch modal coupling neglected in the PAVA. The NACT sensitivity kernels are concentrated around the geometrical rays, while the PAVA sensitivity kernels are constant along the entire ray paths. Synthetic tests performed by Li and Romanowicz (1995) demonstrate that the two approximations retrieve nearly identical pattern of isotropic shear-wave velocity anomalies at all depths in the mantle except

the D$''$ region. The amplitudes of the recovered anomalies in the upper mantle are nearly identical for the PAVA and NACT, but the strength of the anomalies retrieved by the PAVA diminishes in the lower mantle. This experiment and the similarity of recent models obtained using the two methods (Chapter 6) indicate that the PAVA works very well in the upper mantle. The lower mantle anomalies that are underestimated by the PAVA can be successfully imaged by the measurements of body-wave travel times modeled using ray theory. This is demonstrated by the similarity of the lower mantle structures in the model of Megnin and Romanowicz (2000) obtained using the NACT and models constrained in the lower mantle by the measurements of body-wave travel times (Figure 4.18). However, the effects of different approximations on the anisotropic velocity variations have not yet been investigated.

2.4.2 Waveform inversion

Seismogram u depends nonlinearly on the heterogeneous velocity field, and therefore, determination of the Earth's structure requires iterations. Starting with the standard Centroid Moment Tensor solutions (Dziewoński *et al.*, 1981; Dziewoński and Woodhouse, 1983), we invert iteratively for the aspherical perturbation $\delta\oplus$, the moment tensors $\mathbf{f}$, and centroid locations $\mathbf{x}_s$ and times t_s. In order to invert for an incremental change δc_{bs} in structural parameters, we minimize the difference

$$U_i(t) - u_i(t, c_{bs}^{(0)}) = \sum_b \sum_s \frac{\partial u_i}{\partial c_{bs}}(t, c_{bs}^{(0)})\delta c_{bs} \tag{2.49}$$

for each path i. The synthetic seismogram is calculated from 2.45 using model parameters $c_{bs}^{(0)}$ from the previous iteration. Following WD84, we write the normal equation as

$$\sum_{b'} \sum_{s'} A_{bs;b's'} \delta c_{b's'} = b_{bs}, \tag{2.50}$$

where

$$A_{bs;b's'} = \sum_i \int \frac{\partial u_i}{\partial c_{bs}} \frac{\partial u_i}{\partial c_{b's'}} dt, \quad \text{and} \quad b_{bs} = \sum_i \int \frac{\partial u_i}{\partial c_{bs}} \left[U_i(t) - u_i(t, c_{bs}^{(0)}) \right] dt. \tag{2.51}$$

Using the path average approximation, we obtain

$$\begin{aligned} A_{bs;b's'} = \sum_i [& \tilde{S}_{si} \tilde{S}_{s'i} \int \frac{\partial u_i}{\partial \tilde{H}_{bi}} \frac{\partial u_i}{\partial \tilde{H}_{b'i}} dt + \tilde{S}_{si} \widehat{S}_{s'i} \int \frac{\partial u_i}{\partial \tilde{H}_{bi}} \frac{\partial u_i}{\partial \widehat{H}_{b'i}} dt \\ & + \widehat{S}_{si} \tilde{S}_{s'i} \int \frac{\partial u_i}{\partial \widehat{H}_{bi}} \frac{\partial u_i}{\partial \tilde{H}_{b'i}} dt + \widehat{S}_{si} \widehat{S}_{s'i} \int \frac{\partial u_i}{\partial \widehat{H}_{bi}} \frac{\partial u_i}{\partial \widehat{H}_{b'i}} dt], \end{aligned} \tag{2.52}$$

and

$$b_{bs} = \sum_i \left[\tilde{S}_{si} \int \frac{\partial u_i}{\partial \tilde{H}_{bi}} dt + \widehat{S}_{si} \int \frac{\partial u_i}{\partial \widehat{H}_{bi}} dt \right], \tag{2.53}$$

where the averages of S and H are calculated along the i-th path. Equations 2.52 and 2.53 include contributions from each seismogram to the inner-product matrix and data vector, and system of normal equation 2.50 can be solved using the methods discussed in Section 2.5.

The sensitivity of different modes used in the waveform inversion can be visualized as partial derivatives of eigenfrequency with respect to different model parameters. Figure 2.8 shows the

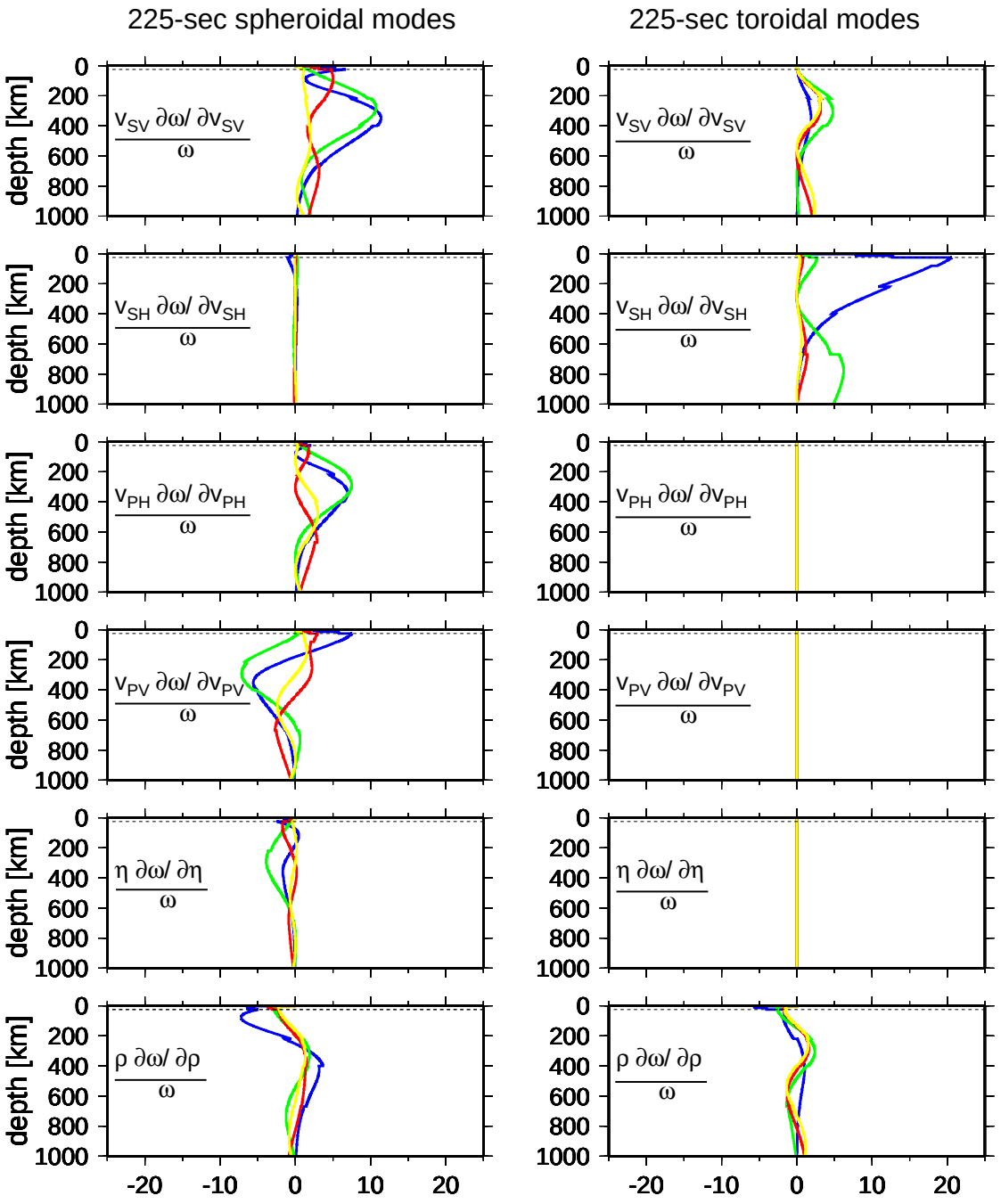

Figure 2.8: Sensitivity of the 225-second spheroidal and toroidal modes to the Earth's structure calculated using PREM. The fundamental mode is shown in blue, 1st overtone in green, 2nd overtone in red, 3rd overtone in yellow. The second spheroidal overtone is omitted because it is the Stoneley mode. The sensitivity kernels are nondimensionalized and they are defined in the same way as in Figure 2.7.

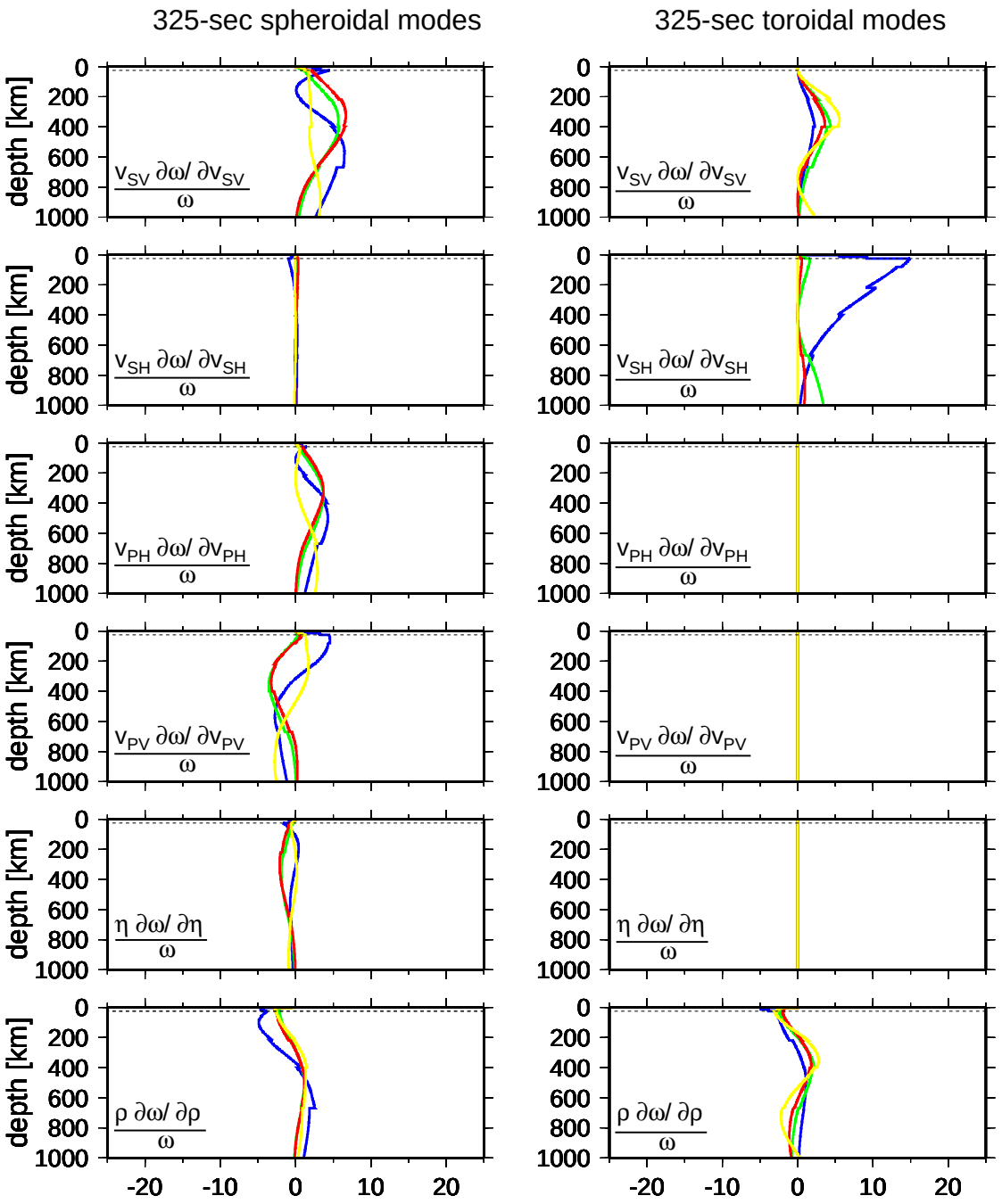

Figure 2.9: Sensitivity of the 325-second spheroidal and toroidal modes to the Earth's structure calculated using PREM. The fundamental mode is shown in blue, 1st overtone in green, 2nd overtone in red, 3rd overtone in yellow. The definition of the sensitivity kernels is the same as in Figure 2.7.

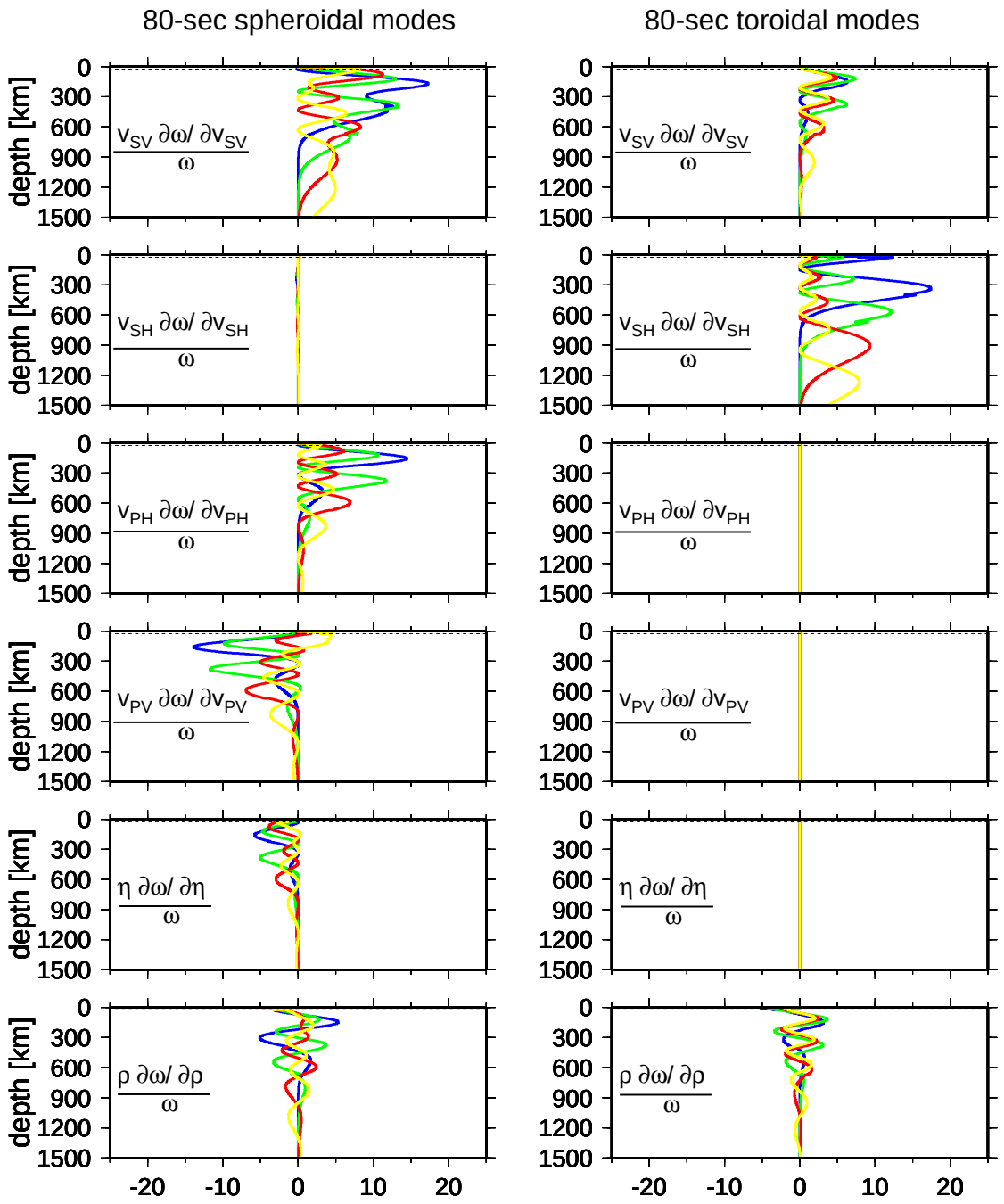

Figure 2.10: Sensitivity of the 80-second spheroidal and toroidal overtone modes to the Earth's structure calculated using PREM. The 1-st overtone is shown in blue, 2nd overtone in green, 3rd overtone in red, 4th overtone in yellow. The definition of the sensitivity kernels is the same as in Figure 2.7.

derivatives for normal-mode eigenfrequencies typical for the mantle-wave portion of the seismograms for 6.5$\leq M_W <$8.0 earthquakes. The long-period modes constrain δv_{SV} and δv_{SH} at significantly larger depths then short- and intermediate-period Rayleigh and Love waves (Figure 2.7). The first spheroidal overtone is as sensitive to the mantle structure as the fundamental mode and hence it is important to include it in the inversion. The sensitivity to variations in the compressional-wave velocities, η, and density are significant, but probably not sufficient to constrain the lateral variations in these parameters. Sensitivities to δv_{PH} and δv_{PV} are incorporated in the three-dimensional inversion assuming certain correlation between variations in compressional- and shear-wave velocities. For η and density, such correlations are not justified, but inversions for one-dimensional variations in these parameters are possible and may be important, as shown in Chapter 4.

Figure 2.9 shows the sensitivity of the very-long-period modes dominating the records of great earthquakes. The waves generated by these events sample the mantle deeper than the 225-second waves (Figure 2.8) and help to constrain the structure of the transition zone. Shorter-period overtones, shown in Figure 2.10, are sensitive to even larger depths.

While derivatives with respect to v_{PH} and v_{PV} have the same sign for some modes in the shallowest 200 km of the mantle, at larger depths, the two derivatives are almost mirror images of each other. This suggests that the sensitivity to variations in P-wave velocities is significant only in the uppermost mantle. At larger depths, spheroidal modes are more sensitive to the P-wave anisotropy than to P-wave isotropic velocity. This pattern is typical for overtones, which consist of body-waves reflected from the Earth's surface (Figure 2.10). Note that sensitivities of body-wave travel times to v_{PH} and v_{PV} plotted as a function of propagation direction show similar behavior (Figure 2.4).

2.4.3 Crustal corrections: a new method

The perturbation in normal-mode eigenfrequency due to a local perturbation in crustal structure can be found by subtracting the eigenfrequency calculated in a reference model from the eigenfrequency calculated in the reference model overlain by the local crustal structure. The crustal structure at a given latitude and longitude can be defined using a global model such as CRUST2.0 (Bassin *et al.*, 2000). Corrections of this type have been used to account for crustal effects on surface waves, but they have not been used in waveform inversions. While surface-wave inversions usually employ only about 20 fundamental modes, building a synthetic seismogram involves all modes up to a certain frequency. Calculating eigenfrequencies of thousands of modes in hundreds of models would be impractical. In addition, identification of many spheroidal mode branches in the reference and local models may be difficult or impossible.

Instead of calculating the exact corrections, WD84 developed a simple and computationally efficient linear approximation to account for perturbations in crustal thickness. We have found that the linear approximation calculated for only one reference model may break down when the perturbations are large, but using linear corrections predicted by four reference models is sufficient to account for nonlinear variations in frequency of all modes for all crustal types in CRUST2.0. Building on this observation, we have developed a new and more accurate method to correct a normal-mode seismogram for crustal effects and present technical details below. Our approach is similar to that of Montagner and Jobert (1988), who proposed that crustal corrections could be calculated accurately and efficiently by decomposing them into a linear and nonlinear part. Recently, this idea has been also implemented by Marone and Romanowicz (2006) in the waveform inversion based on NACT. These authors account not only for nonlinear effects of the crustal structure on the

normal-mode eigenfrequency but also incorporate five different reference models to calculate the sensitivity kernels. While it is not clear whether using variable sensitivity kernels has an appreciable effect on the resulting tomographic model, we will demonstrate that the nonlinear crustal effects on the normal-mode eigenfrequency are significant and should be taken into account in waveform inversions.

First, we build the four models that will serve as an intermediate step between the reference model and the local crustal structure. The models are identical to the reference model except for the shallowest part, which is defined in Table 2.1. For each model, we calculate eigenfrequencies of all modes up to a 40-s cut-off period, and partial derivatives corresponding to the perturbations in the crustal structure.

While integrating along the ray path (equations 2.42 - 2.44), we choose the most appropriate model out of four average models for every point of interest, and write the new correction as a sum

$$\delta\omega_{new} = \delta\omega_{exact} + \delta\omega_{linear}. \tag{2.54}$$

The exact part of the correction $\delta\omega_{exact}$ is the difference in frequency between the selected average model and the reference model. The exact corrections are subject to the mode identification problem, which we address and solve for almost all modes. The eigenfrequencies of free oscillations of the Earth are calculated using the method described in Dziewoński and Woodhouse (1983) and Woodhouse (1988). For a given angular degree l, modes are labeled with the overtone number n, which increases with the increasing eigenfrequency. Branches of spheroidal modes that are sensitive to the structure of the mantle are crossed by branches of the core modes. In different Earth models,

layer	v_p [km/s]	v_s [km/s]	density [g/cm^3]	thickness [km]
Oceanic: thickness of the solid crust = 7 km				
ocean	1.45	0.0	1.02	4
upper crust	4.1	2.0	2.5	2
middle crust	6.6	3.7	2.9	2
lower crust	7.1	3.9	3.0	3
Continental shelf: thickness of the solid crust = 20 km				
ocean	1.45	0.0	1.02	2
upper crust	4.5	2.4	2.6	8
middle crust	6.6	3.7	2.9	6
lower crust	7.2	4.0	3.1	6
Stable continent: thickness of the solid crust = 37 km				
ocean	-	-	-	0
upper crust	5.5	3.1	2.7	14
middle crust	6.5	3.7	2.9	12
lower crust	7.1	3.9	3.0	11
Orogenic: thickness of the solid crust = 57 km				
ocean	-	-	-	0
upper crust	5.8	3.3	2.7	21
middle crust	6.4	3.7	2.8	20
lower crust	7.1	3.9	3.1	16

Table 2.1: Average crustal models used in the calculation of crustal corrections. We combine the upper crust with sediment and ice layers in CRUST2.0. The oceanic, continental shelf, stable continental, and orogenic models are calculated by averaging crust with 12 km $\leq h_{sc}$, 12 km $\leq h_{sc} <$ 25 km, 25 km $\leq h_{sc} <$ 50 km, and $h_{sc} \leq$ 50 km, respectively, where h_{sc} stands for the thickness of the solid crust. In each layer, the thicknesses are averaged spherically, while slownesses and densities are averaged volumetrically.

the intersections occur in different places of the dispersion diagram. As a consequence, some modes cannot be identified by the overtone number. For example, a mantle mode in the reference model and a core mode in the continental model may be labeled with the same n and l. For each average model, we create a tentative list of all modes that may need to be renamed. The lists are created automatically based on the differences

$$q_{PREM}({}_nS_l) - q_{aver}({}_nS_l) \quad \text{and} \quad q_{PREM}({}_nS_l) - q_{aver}({}_{n+1}S_l), \tag{2.55}$$

were q is the attenuation, and the superscripts $PREM$ and $aver$ stand for the reference model

$PREM$ and any of the four average models, respectively. The attenuation of mantle modes is usually significantly different from that of core modes. We inspect plots, such as those shown in Figures 2.11-2.12, and correct the lists manually if necessary. Then, we modify overtone numbers so that the same type of oscillations were labeled with the same n. As an example, for PREM used as a reference, we rename 20, 16, 70 and 182 modes, for the oceanic, continental shelf, stable continental, and orogenic models, respectively. It should be borne in mind that while four normal-mode catalogs can be carefully inspected, such analysis for all crustal types defined in CRUST2.0 would be tedious even for the most dedicated researchers.

For low overtone numbers, all intersections correspond to the Stoneley models characterized by significantly different attenuation from the S and ScS modes. Therefore, all modes up to about the 20-th overtone can be properly identified for all average models. Several higher-order overtones in continental models cannot be identified correctly, but their amplitudes are negligible in the frequency range considered in our analysis of seismograms.

The linear part of the correction in equation 2.54 is obtained using perturbation theory as

$$\delta\omega_{linear} = \sum_{i=1}^{3} \int_{Moho}^{6371\ km} \left[\delta v_S^{(i)} K_v^{(i)} + \delta\rho^{(i)} K_\rho^{(i)}\right]\, dr + \sum_{j=1}^{5} \delta h_j K_j, \tag{2.56}$$

where i=1, 2, and 3 correspond to the lower, middle, and upper crust, and j= 1,2,...,5 to the top of the mantle, upper crust, middle crust, lower crust, and the ocean layer, respectively. To facilitate the linear part of the corrections, we combine the upper crust with sediment and ice layers in CRUST2.0. Partial derivatives $K_v^{(i)} = K_{v_s}^{(i)} + 0.8\ K_{v_p}^{(i)}$ and $K_\rho^{(i)}$ are calculated in the appropriate average model, and the perturbations in shear- and compressional-wave velocities v_s and v_p,

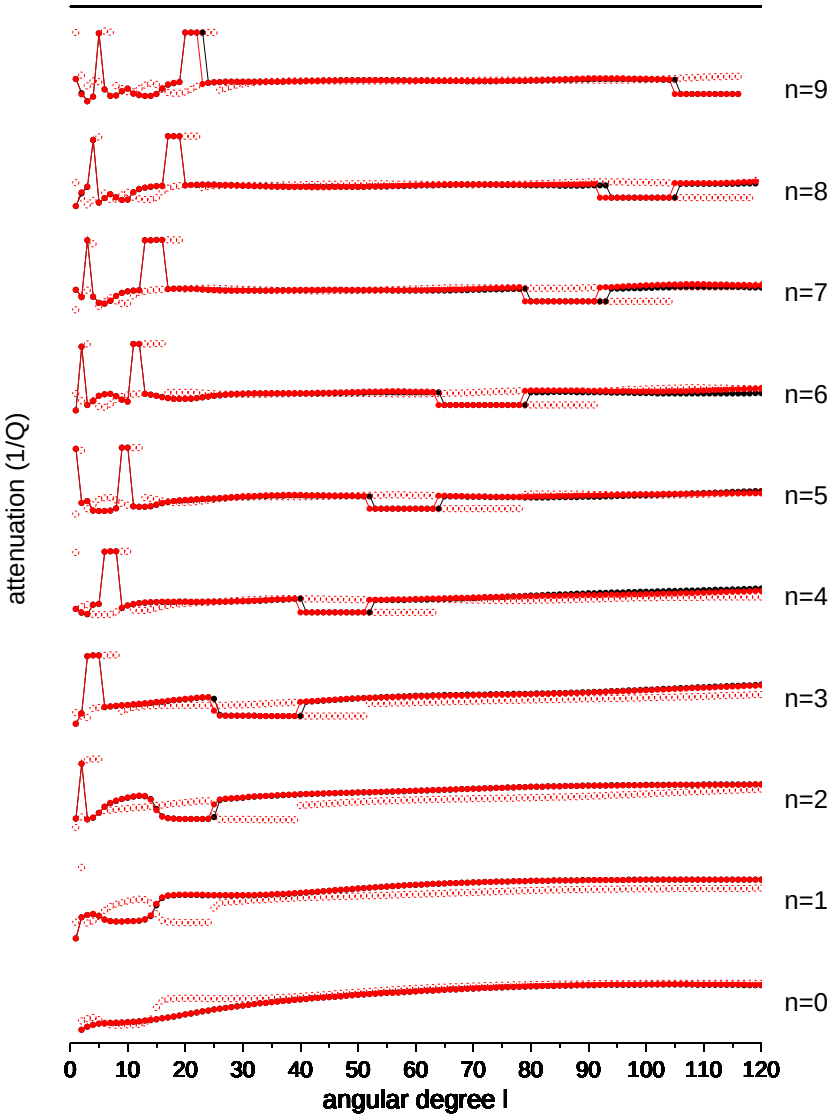

Figure 2.11: Attenuation of spheroidal modes for PREM is shown in black and for PREM overlain by the average continental model derived from CRUST2.0 is shown in red. Solid black and red circles correspond to the overtone number n listed on the right. Open red circles show the attenuation of the $(n+1)$-th overtone in the continental model. By plotting attenuation of the $(n+1)$-th overtone on top of the attenuation of the n-th mode, we can easily tell which one of the two modes in the continental model has attenuation similar to the n-th overtone in PREM. Typically, the n-th overtone in PREM shows similar attenuation to the n-th overtone in the continental model and distinctly different attenuation than the $(n+1)$-th overtone in the continental model. This indicates that same-type oscillations are labeled with the same overtone number n. For some modes, however, the opposite is true and the n-th and $(n+1)$-th overtone numbers need to be interchanged before we calculate the crustal corrections.

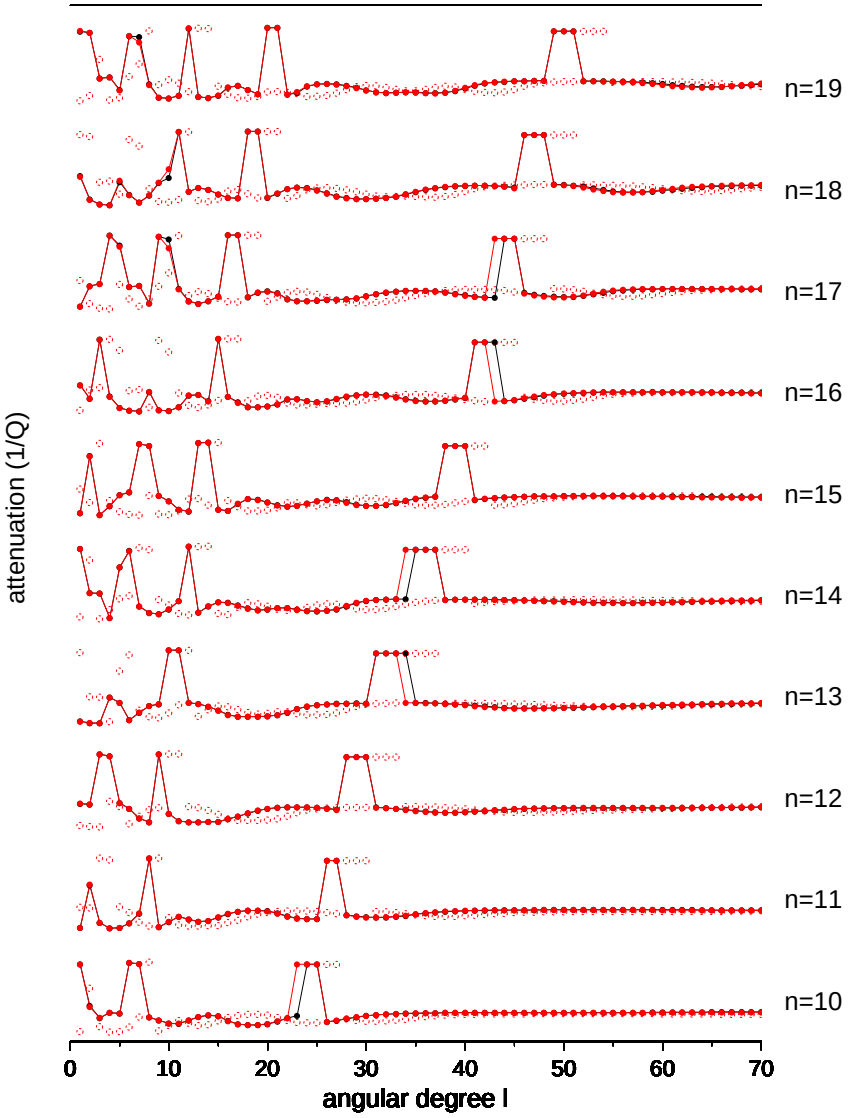

Figure 2.12: Same as Figure 2.11 but for higher overtones.

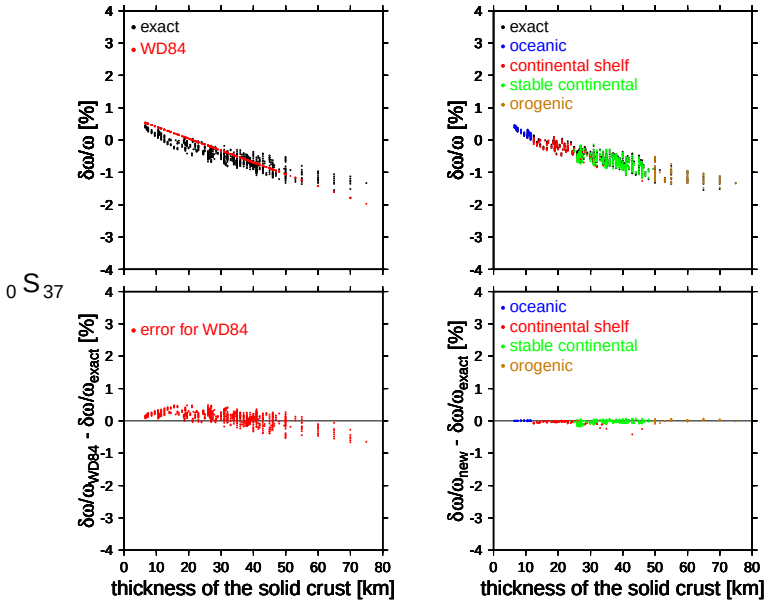

Figure 2.13: Exact and approximate perturbations in eigenfrequency for all 812 crustal types as a function of thickness of the solid crust. The reference model is PREM. The ${}_0S_{37}$ mode is equivalent to 225-second mantle waves. Relative perturbations in eigenfrequency are shown in the upper row while approximation errors are shown in the lower row. The left column corresponds to the WD84 corrections and the right column to the new corrections. Colors indicate different average models used to calculate the linear corrections. Note that the number of distinct crustal types does not represent their abundance. For example, 30% of the Earth's crust is defined by the two most common oceanic crustal types. We select average oceanic, continental shelf, stable continental, and orogenic models to correct for 57, 9.5, 31.75, and 1.75 % of the Earth's crust, respectively.

density ρ, and discontinuity depths h, describe the difference between the local crustal structure in CRUST2.0 and in the average model. Since in CRUST2.0, δv_p is strongly correlated with δv_s with the slope approximately equal to 0.8 and the intercept nearly equal to zero, we reduce the number of perturbations by including only variations in shear-wave velocity in the corrections and adding the partial derivatives with appropriate scaling.

The choice of the most appropriate average model for every point along the ray path depends on the local thickness of the solid crust h_{sc}. If 12 km $\leq h_{sc}$, 12 km $\leq h_{sc} <$ 25 km, 25 km $\leq h_{sc} <$ 50 km, or $h_{sc} \leq$ 50 km, we select the oceanic, continental shelf, stable continental or orogenic model, respectively. However, if the crust overlain by the ocean has 25 km $< h_{sc}$, we choose the

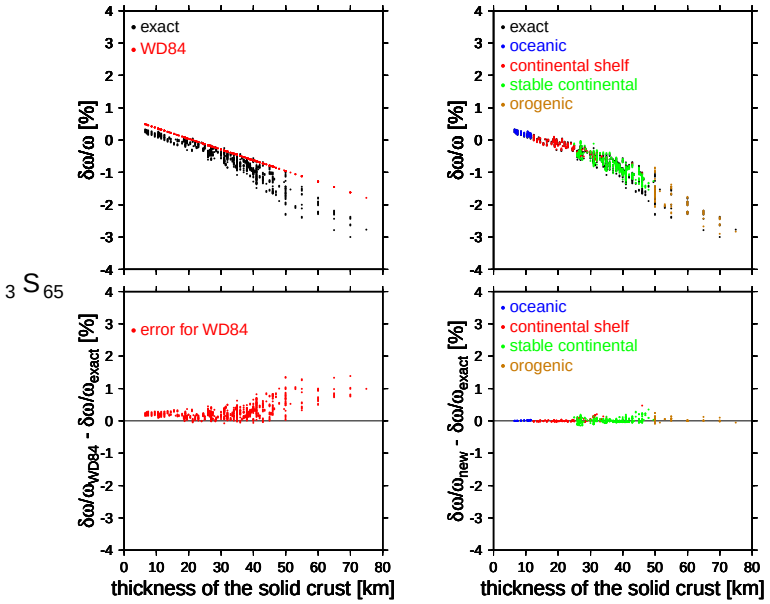

Figure 2.14: Same as Figure 2.13 but for a mode ${}_3S_{65}$, which is equivalent to 80-second body waves.

shelf instead of the stable continental model to account for the perturbation in thickness of the ocean layer.

The nonlinear behavior of frequency due to the perturbation in crustal thickness is shown in Figures 2.13 and 2.14. The slope of the WD84 corrections is appropriate around h_{sc} = 21.4 km, which is the thickness of the solid crust in the reference model PREM. The corrections are, however, inaccurate, because they do not include any details of the crustal structure. Strong nonlinearity is observed when the crust is very thick. In this case, the WD84 method overestimates or underestimates the true corrections by about 1% for some crustal types. The new method is clearly more accurate and accounts for the nonlinear behavior of the partial derivatives even in Tibet, where the crust is very thick. The error of the new corrections almost never exceeds 0.5%.

The crustal corrections and errors of different approximations are shown in a map view in Figures 2.15 and 2.16. The error of the WD84 corrections is systematic under the oceans, and large

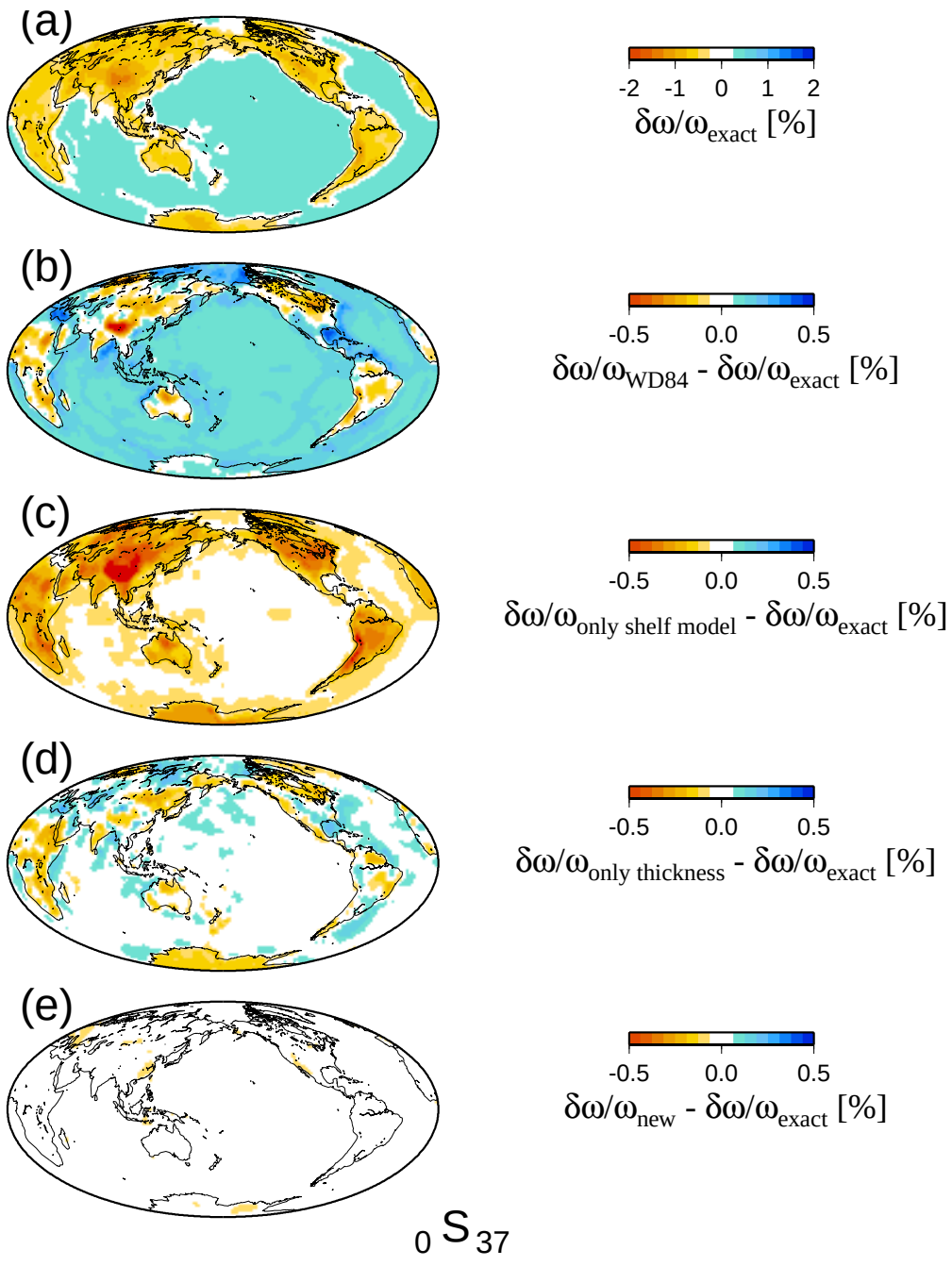

Figure 2.15: Crustal corrections and errors of different approximations for the mode ${}_0S_{37}$. (a) Exact correction for the reference model PREM and crustal model CRUST2.0 with the combined upper crustal layers. (b) Error of the WD84 correction. (c) Error of the correction calculated using only the continental shelf reference model and all linear corrections from equation 2.56. (d) Error of the correction calculated using four average models and perturbations $\delta\omega_{linear} = \delta h_1 K_1 + \delta h_4 K_4$. (e) Error of the new crustal correction calculated using four average models and all linear corrections from equation 2.56.

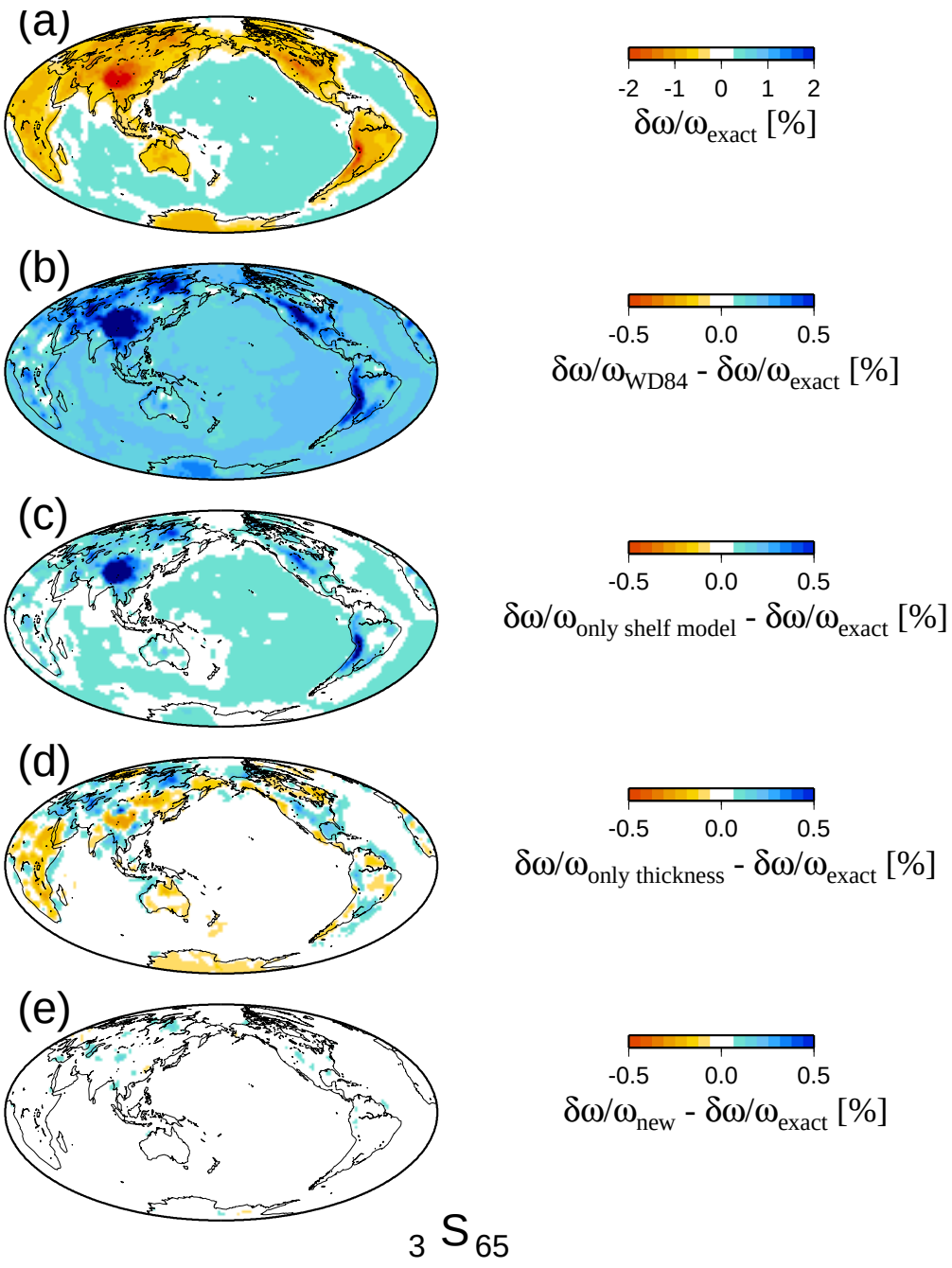

Figure 2.16: Same as Figure 2.15 but for the mode ${}_3S_{65}$.

in regions of thick crust, such as Tibet. If details of crustal structure are considered with only continental shelf model, the corrections are more accurate, but the linear approximation still breaks down under the continents. If we use all four average models and account only for perturbations in crustal thickness, the errors are rather small even in Tibet. Including information about details of the crustal structure further improves the approximation. In the map view, it becomes clear that the largest discrepancies shown in Figures 2.13 and 2.14 correspond to rather rare crustal types.

Application of our new method is computationally feasible. It is necessary to calculate four normal-mode catalogs and crustal partial derivatives, in addition to those calculated for the reference model. Mode identification is performed nearly automatically using a heuristically developed algorithm. Integration of crustal corrections along the ray path increases the time necessary to build synthetic seismograms by a factor of two for a three-dimensional model with about 12,000 free parameters.

2.5 The inverse problem

In Sections 2.2-2.4, we established linear relationships between different types of data and the perturbations in the transversely isotropic Earth model. In this section, we discuss the solution to the linear equations. Because tomographic models are represented in terms of the finite number of basis functions, we apply discrete inverse theory (Menke, 1989). We also explain our choice of regularization for the inverse problem for the spline parameterization of the model.

2.5.1 Solution to the inverse problem

Let us write a system of linear equations as

$$\mathbf{A}\mathbf{x} = \mathbf{d}, \tag{2.57}$$

where $\mathbf{x}$ is the vector of model unknowns, $\mathbf{d}$ is the data vector, and $\mathbf{A}$ is the matrix defining the sensitivity of each observation to each unknown. In the previous sections, we discussed the forward problem, that is the calculation of $\mathbf{d}$ based on the theory of wave propagation. Finding $\mathbf{x}$ from the measured $\mathbf{d}$ and known $\mathbf{A}$ is the inverse problem.

In tomographic inverse problems, the number of observations is usually different from the number of unknowns. Because $\mathbf{A}$ is not a square matrix, it does not possess an inverse, and the exact solution to equation 2.57 does not exist. In practice, we seek the least-squares solution $\mathbf{x}_{LS}$ that minimizes the norm $||\mathbf{A}\mathbf{x}_{LS} - \mathbf{d}||_2$. It can be shown that $\mathbf{x}_{LS}$ is the exact solution of

$$(\mathbf{A}^T\mathbf{A})\mathbf{x}_{LS} = \mathbf{A}^T\mathbf{d}. \tag{2.58}$$

Unless the inner-product matrix $\mathbf{A}^T\mathbf{A}$ is singular, its inverse exists. The solution of the system of normal equations 2.58

$$\mathbf{x}_{LS} = (\mathbf{A}^T\mathbf{A})^{-1}\mathbf{A}^T\mathbf{d} \tag{2.59}$$

can be obtained using a standard Cholesky factorization for positive definite matrices (Trefethen and Bau, 1997). If some unknowns are not sufficiently well-constrained by data, the inner-product

matrix may be singular or close to being singular, and equation 2.59 needs to be regularized. Errors in measurements may also lead to instability of the least-squares solution. We regularize the inverse problem by imposing *a priori* constraints, or damping, in the form

$$\mathbf{B}\mathbf{x} = \mathbf{c}. \tag{2.60}$$

The solution $\mathbf{x}_{DLS}$ of the damped least-squares problem

$$\begin{bmatrix} \mathbf{A} \\ \lambda\mathbf{B} \end{bmatrix} \mathbf{x}_{DLS} = \begin{bmatrix} \mathbf{d} \\ \lambda\mathbf{c} \end{bmatrix} \tag{2.61}$$

is a compromise controlled by λ between fitting the data and satisfying the *a priori* condition, and is given by

$$\mathbf{x}_{DLS} = (\mathbf{A}^T\mathbf{A} + \lambda^2\mathbf{B}^T\mathbf{B})^{-1}(\mathbf{A}^T\mathbf{d} + \lambda^2\mathbf{B}^T\mathbf{c}). \tag{2.62}$$

The inverse problem can always be solved if it is sufficiently regularized. However, the unknowns that are not well-constrained by the measurements will be determined primarily by damping (Boschi and Dziewoński, 1999), which may lead to erroneous interpretation of a tomographic model. In order to constrain the entire model as uniformly as possible, we combine different types of data and control the influence of individual observations on the solution by giving them different weights. The weighted damped least-squares solution can be written as

$$\mathbf{x}_{WDLS} = (\mathbf{A}^T\mathbf{W}\mathbf{A} + \lambda^2\mathbf{B}^T\mathbf{B})^{-1}(\mathbf{A}^T\mathbf{W}\mathbf{d} + \lambda^2\mathbf{B}^T\mathbf{c}). \tag{2.63}$$

Elements of the diagonal matrix $\mathbf{W}$ define weights given to contributions of individual observations to the inner-product matrix $\mathbf{A}^T\mathbf{A}$ and the vector $\mathbf{A}^T\mathbf{d}$.

2.5.2 Geometrical parameterization

In equation 2.17, we expressed the variations in the shear- and compressional-wave velocities, η, and density in terms of basis functions f_j. Because we assume that the elastic parameters and density very smoothly, we choose to parameterize the mantle using smooth functions such as splines or spherical harmonics rather than blocks, which are separated by sharp discontinuities, and allow for no variations between block boundaries. As before, we define each smooth basis function as the product

$$f_j(r, \theta, \phi) = B_b(r) S_s(\theta, \phi), \tag{2.64}$$

which allows to account for different radial and horizontal resolution as a function of depth. To describe variations in the radial direction, we use cubic B-splines (Lancaster and Salkauskas, 1986). An example of B-spline parameterization is shown in Figure 2.17. The spline amplitudes and dis-

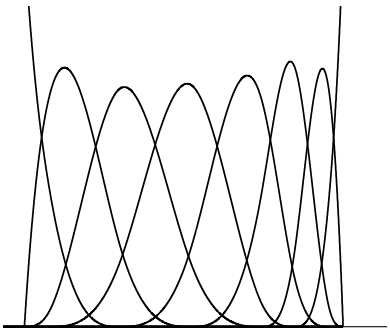

Figure 2.17: Cubic B-splines used to parameterize the model in the radial direction.

tance between adjacent splines may vary, but the sum of all splines must be the same at all depths.

Global tomographic models have been often parameterized in the horizontal direction in terms of real spherical harmonics defined as (Dahlen and Tromp, 1998)

$$Y_{lm}(\theta,\phi) = \begin{cases} \sqrt{2}X_{l|m|}(\theta)\cos(m\phi) & -l \le m < 0 \\ X_{l0}(\theta) & m = 0 \\ \sqrt{2}X_{lm}(\theta)\sin(m\phi) & 0 < m \le l, \end{cases} \tag{2.65}$$

where X_{lm} is the associated Legendre function of degree l and order m. In this work, we employed only degree-zero harmonics and used them to represent spherical averages in the inversion for a new one-dimensional reference model. Lateral variations are described in terms of spherical splines given by (Wang and Dahlen, 1995)

$$S_s(\theta,\phi) = \begin{cases} (\frac{3}{4}\frac{\Delta}{h} - \frac{3}{2})(\frac{\Delta}{h})^2 + 1 & \frac{\Delta}{h} \le 1 \\ \{[-\frac{1}{4}(\frac{\Delta}{h} - 1) + \frac{3}{4})(\frac{\Delta}{h} - 1) - \frac{3}{4}](\frac{\Delta}{h} - 1)\} + \frac{1}{4} & 1 < \frac{\Delta}{h} \le 2 \\ 0 & \frac{\Delta}{h} > 2. \end{cases} \tag{2.66}$$

The amplitude of the spline (Figure 2.18) changes smoothly with the epicentral distance Δ from the spline knot and depends on the average distance h between the knots of the adjacent splines. Spherical splines are local basis functions and can be easily distributed nonuniformly across the Earth's surface. Nonuniform nominal resolution has been used to account for nonuniform data coverage typical for tomographic problem (*e.g.,* Wang *et al.,* 1998; Bijwaard *et al.,* 1998; Boschi *et al.,* 2004; Nettles, 2005). In our study, a denser grid of splines will illuminate details of the

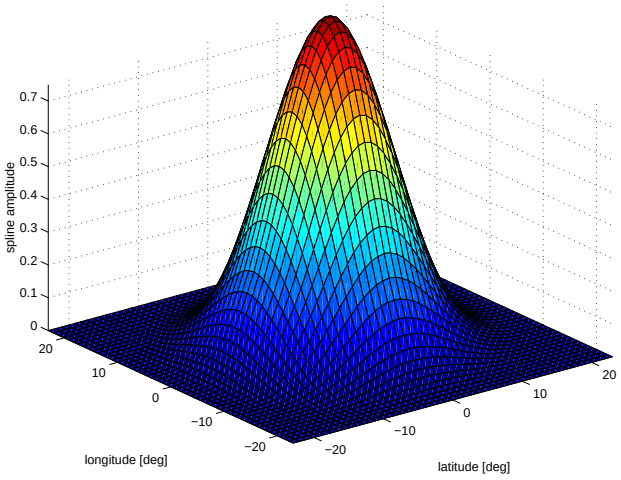

Figure 2.18: Amplitude of a spherical spline centered at the equator and the zero-th meridian. The average distance h is equal to 11.515 degrees as in the global model (Chapter 4), which is parameterized in terms of 362 uniformly distributed splines.

structure under Eurasia, which is crossed by more rays than the global average. Distribution of spline knots and representation of elastic parameters and density in terms of basis functions will be further discussed in Chapters 4 and 5.

2.5.3 Regularization

Because of imperfect data coverage and measurement errors, tomographic inversions have to be regularized by *a priori* constraints. In this work, we minimize the norm or gradient of the solution. For a spline parameterization, matrix **B**, which represents damping in equation 2.61, has to be computed numerically.

Let us express a three-dimensional model $\mathbf{x} = \mathbf{x}(r, \theta, \phi)$ as

$$\mathbf{x} = \sum_i c_i f_i, \tag{2.67}$$

where $f_i = f_i(r, \theta, \phi)$ are basis functions and c_i are model coefficients. To minimize the norm of the solution, we require the quantity

$$\int_V \mathbf{x}^2 dV = \int_V \left(\sum_i c_i f_i \right) \left(\sum_j c_j f_j \right) \, dV \tag{2.68}$$

to be minimum, where the integral is taken over the volume of the region, where regularization is needed. Differentiating with respect to the k-th coefficient c_k and using the chain rule gives

$$\int_V \sum_i \sum_j \left(\frac{\partial c_i}{\partial c_k} c_j + c_i \frac{\partial c_j}{\partial c_k} \right) f_i f_j \, dV = 0. \tag{2.69}$$

After some algebra, we obtain

$$\int_V \left(\delta_{ik} f_i \sum_j c_j f_j + \delta_{jk} f_j \sum_i c_i f_i \right) \, dV = 0, \tag{2.70}$$

or equivalently

$$\sum_i c_i \int_V f_i f_k \, dV = 0. \tag{2.71}$$

The integral defines entries of matrix **B** for norm damping. Similar derivation can be performed for the smoothness constraint. The quantity to be minimized is given by

$$\int_V (\nabla \mathbf{x})(\nabla \mathbf{x}) \, dV = \int_V \left(\sum_i c_i \nabla f_i \right) \left(\sum_j c_j \nabla f_j \right) \, dV. \tag{2.72}$$

Differentiating with respect to c_k, we obtain

$$\sum_i c_i \int_V (\nabla f_i)(\nabla f_k)\, dV = 0, \tag{2.73}$$

where the integral defines entries of the gradient damping matrix. Each basis function f_i is a product of radial and spherical basis functions (equation 2.64) and its gradient can be written explicitly as

$$\nabla f_j(r,\theta,\phi) = S_s(\theta,\phi)\left(\widehat{\mathbf{e}}_r \frac{\partial}{\partial r}\right) B_b(r) + \frac{B_b(r)}{r}\left(\widehat{\mathbf{e}}_\theta \frac{\partial}{\partial \theta} + \frac{1}{\sin\theta}\widehat{\mathbf{e}}_\phi \frac{\partial}{\partial \phi}\right) S_s(\theta,\phi), \tag{2.74}$$

where $\widehat{\mathbf{e}}_\mathbf{r}$, $\widehat{\mathbf{e}}_\theta$, and $\widehat{\mathbf{e}}_\phi$ are unit vectors in the spherical polar coordinates. Spherical splines are easily differentiable cubic polynomials. Radial derivatives of the B-splines can be also easily evaluated (Liu, 1997). In this work, we minimize the radial and horizontal components of the gradient separately, which allows for a better control on the *a priori* constraints.

Because the right-hand side of 2.71 and 2.73 are equal to zero, the weighted damped least-squares solution 2.63 reduces to

$$\mathbf{x}_{WDLS} = (\mathbf{A}^T\mathbf{W}\mathbf{A} + \lambda^2\mathbf{B}^T\mathbf{B})^{-1}(\mathbf{A}^T\mathbf{W}\mathbf{d}). \tag{2.75}$$

The choice of regularization criteria is arbitrary and may strongly affect the tomographic model, especially if the data coverage is poor. If the model $\mathbf{x}$ represents a three-dimensional perturbation with respect to a one-dimensional model, the norm damping tends to increase the correlation between the pattern of heterogeneity with the data coverage. In the inversion for a global model (Chapter 4), we choose the gradient minimization as a more appropriate *a priori* constraint. Minimization

of the Laplacian used, for example, by Trampert and Woodhouse (1995), or the minimization of higher-order derivatives, tends to suppress the smaller-scale components of the model. We do not apply this type of damping in this work. Alternatively, one may solve for the perturbation with respect to a three-dimensional starting model. Our regional model discussed in Chapter 5 is an example of such inversion. Because the norm damping makes the final model more dependent on the starting model than the gradient damping, we prefer to use the latter in the regional inversion. If some model parameters are not well-constrained, norm damping, which stabilizes the inverse problem very efficiently, may have to be combined with the roughness minimization. We minimized both vertical gradients and norm in the inversion for the one-dimensional model (Chapter 4).

Chapter 3

Data

Early tomographic models (*e.g.* Dziewoński *et al.*, 1977; van der Hilst *et al.*, 1997) were obtained using only travel times of teleseismic body waves, which are most sensitive to the heterogeneity near the turning point of the ray in the lower mantle. The uppermost mantle, on the other hand, is better sampled by short- and intermediate-period surface waves, and the transition zone is best sampled by long-period mantle and body waves. When only one type of data is used in the inversion, the resulting tomographic model will be well-constrained only in a limited range of depths and will not reflect the structure and dynamics of the whole mantle (*e.g.* Ritsema *et al.*, 2004). Models obtained from, for example, short-period surface waves do not provide reliable constraints on the thickness of the continental roots. Models obtained from travel times of teleseismic body waves, on the other hand, have gaps in the data coverage in the upper mantle. Following Dziewoński and Woodward (1992), Su *et al.* (1994), Ekström and Dziewoński (1998), and Gu *et al.* (2001a), we combine different types of data and invert them jointly for the shear-wave velocity structure in the whole mantle. Our data set is, however, superior to those used in previous studies. The new travel-time

data set is a combination of measurements made by researchers at Harvard and Scripps, which have never been inverted jointly. The surface-wave data set is several times larger than those used in the older global studies of the mantle. Perhaps most importantly, we have built a new set of waveform data using earthquakes recorded over the period of 10 years.

Given the expanded data, we attempt to learn more about the structure of the mantle compared to the earlier studies. First, we constrain independently vertical variations in v_{SH}, v_{SV}, v_{PH}, v_{PV}, and η, and build a new one-dimensional reference model. Second, we improve the resolution of the heterogeneous structure by using little damping in the global inversion and higher nominal resolution in the regional inversion for the structure beneath Eurasia. Finally, we attempt to determine the anisotropic structure in the lower mantle.

3.1 Body-wave travel times

Seismologists have long used arrival times of body waves to study the deep interior of the Earth. The most abundant collection of the arrivals is available through the bulletins of the International Seismological Centre (ISC). The ISC data are measured at relatively high frequencies of about 0.25-1 Hz, and have been used extensively to illuminate small-scale features such as, for example, lithospheric slabs (*e.g.* van der Hilst *et al.*, 1997). The bulletins contain arrivals measured by different operators at different stations and are, in general, noisy, containing many phase misidentifications and cannot be well-fit by tomographic models. In this work, we use higher-quality data obtained using cross-correlation techniques with dominating periods of about 20 seconds. These long-period and less abundant data constrain long-wavelength patterns of heterogeneity reliably, but their resolution power is not sufficient to delineate features as narrow as the lithospheric slabs.

Phase	Component	Number of observations	σ [s]
Harvard data (Liu, 1997; Liu and Dziewoński, 1998)			
S	H	27,660	2.88
SS	H	11,695	3.06
ScS	H	4,397	2.20
ScSScS	H	1,279	2.69
SS–S	H	5,671	1.63
ScS–S	H	3,471	1.41
S–SKS	H-V	3,671	2.34
SKKS–SKS	V-V	2,232	1.45
Scripps data (Bolton, 1996)			
SS–S	H	16,180	1.68
ScS–S	H	7,902	1.40
Harvard SS-precursor data (Gu and Dziewoński, 2002; Gu *et al.*, 2003)			
SS–S_{400}S	H	18,677	0.38
SS–S_{670}S	H	18,670	0.32
S_{400}S–S_{670}S	H	16,957	0.46

Table 3.1: Body-wave travel time data used in this study. The standard deviation σ of individual measurements for each data set is obtained by comparing residuals of rays traveling along similar paths. Symbols H and V indicate the horizontal and vertical components of seismograms, on which the arrivals were measured.

In this work, we combine three sets of arrival times summarized in Table 3.1. The most diverse data set has been collected at Harvard and consists of travel-time residuals measured by cross-correlation of the observed and synthetic seismograms. The synthetic seismograms have been calculated for PREM by summation of normal modes with a cut-off period of 8 s. Both absolute and differential measurements include diffracted S phases, which sample the lowermost part of the mantle. The second data set collected at Scripps consists of ScS–S and SS–S travel times measured through the cross-correlation of the observed ScS or the Hilbert transformed SS waveforms with the S-wave portion of the seismogram. The Scripps data set is much larger than the Harvard ScS–S and SS–S data sets, but it does not contain the diffracted S phases. This means that the two sets complement each other, and combining the two may help to better constrain the structure of the lower mantle.

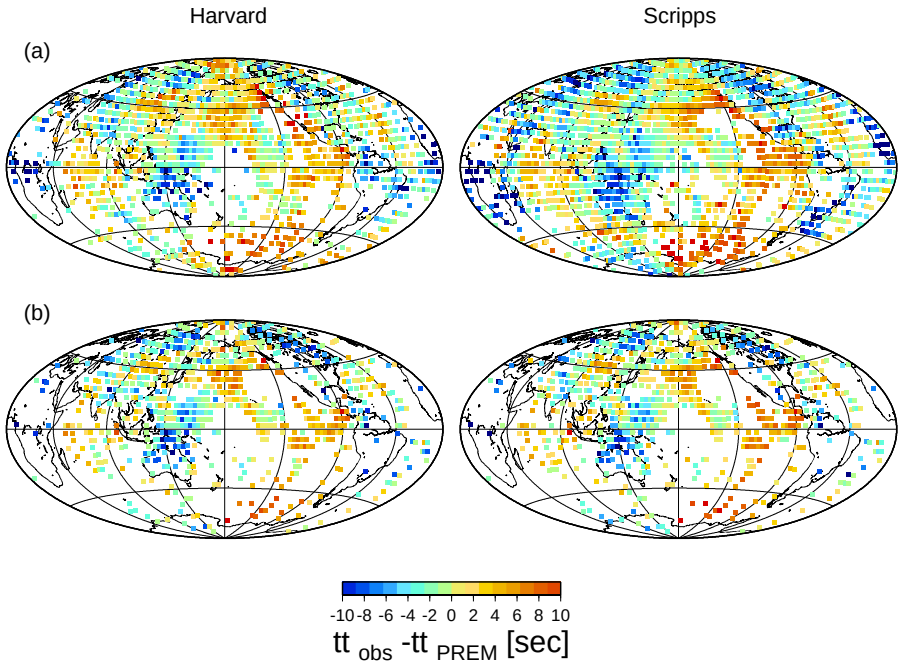

Figure 3.1: SS–S travel-time residuals averaged in 2-by-2-degree cells, plotted at the midpoint between the source and receiver. (a) All data. (b) Only those ray paths that have similar locations of sources and receivers in both data sets. A baseline shift of 1.1 s was added to the residuals measured at Scripps in both (a) and (b), as discussed in the test.

Because Harvard and Scripps data have been measured using different techniques, we investigate their consistency before inverting them jointly for the mantle velocity structure. We compare the two data sets by plotting the SS–S (Figure 3.1) and ScS–S (Figure 3.2) residuals at the location of the midpoints between epicenters and seismic stations. The travel times are corrected for the effects of the crust and Earth's ellipticity, but not for the effects of mantle heterogeneity. The residuals are averaged in 2-by-2-degree cells and plotted when at least one observation is available in the cell. When all data are included (Figure 3.1a), it is not clear whether the SS–S travel times measured using different techniques are consistent with each other. The difference results primarily from different ray-path coverage, and from the presence and lack of the diffracted S phases in the

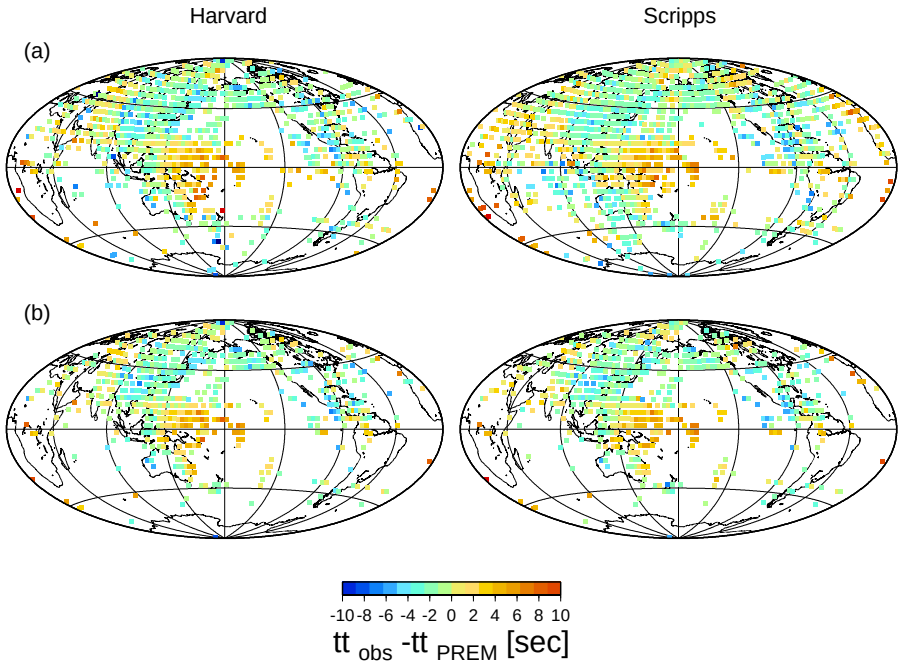

Figure 3.2: ScS–S travel-time residuals averaged in 2-by-2-degree cells, plotted at the midpoint between the source and receiver. (a) All data. (b) Only those ray paths that have similar locations of sources and receivers in both data sets.

Harvard and Scripps data, respectively. In order to make the comparison meaningful, we select only those ray paths that have similar locations of sources and receivers in both data sets. The overlapping subsets, which are again plotted at the locations of the midpoints, are very consistent with each other (Figure 3.1b). Despite similarity of the lateral variations, the average SS–S residual measured at Scripps is smaller by 2 seconds than that of Harvard, and by 1.1 s when only overlapping subsets are considered. We add the 1.1-second correction to the Scripps SS–S residuals prior to inversions. The baseline shift, which is not observed in the ScS–S travel times, might be related to the Hilbert transformation of the SS waveforms or propagation effects near the reflection point. The ScS–S phases measured at Harvard and Scripps (Figure 3.2) are consistent with each other even when all

data are plotted.

We also investigate whether the Harvard and Scripps data are of similar quality. The quality of different data sets is evaluated by analyzing residuals for rays traveling along similar ray paths. Let us consider the measurement error of the residual δt_i to be a random variable drawn from the distribution with the variance σ^2. The difference between two residuals drawn independently from this distribution will have the variance $\hat{\sigma}^2 = 2\sigma^2$. Assuming that the difference $\delta t_i - \delta t_j$ for a pair of rays i and j traveling very similar paths is a result of the normally distributed measurement errors, we can evaluate $\hat{\sigma}^2 = \sum_i \sum_{j \neq i} (\delta t_i - \delta t_j)^2 / n$ for all n pairs in a given data set. The standard deviation $\sigma = \sqrt{\hat{\sigma}^2/2}$ can be then interpreted as the uncertainty estimate of the individual measurement. The quality of differential travel times measured at Harvard and Scripps is very similar (Table 3.1), which, in conjunction with consistency of lateral variations and non-overlapping ray-path coverage, justifies combining the two data sets.

In the inversion of travel times, we prefer to give larger weights to data sets with smaller uncertainty. However, some data, such as the S–SKS residuals, which sample depth ranges not sufficiently constrained by other data, may be given large weights despite higher uncertainty. Relatively high uncertainties of the absolute travel-time measurements result from inaccuracies in the determination of the focal depths and in the crustal velocity structure. Differential observations are, in general, of much higher quality because they involve two rays traveling along almost identical paths near the source and receiver. Consequently, the differential measurements are significantly sensitive only to the subcrustal velocity structure except for the points of surface reflections.

The third data set consists of the precursors of the SS phase measured by Gu and Dziewoński (2002) and Gu *et al.* (2003). This collection provides the most uniform constraints on the topogra-

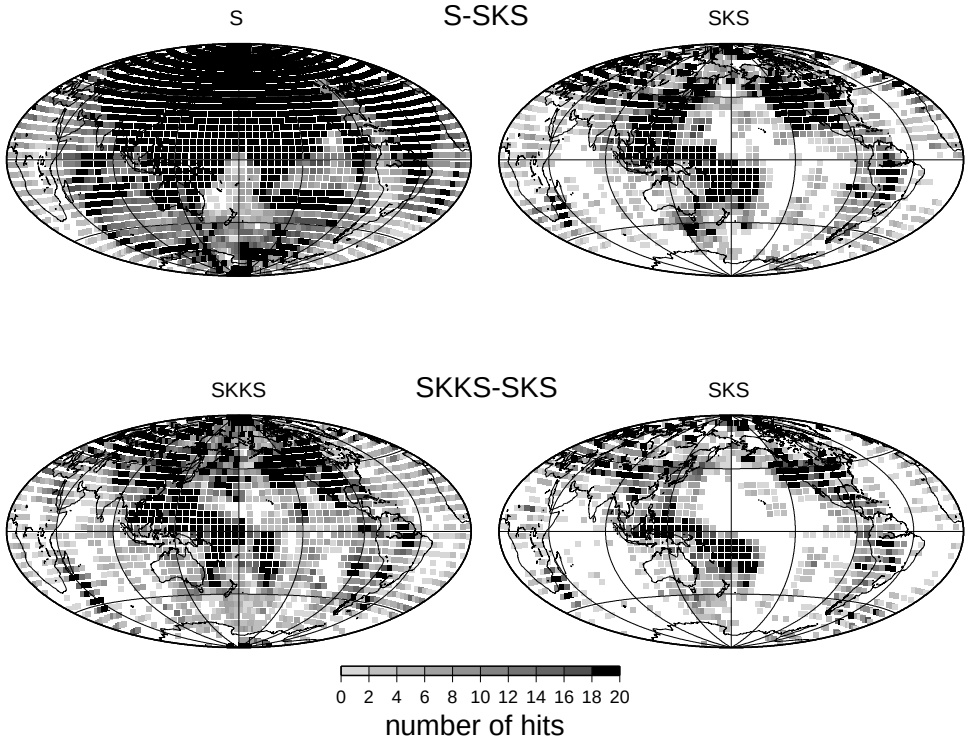

Figure 3.3: Ray-path coverage for individual rays in the S–SKS and SKKS–SKS data sets. The left and right columns correspond to the slower and faster traveling rays, respectively. The gray scale shows the number of rays crossing 5-by-5-degree cells in the lowermost 400 km of the mantle. The hit counts are corrected for different areas of cells at different latitudes. Cells that are not hit by any rays are not plotted.

phy of the transition zone discontinuities out of all data available to seismologists. The precursors have amplitudes too small to be measured on individual seismograms and need to be stacked using a cap-average technique. Owing to the large size of the Fresnel zone of the precursors, it is reasonable to stack seismograms for rays reflected in an area with a diameter as large as 1000-1500 km. This procedure gives residuals at the centers of about 410 approximately equal-area regions rather than residuals for individual rays. The latter, are, however, needed for the simultaneous inversion for the discontinuity topography and the mantle velocity structure. To determine residuals corresponding to individual rays, we follow Gu *et al.* (2003) and calculate them as weighted averages of the residuals at caps near the reflection point. The weight is equal to the amplitude of a spherical spline function,

which decreases with the increasing distance between the cap and the reflection point. To account for the uneven distribution of the data, we weight each residual in the inversion by the square root of the number of observations within the neighboring caps. As a consequence of the interpolation, the values of σ are very low, *i.e.*, the uncertainty is not a meaningful measure of quality of the SS-precursor data.

We wish to correct all our data using CRUST2.0, however, Gu *et al.* (2003) corrected individual seismograms for the effect of CRUST5.1 (Mooney *et al.*, 1998) prior to stacking. In order to improve consistency of the SS-precursor times with other data, we subtract the CRUST5.1 corrections for individual rays and add the CRUST2.0 correction calculated as described in Chapter 2.

An important issue that we attempt to address using travel-time data is the presence of anisotropy in the lowermost mantle. Recent tomographic studies (Panning, 2004; Panning and Romanowicz, 2004) suggest that the lowermost mantle may be anisotropic with v_{SH}, on average, faster than v_{SV}, with some regional perturbations from this trend. To check this result, we perform anisotropic inversions (Chapter 4) using body-wave travel times. In our data, most of the arrivals are recorded on the horizontal component of the seismogram, and therefore are primarily sensitive to the variations in v_{SH} near the bottoming point of the ray (Figure 2.4). The velocity of the vertically propagating shear waves in the lowermost mantle is constrained primarily by the S–SKS and SKKS–SKS times. The S–SKS waves are sensitive to the anisotropic variations, because diffracted S waves travel horizontally while the SKS rays crossing the lowermost mantle at steep angles are sensitive primarily to the variations in v_{SV}. The SKKS rays, which enter the core at shallower angles, are sensitive to anomalies in both v_{SH} and v_{SV} in the D$''$ region, and therefore also have some sensitivity to anisotropic variations. The ray path coverage of the S–SKS and SKKS–SKS data sets is shown in

	Love Waves		Rayleigh Waves	
Period [s]	Ekström *et al.* (1997)	this study	Ekström *et al.* (1997)	this study
35	15,189	58,405	27,948	162,715
37	15,221	58,405	27,986	162,715
40	15,484	59,152	28,140	163,574
45	15,561	59,340	28,251	164,148
50	22,282	81,766	36,301	203,982
60	22,879	83,859	36,994	206,560
75	22,947	83,904	37,240	206,487
100	22,271	79,430	36,876	199,559
150	16,599	55,510	33,092	160,470

Table 3.2: Number of phase anomalies selected for the inversion in this study and in Ekström *et al.* (1997).

Figure 3.3 in terms of the number of individual rays crossing 5-by-5-degree cells in the lowermost 400 km of the mantle. The SKS-coverage is not very good beneath the Indian and Atlantic oceans and under the eastern Pacific, but it is improved by the SKKS rays. Most importantly, the region beneath the western Pacific, which appears to show the strongest anisotropic perturbation from the global average (Chapter 4), is not associated with poor data coverage.

3.2 Surface-wave dispersion

The sensitivity of a surface wave to the Earth's structure is approximately constant along the entire ray path. Owing to excellent ray-path coverage, surface waves provide the best constraints on the lateral heterogeneity in the uppermost mantle out of all data available to geoscientists. Surface waves of different frequencies sample different depth ranges (Figure 2.7), and therefore measurements of dispersion can also resolve vertical variations in the velocity structure. In this work, we employ fundamental-mode Rayleigh and Love waves measured at nine periods between 35 and 150 seconds (Table 3.2). The phase anomalies have been collected by the seismology group at Harvard from seismograms recorded on the Global Seismographic Network and Federation of Broadband

Seismic Networks in the years 1992-2001. The measurement technique described by Ekström *et al.* (1997) involves fitting the observed seismograms in a series of frequency bands starting from the longest periods to avoid cycle skips. The synthetic seismograms are calculated using the Harvard Centroid Moment Tensor solutions (Dziewoński *et al.*, 1981; Dziewoński and Woodhouse, 1983). To isolate the fundamental-mode signal from that of overtones, only events shallower than 50 km were included.

In the inversion, we weight individual observations by the inverse of the uncertainty σ determined by Ekström *et al.* (1997). As in case of body waves, σ is estimated by analyzing measurements for waves traveling along similar paths. The uncertainties correlate well with the goodness-of-fit estimates (Ekström *et al.*, 1997; Nettles, 2005), which suggests that they are good measures of uncertainty.

Extending the phase-anomaly data set compared to that of Ekström *et al.* (1997) increased the number of observations by a factor of four for Love waves and five for Rayleigh waves. To illustrate the improvement in ray path coverage, we plot the number of rays crossing 3-by-3-degree cells for both data sets (Figure 3.4). Even the old data set provides a very good global coverage, which is further improved in our new data set. The path density is much higher in Eurasia than the average density. It is therefore reasonable to expect that the data can resolve more details of the structure beneath Eurasia, and to use higher nominal resolution in this region (Chapter 5). The improvement in path coverage is very significant in south-east Asia, India, and the Iranian Plateau.

The density of the 3-by-3-degree cells is similar to the density of the spherical-spline knots used to parameterize our regional model of Eurasia. Consequently, the hit-count maps show approximately the number of observations constraining coefficients of each horizontal basis function. In

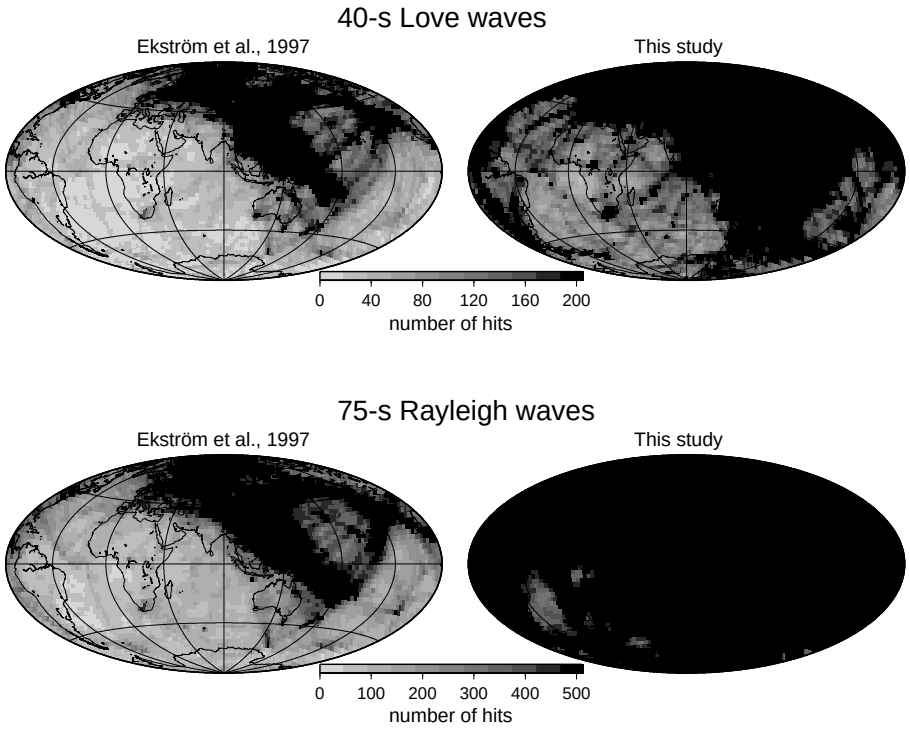

Figure 3.4: Ray-path coverage for surface-wave data used in this study and in Ekström *et al.* (1997). The gray scale corresponds to the number of rays crossing each cell. The 3-by-3-degree cells are comparable with the nominal resolution of the spherical-spline parameterization used in our regional model of Eurasia. The hit counts are corrected for different areas of the cells at different latitudes. In this work, we use only minor-arc observations.

the uppermost mantle beneath Eurasia, the inverse problem is overdetermined with more than 200 rays hitting each cell even for the smallest data sets of short-period Love waves. In the depth range controlled by surface waves, the lateral heterogeneity in our regional model will therefore be very well-constrained and will not depend significantly on the regularization of the inverse problem.

3.3 Mantle and body waveforms

Constraining the structure of the transition zone and uppermost lower mantle represents a major challenge in seismic tomography. Arrivals of body waves turning in this depth range are ex-

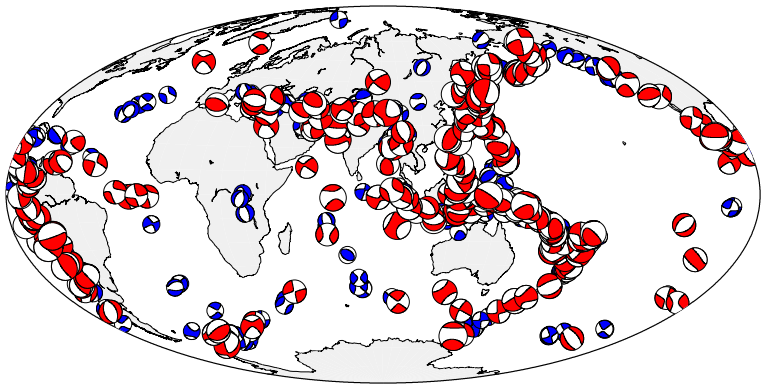

Figure 3.5: Our new waveform data set consists of 219 earthquakes of $6.5 \leq M_w < 8$ and 10 earthquakes of $M_w \geq 8$ from the years 1994-2003. CMT solutions for these events are shown in red. CMT solutions for the events with $6 \leq M_w < 6.5$ that are not included in our inversions, but may be used in the future, are shown in blue.

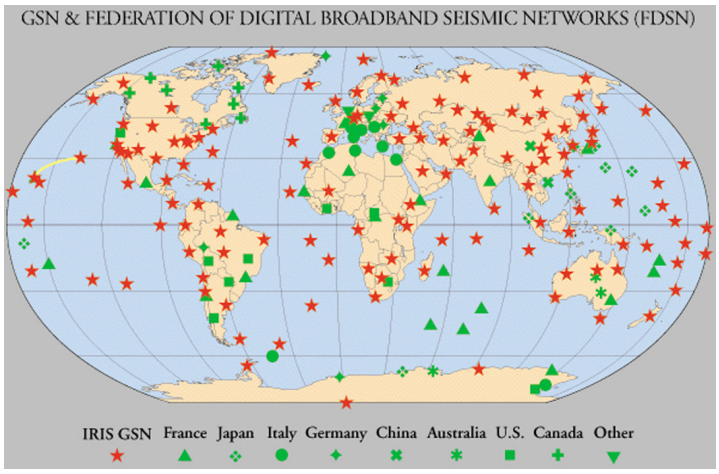

Figure 3.6: The distribution of the broadband seismic stations used in this study.

tremely difficult to identify because of the upper mantle triplications. The sensitivity of 30-150 s fundamental-mode surface waves is small below 250 km (Figure 2.7). Phases of longer-period waves, which sample the transition zone and uppermost lower mantle (Figures 2.8 and 2.9), are difficult to measure because of the decreasing signal-to-noise ratio. Woodhouse and Dziewoński (1984, 1989) and Dziewoński and Woodhouse (1987) developed a method, which incorporates long-period surface and body waves in tomographic inversion by fitting full waveforms rather than individual

This study			Gu *et al.* (2001a)		
Type	Component	Number of paths	Type	Component	Number of paths
Body Waves	V	22,522	Body waves	V+L	6,606
50 s $<$ T	L	22,106	45 s $<$ T	T	5,729
6.5 $\leq M_w <$ 8	T	19,117			
Mantle Waves	V	24,101	Mantle Waves	V+L	3,523
125 s $<$ T	L	16,440	85 s $<$ T	T	2,840
6.5 $\leq M_w <$ 8	T	17,656			
			Mantle Waves	V+L	3,353
			135 s $<$ T	T	2,810
			Mantle waves	V+L	3,470
			200 s $<$ T	T	1,880
Mantle Waves	V	1,062			
200 s $<$ T	L	939			
8 $\leq M_w$	T	1,034			

Table 3.3: Number of paths used in this study and in Gu *et al.* (2001a). Vertical, longitudinal, and transverse components of a seismogram are indicated by V, L, and T, respectively. Our new data set consists of 219 events with 6.5 $\leq M_w <$ 8, which are comparable in magnitude with the earthquakes used by Gu *et al.* (2001a). Additionally, we collect very-long-period seismograms of 10 great earthquakes.

arrivals. We use their method to match waveforms of fundamental modes and all overtones up to the cut-off frequency. The mathematical background of this technique is explained in Chapter 2.

Several mantle models obtained at Harvard have been constrained by fitting long-period waveforms (*e.g.*, Woodhouse and Dziewoński, 1984; Dziewoński and Woodward, 1992; Su *et al.*, 1994; Ekström and Dziewoński, 1998; Gu *et al.*, 2001a, 2003; Antolik *et al.*, 2003). The data sets used in these inversions, however, are rather small, and do not include seismograms available in the recent years. During the last decade, many new stations have been deployed in remote and previously not instrumented regions. The seismograms recorded at these sites provide new constraints on the structure of the Earth's mantle. We use seismograms from the years 1994-2003 to build a new set of 219 well-recorded $6.5 \leq M_w < 8$ earthquakes and 10 great ($M_w \geq 8$) earthquakes (Figure 3.5). The Harvard CMT solutions of these events are shown in red. The earthquakes with $6 \leq M_w < 6.5$,

which, at this point, are not included in the inversion, are shown in blue. We may use them in the future to improve the global coverage, even though the signal-to-noise ratio is not as good as for the larger events. Figure 3.6 shows the distribution of broadband seismic stations used in this study. The stations are distributed mainly on continents. Consequently, the data coverage is better in the northern hemisphere than in the southern hemisphere. In Table 3.3, we compare the number of seismograms used in this study and in Gu *et al.* (2001a). For $M_w < 8$ event, we have increased the number of paths by a factor of 3.5 to 12 for different types of waveforms. An additional data set is created from very long-period seismograms recorded for 10 great earthquakes. These data are very sensitive to the structure of the transition zone and uppermost lower mantle.

In order to ensure a good global coverage, we select earthquakes that have occurred over 10 years, and to decrease computational time, we divide the Earth into approximately equal-area 4-by-4-degree regions and typically select only the best-recorded event in each region. We allow two earthquakes in a region if they provide significantly different information about the Earth's structure due to different magnitudes or focal depths.

The seismograms of the 2003 earthquakes, as well as all $M_w < 6.5$ events, have been edited manually by Adam Dziewoński and the seismograms of the $M_w \geq 6.5$ from the years 1994-2002 have been edited automatically by Göran Ekström. The portion of a seismogram included in the inversion depends on the misfit between the data and the synthetics. When the fit is acceptable, the mantle waves included in the inversion contain the minor and major arc arrivals as well as the higher-order orbits. In Figure 3.7 we show examples of the seismograms, which include arrivals up to the fifth consecutive onsets of Rayleigh and Love waves. Smaller-amplitude phases away from major arrivals also provide useful information about the Earth's structure. For example, the v_{SV}

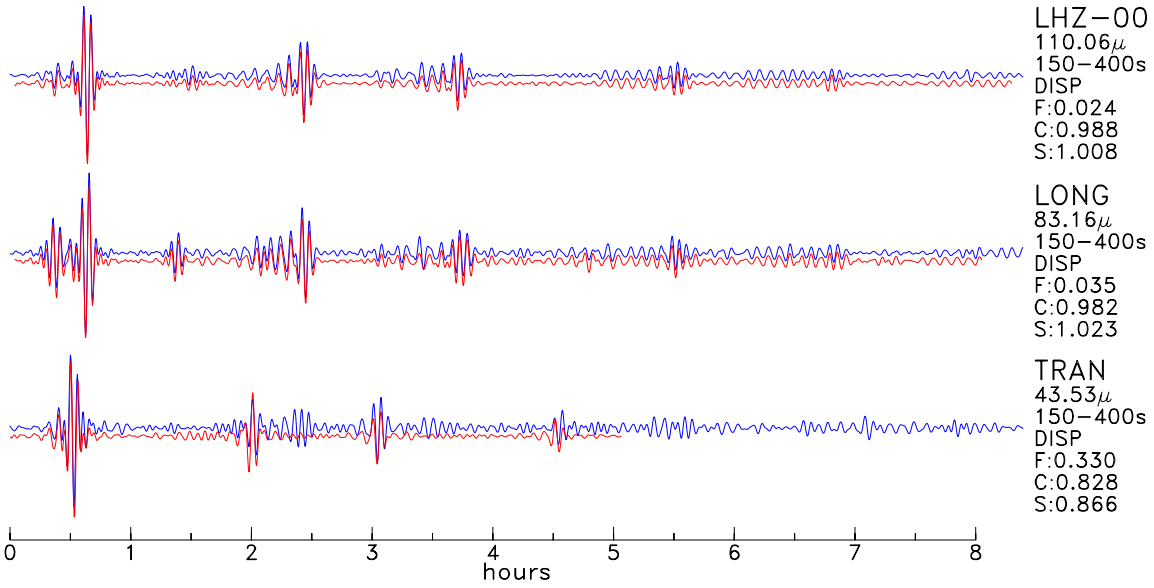

Figure 3.7: Three-component seismogram for mantle waves from the M_w=7.2 earthquake in western Siberia that occured on Sep 27, 2003. LHZ, LONG, and TRAN stand for the vertical, longitudinal, and transverse components, respectively. The seismograms have been filtered between 150 and 400 seconds. The observed seismograms are shown in blue while the synthetics are shown in red.

sensitivity of the first overtone preceding the major Rayleigh-wave arrival is as large as that of the fundamental Rayleigh wave of the same period (Figure 2.7).

Body-wave seismograms are filtered between 50 and 150 seconds and are usually dominated by the S and SS phases (Figure 3.8). In the CMT inversions, starting at M_w=6.5, body waves are given smaller weight than the mantle waves recorded on the same path, because the high-frequency contents of a seismogram diminishes with the increasing earthquake magnitude relative to the lower frequencies. The weight of body-wave seismograms approaches zero at M_w=7.5.

The vertical portions of the seismograms included in the inversion are usually longer that those recorded at longitudinal and transverse components, which may lead to overfitting of Rayleigh waves compared to Love waves. In order to constrain variations in v_{SH} as well as variations in v_{SV}, we build the inner-product matrices separately for different component data and weight them to

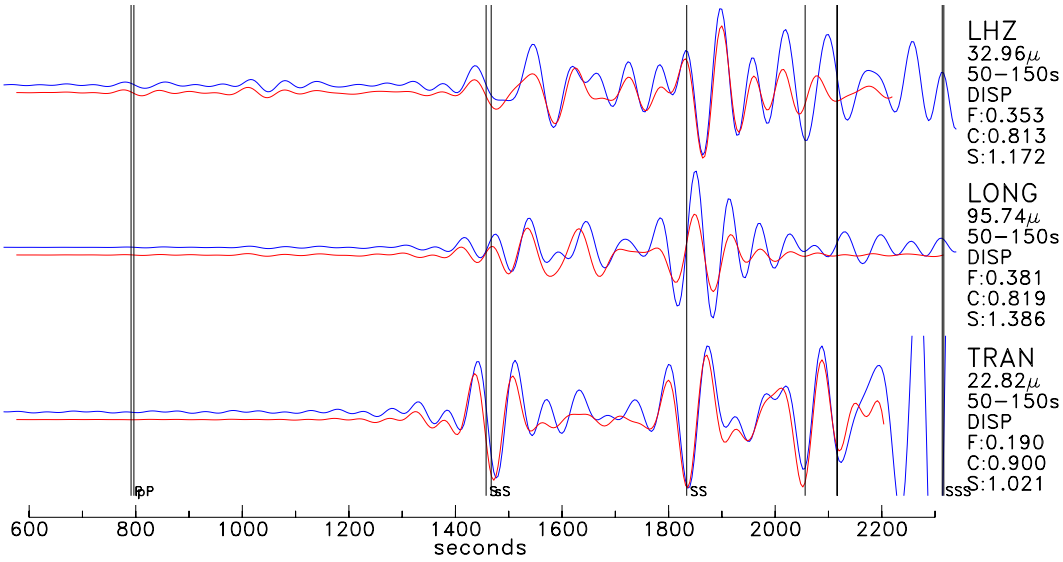

Figure 3.8: Same as 3.7 but for body waves filtered between 50 and 150 seconds.

have a similar size prior to the inversion. The average values of the weighted inner-product matrices corresponding to different data sets are plotted and further discussed in Section 4.2.2.

Chapter 4

Modeling velocity structure on a global scale

Tomographic velocity models provide most detailed view on the structure of the Earth's mantle out of all data available to geoscientists. While models of compressional-wave velocities offer higher resolution than the models of shear-waves, the mantle is sampled more uniformly by waves that are primarily sensitive to the variations in shear-wave velocities. In this chapter, we combine surface- and body-wave data that probe the mantle at all depths, and develop a new global three-dimensional whole-mantle model of shear-wave velocities.

Our new model, when compared with older models developed at Harvard (*e.g.* Gu *et al.*, 2001a), is constrained by a larger and more diverse data set, developed on top of a new reference model, accounts for lateral anisotropic variations, and nonlinear crustal effects on seismograms. We compare the new model with other tomographic models, and discuss implications on the dynamics of the Earth's mantle. We also isolate and quantify the effects of different improvements in the modeling

technique on the velocity structure and Centroid Moment Tensor (CMT) solutions.

4.1 New one-dimensional reference model

Anderson (1979) proposed that the Lehmann discontinuity at 220-km depth has a global extent and represents the base of a low velocity zone. The 220-km discontinuity defined as such was incorporated in PREM (Dziewoński and Anderson, 1981), where it also defines the base of the anisotropic layer. Anisotropic three-dimensional models (*e.g.*, Ekström and Dziewoński, 1998) calculated as a perturbation with respect to PREM show the same globally averaged anisotropic velocities as the reference model. Since the 220-km discontinuity now appears not to have a global extent (*e.g.*, Gu *et al.*, 2001b), or may be characterized by a negative velocity gradient (*e.g.* Grand and Helmberger, 1984; Kumar *et al.*, 2006), it is desirable to investigate anisotropic velocity structure in the mantle independently of PREM. Boschi and Ekström (2002) and Nettles (2005), for example, have started tomographic inversions using one-dimensional isotropic models without the 220-km discontinuity. Their final models show depth-variations of globally averaged anisotropic shear-wave velocities that are significantly different than in PREM. However, the authors have been unable to constrain parameters other than shear-wave velocities as they used only short- and intermediate-period surface waves in the inversion. Their models have P-wave velocities that are too fast above the 220-km discontinuity, and η equal to one at all depths, and consequently cannot fit long-period Rayleigh-wave and P-SV seismograms. Since our combined data are capable of resolving one-dimensional variations in all five elastic parameters of a transversely isotropic model, as well as the density, we invert for a new one-dimensional reference model of the mantle before building the three-dimensional model.

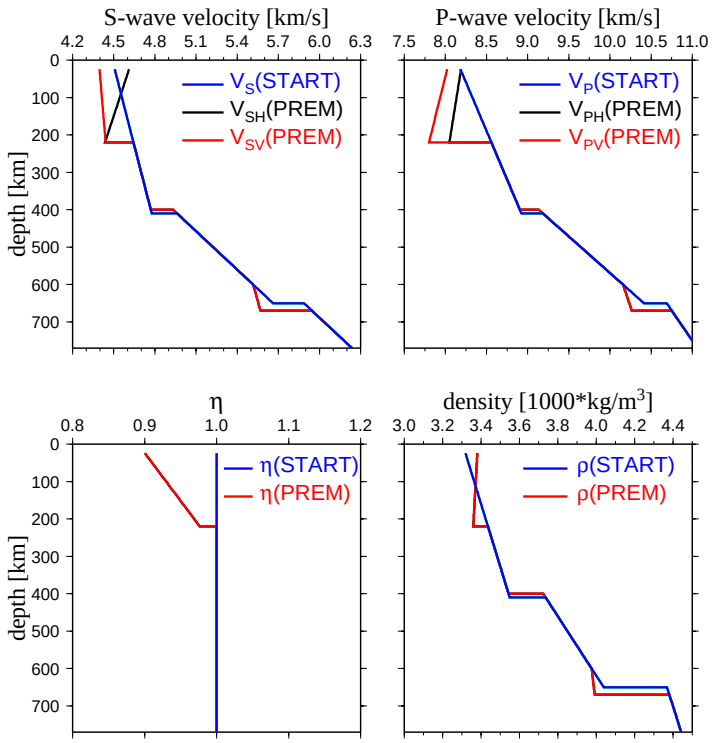

Figure 4.1: The starting model START used in the inversion for a new one-dimensional reference model of the mantle is shown in blue, PREM is shown in black and red. The changes with respect to PREM are accommodated by linear extrapolation at 220, 400, 600 and 670 km.

4.1.1 Starting model

The starting model START used in the inversion for a new one-dimensional reference mantle model is shown in Figure 4.1. To account for changes in elastic parameters, density, and attenuation with respect to PREM near 220, 400, 600, and 670 km, we use linear extrapolation. Our starting velocity model is isotropic at all depths and continuous at a depth of 220-km, similar to the starting model of Boschi and Ekström (2002) and Nettles (2005). Furthermore, we remove the second-order discontinuity at 600 km defined in PREM. We fix the boundaries of the transition zone discontinuities at 410 and 650 km. These depths are consistent with the most robust constraints available on topography of these discontinuities (Gu *et al.*, 2003). Flanagan and Shearer (1998), however,

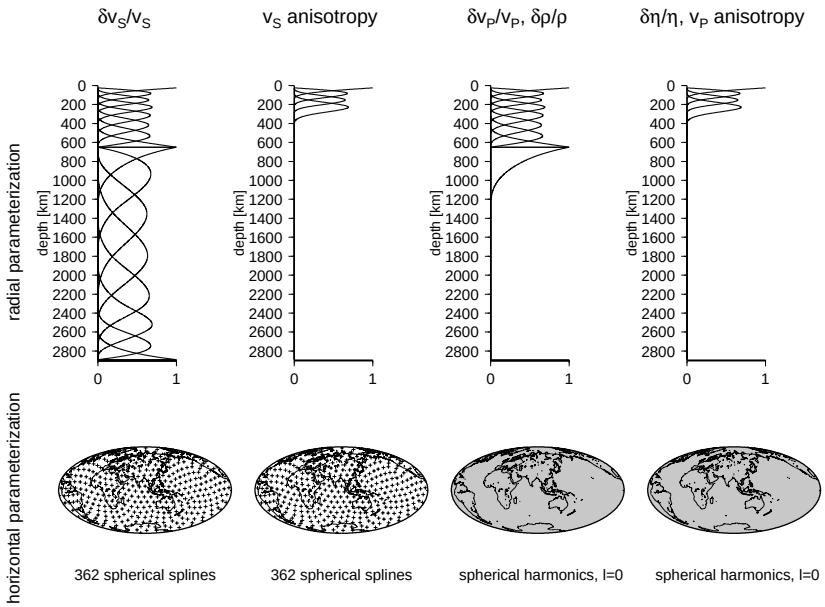

Figure 4.2: Three-dimensional parameterization used in the derivation of the new reference model REF of the mantle. At a given iteration, a new model is calculated as a spherical average of a three-dimensional perturbation with respect to the previous model. Pluses indicate knots of 362 spherical splines used to describe lateral variations in shear-wave velocity and anisotropy. Degree-zero spherical harmonics represent perturbations in compressional-wave velocity, anisotropy, η, and density. The number of cubic splines used to describe vertical variations varies between 4 and 16 for different parameters.

estimate the mean depths of these discontinuities to be 418 and 660 km, respectively. We replace the attenuation structure defined in PREM with that of the model QL6 (Durek and Ekström, 1996), which fits surface-wave and normal-mode data better. Unlike elastic parameters in START, the attenuation in QL6 is discontinuous at 80 and 220 km, which, however, leads to insignificant velocity discontinuities in the new reference model at periods other than the reference period of 1 second.

4.1.2 Parameterization and inversion

The new reference model is obtained through iterative inversion of all data described in Chapter 3 except for the measurements of the SS precursors. In the first iteration, we solve for perturbations with respect to START. The solution is then used as a reference model in the second iteration and

the final reference model is obtained after three iterations.

The density and η parameter are expanded over the basis functions according to equation 2.17. Instead of expanding perturbations in v_{SH}, v_{SV}, v_{PH}, and v_{PV}, we parameterize the model in terms of isotropic variations

$$\frac{\delta v_S}{v_S^0} = \frac{\frac{\delta v_{SH}}{v_{SH}^0} + \frac{\delta v_{SV}}{v_{SV}^0}}{2} \quad \text{and} \quad \frac{\delta v_P}{v_P^0} = \frac{\frac{\delta v_{PH}}{v_{PH}^0} + \frac{\delta v_{PV}}{v_{PV}^0}}{2}, \tag{4.1}$$

and anisotropic variations

$$\frac{\delta a_S}{a_S^0} = \frac{\delta v_{SH}}{v_{SH}^0} - \frac{\delta v_{SV}}{v_{SV}^0} \quad \text{and} \quad \frac{\delta a_P}{a_P^0} = \frac{\delta v_{PH}}{v_{PH}^0} - \frac{\delta v_{PV}}{v_{PV}^0}, \tag{4.2}$$

where the superscript '0' indicates the reference model from previous iteration, and a denotes a measure of anisotropy. Velocities of vertically and horizontally polarized waves can be retrieved from $\frac{\delta v_S}{v_S^0}$, $\frac{\delta a_S}{a_S^0}$, $\frac{\delta v_P}{v_P^0}$, and $\frac{\delta a_P}{a_P^0}$. Inverting for isotropic and anisotropic variations is, however, not equivalent to the inversion for velocities of horizontally and vertically polarized waves because the regularization affects different parameters. We prefer the former approach, because it allows for smooth variations in anisotropy, which is thought to reflect large-scale dynamic processes in the mantle.

To ensure good fit to all data, at a given iteration, we calculate the new model as a spherical average of a three-dimensional model rather than inverting for a spherically-symmetric model. More specifically, we solve for three-dimensional variations in shear-wave velocity and anisotropy, one-dimensional variations in compressional-wave velocity and anisotropy, η, density, and CMTs for all earthquakes. The compressional-wave velocities are determined independently of shear-wave

velocities.

Lateral variations in shear-wave velocity and anisotropy are expressed in terms of 362 spherical splines and the vertical variations are parameterized by 16 radial cubic splines (Figure 4.2). The model is heavily damped in the lower mantle so that the shear-wave velocity converges to PREM at a depth of 1320 km. Our data are unable to resolve lateral variations in the compressional wave velocities, η, and density, and therefore we invert only for global averages in these parameters at each depth. The global averages of compressional-wave velocities and density are quite well-constrained by our data in the upper and mid-mantle, but not as well constrained in the lowermost mantle. Since START is different than PREM in the upper mantle and the uppermost lower mantle, we use all upper mantle splines and one spline in the lower mantle in the inversion for the density and v_P. The density and v_P converge to PREM as the amplitude of the lower mantle spline converges to zero at 1320 km. We find η and anisotropic variations below 220 km to be small and constrain them to vanish at 410 km by using only the four uppermost splines.

Density perturbations $\frac{\delta\rho}{\rho_0}$ are additionally constrained to match the total mass and moment of inertia of the Earth by

$$M_{TRUE} - M_0 = \int_0^R 4\pi r^2 \rho_0 \frac{\delta\rho}{\rho_0}\, dr \tag{4.3}$$

and

$$I_{TRUE} - I_0 = \int_0^R 4\pi r^2 (\frac{2}{3} r^2) \rho_0 \frac{\delta\rho}{\rho_0}\, dr, \tag{4.4}$$

where the integral is taken over the radius r, R is 6371 km, M_{TRUE} of $5.974 \cdot 10^{24}$ kg is the Earth's

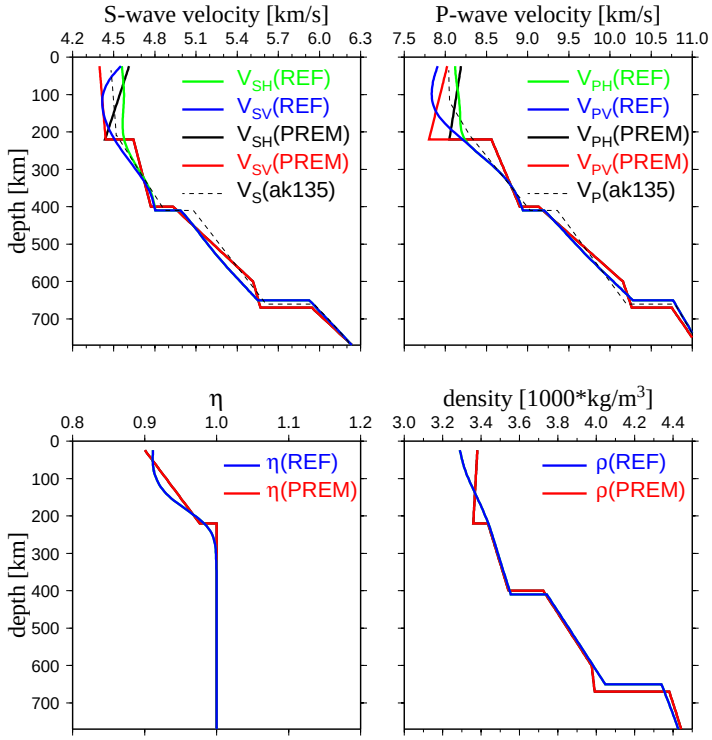

Figure 4.3: The new reference model REF plotted with PREM (Dziewoński and Anderson, 1981) and ak135 (Kennett *et al.*, 1995). Our new reference model REF is continuous at 220 km. Shear-wave anisotropy is maximum at about 125 km, and becomes very weak below 220 km. The profile of η is consistent with PREM. The average v_P at shallow depths is slower than in PREM and is similar to that in the model ak135 constrained by P and P_n travel times.

mass, and the moment of inertia I_{TRUE} is given by 0.3308 $M_{TRUE}R^2$, as in PREM (Dziewoński and Anderson, 1981).

4.1.3 New reference model

In order to independently solve for variations in six parameters, we find it necessary to regularize the inverse problem using a combination of smoothness and norm damping. Nevertheless, the following features of the new model are robust and do not depend strongly on regularization. The new model REF, unlike PREM, but in agreement with Nettles (2005), has the maximum shear-wave anisotropy at about 125 km (Figure 4.3). In order to fit the waveform data as well as PREM, η must be less

than one in the top 200 km of the mantle, and compressional-wave velocities must be significantly lower than those of Nettles (2005), which were obtained by scaling $\delta v_P/v_P = 0.55\ \delta v_S/v_S$. The profile of η in the new model is similar to that in PREM. Although the anisotropic discontinuity is not imposed at 220 km, we find, in agreement with PREM, that significant anisotropy is not required by the data below this depth. In REF, anisotropy is therefore constrained to vanish at 410 km.

The following features of the model are not very well constrained or depend strongly on damping. The strength of anisotropy of compressional waves trades off with density and η, and it is not clear whether it is indeed different than that of shear waves. The average P_n velocity in REF is lower than in PREM and similar to that in model ak135 (Kennett *et al.*, 1995) constrained by P and P_n data. The presence and strength of positive $\partial v_P/\partial r$ gradients depends on damping and cannot be well resolved by surface-wave data. The positive $\partial\rho/\partial r$ gradient observed in PREM is not required to fit the data, but the details of the density profile also strongly depends on regularization. Elevating the top of the lower mantle by 20 km is compensated by reduced velocities in the upper mantle and density in the lower mantle. The radial resolution in this depth range is, however, poor, and the perturbations in velocity and density are distributed over several hundred kilometers.

We conclude that one-dimensional shear-wave velocity structure in REF is well-constrained by our data, and that other parameters, whose determination is necessary to fit the data, show variations at least as reasonable as those in PREM.

4.2 Global three-dimensional shear-wave velocity model

Our new three-dimensional model S362ANI is calculated using the same techniques as we used in the derivation of the reference model REF. The data set is extended by adding the measure-

ments of travel times of SS precursors. The parameterization of the three-dimensional model is slightly different since we invert for the topography of the discontinuities but not for the variations in compressional-wave velocities, η, and density. In this section, we compare S362ANI with other tomographic models and discuss the similarities and differences in the context of mantle dynamics. We also investigate the effect of improvements in the model on the velocity structure and the CMT solutions.

4.2.1 Parameterization

Although our combined data are able to determine vertical variations in five elastic parameters and density in the mantle, they do not provide enough constraints to resolve laterally heterogeneous structure in all these parameters. To reduce the number of free parameters, it is necessary to use simplifying assumptions about the elastic tensor. We follow Ekström and Dziewoński (1998), and assume that

$$\frac{\delta v_{PH}}{v_{PH}} = 0.55\frac{\delta v_{SH}}{v_{SH}}, \quad \text{and} \quad \frac{\delta v_{PV}}{v_{PV}} = 0.55\frac{\delta v_{SV}}{v_{SV}}, \tag{4.5}$$

where all perturbations are defined with respect to REF. The scaling between relative perturbations in equation 4.5 is roughly consistent with the anomalies predicted for purely thermal effects (Karato, 1993) and with the modeling of compressional- and shear-wave velocity in the mantle (Robertson and Woodhouse, 1996; Su and Dziewoński, 1997; Masters *et al.*, 2000). These tomographic studies indicate that in the lowermost mantle, however, the scaling factor may be about two times lower and v_P and v_S may not correlate perfectly. Our data are sensitive primarily to the variations in shear-wave velocities and do not have enough resolving power to determine the scaling factor. Our

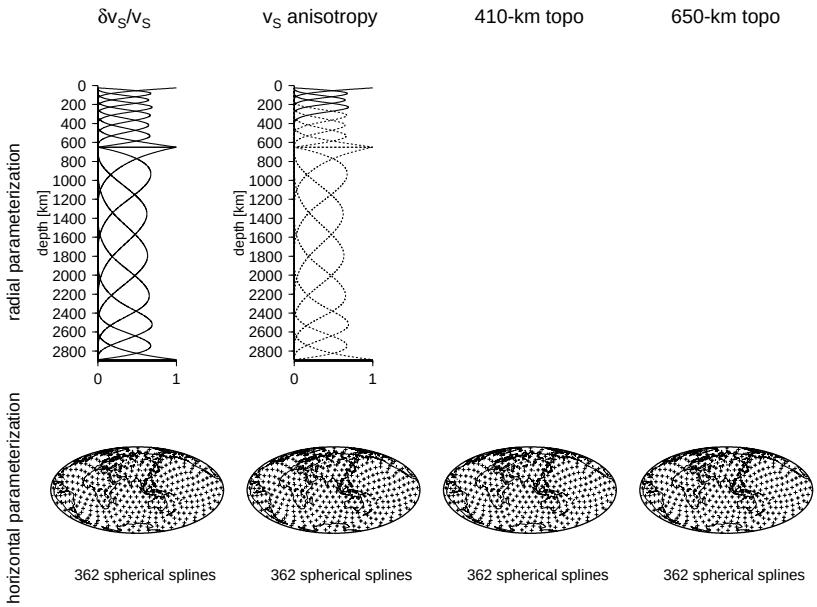

Figure 4.4: Parameterization of the new global three-dimensional model of shear-wave velocity in the mantle. Pluses indicate knots of 362 spherical splines used to parameterize lateral heterogeneity in shear-wave velocity and anisotropy, as well as topography of the 410- and 650-km discontinuities. Vertical variations in isotropic velocity are parameterized in terms of 16 cubic splines split at 650 km. In our preferred model S362ANI, we use only the four uppermost splines (solid line) to parameterize anisotropic variations. In the experiment described in Section 4.2.5, we invert for anisotropic variations using all 16 splines (dashed line).

experiments indicate, however, that models obtained using the scaling factor equal to 0.55 are nearly identical to those obtained using the factor equal to 1.

As in the derivation of the reference model, we invert for isotropic and anisotropic variations in shear-wave velocity (equations 4.1 and 4.2) rather than for $\frac{\delta v_{SH}}{v_{SH}}$ and $\frac{\delta v_{SV}}{v_{SV}}$. This approach allows us to minimize the roughness of both isotropic and anisotropic velocity variations. Petrological constraints suggest that there is a correlation between compressional- and shear-wave anisotropy (Montagner and Anderson, 1989), and therefore in equation 4.5 we scale velocities of both horizontally and vertically polarized waves, which is equivalent to scaling the isotropic and anisotropic perturbations. Finally, we neglect the sensitivity of our data to lateral variations in η and density.

Figure 4.4 shows the geometrical parameterization of the global 3-D model. Shear-wave veloc-

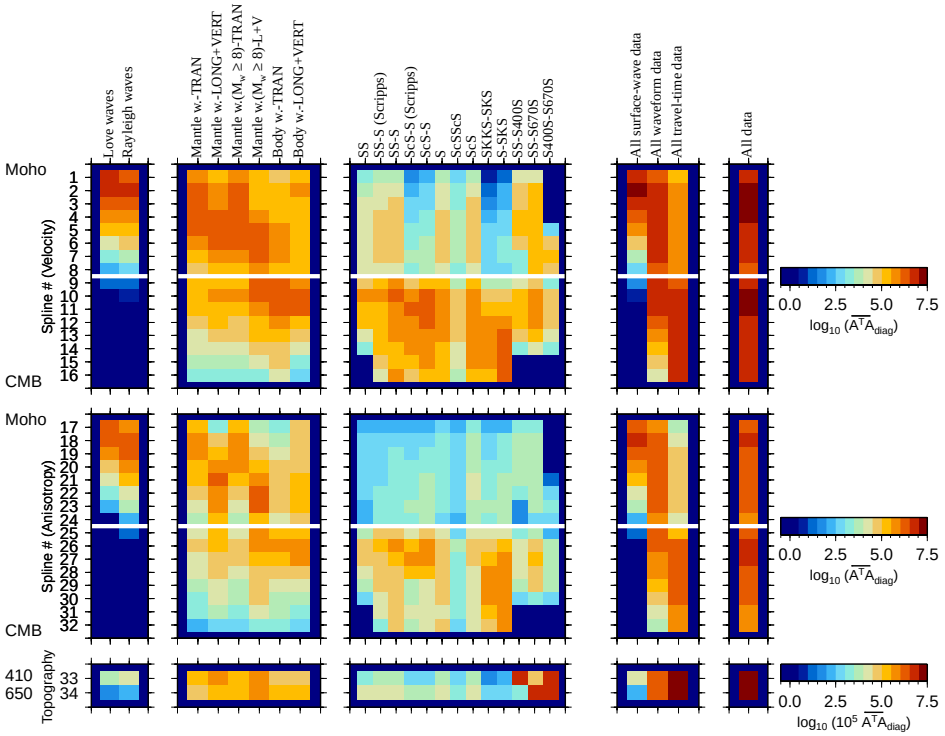

Figure 4.5: Sensitivity of different data sets calculated as global averages of the diagonal elements of the inner-product matrix $A^T A$ for every cubic spline and for topographies of the transition zone discontinuities. The inner-product matrices are weighted in the same way as in the inversion for the global three-dimensional model. The panels on the right show cumulative sensitivities for surface-wave, waveform, and travel-time data, and for all data combined. LONG, TRAN, and VERT indicate longitudinal, transverse, and vertical components of a seismogram, and 'w.' denotes waveforms. Different scale was used for the topography sensitivity since it is much smaller than the velocity and anisotropy sensitivities.

ity, anisotropy and topography of the transition zone discontinuities are parameterized horizontally by 362 spherical splines. To describe isotropic velocity variations in the radial direction, we use 16 radial cubic splines split at 650 km. In our preferred model, we constrain anisotropy to vanish at 410 km by solving for coefficients corresponding to the uppermost four splines. In the experiment described in Section 4.2.5, we invert for anisotropic variations using all 16 cubic splines.

4.2.2 Sensitivity and weighting of different data sets

Figure 4.5 shows how different data sets constrain velocities in different depth ranges in the mantle. The sensitivity is defined as a global average of the diagonal elements of the inner-product matrix $A^T A$ (Gu *et al.*, 2001a). Compared to Gu *et al.* (2001a), our plot was extended by adding anisotropy, discontinuity topography, and cumulative sensitivities for different data sets, and does not employ any normalization. The velocity structure of the uppermost mantle is determined primarily by short- and intermediate-period surface waves. Long-period waveforms provide best constraints on the velocities between 200 and 1000 km. Velocities in the lower mantle are determined by the diverse set of travel times of teleseismic body waves.

Elements of each matrix in Figure 4.5 are multiplied by the same weighting factors as in the inversion. We select weighting that allows us to constrain all cubic splines as uniformly as possible. The cumulative sensitivity plotted in the right panel demonstrates that our data constrain fairly uniformly all radial basis functions. The average value of the $A^T A$ is maximum for splines 2 and 10, and it is only 10 times higher for these splines than for the most weakly constrained spline at the bottom of the upper mantle.

Anisotropy is well constrained by surface-wave data in the uppermost mantle. In the transition zone, anisotropy is determined primarily by waveforms, which show much higher sensitivity for vertical and longitudinal components than for the transverse component. Consequently, determination of the anisotropic structure at the bottom of the upper mantle is difficult. The D$''$ region above the core-mantle boundary is best sampled by diffracted S waves, which are recorded only on the horizontal component of the seismograms, and therefore, sensitive only to variations in v_{SH}. Differential SKKS–SKS and S–SKS times are sensitive to both v_{SH} and v_{SV}, and we give these

data large weights in the inversion to constrain anisotropic variations at the bottom of the mantle (Section 4.2.5).

Topography of the transition zone discontinuities is determined primarily by travel times of the SS precursors. Long-period waveforms are also significantly sensitive to perturbations in discontinuity depths. Despite low lateral resolution, this sensitivity allows for correcting the velocities and density in the new reference model for the effect of shifts in discontinuities with respect to PREM.

4.2.3 Inversion

We use REF as a reference in the inversion for a three-dimensional shear-wave velocity model. Sensitivity kernels for all data are calculated for REF and perturbations in isotropic and anisotropic velocities are defined with respect to REF. We assume that inversions of surface-wave phase anomalies and body-wave travel times are weakly nonlinear. Consequently, the inner-product matrices and data vectors for these data sets are calculated only once. In contrast, the waveform inversion is a strongly nonlinear problem and has to be solved iteratively. The data vectors for waveform data and the CMT solutions are updated as we iteratively improve the three-dimensional model. Owing to a slow rate of convergence, waveform inversions usually involve using a three-dimensional starting model. For example, Gu *et al.* (2001a) started their inversion with an older, long-wavelength model of Su *et al.* (1994). In our case, using an existing three-dimensional model is not possible, because no such models have been developed for the reference model REF. Therefore, we build a new starting model by inverting only surface-wave data for coefficients corresponding to the five uppermost B-splines in the isotropic part, and four uppermost splines in the anisotropic part of the model. In the first iteration of waveform inversion, we calculate synthetic seismograms for this model, and

determine new CMTs starting with the standard Harvard CMT solutions. From the difference between the synthetic and observed seismograms, we determine partial derivatives for the structural inversion. Then, we add inner-product matrices and data vectors for waveform, surface-wave, and body-wave travel-time data, as well as damping, and invert them jointly for the velocity structure and discontinuity topographies. The model is then used in the next iteration of waveform inversion and convergence is achieved after several iterations.

In this work, we invert for perturbation with respect to the one-dimensional model REF. Some authors, however, prefer to subtract predictions of their favorite three-dimensional model from the data vector and invert for perturbations with respect to such model (*e.g.* Gu *et al.*, 2001a). Because damping affects the solution of the inversion, our approach yields a model that is smooth or small with respect to a one-dimensional model REF, whereas the latter approach minimizes smoothness or norm with respect to an arbitrarily chosen target model. We prefer the former approach, because it makes the final solution independent of any imperfections in three-dimensional models.

Although our combined data constrain the model at all depths in the mantle, some regions are sampled by only few rays. Tomographic models are most sensitive to the choice of the regularization in such poorly sampled regions. In particular, models regularized by norm damping have a tendency to correlate with the noneven data coverage, as demonstrated by Boschi and Dziewoński (1999). We choose to minimize only vertical and horizontal roughness rather than the norm of the solution.

4.2.4 Isotropic velocity structure

In this section, we present isotropic shear-wave velocity structure in our new model S362ANI and compare it with other models of the Earth's mantle. Our new model and the model S362D1 of

Gu *et al.* (2001a) both have been derived from combined data sets of surface-wave, waveform, and travel-time data using similar techniques. In the calculation of S362ANI, however, we have included several times more observations, lateral variations in anisotropy, used a different reference model, starting model, more accurate crustal model and crustal corrections, and a different amount of damping. The comparison is therefore important for understanding the advantages of combining new data sets and improvements in the modeling techniques.

We also compare S362ANI with other models obtained from different data by different authors. The model SB4L18 of Masters *et al.* (2000) was derived from measurements of surface-wave dispersion, body-wave travel times, and normal-mode splitting functions. The model SAW24B16 of Megnin and Romanowicz (2000) was calculated through the inversion of surface- and body-wave waveforms. These two models, as well as S362ANI and S362D1, are therefore constrained at all depths in the mantle and their comparison is important for the identification of the consistent anomalies in shear-wave velocity models.

The model of Nettles (2005) was obtained from the same 35-150 second surface-wave data set as S362ANI and additional measurements at periods up to 300 seconds. Because Nettles (2005) accounted for lateral variations in the sensitivity kernels and depth of the Moho, which we neglect in this study, the comparison of her model with S362ANI is important for understanding the benefits of using a more sophisticated modeling technique. This problem is discussed in detail in Section 4.2.7.

The *a priori* model 3SMAC of Nataf and Ricard (1996) was constructed using thermal, mineralogical, and laboratory data. Comparison of 3SMAC with tomographic models helps us to understand properties of seismological models that are not predicted by near-surface observables.

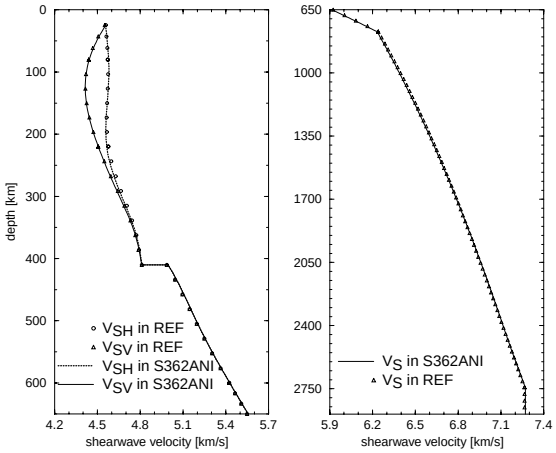

Figure 4.6: Globally averaged shear-wave velocities in S362ANI (curves) and in the reference model REF (symbols).

We plot lateral velocity variations in S362ANI with respect to the reference model REF with global averages removed at each depth. Deviations of the averages in S362ANI from REF are very small (Figure 4.6), which is not surprising given that REF has been derived from the same data set as S362ANI (except the SS precursors).

At a depth of 70 km (Figure 4.7), the pattern of heterogeneity in tomographic models is dominated by negative anomalies along the mid-ocean ridges and regions of back-arc extension. The negative anomalies in S362ANI are narrower than in S362D1, suggesting a higher resolution of the former model. Small-scale features in S362ANI show significant power (Figure 4.8) while in S362D1, the variations at harmonics at degrees higher than 10 almost completely disappear. The long-wavelength features at shallow depths in the two models are very well correlated with each other (Figure 4.9). The signatures of the mid-ocean ridges are much stronger in tomographic models than in 3SMAC, which suggests that velocity variations predicted *a priori* are underestimated, and may not fit seismological data. In particular, the East Pacific Rise anomaly is characterized by two times stronger perturbations than the predictions of 3SMAC.

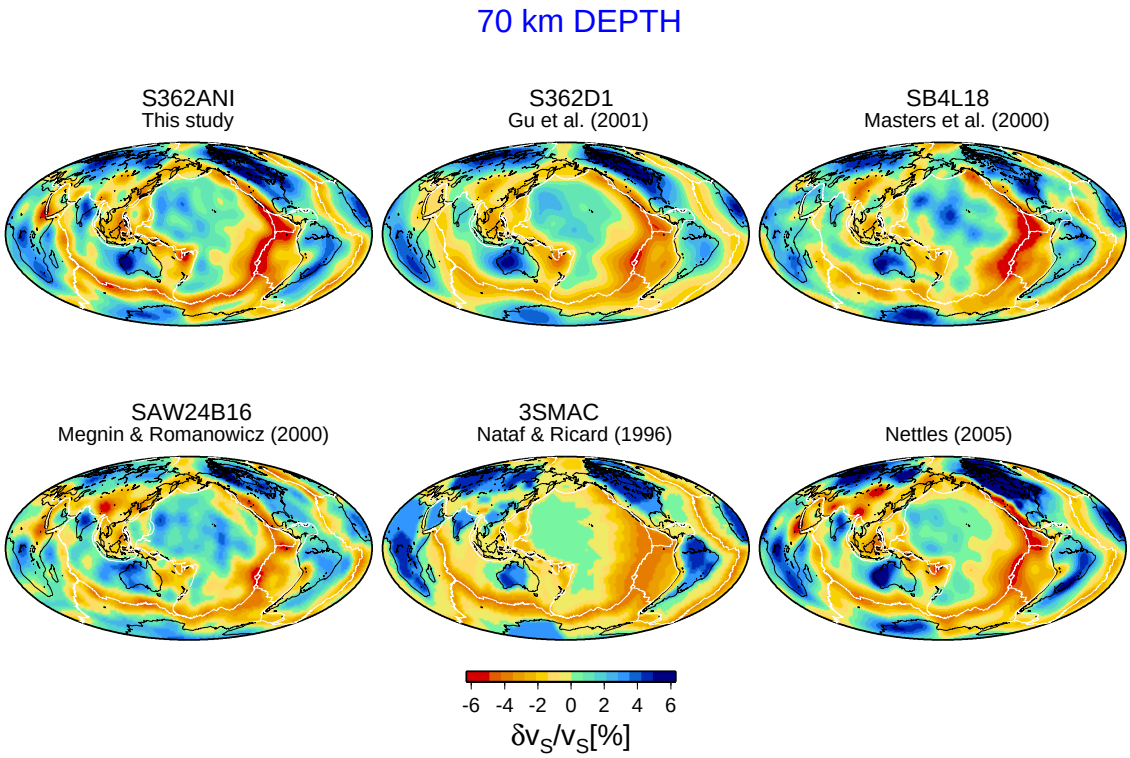

Figure 4.7: Isotropic velocity anomalies defined as $\frac{\delta v_S}{v_S} = (\frac{\delta v_{SH}}{v_{SH}} + \frac{\delta v_{SV}}{v_{SV}})/2$ in different models plotted at a depth of 70 km with the appropriate global average removed. Perturbations in S362ANI are defined with respect to REF; in S362D1, SB4L18, and SAW24B16, with respect to PREM; and in 3SMAC and Nettles (2005), with respect to the global averages.

We find, in agreement with other tomographic models, that slow-velocity anomalies beneath mid-ocean ridges are required by the data at 150 km (Figure 4.10), but they are not observed in 3SMAC at this depth. In the tomographic models, the ridge signatures vanish at about 200-250 km. This is much shallower than in models of Zhou *et al.* (2006) and Su *et al.* (1992), who suggest that hot upwellings beneath ridges observed at 400 km may play important role in driving plate tectonics. In particular, we do not observe the ridge signal at large depths under the North Atlantic and Red Sea reported by Zhou *et al.* (2006). At 150 km, the strongest anomalies are observed beneath continents. The velocity structure at this depth is well constrained by surface-wave data, and despite using different data sets, parameterization, and modeling techniques, different researchers obtain similar

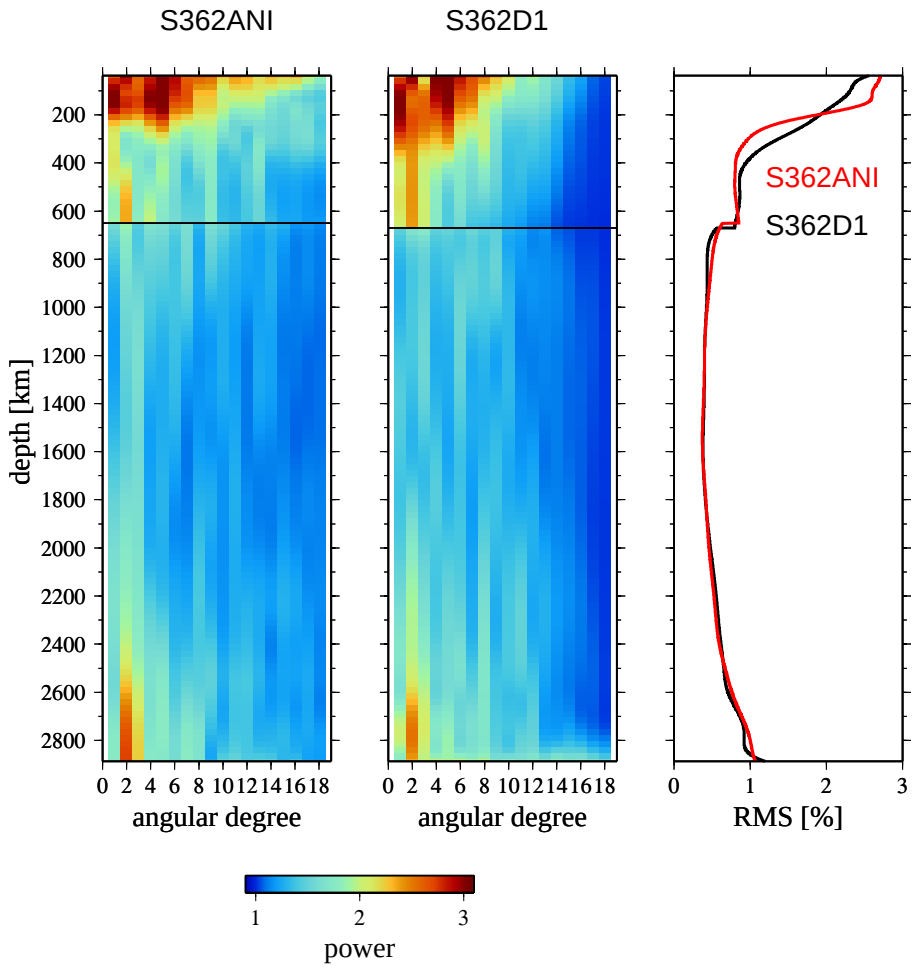

Figure 4.8: Left and middle panels: power spectra of lateral isotropic velocity variations in S362ANI and S362D1. More specifically, we plot $log_{10}(10 + 1000 * power)$ for harmonics up to degree 18. Right panel: root-mean-square value of lateral isotropic velocity variations in S362ANI and S362D1.

images.

At 250 km, differences between velocities beneath continents and oceans in S362ANI are much weaker than at 150 km (Figure 4.11). Positive anomalies are also weak in the majority of tomographic models, but they appear to be overestimated in 3SMAC. Strong positive anomalies beneath continents are also observed in S362D1. This model is significantly smoother in the upper mantle than S362ANI, as shown in the power spectra in Figure 4.8. Strong heterogeneity at degree five,

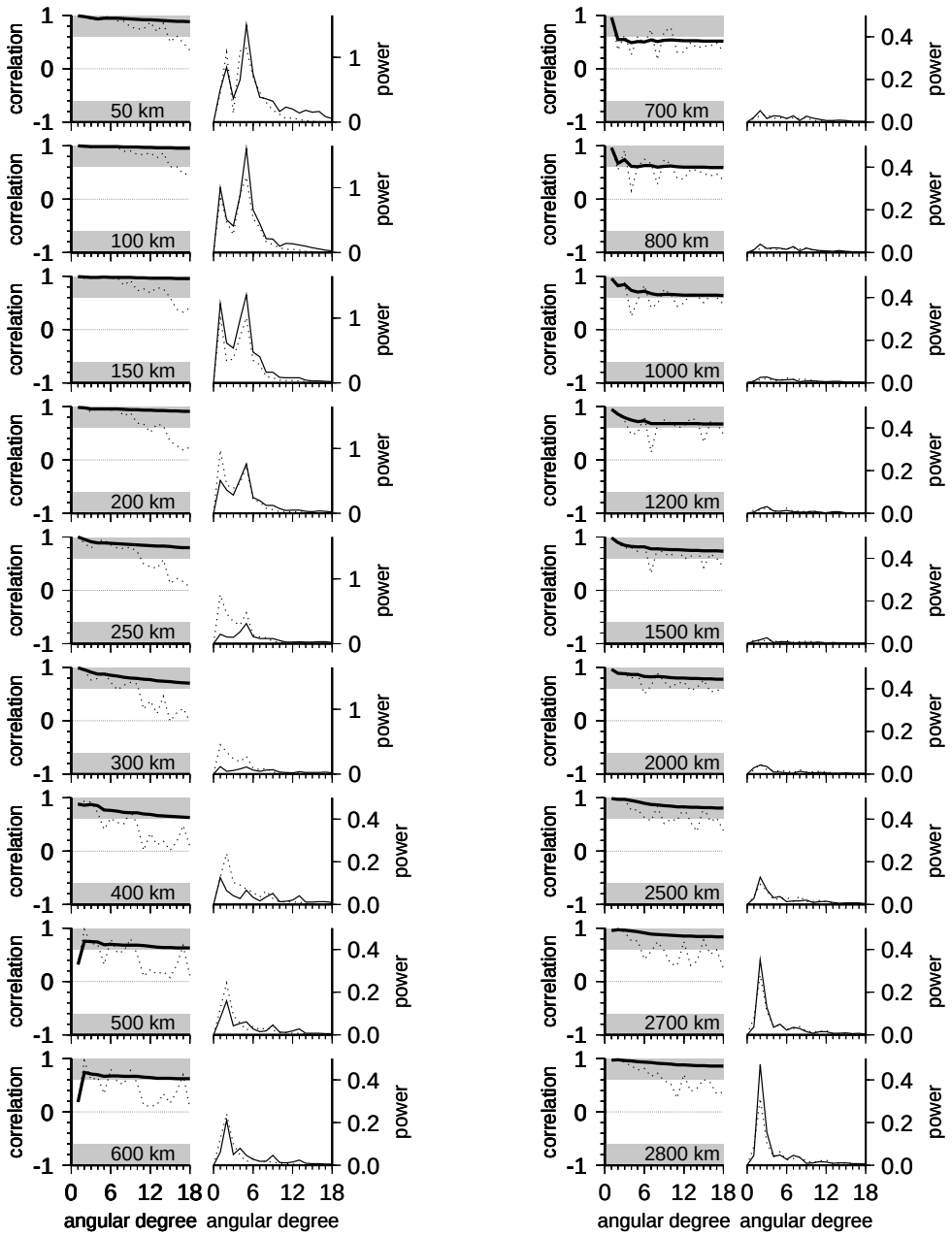

Figure 4.9: Correlation and power spectrum at different depths in models S362ANI and S362D1. Correlation for particular harmonics is shown as a dotted line while cumulative correlation is shown as a thick solid line. Shaded areas indicate correlation higher than 0.6 and lower than -0.6 chosen arbitrarily to distinguish between high and low correlation. Power for S362ANI is shown as a solid line and for S362D1 as a dashed line.

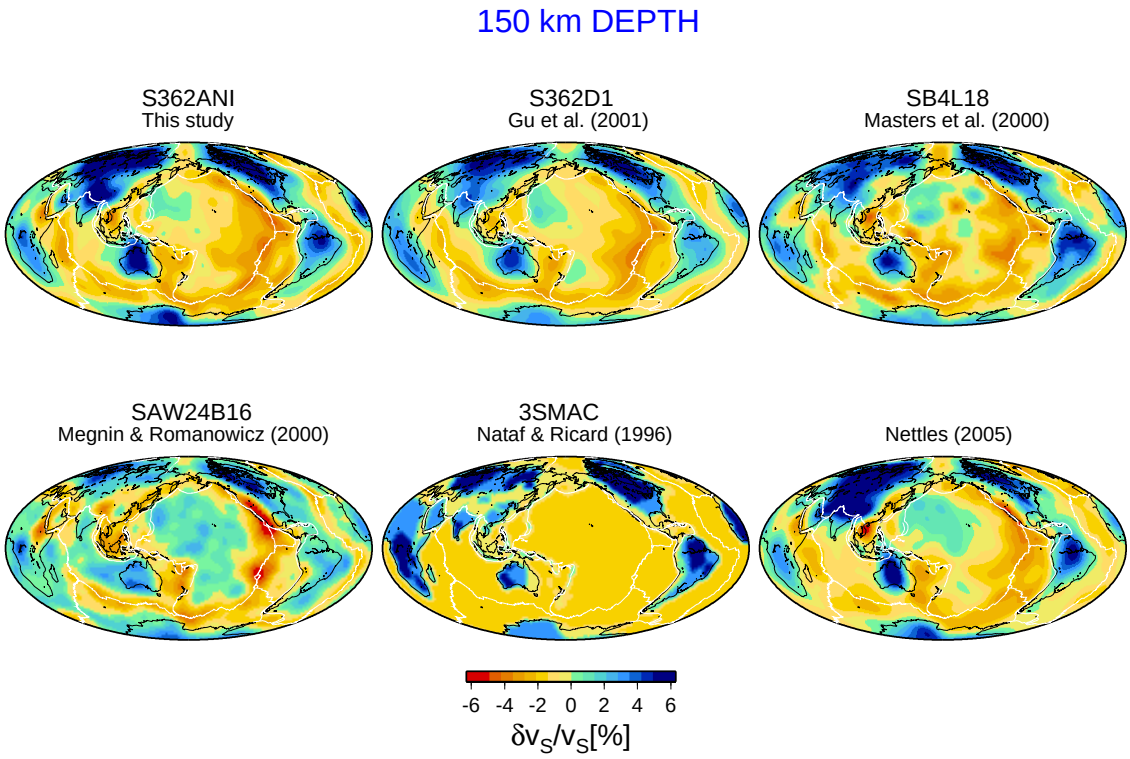

Figure 4.10: Same as Figure 4.7, but at a depth of 150 km. The strongest anomalies are observed beneath continents. Negative anomalies beneath mid-ocean ridges persist to at least 150 km in tomographic models but they are not present in 3SMAC.

which corresponds to the characteristic wavelength of continents, continues down to 350 km in S362D1, whereas in S362ANI it vanishes rapidly at about 250 km. Our experiments indicate that a model with the isotropic velocity structure as smooth in the radial direction as in S362D1, does not allow for resolving the change in the anisotropic pattern between 50 and 150 km reported by Ekström and Dziewoński (1998). We also find that, in order to resolve heterogeneities required by the surface-wave data in the uppermost mantle, and at the same time regularize the model sufficiently at larger depths, it is necessary to damp radial gradients in the uppermost 400 km of the model about five times less than at larger depths. Lighter damping, in conjunction with the implementation of more accurate crustal corrections (Section 4.2.10), prevents mapping the fast velocities

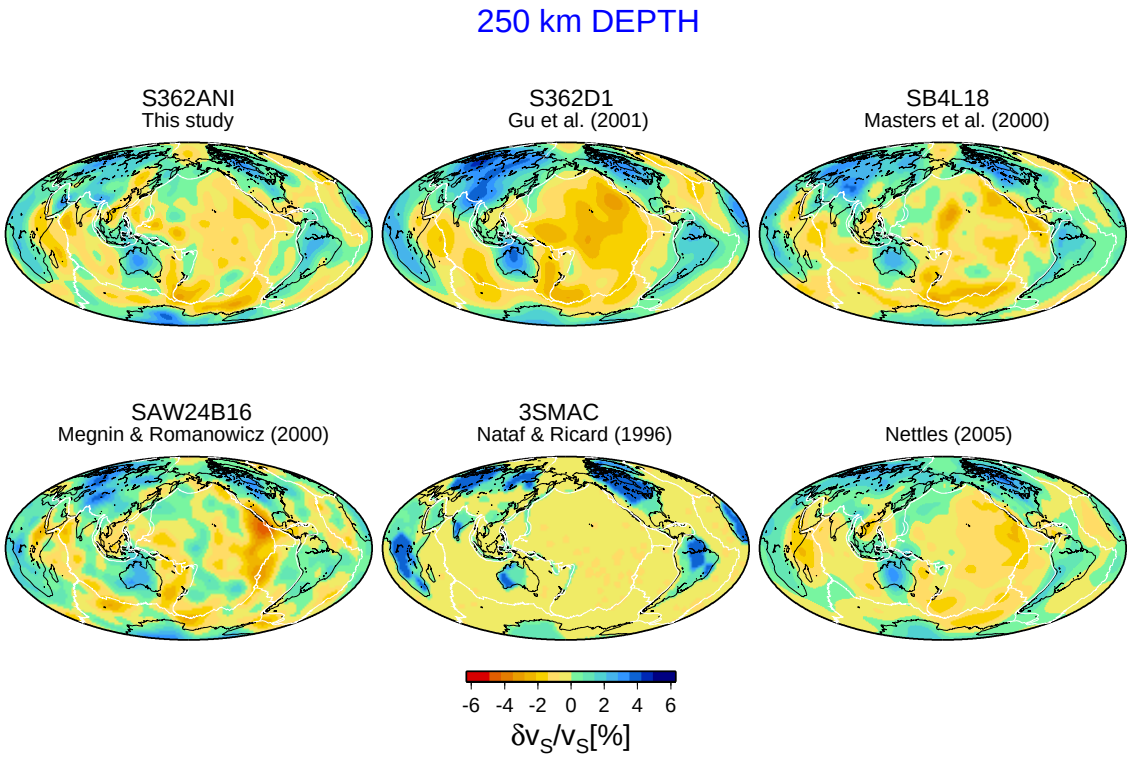

Figure 4.11: Same as Figure 4.7, but at a depth of 250 km. In S362ANI, positive velocity anomalies beneath continents at 250 km are weak, which suggests that continental roots may not extend below 250 km. In the majority of tomographic models, the high-velocity anomalies are slightly stronger at this depth, whereas in the *a priori* model 3SMAC, they are much stronger.

beneath continents to depths larger than 250 km. Such moderately thick continental signatures are consistent with the models of, for example, Priestley and Debayle (2003) and Nettles (2005), but S362D1 shows significant fast velocity anomalies even at a depth of 350 km (Figure 4.12). Faster-than-average velocities beneath continents below the 250-km depth are also observed in our new model S362ANI, but they are very weak and it is not clear whether they represent true velocity anomalies. Primarily thermal origin of the velocity anomalies in the uppermost 200 km of the mantle is suggested by the correlation of S362ANI with the recent model of attenuation (Dalton 2006, in preparation), however, we cannot rule out the presence of some chemical heterogeneity in this depth range. Velocity anomalies below 200 km extending down to 400 km beneath continents may

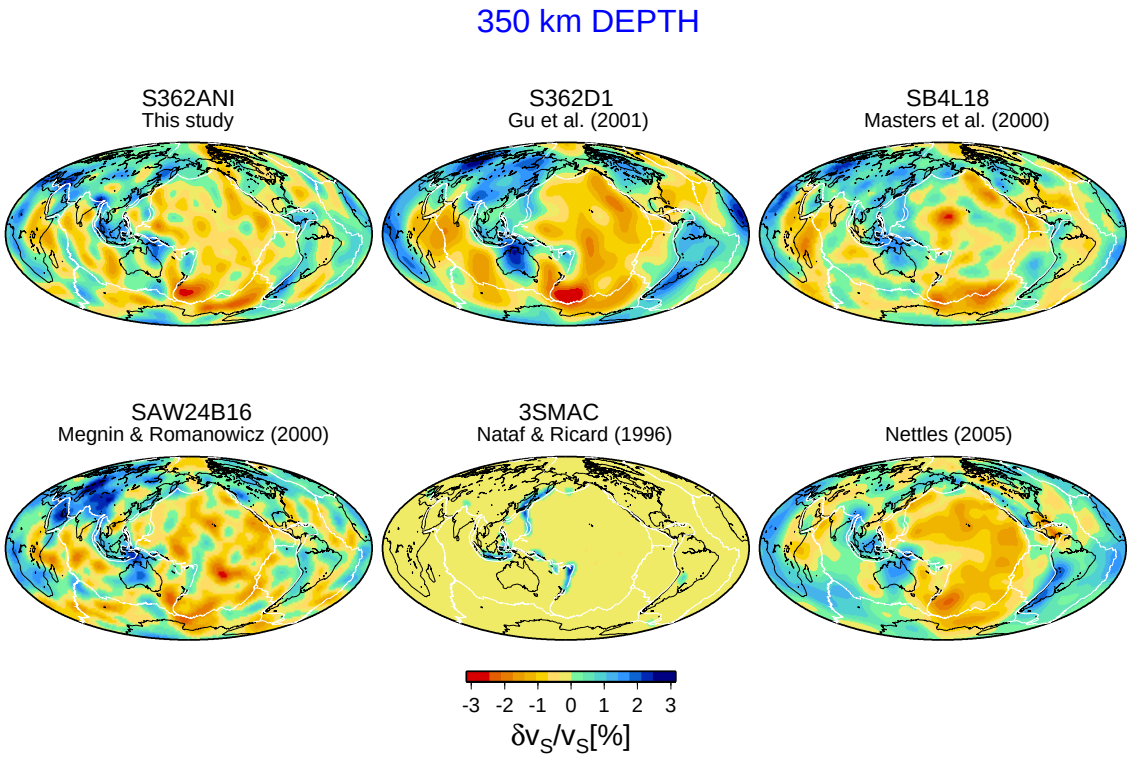

Figure 4.12: Same as Figure 4.7, but at a depth of 350 km and plotted with a different color scale. Strong continental signatures are still observed in S362D1 and SAW24B16, but they are much weaker in other models. The *a priori* model 3SMAC does not show any heterogeneous structures except the subducting slabs, while velocity variations in tomographic models away from the subduction zones are up to 3%.

be explained in terms of chemical heterogeneity (Jordan, 1975, 1978, 1981a) or higher-than-average viscosity (Shapiro *et al.*, 1999).

The only significant anomalies observed in 3SMAC at 350 km are lithospheric slabs beneath the western Pacific and Indonesia. Tomographic models, however, show global patterns of anomalies as strong as 3%, which explains why the *a priori* model cannot fit long-period waveforms.

We find that the uppermost mantle, which is characterized by significant differences between continents and oceans, is separated from the transition zone by a less heterogeneous region between 300 and 500 km. Both power spectra and root-mean-square variations show a minimum in this depth range (Figure 4.8). In contrast, vertical velocity variations in S362D1 are so smooth that the

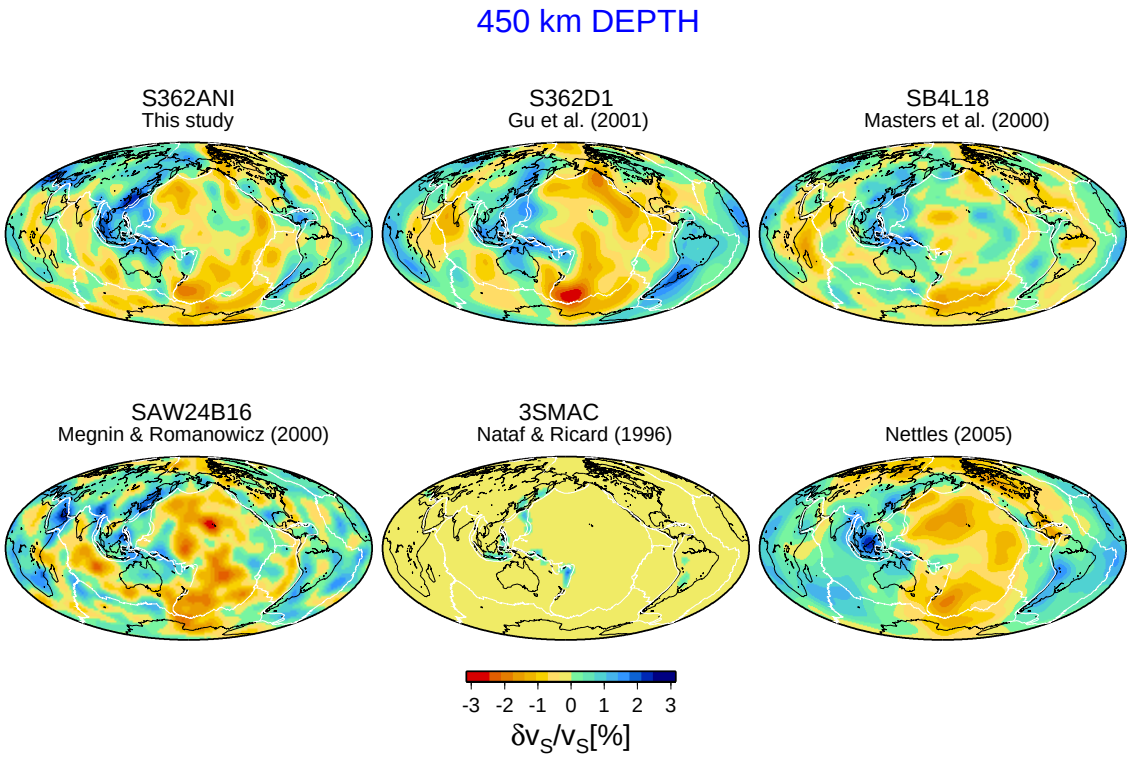

Figure 4.13: Same as Figure 4.7, but at a depth of 450 km and plotted with a different color scale.

power of heterogeneity at degrees 1-3 appears to be strong throughout the entire upper mantle.

One of the most pronounced, but not discussed in the literature, features of the weakly heterogeneous region between 300 and 500 km is the slow velocity anomaly southeast of New Zealand observed in all tomographic models (Figure 4.13). Interestingly, it is stronger at 350-450 km than at shallower depths. While the anomaly is centered on the Pacific-Antarctic Ridge in SB4L18 and SAW24B16, it is shifted towards New Zealand in all models derived at Harvard.

The depth range between 400 and 800 km is characterized by the lowest correlation between S362ANI and S362D1, which is as low as 0.5 at 700 km (Figure 4.9). The lowermost spline in the upper mantle is not as well-constrained as other radial basis functions, and is therefore more sensitive to the differences in the modeling technique. The discrepancy at the bottom of the upper

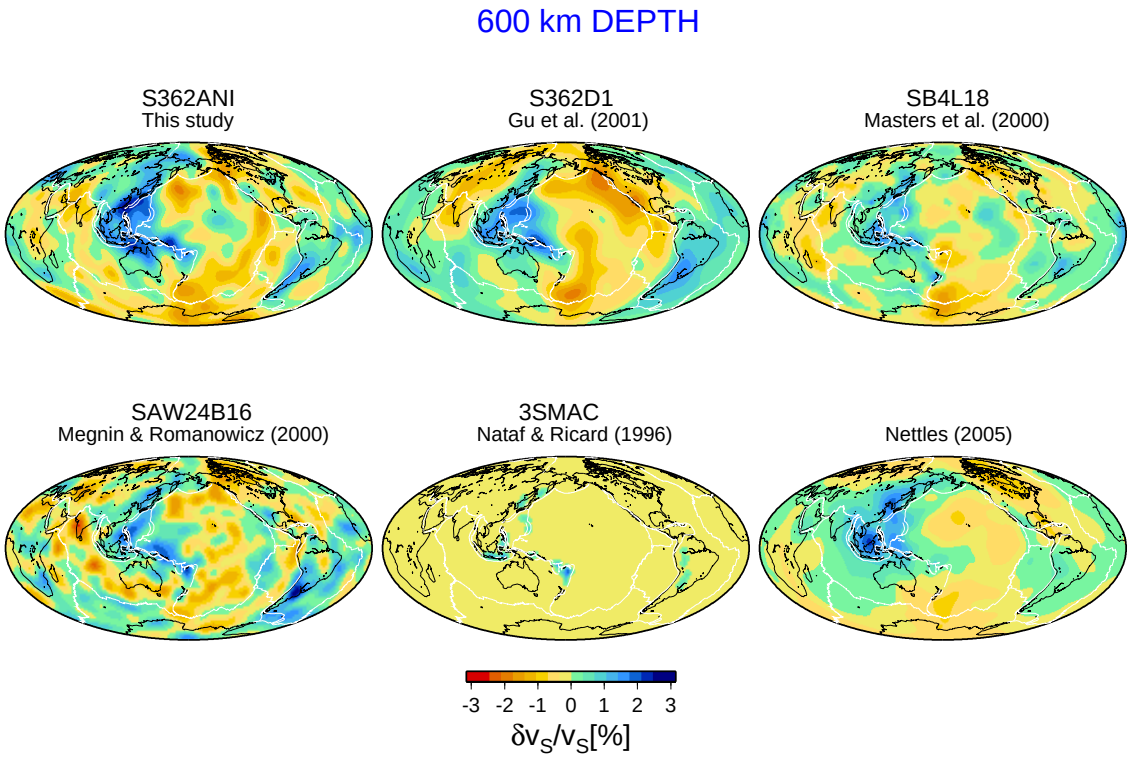

Figure 4.14: Same as Figure 4.7, but at a depth of 600 km and plotted with a different color scale. The variations are stronger than at 450 km, and are dominated by low velocities beneath the Pacific and high velocities beneath subduction zones.

mantle may, for example, result from damping towards a different target model in the inversion. The S362ANI is damped towards the spherically symmetric reference model REF, whereas S362D1 is damped towards S12WM13 (Su *et al.*, 1994), a long-wavelength model, which is continuous across the boundary between the upper and lower mantle. Despite some differences, all models show fast velocity anomalies beneath subduction zones at 600 km and slow velocities beneath the Pacific and North America (Figure 4.14). These structures are responsible for a strong power at degree two at the bottom of the transition zone (Figure 4.8).

Below the upper-lower mantle boundary, the whole-mantle models S362ANI, S362D1, SB4L18, and SAW24B16 reveal much weaker fast velocities beneath the subduction zones (Figure 4.15).

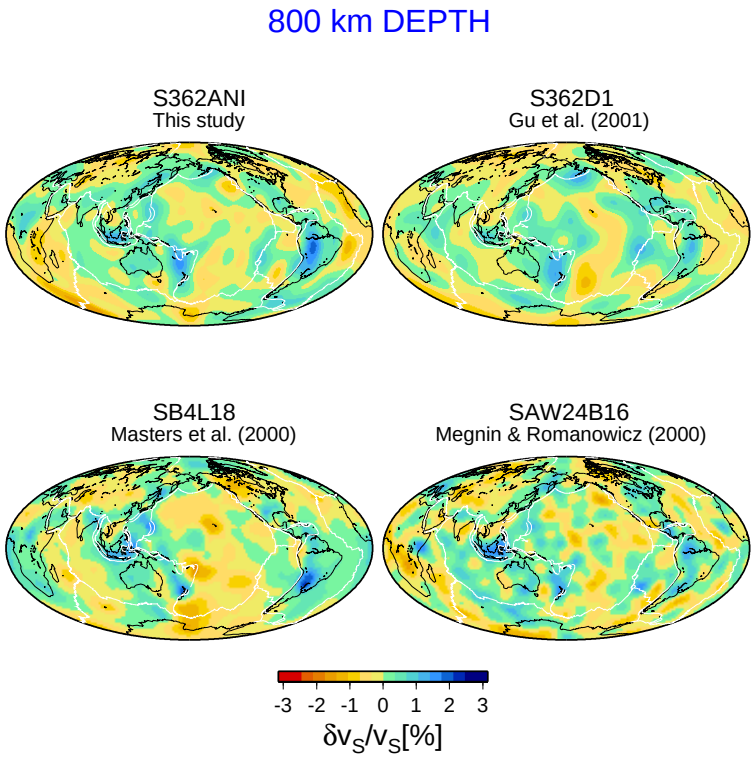

Figure 4.15: Same as Figure 4.7, but at a depth of 800 km and plotted with a different color scale. The amplitudes of the anomalies are much smaller than above the 650-km discontinuity. The models 3SMAC and Nettles (2005) are no longer displayed since they are upper mantle models.

While the presence of these anomalies may suggest that lithospheric slabs penetrate below the transition zone, the dramatic fall-off in the power spectrum and root-mean-square value suggest a significant change in the structure at 650 km. This has been interpreted as an indication of the change in the flow pattern (Gu *et al.*, 2001a). The rapid decrease in the strength of S362ANI is not caused by the regularization, since perturbations above the 650-km discontinuity are damped as strongly as perturbations in the lower mantle.

An independent observation of the interaction of slabs with the upper-lower mantle boundary comes from the modeling of topographies of the transition zone discontinuities. The topographies in S362ANI are determined by the same set of SS-precursor data as in the model TOPOS362D1 of

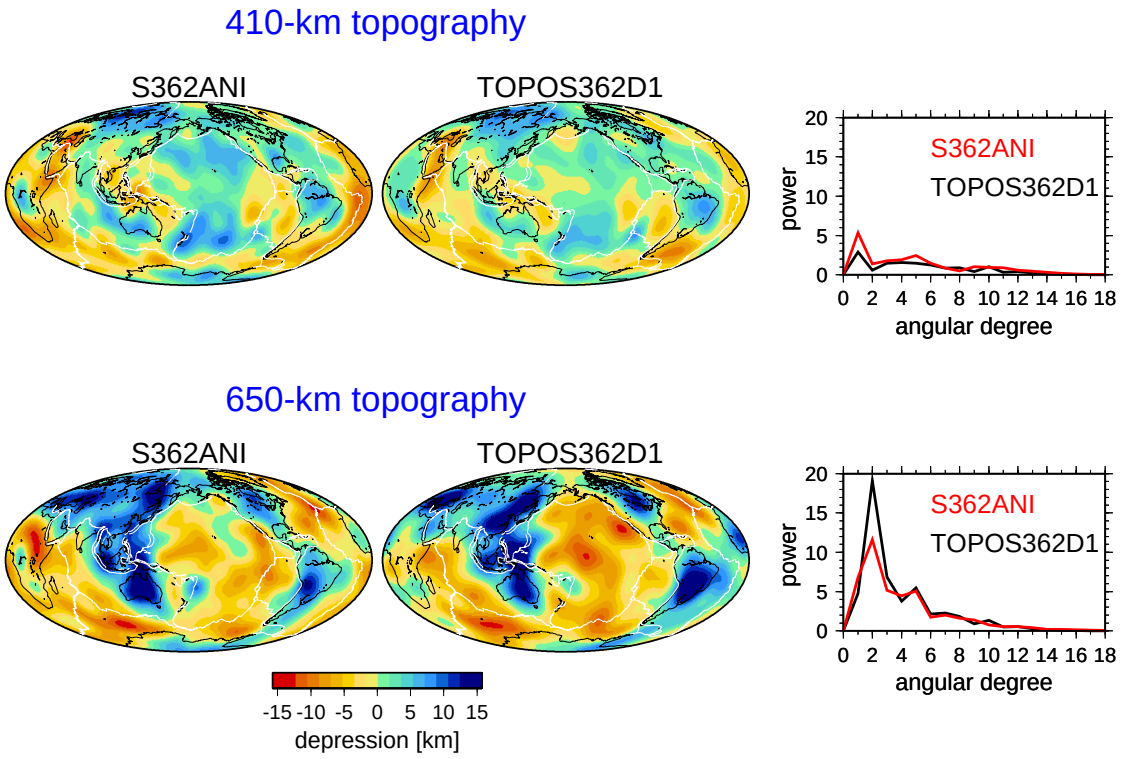

Figure 4.16: Topography of the 410- and 650-km discontinuities in S362ANI and TOPOS362D1. The topographies in the two models are similar to each other. Some minor differences are caused by differences in the velocity structure in the upper mantle. The right column shows power spectra of the topographies. The topography at 410 km is weaker, and is not correlated with the topography of the 650-km discontinuity. Depressions in the 650-km discontinuity are correlated with the positive anomalies in the transition zone shown in Figure 4.14.

Gu *et al.* (2003). However, the velocity structure in our new model is somewhat different than in TOPOS362D1. Since topography trades off with velocity, the comparison between topographies in the two models provides insight into the robustness of our results. In S362ANI, the discontinuities are, on average, nearly exactly at 410 and 650 km, which is very similar to the depths of 409 and 649 km reported by Gu *et al.* (2003). Lateral depth variations in the two models are similar to each other (Figure 4.16) with only two appreciable differences. First, the elevation at 650 km beneath the Pacific in the new model is smaller in S362ANI and caused by higher velocities in the transition

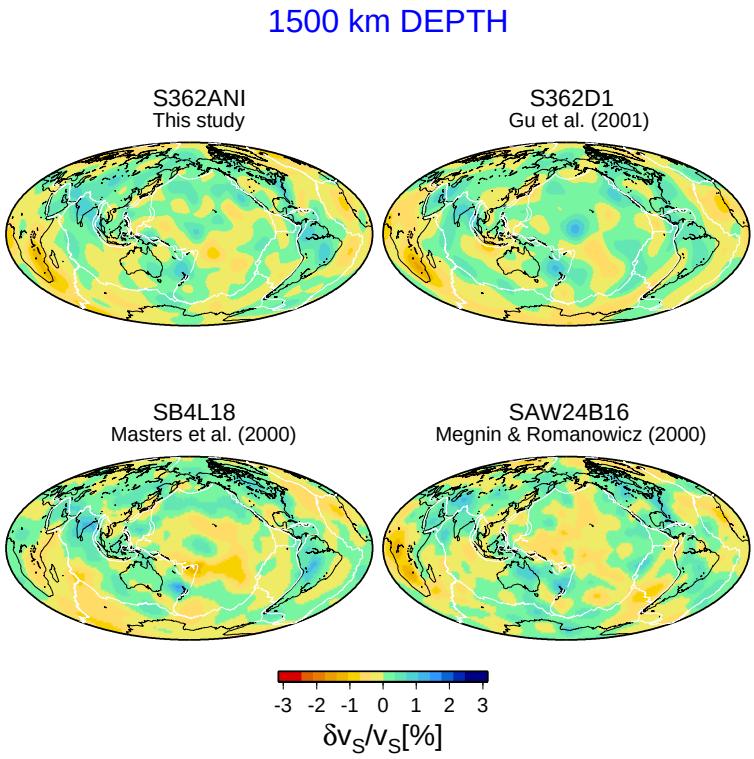

Figure 4.17: Same as Figure 4.7, but at a depth of 1500 km and plotted with a different color scale. Slab signatures are not observed at this depth.

zone. Second, the 650-km discontinuity shows a significant elevation beneath eastern Africa not observed in TOPOS362D1, which results from lower velocities in the transition zone in the new model. The difference in strength between topography of the 410- and 650-km discontinuities in S362ANI is less pronounced than in TOPOS362D1, but still significant.

In the mid-mantle, we do not observe strong slab signatures beneath subduction zones, in agreement with other long-wavelength tomographic models (Figure 4.17). This result is also consistent with the systematic comparison of different tomographic models by Fukao *et al.* (2001), who found that many slabs do not penetrate below 1000 km. The model S362ANI is, however, inconsistent with the presence of slabs at the bottom of the mantle reported by Grand *et al.* (1997). At 1500 km,

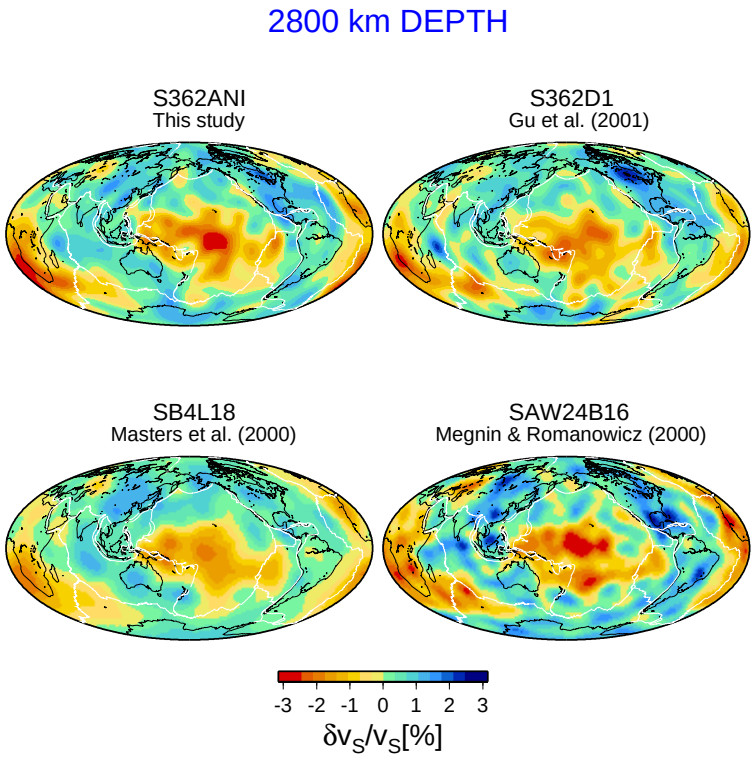

Figure 4.18: Same as Figure 4.7, but at a depth of 2800 km and plotted with a different color scale. In all models, the pattern of heterogeneity is dominated by slow-velocity anomalies beneath the Pacific and Africa, often referred to as the 'superplumes'.

SB4L18 shows negative anomalies in the Pacific, which are not nearly as strong in other models. The presence of these anomalies, which extend from the base of the mantle to this depth, indicates that SB4L18 is significantly smoother in the lower mantle than other models. We also observe an emerging pattern of fast-velocity anomalies around the Pacific.

In the lowermost mantle, S362ANI is dominated by large-scale slow-velocity anomalies beneath the Pacific and Africa (Figure 4.18). These features have been known since the first tomographic studies (Dziewoński *et al.*, 1977; Dziewoński, 1984), and are surrounded by fast-velocity anomalies. Interestingly, these negative anomalies become as strong as –3%, while positive anomalies reach only +1.9%. In S362ANI, the Pacific anomaly has a maximum located north-east of Fiji, which

is slightly stronger than in S362D1. In general, the lateral extent of the anomalies in all models is similar and the correlation between S362ANI and S362D1 at the bottom of the mantle is very high (Figure 4.9).

4.2.5 Where is the mantle anisotropic?

Evidence for the presence of anisotropy in the upper mantle includes the discrepancy between models constrained by Rayleigh and Love waves, shear-wave splitting, and azimuthal variations of P_n velocities (see, for example, Anderson, 1989). The presence of anisotropy in the upper mantle can be explained in terms of preferred orientation of anisotropic crystals in the convecting asthenosphere or a frozen-in anisotropy reflecting deformation processes in the lithosphere.

The presence of anisotropy has also been reported at larger depths in the mantle, in particular, in the D$''$ region. Regional studies (Vinnik *et al.*, 1989; Kendall and Silver, 1996; Lay *et al.*, 1998; Kendall, 2000; Fouch *et al.*, 2001) usually show $v_{SH} > v_{SV}$ anisotropy based on faster arrivals of shear waves bottoming in D$''$ recorded on the transverse component than those recorded on the radial component. Lattice preferred orientation, horizontal layering or aligned inclusions (Kendall and Silver, 1996; Karato, 1998) have been discussed as a possible origin of the anisotropy at the bottom of the mantle. The presence of the anisotropic post-perovskite phase in the lowermost mantle has been suggested by experimental results (Murakami *et al.*, 2004; Oganov and Ono, 2004; Shim *et al.*, 2004). Panning and Romanowicz (2004) made the first attempt to map the anisotropy in the whole-mantle on a global scale and reported the presence of significant anisotropic variations both in the D$''$ region and in the transition zone (Panning, 2004). Their model was obtained using only waveform data, whereas the lower mantle structures in our inversions are constrained primarily by

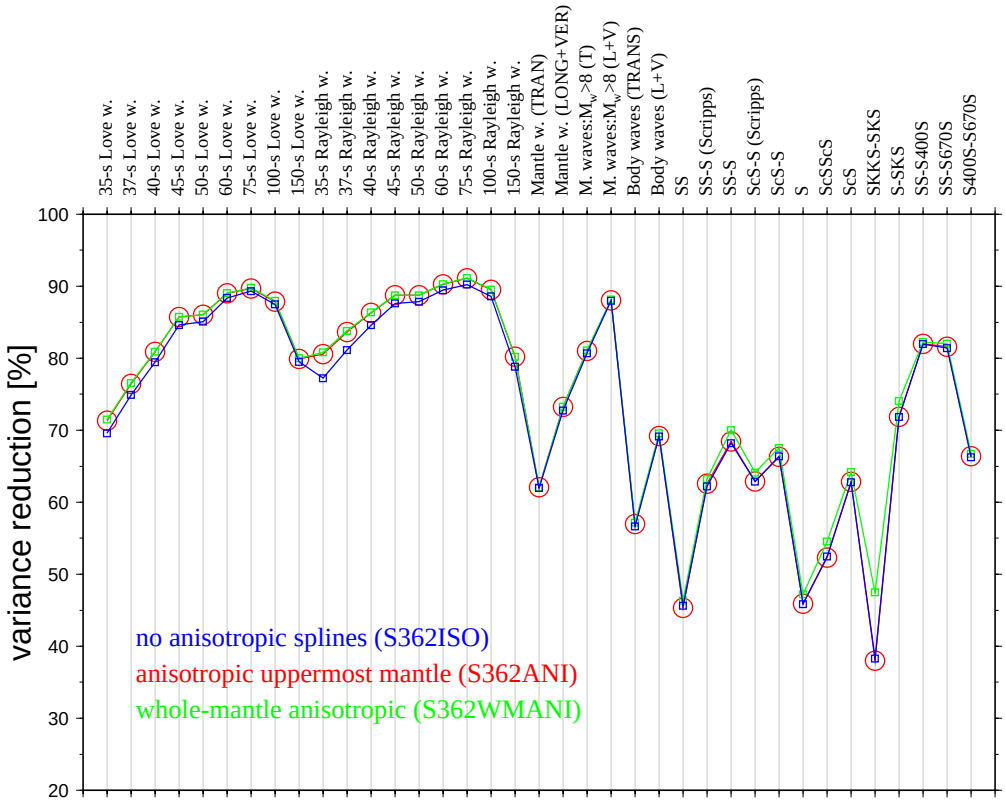

Figure 4.19: Variance reduction for S362ANI (in red), for the model S362ISO without lateral variations in anisotropy (in blue), and for the whole-mantle anisotropic model S362WMANI (in green). The variance reduction was calculated separately for measurements of surface-wave phase velocities at different periods, for different types of waveforms, and different data sets of body-wave travel times. Including anisotropy in the uppermost mantle significantly improves the fit of the surface-wave data. The travel-time data are fit much better if anisotropy is allowed in the lower mantle.

the body-wave travel times. It is therefore informative to repeat the experiment by Panning and Romanowicz (2004) and invert our combined data set for a whole-mantle anisotropic model. As a result, we obtain a model S362WMANI characterized by significant anisotropic variations both in the mantle transition zone and in the D$''$ region. This, however, does not necessarily mean that the variations reflect the true anisotropic velocity structure. The anisotropy in the model may, in fact, be an artifact of the overparameterized inversion with insufficient data coverage.

In order to test the robustness of the whole-mantle anisotropic model, we perform two ex-

periments. First, we investigate whether anisotropy is required by the data at different depths in the mantle. Figure 4.19 summarizes the data fits for three different models: our preferred model S362ANI with anisotropy confined to the four uppermost radial splines; a model S362ISO with no lateral anisotropic variations; and the whole-mantle anisotropic model S362WMANI.

The variance reduction for surface-wave and travel-time data is calculated as

$$\text{variance reduction} = 100\% \left[1 - \frac{\sum_i (\sum_j A_{ij} m_j - d_i)^2}{\sum_i d_i^2} \right], \tag{4.6}$$

where m_j is the j-th model coefficient, A_{ij} is the data kernel matrix, and d_i is the i-th phase anomaly or travel-time residual with respect to the reference model REF overlain by CRUST2.0. For the waveform data we use a formula

$$\text{variance reduction} = 100\% \left(1 - \sum_i \frac{\int \varepsilon_i^2(t) dt}{\int s_i^2(t) dt} \right), \tag{4.7}$$

where t is the time, s_i is the i-th seismogram recorded for a given earthquake, and ε_i is the difference between the observed and synthetic seismograms. We calculate variances for all 219 earthquakes of $6.5 \leq M_w < 8$ and for 10 great earthquakes, but we plot only median variances for each group of events in Figure 4.19.

Including lateral variations in anisotropy clearly improves the fit to the surface-wave data. As expected, anisotropy in the uppermost mantle does not affect significantly the variance reduction for waveforms and body-wave travel times since these data sets have their maximum sensitivity at larger depths. The fit for waveform data is also not significantly improved when anisotropy is allowed in the whole mantle. The variance reduction for waveforms cannot be directly compared with the

variance reduction of surface-wave phase anomalies because of different definitions. However, since the improvement for S362WMANI with respect to S362ANI is marginal, we conclude that anisotropy in the transition zone is not required by waveform data. Anisotropy in the lower mantle reduces the variance for some travel-time data, especially those sensitive to the structure of the lowermost mantle. In particular, the SKKS–SKS residuals show a dramatic improvement. This improvement is only partially caused by the reduction of the average shift between the SKKS and SKS residuals attributed by to the core signal (Liu, 1997), and it remains significant even if we remove the average from the SKKS–SKS residuals.

Our first experiment demonstrates that anisotropy in the uppermost and lowermost mantle improves the data fit. Since the anisotropic pattern at the bottom of the mantle in S362WMANI (Figure 4.20), as well as in the model of Panning and Romanowicz (2006), is correlated with the isotropic one, it is important to investigate the velocity-anisotropy trade-offs. We perform the second experiment to check whether lateral anisotropic variations, such as those in S362WMANI, could be obtained by the inversion of our data, if the true Earth's mantle were purely isotropic. To address this problem, it is necessary to create synthetic data predicted by the isotropic mantle. The isotropic part of S362WMANI is a good approximation of velocities in the mantle, but the perturbations are likely to be underestimated owing to the regularization applied in the inversion. Therefore, in order to create synthetic data, we multiply coefficients $\mathbf{m}^{ISO}$ of the isotropic part of S362WMANI by an arbitrarily chosen factor of three. The anisotropic perturbations are set to zero. The synthetic data $\mathbf{d}^{SYNISO}$ are obtained from $\mathbf{d}^{SYNISO} = \mathbf{A}\ (3\ \mathbf{m}^{ISO})$, where $\mathbf{A}$ is the data kernel for all surface-wave, waveform, and body-wave travel-time data. The synthetic data are inverted for a whole-mantle anisotropic model using exactly the same damping as that used in the calculation of

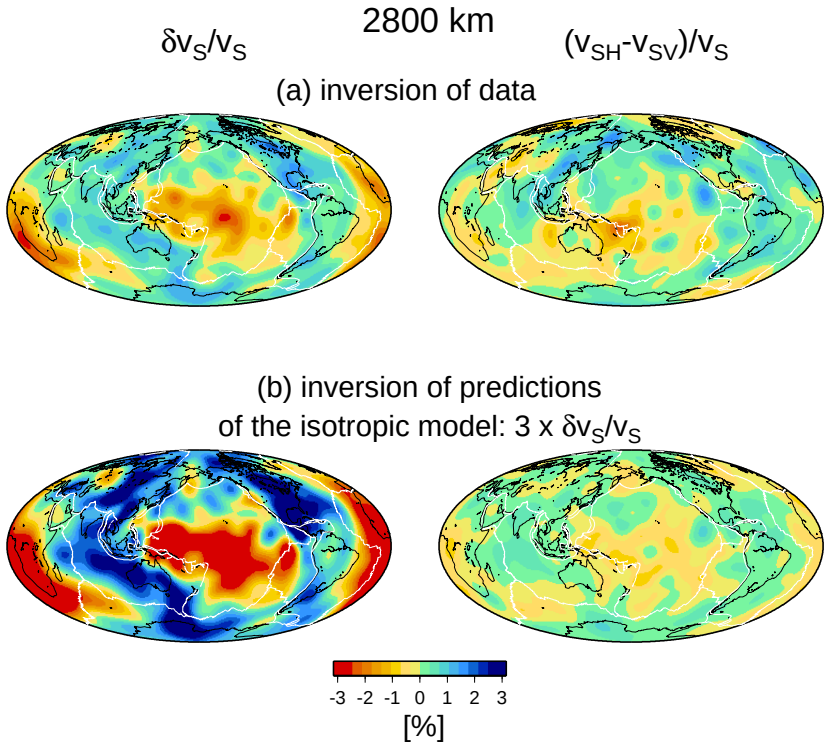

Figure 4.20: (a) Isotropic and anisotropic variations at 2800 km in the whole-mantle anisotropic model S362WMANI. (b) Isotropic and anisotropic variations at 2800 km obtained by inverting the synthetic data predicted by a strong isotropic input model. These spurious anisotropic variations are similar to those obtained by inverting the data, which suggests that the latter may also be an artifact of the inversion.

S362WMANI. The output model (Figure 4.20b) shows a strong isotropic structure similar to that in the input model 3 $\mathbf{m}^{ISO}$. The anisotropic structure in the output model is an artifact and represents the leakage of the isotropic signal into the anisotropic part of the model. These spurious anisotropic variations are similar to those obtained by inverting the data, which suggests that the latter may also be an artifact of the inversion.

The spurious anisotropic variations are not as strong as the anisotropic variations obtained from the data despite the multiplication factor of 3. Although the velocity-anisotropy trade-offs at 2800 km do not appear to be sufficiently strong to explain the anisotropic variations, they are about an

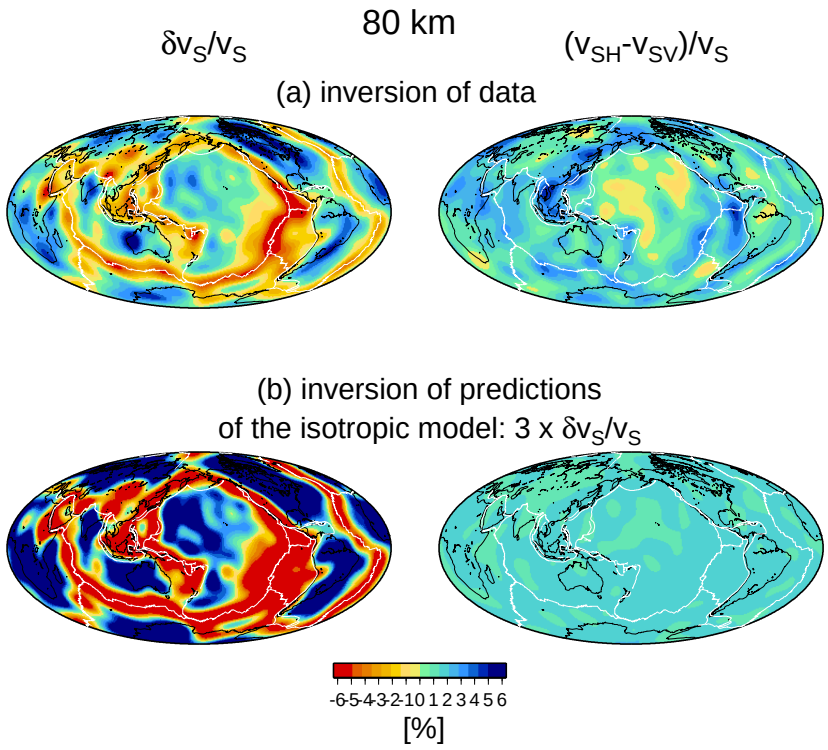

Figure 4.21: Same as Figure 4.20, but for the depth of 80 km and plotted with a different color scale. The spurious anomalies in (b) are much weaker compared to those at 2800 km, which demonstrates that the velocity-anisotropy trade-offs in the upper mantle are much less significant than in the lowermost mantle.

order of magnitude stronger than the trade-offs in the uppermost mantle. At 2800 km, the anisotropic perturbations in the output model are almost as big as in S362WMANI. In contrast, at 80 and 150 km depth, the anisotropic perturbations in the output synthetic model are weaker than 1%, which is only a fraction of the 5-6% variations obtained from the data (Figures 4.21 and 4.22). Furthermore, anisotropic variations at shallow depths are very weakly correlated with the isotropic variations, and therefore unlikely to be caused by trade-offs.

To conclude, we recognize that there is evidence for the presence of anisotropy in the deep mantle (for review, see Kendall, 2000) and that anisotropic anomalies in the D'' region reported by

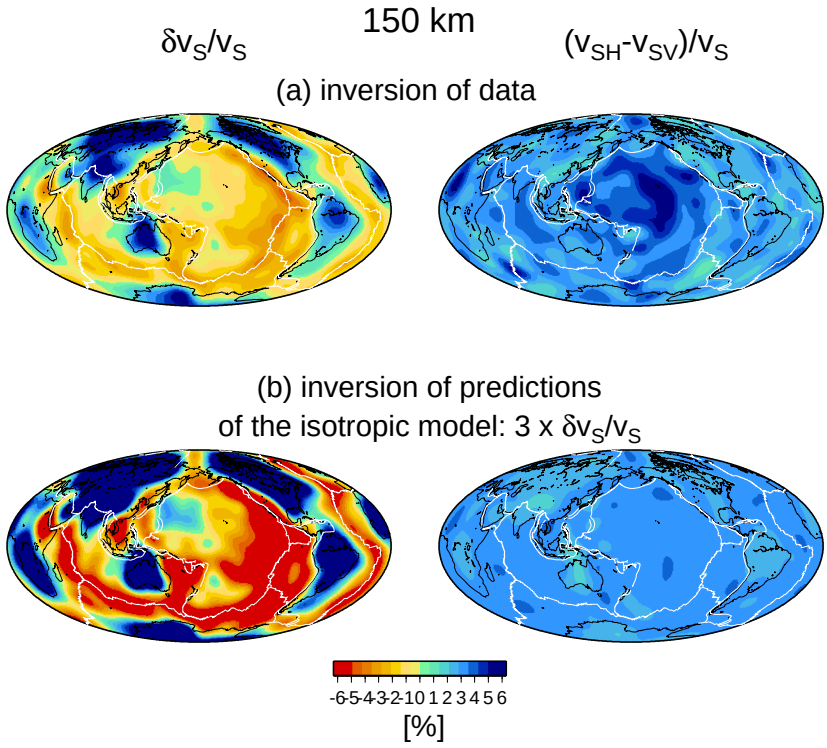

Figure 4.22: Same as Figure 4.20, but for the depth of 150 km and plotted with a different color scale.

Panning and Romanowicz (2006) may be real. We find that allowing for anisotropy in the uppermost and lowermost mantle improves data fits, yet, anisotropy in the transition zone and the mid-mantle is not warranted by our data. While the contamination of the isotropic signal into the anisotropic variations is negligible in the uppermost mantle, it is significant in the lowermost mantle, and may be responsible for a high correlation between the isotropic and anisotropic variations near the core-mantle boundary in S362WMANI. Alternatively, the most heterogeneous region at the bottom of the mantle may be also most anisotropic. It is therefore difficult to prove or disprove whether anisotropic variations in D$''$ in the global model of Panning and Romanowicz (2006) and our model S362WMANI are real. In the following section, we focus on anisotropy in the uppermost mantle

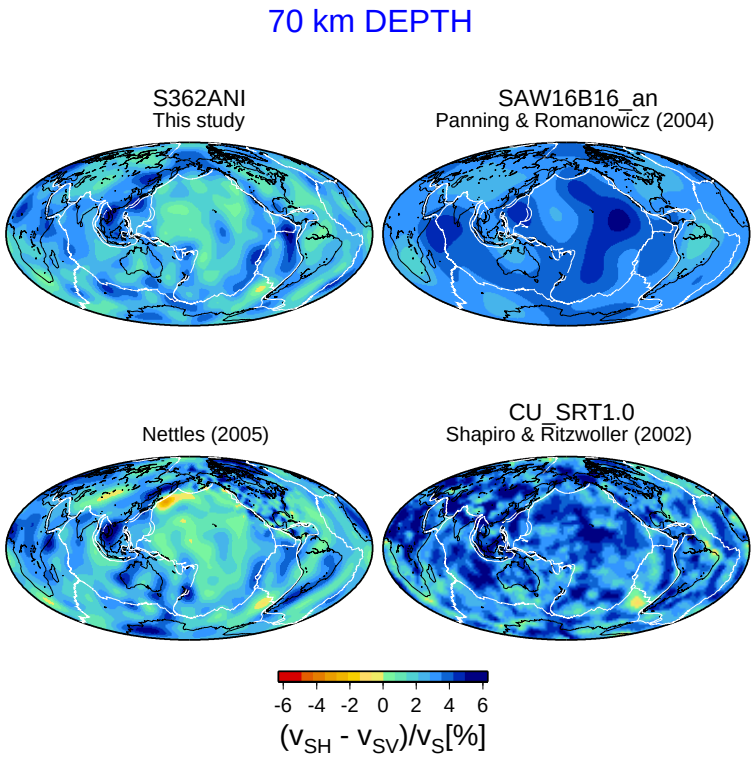

Figure 4.23: Absolute anisotropic variations in four tomographic models at a depth of 70 km including the reference model. The average anisotropy clearly depends on the reference model used in the inversion. In the calculation of our model S362ANI we used REF, while Panning and Romanowicz (2004) and Shapiro and Ritzwoller (2002) used PREM as a reference. Nettles (2005) used a model without the 220 km as a starting model and inverted iteratively for a 3-D model.

based upon our preferred model S362ANI. We also compare the anisotropic variations at all depths in the mantle in S362WMANI with the recent model of Panning and Romanowicz (2006).

4.2.6 Anisotropic velocity structure

In this section, we first discuss anisotropy in the uppermost mantle in our preferred model S362ANI, in which the anisotropy is confined to the four uppermost radial splines, and is very similar to that in S362WMANI in the uppermost 200 km of the mantle. We then compare the anisotropic variations at all depths in the mantle in S362WMANI with the model of Panning and Romanowicz (2006).

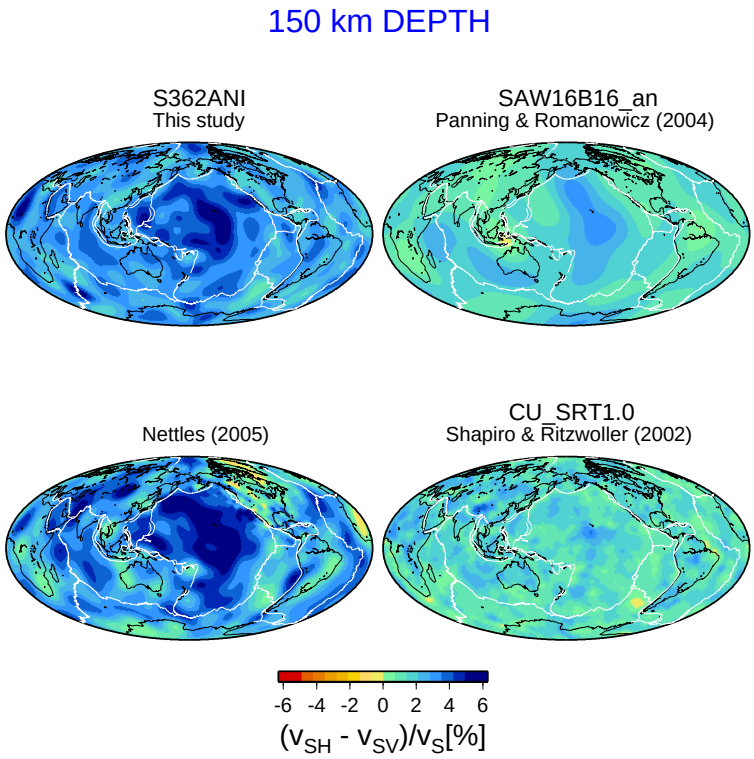

Figure 4.24: Same as Figure 4.23 but for a depth of 150 km. In our model, anisotropy beneath Pacific is significantly stronger than the global average, in contrast to anisotropy at 70-km depth.

We find anisotropic variations at 70 km beneath oceans to be similar to those in the model of Nettles (2005) obtained from a similar set of surface-wave measurements (Figure 4.23). Anisotropy beneath continents, however, is weaker and less variable in S362ANI. Both models, unlike SAW16B16_an (Panning and Romanowicz, 2004) and CU_SRT1.0 (Shapiro and Ritzwoller, 2002), are characterized by a significant change in lateral anisotropic variations between 70 and 150 km with the most pronounced perturbation beneath the Pacific anomaly (Figure 4.24). The Pacific anomaly was first reported by Ekström and Dziewoński (1998), who hypothesized that it might be caused by a small-scale convection or the injection of material into the asthenosphere by mantle plumes.

The SAW16B16_an also shows a positive anomaly at 150 km beneath the Pacific compatible

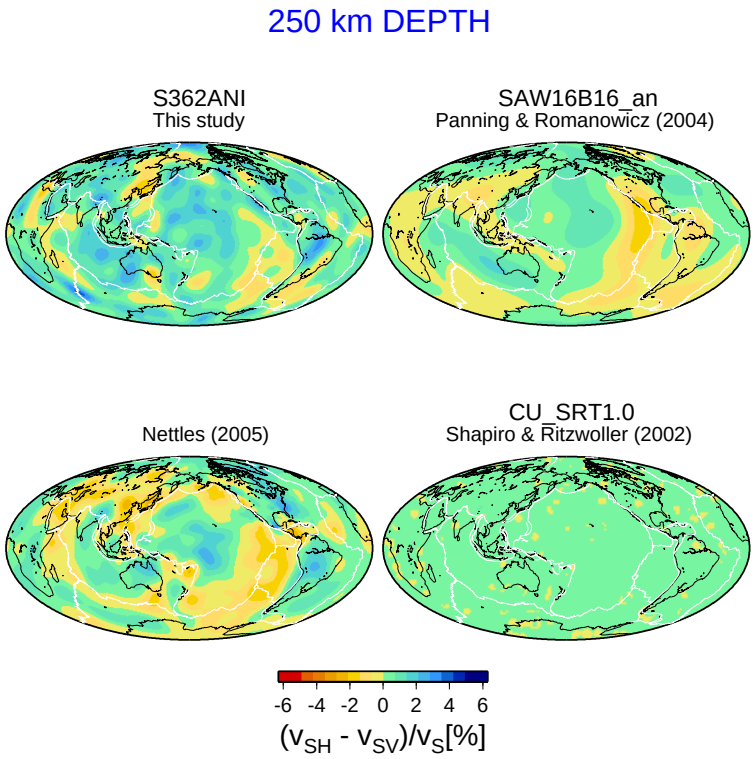

Figure 4.25: Same as Figure 4.23, but for a depth of 250 km. In our model, the average anisotropy becomes weak but lateral anisotropic variations are even more significant than at a depth of 150 km.

with the two Harvard models, but the pattern at 70 km has the opposite sign when compared with S362ANI. The change in the lateral variations between 70 and 150 km in SAW16B16_an are not resolved, likely because this model is not constrained by surface waves at periods shorted than 60 s. Lateral variations in CU_SRT1.0 are significant only at shallow depths and are not correlated with our model. At 150 km Nettles (2005) finds stronger lateral variations than S362ANI. At 250 km, all models, except CU_SRT1.0, show a positive anomaly beneath the central Pacific and a negative anomaly beneath the southeastern Pacific (Figure 4.25). The variations in S362ANI are weak since anisotropy is constrained by the parameterization to decrease with depth.

Our model S362ANI, like the reference model REF, is characterized by a maximum average

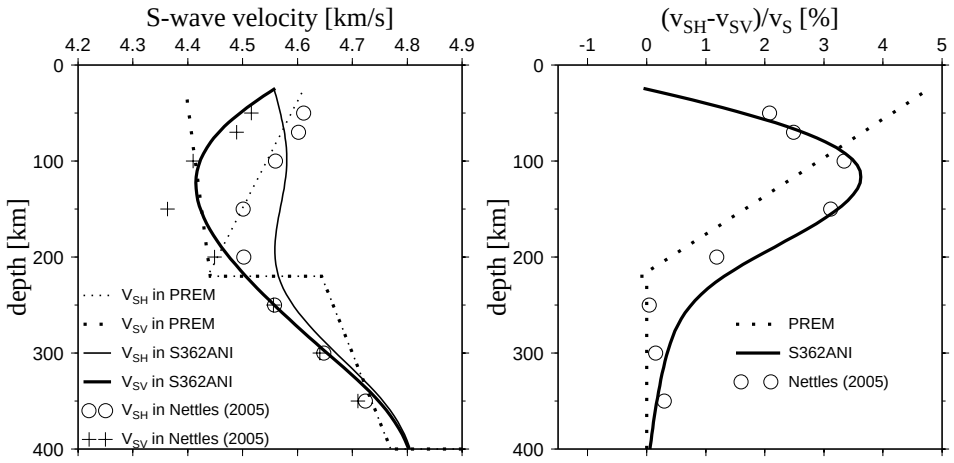

Figure 4.26: Globally averaged shear-wave velocities in S362ANI and the model of Nettles (2005) plotted with PREM.

anisotropy at about 120 km (Figure 4.26). At this depth, v_{SH} is, on average, faster than v_{SV} by almost 4%. The globally averaged anisotropy in S362ANI vanishes at the Moho. The radial profile of average anisotropic variations in the model of Nettles (2005) is similar to ours, but anisotropy in her model vanishes more rapidly below 200 km.

Although globally averaged anisotropy in S362ANI is largest at 120 km, the root-mean-square value of the lateral variations has a local minimum around this depth (Figure 4.27). This suggests that crystals are most strongly and uniformly aligned at this depth, assuming that lattice preferred orientation is responsible for the seismically detected anisotropy. The strongest root-mean-square lateral variations are observed at the Moho where the anisotropic model is dominated by the degree 2-5 structures: the weak anisotropy beneath the Pacific and continents, and stronger anisotropy in the subduction zones in the northwestern Pacific and Southeast Asia.

Below 200 km, the globally averaged anisotropy nearly vanishes, but the root-mean-square

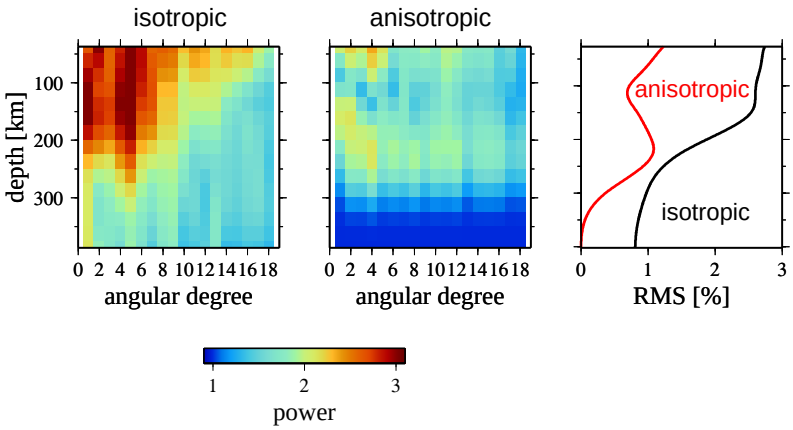

Figure 4.27: Power spectrum and the root-mean-square value of isotropic and anisotropic lateral variations in the uppermost mantle in S362ANI. The lateral anisotropic variations show a local minimum at 120-km depth, which coincides with the strongest average anisotropy, and may be related to the strongest alignment of the minerals in the convecting mantle at this depth.

values of the lateral variations show a local maximum at 220 km with the dominating power at degrees 2, 3, and 4. The presence of this secondary maximum indicates more lateral variability in the flow compared to the depth of 120 km. While the 200-km maximum may represent true variations, it is important to note that the anisotropy beneath 200 km strongly depends on the regularization. For example, increasing vertical smoothness of the isotropic part of the model causes anisotropy at this depth to correlate strongly with the distribution of continents. Such behavior may result from projecting the errors in the crustal model into this part of the mantle model. Another possibility is that the unmodeled anisotropy at larger depths observed by Nettles (2005) may be mapped into the depths of 200-250 km in our model. This explanation is, however, less likely since we do not find strong indications of anisotropy in the waveform data.

Figure 4.28 shows velocity and anisotropy profiles in S362ANI for different tectonic types defined by Jordan (1981b). In oceanic regions, velocities increase with age of the seafloor. Depths of the low velocity zone and of maximum anisotropy also increase with age. In the Pacific, however,

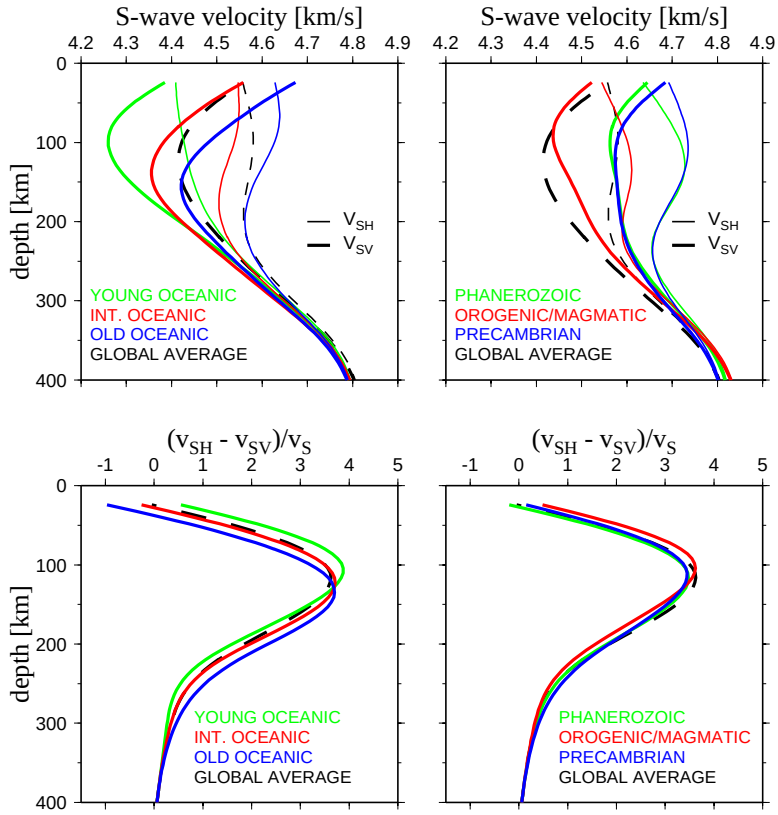

Figure 4.28: Top panels: velocities of the horizontally (thin line) and vertically (thick line) polarized shear waves in S362ANI for different regions of Jordan's (1981b) tectonic regionalization, GTR-1. Bottom panels: regional variations in anisotropy $(v_{SH} - v_{SV})/v_S$, where v_S=$(v_{SH} + v_{SV})/2$. Black dashed lines correspond to the global averages in S362ANI. Green, red, and blue lines in the left panels correspond to the oceanic crust younger than 25 Ma, of intermediate age, and older than 100 Ma, respectively. In the right panels, green lines correspond to the Phanerozoic platforms, red lines to the Phanerozoic orogens and magmatic belts, and blue lines to the pre-Cambrian shields and platforms.

the anisotropy is not correlated with the lithospheric age, as shown by Ekström and Dziewoński (1998). In continental regions, velocities are highest in the pre-Cambrian regions. Phanerozoic platforms are characterized by slightly lower velocities and regions of recent orogenic or magmatic activity show much lower velocities. While these conclusions agree well with Nettles (2005), we do not observe strong and variable anisotropy among the continental regions reported by Nettles (2005). One reason for the discrepancy may result from different regularization of the inverse problem. Vertical variations in anisotropy are stronger than the velocity variations and are very sensitive

to the amount of gradient damping. Other possible reasons for the discrepancy include inverting for η and using waveform data in this study, or more accurate method used to account for the varying depth of the Moho in the model of Nettles (2005). In all cases, the anisotropic variations beneath continents in S362ANI should be interpreted with caution.

In Figure 4.29, we compare our whole-mantle anisotropic model S362WMANI with the model of Panning and Romanowicz (2006). Anisotropic variations in the uppermost part of S362WMANI are almost identical to those in S362ANI. The model of Panning and Romanowicz (2006), on the other hand, shows little change in lateral variations between 50 and 150 km, similar to the model of Megnin and Romanowicz (2000). At 300 km, we observe, in agreement with Panning and Romanowicz (2006), negative $v_{SV} > v_{SH}$ anomalies beneath the East Pacific Rise and positive $v_{SH} > v_{SV}$ anomalies beneath continents. At 500 km, Panning and Romanowicz (2006) find v_{SV} to be slightly faster than v_{SH} beneath mid-ocean ridges, a pattern which is not observed in S362WMANI. In the uppermost lower mantle, the two models are anticorrelated; the model of Panning and Romanowicz (2006) shows similar lateral variations to those at 300 km. This suggests that even if this part of the mantle is anisotropic, the anisotropy cannot be easily resolved by the waveform data. In the mid-mantle, Panning and Romanowicz (2006) find very little anisotropy, and in our model the variations are slightly stronger and of the order of 1%. Anisotropy becomes stronger in the D$''$ region and the very-long-wavelength patterns roughly agree in the two models. Positive anomalies are observed beneath eastern Asia, western North America, and South America, whereas negative anomalies are correlated with the Pacific and African slow-velocity anomalies.

Panning and Romanowicz (2006) emphasize the importance of the $v_{SV} > v_{SH}$ anomalies, which may result from the predominance of the vertical flow in some regions of the mantle. In

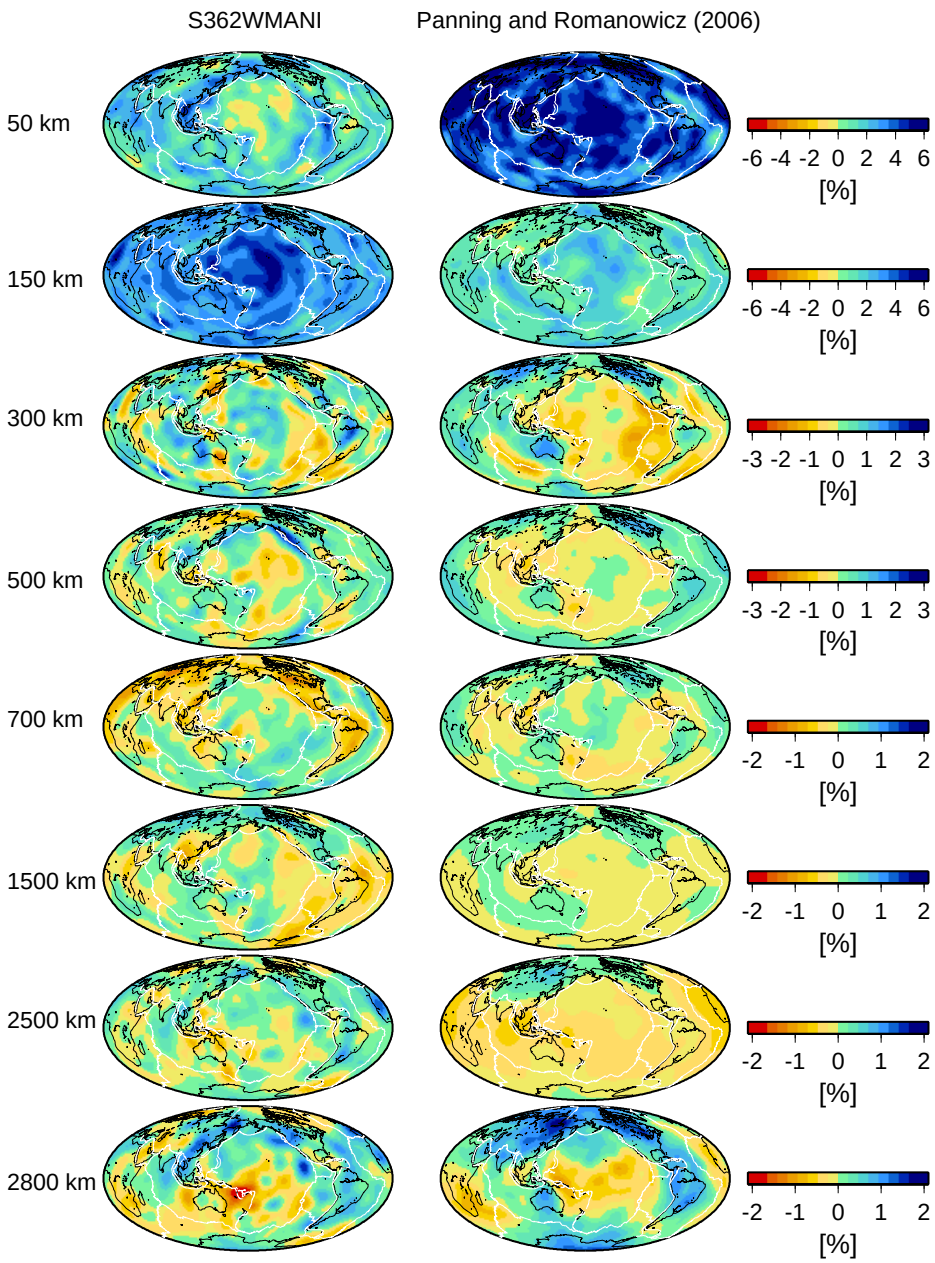

Figure 4.29: Anisotropic velocity variations $(v_{SH} - v_{SV})/v_S$ in our whole-mantle anisotropic model S362WMANI and in the model of Panning and Romanowicz (2006). The differences in the averages in the upper mantle result from using different reference models. At 300 km, both models show negative anomalies beneath the East Pacific Rise and positive anomalies beneath continents. The anisotropic structure in the uppermost lower mantle is difficult to determine; the models are anticorrelated with each other. The most prominent anomalies found in the lowermost mantle are correlated with the location of the 'superplumes' observed in the isotropic velocity models.

their model, such negative anomalies are observed beneath mid-ocean ridges at 300 km, and in the Pacific and African 'superplumes' at the bottom of the mantle. We find some indications of negative anomalies in oceanic regions at depth of 300 km, which are, however, usually offset from the location of the mid-ocean ridges, and vanish in the transition zone. In our model, the Pacific and southern Africa also show the $v_{SV} > v_{SH}$ pattern, which may suggest the presence of vertical thermal upwellings in these regions. It is not clear whether these anomalies are real, since allowing for anisotropy below 200 km in the inversion does not improve a fit significantly for our waveform data, as discussed in Section 4.2.5.

4.2.7 Comment on laterally varying sensitivity kernels and depth of the Moho

In this section, we discuss the effects of two simplifying assumptions used in the derivation of S362ANI. First, we assume that solving a linear inverse problem with sensitivity kernels predicted by the reference model REF is sufficient to determine realistic lateral variations in shear-wave velocity. In fact, the sensitivity of seismic waves depends on the laterally heterogeneous structure and determination of the three-dimensional structure is therefore a nonlinear problem. Second, we assume that corrections discussed in Chapter 2 remove all crustal effects from phases or travel times of seismic waves, leaving our data sensitive exclusively to the structure of the mantle. However, our radial parameterization does not account for variations in the depth of the Moho, which means that our model is defined, but meaningless, within the continental crust below 24.4 km, and that mantle structures shallower than 24.4 km beneath oceans remain unmodeled.

The main reason for assuming sensitivity based only upon the reference model REF is that accounting for lateral variations in sensitivity in the inversion of long-period waveforms would be

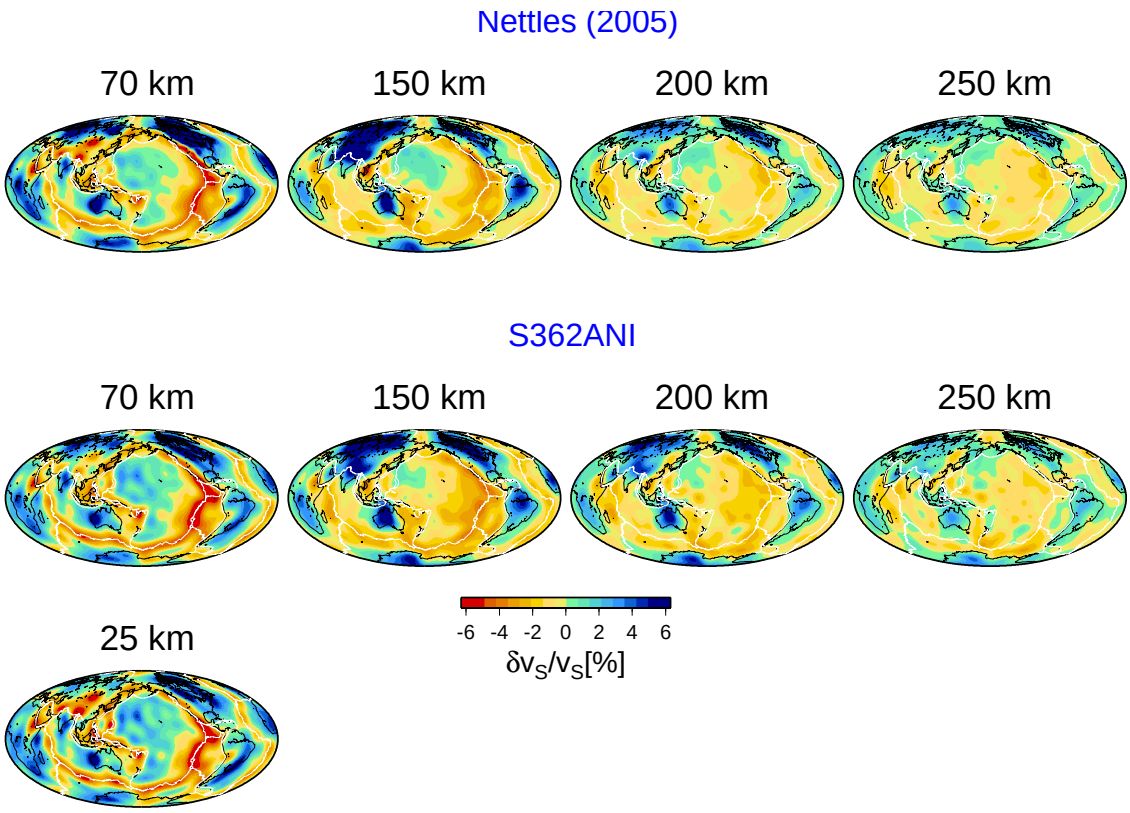

Figure 4.30: Isotropic variations in S362ANI and the model of Nettles (2005). Stronger anomalies in oceanic regions and weaker anomalies beneath continents at 70 km result from neglecting some higher-order effects of lateral variations in the depth of the Moho in the inversion for S362ANI.

computationally unfeasible. Constant depth of the Moho is required to make the inversions of surface waves and waveforms consistent with each other. For the case of surface-wave tomography, both the nonlinearity of the inverse problem and variations in the Moho depth have been addressed by Boschi and Ekström (2002) and subsequently by Nettles (2005). In this section, we discuss these two issues jointly, although they are two separate problems. These issues are addressed through the comparison of S362ANI with the model of Nettles (2005). The comparison is likely to give us insight into the effects of our simplifying assumptions because of the similarity in modeling techniques and data used in the derivation of the two models. Both models are parameterized laterally

on a global scale in terms of 362 spherical splines and vertically using a similar number of radial B-splines, they are transversely isotropic, and in both cases, regularization involves minimization of horizontal and vertical roughness. Nettles (2005) used the same set of 35-150 surface-wave data as in this study with the additional small set of 150-350 second measurements.

The model of Nettles (2005) shows similar pattern of lateral heterogeneity in the uppermost mantle as S362ANI (Figure 4.30). The only significant difference is the magnitude of perturbations at 70 km. Mid-ocean ridges show stronger negative anomalies in S362ANI, whereas fast-velocity anomalies within the continental lithosphere are stronger in the model of Nettles (2005). These differences cannot result from different regularization, because stronger damping would diminish both positive and negative anomalies. Another potential cause of the discrepancy between the two models is the nonlinear approach employed by Nettles (2005). Additional iteration, however, should increase amplitudes of both positive and negative anomalies.

The differences between the two models at 70 km most likely result from the less accurate method used to account for variations in crustal thickness in the calculation of S362ANI. The Moho beneath mid-ocean ridges is approximately at a depth of 9-10 km. Our model, however, is defined up to a depth of 24.4 km, leaving the strongly heterogeneous uppermost 15 km of the suboceanic mantle unmodeled. The unmodeled structures are mapped to the uppermost part of S362ANI, which consequently shows stronger negative anomalies beneath ridges than the model of Nettles (2005) parameterized up the Earth's surface and with the sensitivity kernels integrated up to Moho depth in CRUST2.0. Beneath continents, on the other hand, our parameterization makes the mantle extend about 15 km too shallow into the crust. This leaks fast-velocity anomalies into the crust, causing the continental lithosphere at 70 km to be slower than in the model of Nettles (2005). This effect is

most pronounced in the North America, where positive anomalies at 25 km in S362ANI are stronger than 5%, but velocities at 70 km are too low.

In fact, all anomalies beneath oceans are stronger in S362ANI, and all anomalies beneath continents are stronger in the model of Nettles (2005) at 70 km. For example, positive anomalies at 70 km beneath the northwestern Pacific have higher amplitudes in S362ANI, which can be explained, as in case of the negative anomalies along the ridges, by mapping the unmodeled structures into the mantle. Negative anomalies beneath southern and southeastern Asia show the same behavior as the positive anomalies beneath continents; they are much weaker in S362ANI.

At 150 km, the models are very similar to each other. Our model shows slightly stronger anomalies beneath mid-ocean ridges and the North America, and slightly weaker anomalies in Eurasia. At 200 km, the differences are more pronounced, but this is more likely the effect of including long-period waveforms in our inversion, which were not used by Nettles (2005). The systematically weaker anomalies are more likely to result from stronger damping used by Nettles (2005).

At 250 km, the two models are both very weak. This indicates that modeling errors at shallow depths do not significantly affect the depth extent of slow velocity anomalies beneath ridges and fast velocity anomalies beneath continents. Ridge signatures at 200 km are slightly stronger in S362ANI, which is likely to be caused by different damping. Both models show a dramatic decrease in the strength of continental anomalies between 150 and 250 km, which probably represents negative velocity gradients or a discontinuity at the base of the lithosphere.

Boschi and Ekström (2002) presented a similar analysis to ours and reported very similar effects of using constant and varying sensitivity kernels and depths of the Moho. They concluded that improvements in the modeling technique lead to a significantly different model, but they did

not present evidence that using laterally varying sensitivity kernels has a significant effect on the model. Our comparison indicates that differences between the two models at shallow depths can be explained in terms of differences in parameterization, and at, larger depths by different regularization. The inversion of 35-150 second surface-wave data is likely to be only weakly nonlinear if a reasonable reference model is used. Nettles (2005) and Boschi and Ekström (2002) reported appreciable differences between models obtained after the first and second linear iterations. However, they both used an unreasonably fast and purely isotropic starting model, which is at least partially responsible for the differences. In contrast, we use the anisotropic reference model REF, and the prior inversion for REF may have a similar effect on the final model as the first iteration of Boschi and Ekström (2002) and Nettles (2005).

Finally, we recognize that the anisotropic structure beneath continents is significantly different in S362ANI than in the model of Nettles (Figure 4.23). We cannot rule out that this discrepancy is caused by using a less accurate method to account for the variations in the depth of the Moho in the inversion for our model. The effects of using laterally varying sensitivity kernels on the ability to retrieve regional-scale details of the structure are yet to be demonstrated.

4.2.8 Effect of the reference model

In order to investigate the effect of using a new reference model REF on the velocity structure and CMT solutions, we have calculated a three-dimensional model S362ANI_PREM. It was obtained from the same data and using identical techniques and regularization as S362ANI, but using PREM as a reference model. The two models are also parameterized in the same way with one minor exception; radial B-splines in S362ANI_PREM are split at a depth of 670 km rather than 650 km.

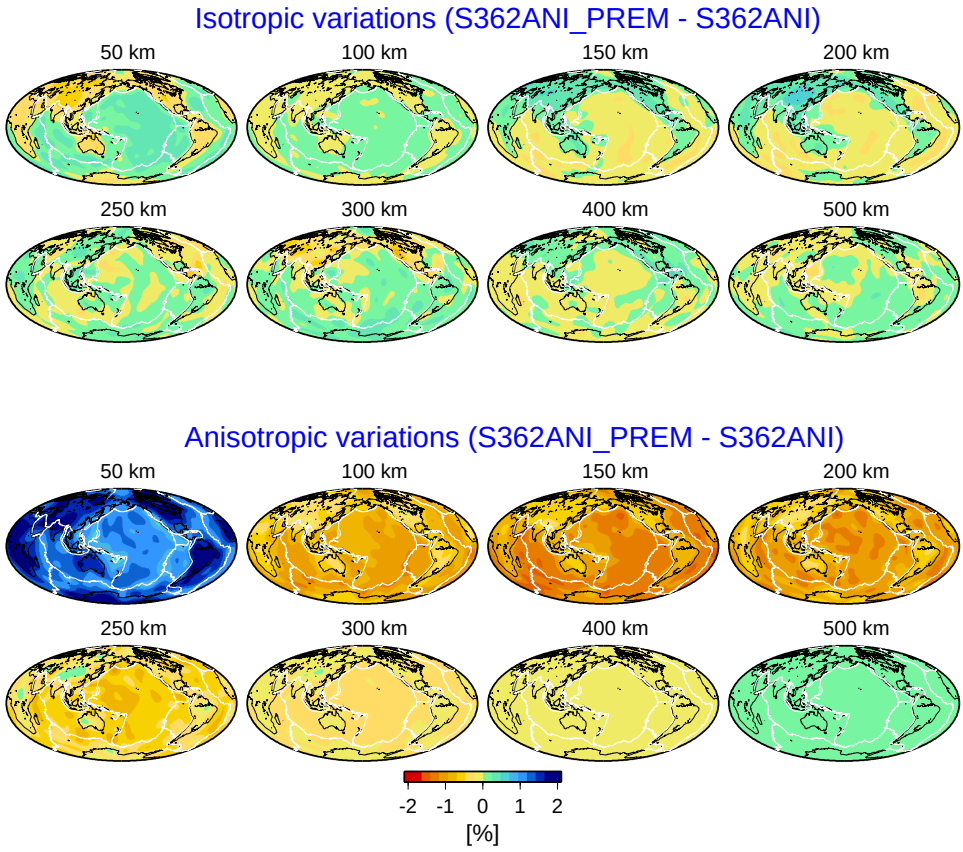

Figure 4.31: Difference between lateral variations in S362ANI_PREM and S362ANI. Global averages in both models were removed from the isotropic variations before calculating the differences. The differences are small compared to the observed anomalies, which indicates that lateral isotropic and anisotropic variations in the upper mantle have little sensitivity to the choice of the reference model.

Figure 4.31 shows the difference between lateral variations in S362ANI_PREM and S362ANI. The differential patterns are not random; at shallow depths, for example, they are correlated with the distribution of continents. The discrepancies are, however, rarely larger than 0.4% and usually do not exceed 0.2%. In the lower mantle, the differences are even smaller and do not exceed 0.2%, and therefore they are not included in the figure. Depth variations of the average anisotropy are significantly different in the two models, but this does not have a strong effect on the lateral anisotropic variations. The choice of the reference model, therefore, has little effect on the modeled lateral

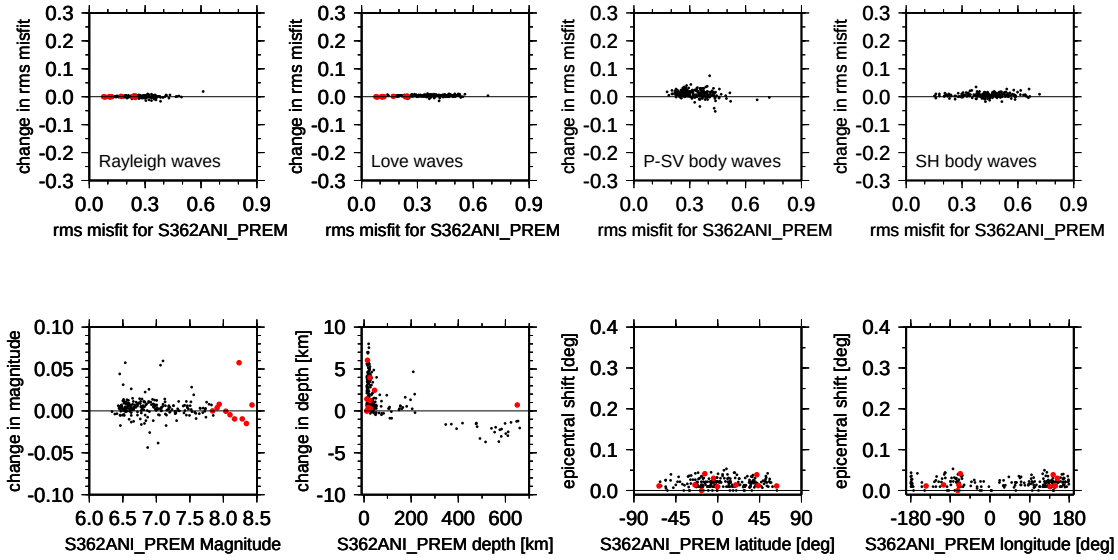

Figure 4.32: Effect of using REF rather than PREM on the Centroid Moment Tensor solutions for individual earthquakes. Black dots correspond to $6.5 \leq M_w < 8$ events and red dots represent earthquakes with $M_w \geq 8$. Changes in the root-mean-square misfit, magnitude, focal depth, and the epicentral shift represent differences between the CMT solutions for S362ANI and S362ANI_PREM. The epicentral shift is plotted both as a function of the epicentral latitude and longitude.

heterogeneities.

Figure 4.32 summarizes differences between CMT solutions for S362ANI and S362ANI_PREM. Our preferred model S362ANI systematically improves the fits, but the median improvement is small, and ranges between 0 to 1% for different types of data. Estimates of the magnitudes for the two models are nearly identical. Changes in focal depths are more significant. Epicentral shifts are smaller than 5 km, and do not show any azimuthal dependence.

The comparison of the root-mean-square misfits indicates that REF+S362ANI fit the waveforms as well as PREM+S362ANI_PREM, and that the 220-km discontinuity in the PREM model is not required by the waveform data. However, we cannot demonstrate that REF+S362ANI fit our surface-wave and body-wave travel-time data as well as PREM+S362ANI_PREM. Since measure-

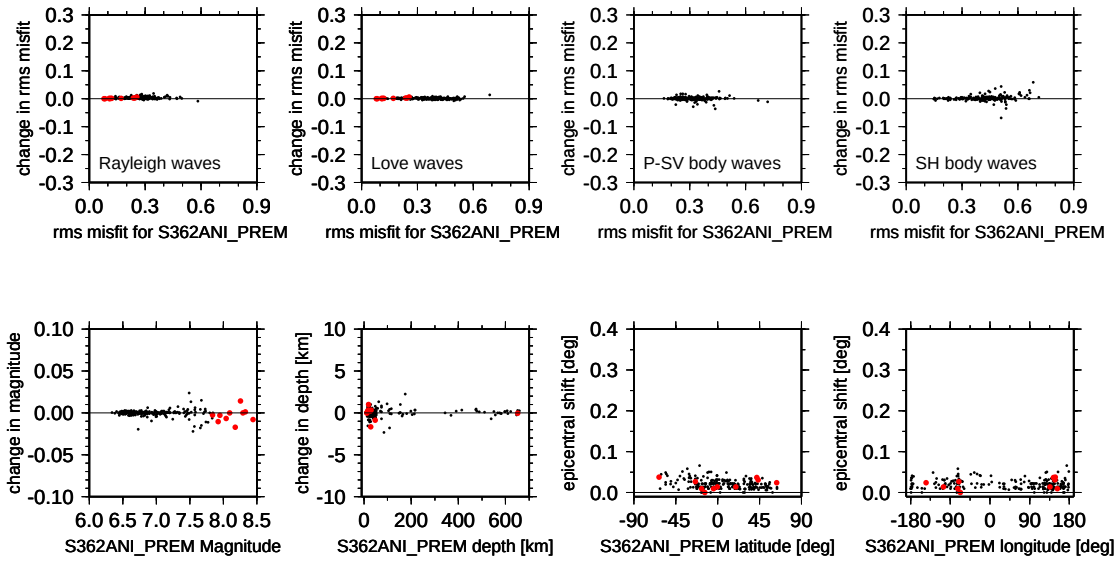

Figure 4.33: Effect of neglecting lateral anisotropic variations on the Centroid Moment Tensor solutions for individual earthquakes. As in Figure 4.32, black dots correspond to 219 earthquakes of $6.5 \leq M_w < 8$ and red dots represent 10 earthquakes with $M_w \geq 8$. Changes in the root-mean-square misfit, magnitude, focal depth, and the epicentral shifts represent differences between the CMT solutions for S362ANI and S362ISO.

ments of phases and travel times are defined as residuals with respect to a reference model, the variance reduction for these data sets represents an improvement with respect to a reference model and is not an independent measure of fit.

4.2.9 Effect of anisotropy

In order to quantify the effect of anisotropy on the CMT solutions and the velocity structure, we have developed a model S362ISO in the same way as S362ANI without allowing for anisotropic variations in the upper mantle. The summary of data fits for S362ISO were presented and discussed in Section 4.2.5. Here, we show the improvement in root-mean-square misfits for individual earthquakes (Figure 4.33). Allowing for anisotropy in the uppermost mantle improves fit marginally with

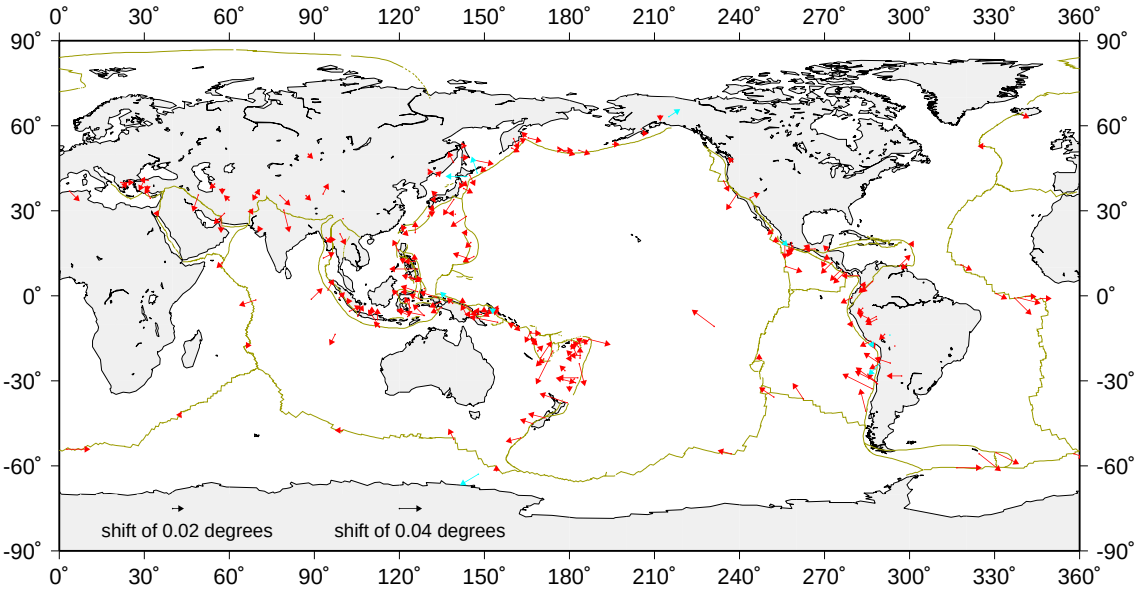

Figure 4.34: Epicentral shifts for the CMT solutions for S362ANI with respect to CMT solutions for S362ISO. Red arrows correspond to the $6.5 \leq M_w < 8$ events and green arrows correspond to the earthquakes with $M_w \geq 8$. Plate boundaries are shown in yellow lines.

the median change between 0 and 0.2% for different data sets. The changes in earthquake magnitudes and hypocentral coordinates are also very small. The epicentral shifts, however, show certain trends (Figure 4.34). Earthquakes in South America and in the eastern Pacific are systematically relocated toward the center of the Pacific if anisotropy is allowed in the model. The Aleutian events are shifted in the southeastern direction, while Indonesian and Izu-Bonin events are relocated toward Philippines. The epicentral shifts due to anisotropy are small, but their azimuthal dependence indicates that long-period waveforms are somewhat sensitive to the lateral anisotropic variations.

Neglecting anisotropy in the inversion significantly affects isotropic variations in the upper mantle (Figure 4.35). The effect is of the order of 1% throughout the Earth. The difference between S362ISO and S362ANI beneath the Pacific and Southeast Asia is as big as 2%, which is comparable with the amplitude of the isotropic variations in these regions. The CMT solutions for earthquakes

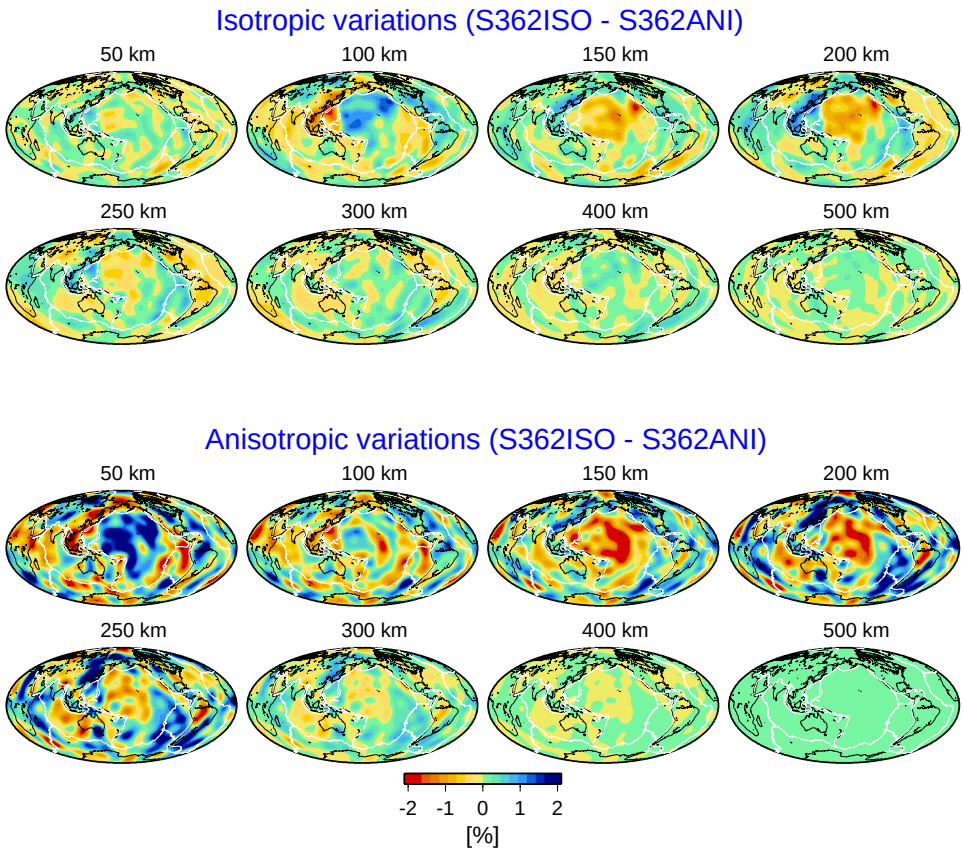

Figure 4.35: Difference between lateral variations in S362ISO and S362ANI. Global averages in the isotropic variations were removed from both models before calculating the differences. The differences in isotropic velocities in the Pacific and Southeast Asia are as large as the isotropic variations. Differences in anisotropic variations represent the anisotropy in S362ANI since S362ISO is isotropic.

in the Pacific and Southeast Asia are strongly affected by the velocity of seismic waves in these highly anisotropic regions, which explains the systematic trends in epicentral shifts.

4.2.10 Effect of crustal corrections

In the determination of Harvard CMT solutions, seismograms are corrected for crustal effects assuming that a perturbation in the crustal thickness has a linear effect on the perturbation in the normal-mode eigenfrequency. In Chapter 2, we have shown that crustal effects are, in fact, nonlin-

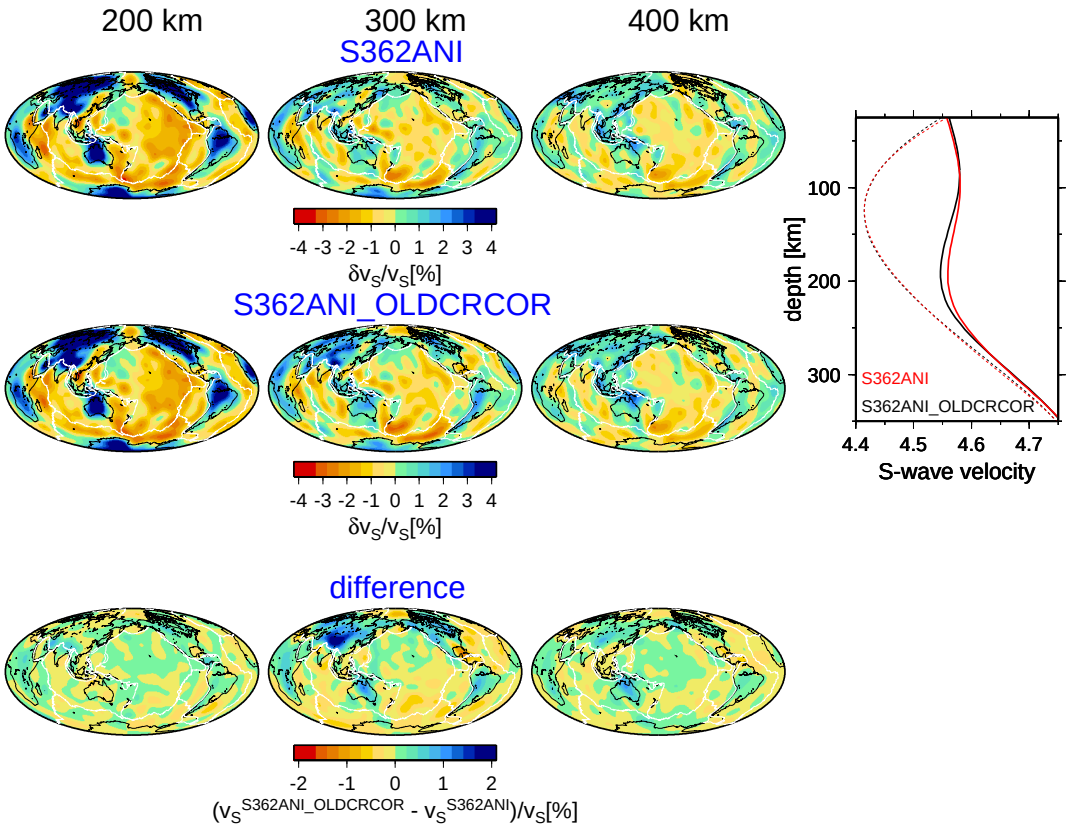

Figure 4.36: Left: isotropic velocity variations in S362ANI and S362ANI_OLDCRCOR, global averages removed. The model obtained using linear crustal corrections shows fast velocity anomalies beneath continents extending to larger depths than in S362ANI. Right: globally-averaged v_{SH} (solid lines) and v_{SV} (dashed lines) velocities in the two models.

ear, and in the calculation of the new model S362ANI, we have applied nonlinear corrections.

In order to investigate how the improvement in crustal corrections affects the mantle model and the CMT solutions, we have built a model S362ANI_OLDCRCOR using the standard linear corrections and compare it with S362ANI. Lateral variations in the two models are, in general, similar to each other. The only significant difference is observed between depths of 250 and 350 km, where linear crustal corrections cause the fast-velocity anomalies beneath continents to extend to larger depths than in S362ANI (Figure 4.36). Since the determination of thickness of the continen-

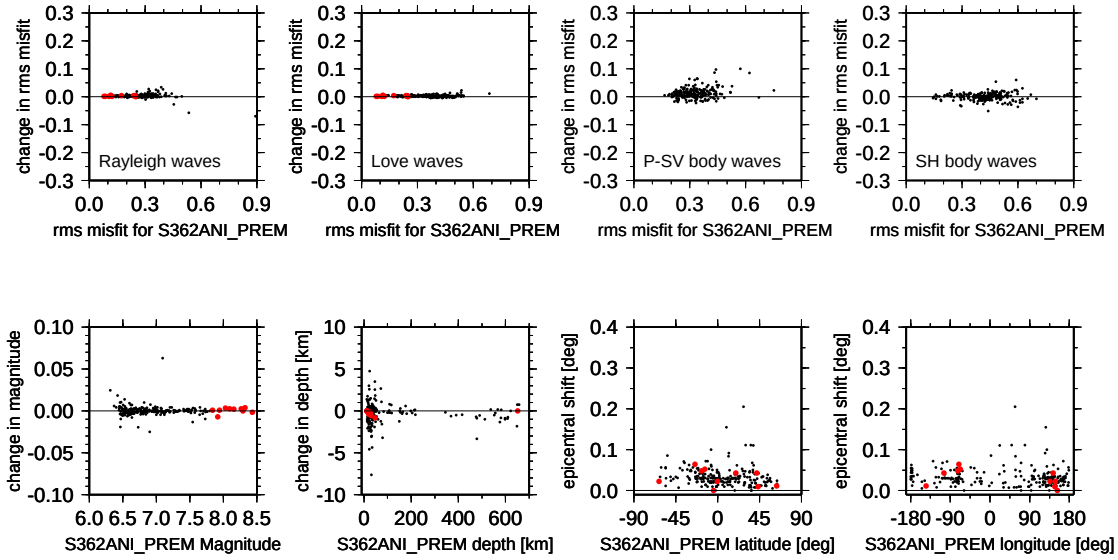

Figure 4.37: Effect of the crustal corrections on the Centroid Moment Tensor solutions for individual earthquakes. As in Figure 4.32, black dots correspond to $6.5 \leq M_w < 8$ events, and red dots represent earthquakes with $M_w \geq 8$. Changes in the root-mean-square misfit, magnitude, focal depth, and the epicentral shifts represent differences between the CMT solutions for S362ANI and S362ANI_OLDCRCOR.

tal plates is one of the fundamental questions addressed by mantle tomography, we conclude that developing more accurate crustal corrections for normal-mode synthetic seismograms represent a significant improvement in studying the structure of the Earth's mantle.

The new crustal corrections significantly affect the globally averaged velocities of horizontally-polarized shear waves. Differences in radial v_{SH} profiles may be responsible for the differences in focal depths determined for the two models (Figure 4.37). Our preferred model S362ANI fits the data systematically better than S362ANI_OLDCRCOR, but the median improvement is marginal and varies between 0 and 1% for different types of data. Magnitude estimates are almost insensitive to the types of crustal corrections. The effect on epicentral shifts is more significant than that of anisotropy. The shifts show systematic azimuthal trends in the continental regions (Figure 4.38).

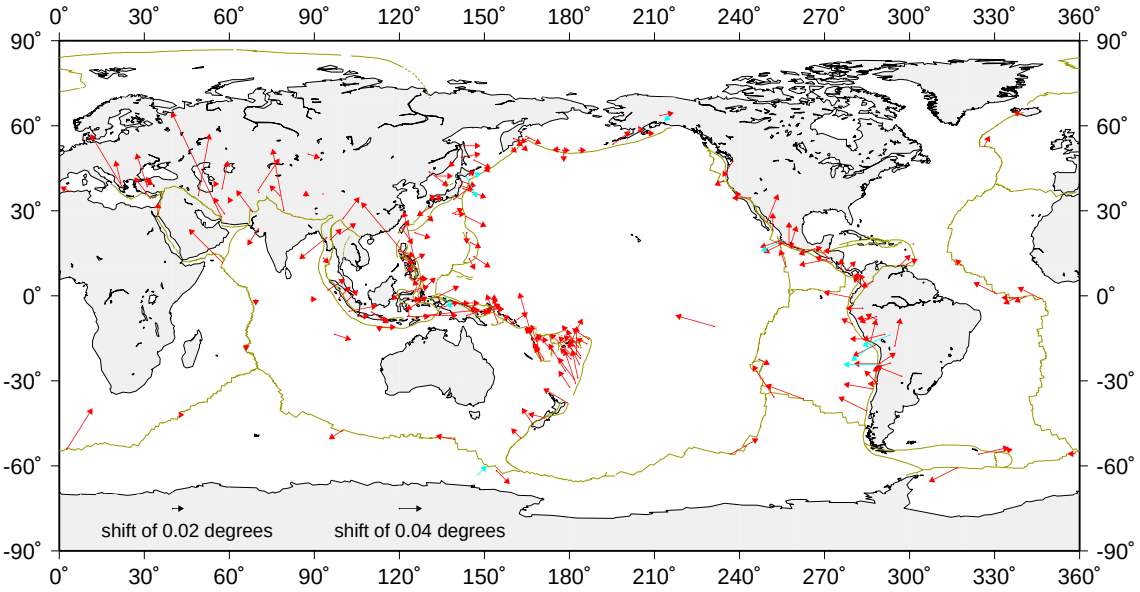

Figure 4.38: Epicentral shifts for the CMT solutions for S362ANI with respect to the solutions for S362ANI_OLDCRCOR. Red arrows correspond to the $6.5 \leq M_w < 8$ events and green arrows correspond to the great earthquakes.

The most significant effect is observed is Eurasia, where using more accurate crustal corrections relocates nearly all earthquakes in the northeastern direction. For example, the event E030499A in southern Iran is shifted by more than 20 km, and the South American events are systematically relocated towards the Pacific. Many of the waves used to locate both Eurasian and the South American events propagate through regions characterized by a very thick crust, where linear corrections show most significant errors. In contrast, epicentral shifts for earthquakes in the oceanic regions show little azimuthal trends and are usually smaller than for continental earthquakes.

4.2.11 Comparison with the CMT solutions for SH8/U4L8

Figure 4.39 show the comparison of the CMT solutions for S362ANI with the solutions obtained using a model SH8/U4L8 (Dziewoński and Woodward, 1992). This model is routinely used in the

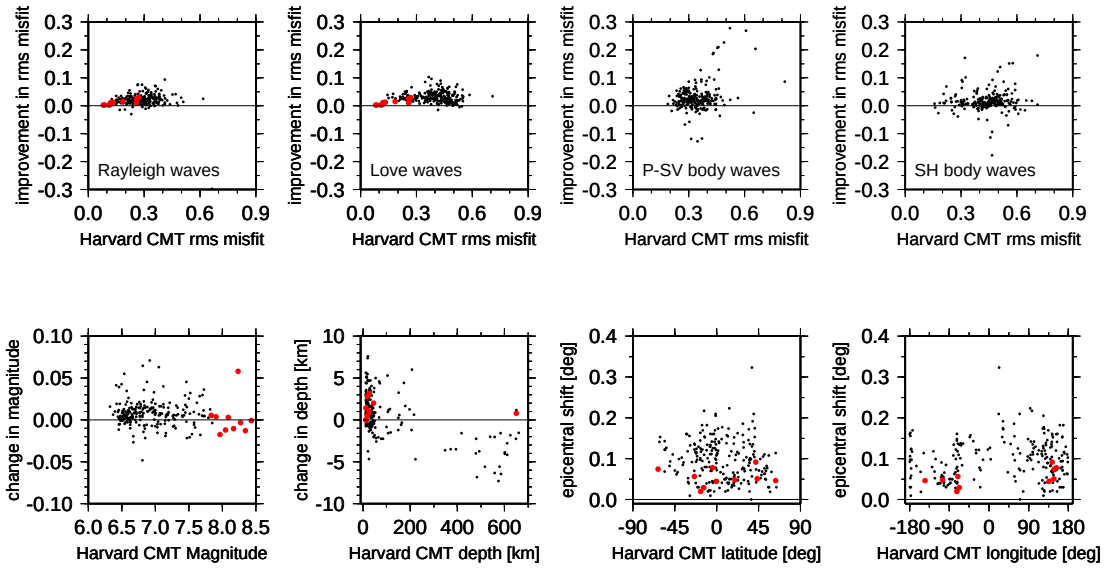

Figure 4.39: Effect of using the new model S362ANI on the Centroid Moment Tensor solutions for individual earthquakes. Black dots correspond to 219 earthquakes of $6.5 \leq M_w < 8$, and red dots represent 10 great earthquakes. The improvement in the root-mean-square misfit is the difference between root-mean-square misfit for each individual event calculated using S362ANI and the root-mean-square misfit of the CMT solutions determined using a model SH8/U4L8 of Woodward and Dziewoński (1992). Changes in magnitude, focal depth, and the epicentral shift represent differences between the CMT solutions for S362ANI and the SH8/U4L8 solutions.

calculation of the standard Harvard CMT solutions. In this study, however, the seismograms have been measured manually by Adam Dziewoński and automatically by Göran Ekström in different time windows than the published Harvard CMT solutions. The model SH8/U4L8, defined as a perturbation with respect to PREM, does not account for lateral variations in anisotropy, and has been derived from a relatively small data set using linear crustal corrections. The CMT solutions calculated for S362ANI therefore include improvements due to higher resolution, anisotropy, and a new reference model, as well as the more accurately calculated crustal corrections. We isolated some of these effects in the previous sections, and the comparison presented here represents the cumulative effect of the new model on the CMTs.

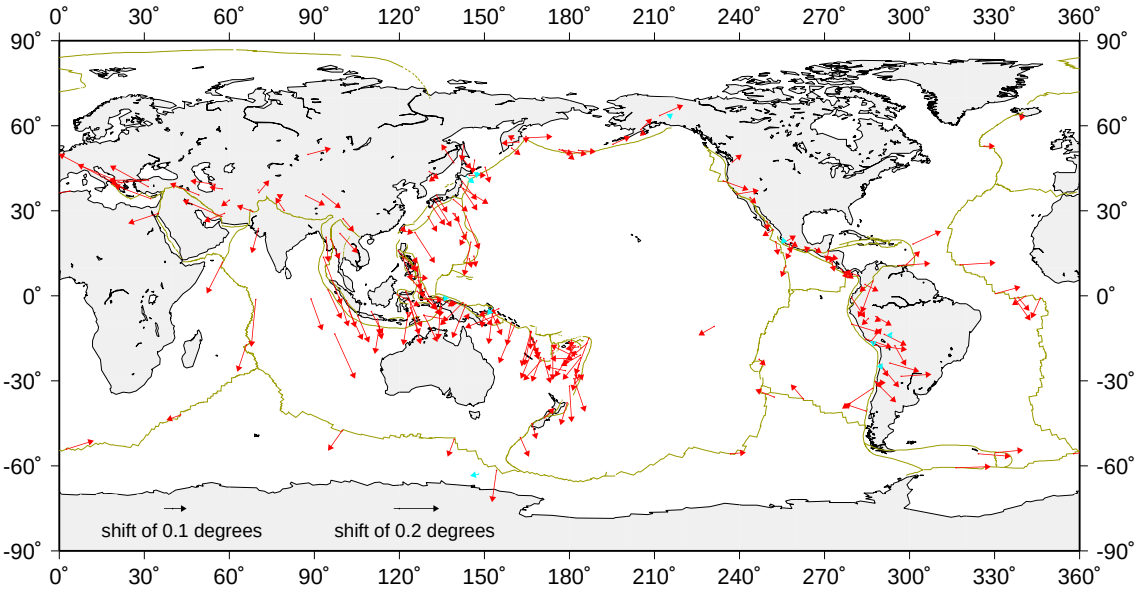

Figure 4.40: Epicentral shifts for the CMT solutions for S362ANI with respect to the SH8/U4L8 solutions. Red arrows correspond to the $6.5 \leq M_w < 8$ events, and green arrows correspond to the great earthquakes. Note that the epicentral shifts are plotted on a different scale than in Figures 4.34 and 4.38.

Seismograms calculated for the model S362ANI systematically improve the fit to the observed mantle and body waves recorded on all components. The improvement for earthquakes with $M_w > 8$ has the median of about 1% for both Rayleigh and Love waves. A more significant effect is observed for smaller earthquakes, where the median improvement is larger than 3% for Love waves, 2% for Rayleigh and P-SV body waves, and 1% for SH body waves. For many earthquakes, the improvement exceeds 5%. Better data fits lead to slightly higher magnitudes, but the increases are rarely more than 0.05. The depth of shallow earthquakes is usually increased by few kilometers, whereas deep earthquakes are usually pushed slightly shallower by S362ANI. The comparison with Figures 4.32 and 4.37 indicates that this behavior is caused by using different reference model and crustal corrections. The overall change in hypocentral depth is smaller than 8 km for all events.

The epicenters are shifted usually by about 5 km for earthquakes larger than M_w=8 and by

about 10 km for smaller earthquakes. Earthquakes in the Indian Ocean and western Pacific are systematically relocated to the South (Figure 4.40). The epicentral shifts are also larger, and are plotted on a different scale compared to Figures 4.34 and 4.38. The shifts around the Mediterranean basin and Middle-East are predominantly in the northwest direction. The single largest shift of 32 km is observed for a M_w=6.4 event that occurred on June 15, 1995 in Greece. The South American earthquakes tend to move southeast, but two off-shore events are relocated towards the Pacific. The continental earthquakes in South America show the opposite azimuthal trend compared to the effects of anisotropy and crustal corrections, which demonstrates that the effect of lateral isotropic variations is dominant in the determination of the epicenters.

Results presented in this section indicate the robustness of the CMT solutions, in particular, for earthquake magnitudes and focal depths. The epicentral locations show certain trends related to the lateral heterogeneities in the velocity model, and discrepancies of 15 km between the CMT solution for S362ANI and SH8/U4L8 are not uncommon. The effect of S362ANI on the CMT solutions for smaller earthquakes, for which seismograms of short- and intermediate-period surface-waves comprise the main constraints, has not been investigated in this study.

Chapter 5

Regional model of the upper mantle beneath Eurasia

The variety of tectonic provinces in the Eurasian continent makes it an interesting region to study for a geoscientist. Modeling seismic velocities beneath cratons that are far away from continental boundaries may help to understand the state of the lithosphere that is not affected by the flow in the suboceanic mantle. Studying regions of recent tectonic activity associated with the closing of the Tethys Ocean may provide an insight into the processes of subduction and continental collision.

Different parts of Eurasia have been extensively studied using forward modeling techniques and seismic tomography. While investigating small portions of Eurasia may help to understand the local velocity structure, a continental-scale model is necessary for, for example, a systematic comparison of lithospheric thickness in different parts of the continent, or providing a snapshot of large-scale geodynamic processes. To date, only one tomographic model has been developed that encompasses the structure of the entire Eurasian continent with regional-scale detail (Shapiro and Ritzwoller,

2002) .

There are several reasons why no other such models exist. Direct arrivals of teleseismic body waves reported by the International Seismological Centre are significantly sensitive to the upper mantle structure only within a narrow cone beneath sources and receivers. While ray-path coverage for such data in the tectonically active regions is fairly good, northern Eurasia is essentially aseismic, and the limited number of seismic stations does not provide sufficient data coverage to build a tomographic model. Body waves that are multiply reflected from the surface sample the northern Eurasia and can be used to study the upper-mantle structure (Grand and Helmberger, 1985). These data, however, are not numerous enough to construct a well-constrained regional-scale tomographic model. There are observations of regional-distance body waves from, so-called, Peaceful Nuclear Explosions carried out in the former Soviet Union, which bottom in the upper mantle in northern Eurasia, and they have been used to develop several compressional-wave velocity models (*e.g.*, Ryberg *et al.*, 1996; Morozova *et al.*, 1999; Nielsen and Thybo, 1999). These models, however, are only two-dimensional in the direction of seismic profiles. The identification of triplicated arrivals in these models is based on the careful analysis of the seismic profiles. Such identification is very difficult in the three-dimensional case, as shown by Garnero *et al.* (1992) and Kustowski *et al.* (2003).

Unlike body waves, surface waves provide much better data coverage in Eurasia, as shown in Figure 3.4. Surface-wave tomographic studies have been performed for several regions in Eurasia (*e.g.*, Priestley and Debayele, 2003; Boschi *et al.*, 2004; Maggi and Priestley, 2005). Constraining the structure beneath the entire continent, however, involves an inversion of a large data set hence inversion of a massive matrix. While several investigators have performed such inversions to de-

velop models of North America (van der Lee and Nolet, 1997; Godey *et al.*, 2004; Nettles, 2005), achieving the resolution of 200-300 km in Eurasia would involve more than 20,000 unknowns. The computational cost may, in part, explain why only one model of Eurasia (Shapiro and Ritzwoller, 2002) has been developed so far.

Shapiro and Ritzwoller (2002) developed their model using measurements of surface waves at periods shorter than 200 seconds. In our inversion, we use several times more measurements of surface-wave phase velocities, which may potentially allow for resolving more details of the structure. Even more importantly, we also include long-period waveforms that constrain structures at depths larger than 250 km, which were not successfully resolved by the earlier model.

In this chapter we present our model and identify some features that have previously been reported by different researchers. We compare the model with that of Shapiro and Ritzwoller (2002) and discuss the advantages of using larger and more diverse data sets in the inversion. Finally, we focus on an interesting feature of our model, the zone of sharp velocity gradients at a depth of about 200 km, which we infer to be the base of the lithosphere. We also show that this is a robust feature that was resolved because we used a new reference model REF instead of PREM.

5.1 Parameterization

As in the inversions for the one-dimensional reference model REF and the global three-dimensional whole-mantle model S362ANI, we choose to parameterize our regional model of Eurasia in terms of isotropic and anisotropic variations in shear-wave velocities (equations 4.1 and 4.2). This choice of parameters allows us to minimize the roughness of perturbations in both average velocity and anisotropy.

The global model S362ANI is parameterized horizontally in terms of 362 splines, whose centers are approximately 11.5 degrees apart from each other. Such coarse geometrical parameterization does not allow for resolving velocity anomalies smaller than about 1000 km. Imaging regional-scale features in Eurasia therefore requires higher nominal resolution than the global set of 362 splines, but the resolvable length-scale and the choice of the optimal parameterization depend on several factors. We choose a uniform parameterization throughout Eurasia with the nominal resolution of about 300 km. In the following paragraphs, we present motivation for this choice.

First, all unknowns in the inverse problem should be well-constrained by the data. In case of nonuniform data coverage, an excessive parameterization of the model may lead to a solution that strongly depends on the regularization and therefore is not robust. In order to reduce the instability of the inversion due to the nonuniform data coverage, some authors (*e.g.*, Bijwaard *et al.*, 1998) adjust the nominal resolution of their block models based on the number of rays crossing each block. While this approach may lower the number of unknowns poorly constrained in the inversion of body-wave travel times, it is not necessary in our case, because of excellent data coverage. At all frequencies, at least 200 surface waves sample every 3-by-3-degree block in Eurasia, as shown in Figure 3.4. The 3-by-3-degree cells correspond to the nominal resolution of about 300 km implemented in our regional model. The number of ray paths for long-period waveforms is several times smaller than for short- and intermediate-period surface waves, but it is still very high. Therefore, we choose a simple, uniform parameterization in the entire region of interest, similar to the parameterizations used in regional inversions of Boschi *et al.* (2004) and Nettles (2005).

Second, the limits of the resolution of a tomographic model depends on the resolving power of the data, which is limited owing to the finite wavelength of seismic waves, theoretical approxima-

tions, and noise. The resolution limits can be predicted theoretically, but estimates vary between different research groups. For example, Yoshizawa and Kennett (2002) find that the width of a 40-s Rayleigh wave is around 200 km and conclude that the resolution of tomographic images derived from rays crossing each other should be of the order of 300 km. Spetzler *et al.* (2002), on the other hand, argues that, because of scattering effects, ray theoretical surface-wave tomography is limited to resolving anomalies larger than about 1500 km for 40-s Love waves and about 3000 km for 150-s Love waves. However, Boschi *et al.* (2004), based upon 35-s and longer-period Love and Rayleigh waves and ray theory, imaged anomalies of wavelengths shorter than 1000 km that are consistent with high-resolution compressional-wave velocity models and tectonic reconstruction of the Mediterranean even at a depth of 250 km. Given that our data set is several times larger than that of Boschi *et al.* (2004), we expect to resolve heterogeneities of length-scales of several hundred kilometers and choose the parameterization with nominal resolution of about 300 km. Even if the resolving power of our data is not sufficiently good to determine anomalies this small, the solution of the inverse problem should be robust. Boschi and Dziewoński (1999) showed that in regions of good data coverage, the roughness minimization in the overparameterized inverse problem leads to nearly identical results as using lower nominal resolution. Therefore, we regularize the inverse problem by minimizing both the horizontal and vertical roughness of the solution.

Third, our data do not have enough power to resolve details of the crustal structure, and we choose to correct all data using an *a priori* model CRUST2.0 (Bassin *et al.*, 2000). The CRUST2.0 is defined on a 2-by-2-degree grid. Because our shortest-period measurements are significantly sensitive to the crustal structure, the model used in our crustal corrections sets the upper bound for the resolving power to be about 200 km.

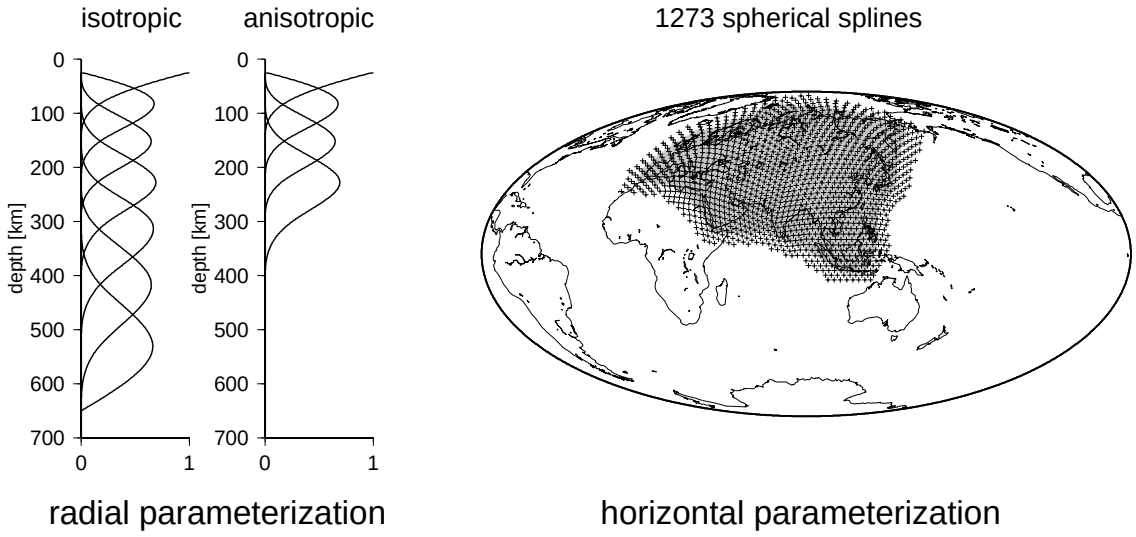

Figure 5.1: Geometrical parameterization of the regional model of Eurasia. Isotropic velocity perturbations $(\delta v_{SH}/v_{SH} + \delta v_{SV}/v_{SV})/2$ are represented in the vertical direction by seven B-splines in the upper mantle, which converge to zero at a depth of 650 km. Anisotropic perturbations $\delta v_{SH}/v_{SH} - \delta v_{SV}/v_{SV}$ are represented by four B-splines. Both isotropic and anisotropic perturbations are parameterized horizontally in terms of 1273 spherical splines, which are approximately 2.9 degrees apart from each other. The shaded area in Eurasia defines the model region, and is further discussed in Section 5.2.

Figure 5.1 shows knots of 1273 splines that we use to represent regional-scale perturbations in Eurasia in the horizontal direction. The knots are approximately 2.9 degrees apart from each other, and cover the entire continent. Since we include our global data set in the inversion, it is necessary to account for the propagation effects outside of Eurasia. Such effects can be best predicted by the global model S362ANI, which has been derived from the same global data set as we intend to use in the regional inversion. The accurate estimation of the propagation effects outside of Eurasia is essential in our inversion. Namely, we will subtract predictions of the global model from the observations using S362ANI, and invert the corrected data for the finer-scale perturbations in Eurasia with respect to S362ANI.

Although we expect to achieve better lateral resolution of the model in Eurasia than in the global model, we do not attempt to increase vertical nominal resolution of the regional model. The results

of Boschi *et al.* (2004) and Nettles (2005) suggest that it is difficult to achieve vertical resolution better than 60 km using measurements of surface-wave dispersion. The resolution of nearly 60 km can be achieved using the parameterization of our global model, where knots of the B-splines are 50 km apart from each other in the uppermost 75 km of the mantle and 75 km apart from each other down to a depth of 300 km. Therefore, we use B-splines with the same spacing as in the global model.

Since the resolving power of our data in the lower mantle is not as good as in the upper mantle, we aim to determine regional-scale features in Eurasia only above the 650-km discontinuity. To avoid numerical instabilities associated with the transition from finely parameterized upper mantle to the coarsely parameterized lower mantle, the high resolution part of the model is constrained to vanish at 650 km. The sensitivity of the data to the heterogeneity in the lower mantle is accounted for by removing predictions of S362ANI from the data vector. Finer-scale anisotropic variations are defined only for four B-splines, since we have not found strong evidence for significant anisotropy below 200 km, as discussed in Chapter 4.

The total number of coefficients defining the model of Eurasia is 21,967. The finer parameterization involves 14,003 new coefficients, whereas the remaining 7,964 coefficients are fixed to the values defined in the global model S362ANI. The number of parameters is relatively small, since we confine the anisotropic perturbations to the uppermost four splines in the model. In contrast, in models defined in terms of the variations in v_{SH} and v_{SV} (*e.g.*, Boschi *et al.*, 2004; Nettles, 2005), anisotropy is defined in the same depth range as the isotropic part of the model. Consequently, the North America model of Nettles (2005), for example, requires nearly as many coefficients as our model of Eurasia despite much smaller size of the region of interest and the same nominal

resolution.

5.2 Inversion

As mentioned in the previous section, we choose to invert for the model of Eurasia as a perturbation with respect to the global model S362ANI. To accommodate the corrections for the predictions of the global model, we incorporate its coefficients $m^{S362ANI}$ as a part of the model of Eurasia and write

$$m^{eura} = \begin{pmatrix} m^{global} \\ \\ m^{regional} \end{pmatrix}, \tag{5.1}$$

where the coefficients $m^{regional}$ correspond to the finer parameterization in Eurasia shown in Figure 5.1. The sensitivity matrix A for all data sets is calculated using the reference model REF for the m^{eura} parameterization. To correct the data vector using predictions of the global model, we define a reference model S362ANI with elements of the

$$m_0^{eura} = \begin{pmatrix} m^{S362ANI} \\ \\ 0 \end{pmatrix}. \tag{5.2}$$

The predictions of m_0^{eura} are subtracted from the observed data vector $A^T d^{obs}$, and the new data vector

$$(A^T d)^{cor} = A^T d^{obs} - A^T A m_0^{eura}, \tag{5.3}$$

is then inverted for the regional structure of Eurasia by

$$m^{regional} = (A^T A + D^T D)^{-1}_{reg} (A^T d)^{cor}_{reg}, \tag{5.4}$$

where the subscript 'reg' indicates that only coefficients corresponding to the regional part of the model. The damping matrix D minimizes the vertical and horizontal roughness of $m^{regional}$ with respect to the global model S362ANI.

To invert for the model of Eurasia, we use the same data as in the inversion for the global model except the measurements of the SS precursors, which do not have enough resolving power to determine regional-scale topography variations. The long-wavelength topographies are imposed on the regional model as a part of S362ANI. We weight particular data sets in the same way as in the inversion for a global model. As a consequence, contribution of body-wave travel times is marginal. Increasing the weight of these data, however, would lead to the instability of the inversion, as teleseismic body waves are primarily sensitive to the structure of the lower mantle.

Since the inversion of waveforms is nonlinear, we first build a starting model that is as close to the final solution as possible by inverting only surface-wave data for the perturbations in Eurasia using only the five uppermost isotropic B-splines. This starting model is then used to calculate synthetic seismograms and partial derivatives for the waveform inversion. Then, the surface-wave, waveform, and travel-time data are inverted jointly using all B-splines shown in Figure 5.1.

The solution of equation 5.4, that is, the high-resolution perturbations with respect to the global model, are shown in Figure 5.2 at the depth of 80 km. The perturbations have shorter wavelengths and are not correlated with the velocity anomalies in the global model. This suggests that the

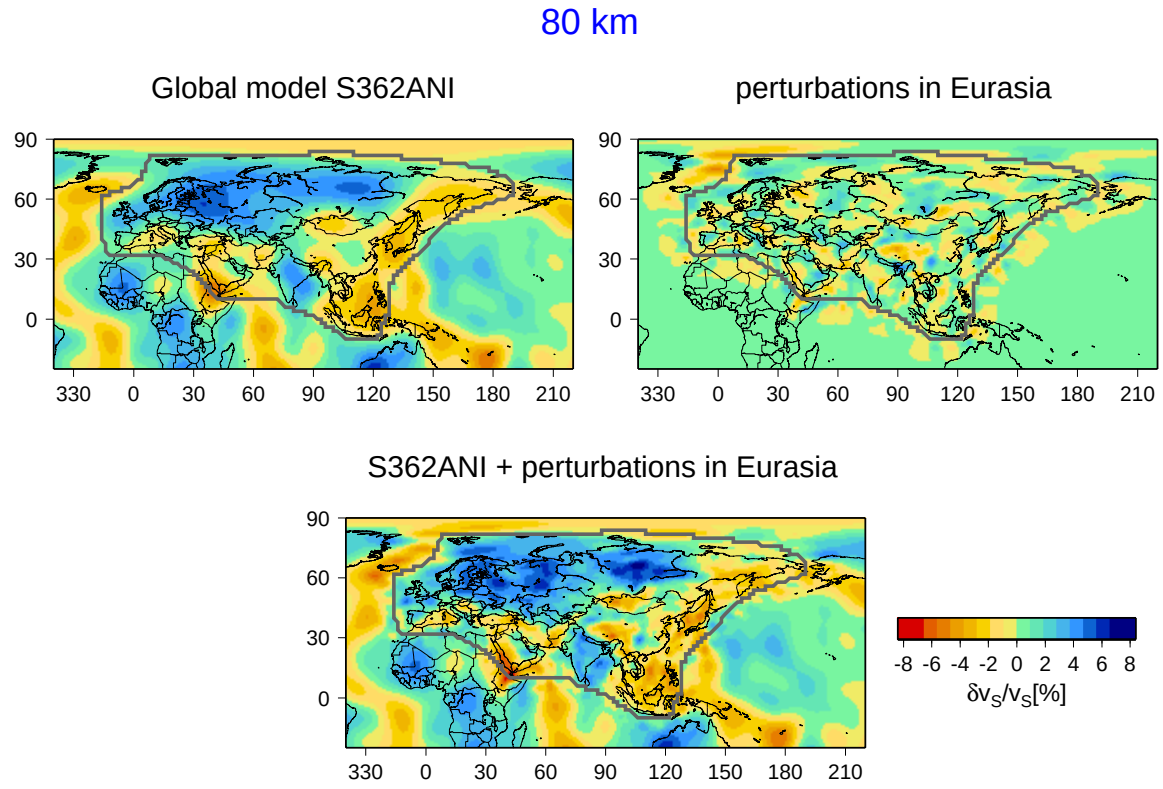

Figure 5.2: Isotropic velocity variations $(\delta v_{SH}/v_{SH} + \delta v_{SV}/v_{SV})/2$ at a depth of 80 km in Eurasia. Upper-left panel shows the variations in the low-resolution global model S362ANI. Upper right panel shows the high-resolution perturbations with respect to S362ANI obtained from equation 5.4. Bottom: the sum of S362ANI and the high-resolution perturbations. The global average has been removed from the low-resolutions perturbations, but not from the high-resolution perturbations. The model region is surrounded by the gray line.

regional inversion reveals structures that have not been modeled in S362ANI due to coarse parameterization rather than due to strong damping. Indeed, when the regional perturbations are added to the global model, they reveal more small-scale details in Eurasia. For example, the East European Craton in the global model appears as one high velocity anomaly. In the regional model, however, it is possible to distinguish between the anomalies beneath the Urals and Baltic Shield. Low velocity anomalies along tectonically active regions in the southern part of the continent also show structures more correlated with surface tectonics in the regional model than in S362ANI. Some of the anoma-

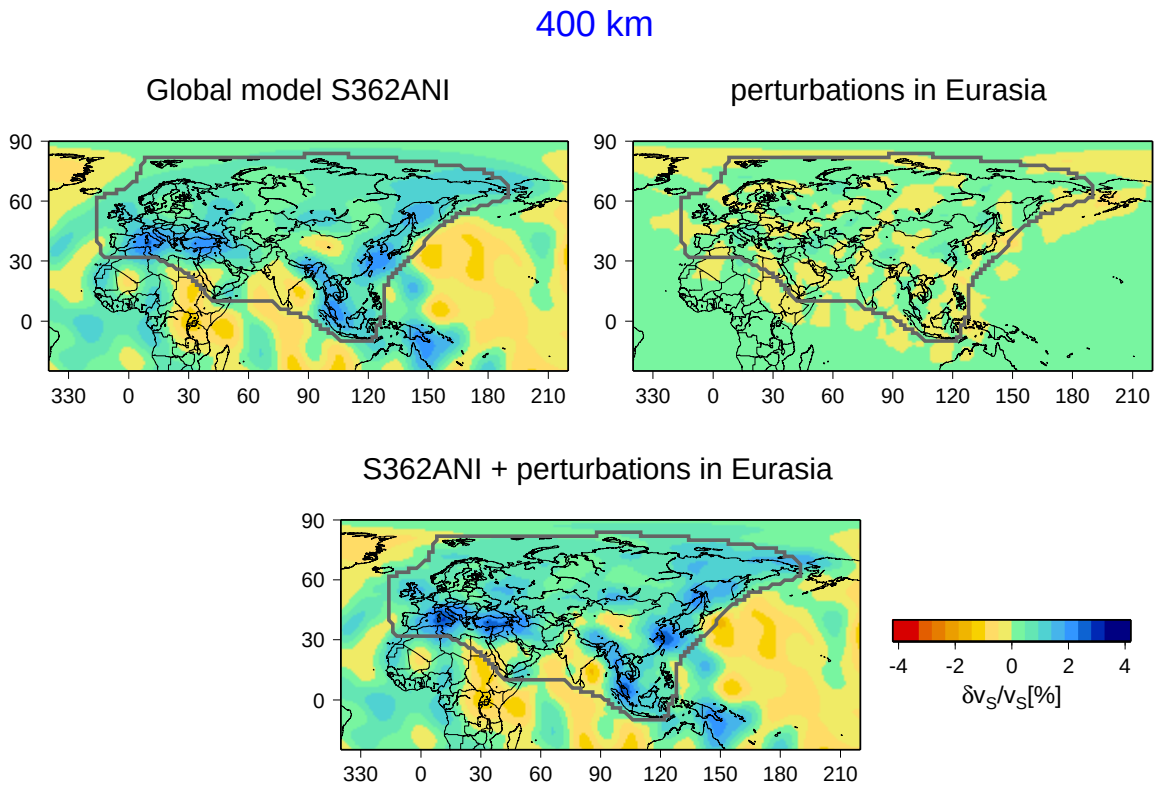

Figure 5.3: Same as Figure 5.2 but for the depth of 400 km and plotted with a different color scale.

lies in the regional model have a diameter less than 500 km, which demonstrates that the choice of a nominal resolution of about 300 km is adequate.

The anomalies in the regional-model at a depth of 400 km (Figure 5.3) are slightly stronger than in the global model but, in general, do not show any new details of the structure, perhaps due to poorer resolution at this depth. The regional model at this depth is consistent with, and slightly less damped, than the global model. Fast-velocity anomalies beneath the tectonically active regions dominate the pattern of heterogeneity in Eurasia at 400 km, and have a diameter of approximately 1000 km. This is much less than the 3000-km resolution limit for 150-s Love waves estimated by Spetzler *et al.* (2002).

The shaded area in Figure 5.1 and the area bound by the grey curve in Figures 5.2 and 5.3 define the model region. The dense grid of 1273 splines, however, extends beyond this region and consequently, perturbations are non-zero outside of this region. The zone of splines centered outside of the shaded region serves as a buffer zone, which absorbs the modeling errors resulting from the two-stage inversion for a global and regional model. Nettles (2005) has found that if such buffer zone is defined, the velocities within the model region are determined more accurately. However, only anomalies within the model region are considered to be robust, while velocity anomalies outside of that region may be subject to modeling errors.

While Nettles (2005) has shown that the modeling errors are smaller if the finer model within the region of interest is determined simultaneously with the global model, we choose the iterative approach. The iterative method simplifies the inverse problem for a selected region, and avoids numerical instabilities resulting from the nonuniqueness of the solution that often exist for the simultaneous inversion.

5.3 Isotropic velocity variations

In this section we compare our model of Eurasia S2.9EA with the model CU_SRT1.0 of Shapiro and Ritzwoller (2002). The model CU_SRT1.0 was obtained from a combined data set of group (Levshin *et al.*, 1989) and phase (Trampert and Woodhouse, 1995; Ekström *et al.*, 1997) velocity measurements. Although CU_SRT1.0 is a global model, Shapiro and Ritzwoller (2002) focus their interpretation on Eurasia, where the data coverage is best. The regional-scale anomalies in Eurasia are represented by a 2-by-2-degree block parameterization. The CU_SRT1.0 is, therefore, a natural choice for a comparison with our model.

We emphasize two differences between S2.9EA and CU_SRT1.0. First, the velocity structure in CU_SRT1.0 is well constrained by the surface-wave data only within the uppermost 200-250 km of the mantle, whereas long-period waveforms used in this study provide additional constraints on the structures at larger depths. The comparison between the two models should therefore help to understand the merits of combining more diverse data sets in the determination of the structure of the whole upper mantle. Second, we simply correct our data for crustal effects using CRUST2.0 (Bassin *et al.*, 2000), while Shapiro and Ritzwoller (2002) invert for the crustal structure starting with a modified version of CRUST5.1 (Mooney *et al.*, 1998), and account for the variations in the depth of the Moho. The comparison of the two models should therefore be helpful in understanding how the different and, arguably, less accurate approach used in this study affects the velocities in the mantle.

5.3.1 Comparison with CU_SRT1.0

The distribution and amplitudes of lateral velocity variations at 80 km in our model S2.9EA are very similar to those in CU_SRT1.0 (Figure 5.4). The similarity between the two models indicates that the structure of the upper mantle in CU_SRT1.0 is primarily constrained by the data of Ekström *et al.* (1997), which is a subset of the surface-wave data used in the calculation of S2.9EA. The two models have a comparable resolution; the shortest-wavelength anomalies are slightly smaller in S2.9EA. The slow-velocity anomalies in southern Eurasia are less pronounced in CU_SRT1.0, but their lateral extent is the same as in our model. At the same time, fast-velocity anomalies have a slightly larger extent in CU_SRT1.0, which indicates that Eurasia, in this model, is slightly faster than in S2.9EA.

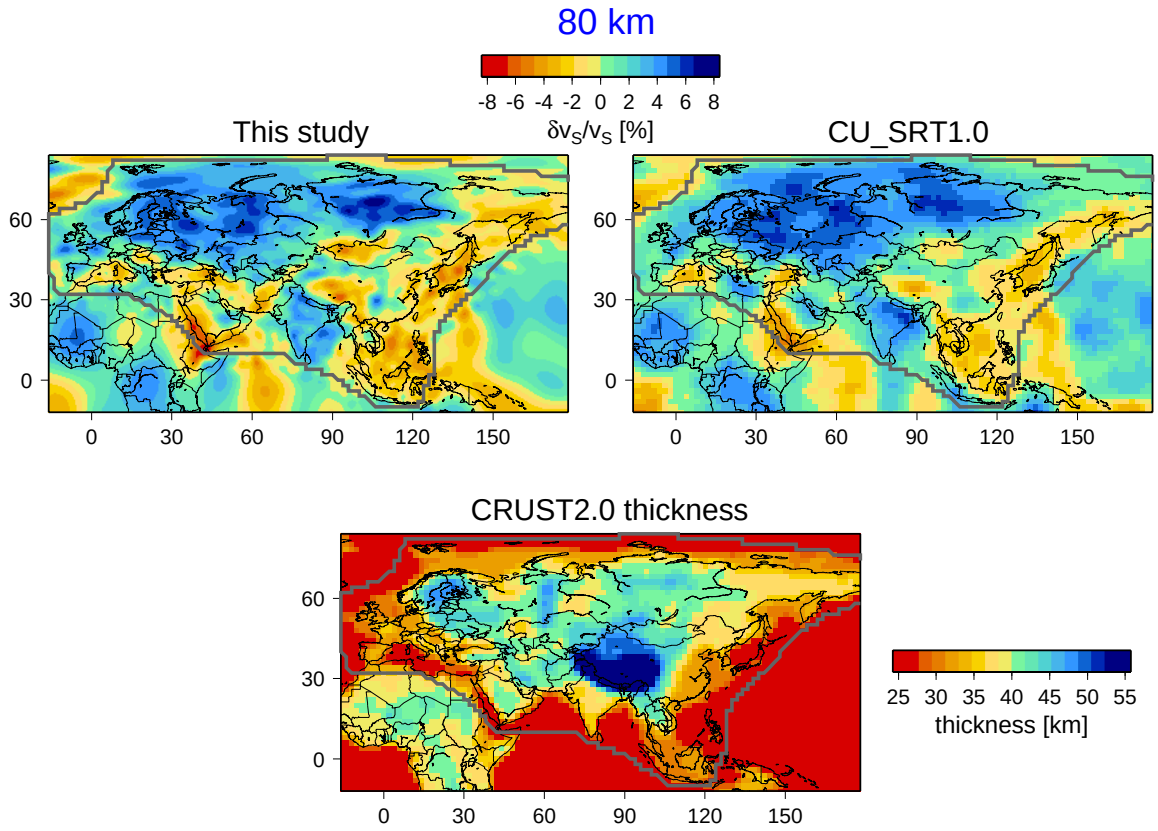

Figure 5.4: Top panels: isotropic velocity variations $\delta v_S/v_S = (\delta v_{SH}/v_{SH} + \delta v_{SV}/v_{SV})/2$ in our model S2.9EA (left) and CU_SRT1.0 of Shapiro and Ritzwoller (2002, right) at a depth of 80 km. The variations in S2.9EA are calculated with respect to the reference model REF and plotted after removing the average in the global model S362ANI. The variations in CU_SRT1.0 are defined as $\delta v_S/v_S$, where $v_S = (v_{SH} + v_{SV})/2$ and plotted with respect to the average velocity at 80 km. Bottom panel: thickness of the solid crust in CRUST2.0 (Bassin *et al.*, 2000). The gray line indicates the model region defined in Section 5.1.

In certain parts of the continent, velocity variations at a depth of 80 km are correlated with the crustal thickness. In northern Eurasia, for example, anomalously thick crust of the East European Craton, the Urals, and Siberia is underlain by faster-than-average mantle. The same pattern is observed in the model of Shapiro and Ritzwoller (2002), who used a different method to account for crustal heterogeneity.

At 150 and 250 km, slow-velocity anomalies in eastern Eurasia are more pronounced in S2.9EA and fast-velocity anomalies are slightly stronger in CU_SRT1.0 (Figure 5.5). The differences there-

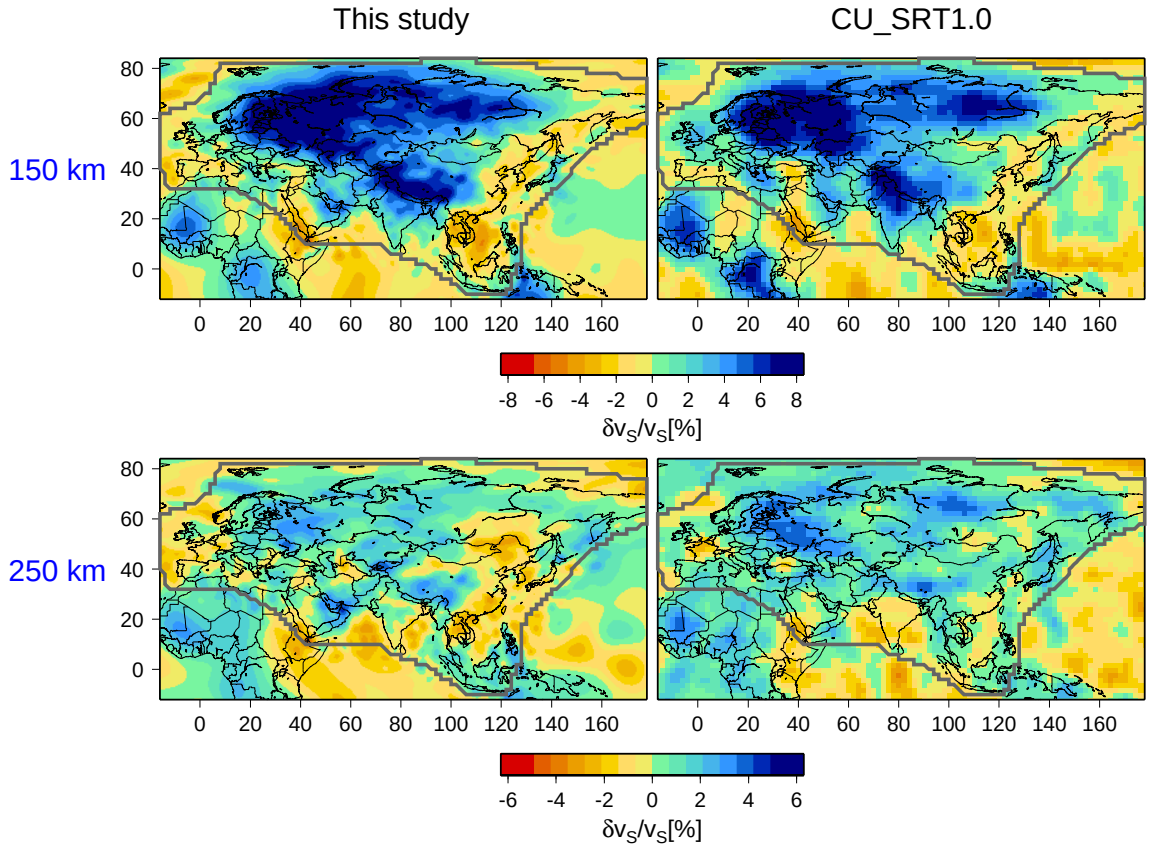

Figure 5.5: Same as the top panels in Figure 5.4 but for the depths of 150 and 250 km. The strong velocity anomalies observed at a depth of 150 km become very weak at 250 km. Note that different color scales are used for different depths.

fore result from different average velocities while lateral variations appear to be consistent in the two models. The most pronounced features at a depth of 150 km are fast-velocity anomalies beneath the East European Platform, Siberia, and Tibet, which nearly vanish at a depth of 250 km. The dramatic decrease in the strength of these anomalies is observed in both models, and is therefore unlikely to result from poor constraints on deeper structures in CU_SRT1.0, or inaccurate treatment of the crust in our model. The dramatic change in the strength of heterogeneity between 150 and 250 km will be further discussed in sections 5.3.2 and 5.3.4.

At 396 km, our model is dominated by fast-velocity anomalies beneath the Mediterranean Basin,

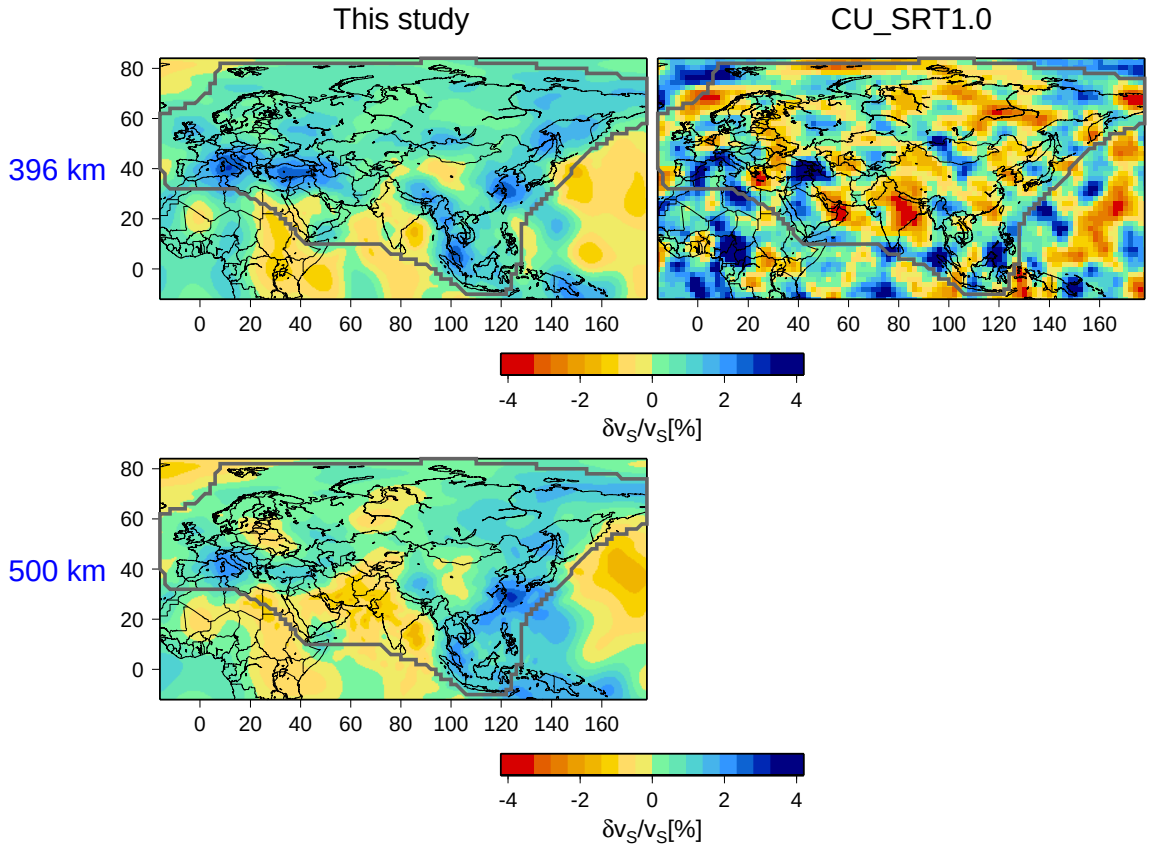

Figure 5.6: Same as the top panels in Figure 5.4 but for the depths of 396 and 500 km. At 396 km, our model is dominated by fast-velocity anomalies beneath the regions of current and past subduction; these features are not resolved in CU_SRT1.0. The online version of the model CU_SRT1.0 is not defined below a depth of 396 km.

Turkish Plateau, Tibet, and the subduction zones in the southeastern and eastern Eurasia (Figure 5.6). These anomalies have amplitudes up to 3% and are correlated with the distribution of the regions of current and past tectonic activity. In contrast, CU_SRT1.0 shows stronger anomalies and different pattern at 396 km than at 80 km. These strong anomalies at 396 km are unlikely to represent true mantle structures, since the sensitivity of data used by Shapiro and Ritzwoller (2002) diminishes below 200-250 km and becomes very small at 400 km. The authors recognize that their model is worthy of interpretation only above a depth of about 250 km. The model CU_SRT1.0

is available online at http://ciei.colorado.edu/∼nshapiro/MODEL/ only down to a depth of 396 km, although the radial parameterization extends to 1000 km depth. However, an adequate regularization of the inverse problem should yield weak and smooth perturbations at this depth.

The fast-velocity anomalies underlying shallow slow-velocity anomalies in tectonically active regions, such as those in our model, have also been observed in other tomographic models. Such regions may be underlain by cold and fast subducting lithosphere, as predicted by the tectonic reconstruction of the Mediterranean basis (de Jonge *et al.*, 1994), and confirmed by surface- (Boschi *et al.*, 2004) and body-wave tomography (Spakman *et al.*, 1993). The presence of the fast compressional-wave velocity anomalies beneath Tibet has been reported by Tilman *et al.* (2003), and can be explained through the thickening of the lithosphere followed by the downwelling (Conrad, 2000) or the pull of the sinking oceanic lithosphere.

At a depth of 500 km, the pattern of heterogeneity in our model is still dominated by the fast velocity anomalies beneath tectonically deformed regions. The mantle structure is, in general, more heterogeneous in the transition zone than at a depth of 396 km, and some velocity anomalies at depth of 500 km are stronger than at 396 km. On the other hand, fine-scale perturbations with respect to the global model are constrained to vanish at a depth of 650 km, which causes the strength of some anomalies to decrease with depth in the transition zone.

5.3.2 Structure of the stable part of the continent

Figure 5.7 shows cross sections through the upper mantle velocity structure in northern Eurasia. Strong negative anomalies in the uppermost part of CU_SRT1.0 represent crustal velocities, which are much lower than the global average velocities at these depths. Such negative anomalies are not

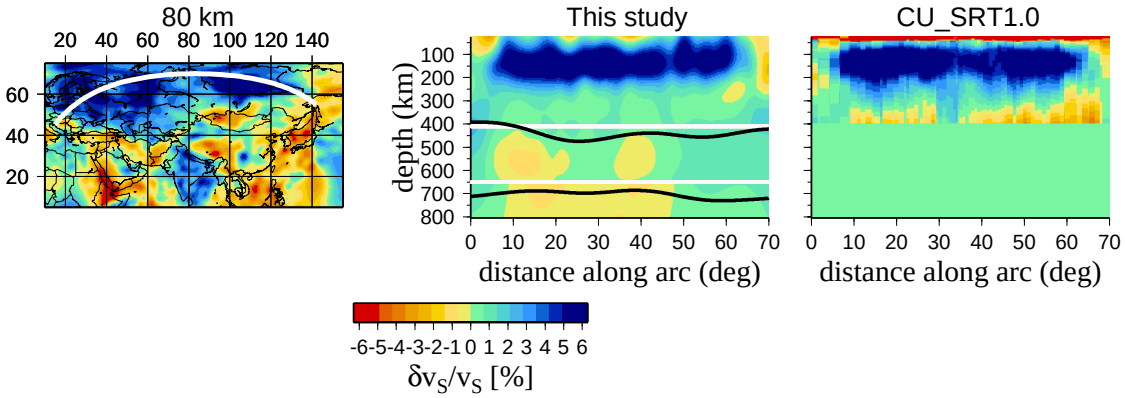

Figure 5.7: Left panel: isotropic velocity perturbations in our model S2.9EA at a depth of 80 km. The while line indicates the location of the cross sections through S2.9EA and the model CU_SRT1.0 of Shapiro and Ritzwoller (2002) shown in the middle and right panels, respectively. The velocity perturbations are plotted with global averages removed. The white lines in the middle and right panels indicate the 410- and 650-km depths. The black lines represent the topographies of the transition zone discontinuities plotted with the five-fold exaggeration. Both models show fast-velocity anomalies in the continental lithosphere along the entire cross section through northern Eurasia, which diminish abruptly at depths of 200-250 km.

observed in S2.9EA, because the mantle is parameterized in our model up to a constant depth of the 24.4 km. Our model is therefore meaningless above the depth of the Moho. Despite differences in crustal depths, both models show relatively weak positive anomalies between depths of 50 and 100 km. The positive anomalies become very strong between 100 and 180 km, and nearly vanish at 250 km. In our model, the most dramatic negative gradient in velocity is observed at about 220 km beneath the East European Craton and the Urals, and about 190 km beneath Siberia. In CU_SRT1.0, the fast-velocity anomalies beneath Siberia are as thick as beneath the East European Craton. The strong positive lithospheric anomalies in both models have similar amplitudes, and are bounded by nearly equally sharp gradient between 150 and 250 km. Below 300 km, our model is weak and smooth, but CU_SRT1.0 shows strong slow-velocity anomalies that probably result from insufficient damping and poor constraints on the structure at these depths.

The presence of approximately 200-km thick layer of fast-velocity anomalies in our model is

consistent with the model of Priestley and Debayle (2003), who inverted surface-wave data for a tomographic model of the uppermost mantle beneath Siberia. Priestley and Debayle (2003) argue these anomalies represent the seismic lithosphere, which is likely to be somewhat thicker than the thermal lithosphere defined as a conductive boundary layer (Jaupart and Mareschal, 1999). Our results, however, do not agree with the findings of Artemieva and Mooney (2001), who reported the thermal lithosphere beneath Siberia to be thicker than 350 km. Artemieva and Mooney (2001) also found the lithosphere to be only 125-km thick beneath the Urals and 175- to 250-km thick beneath the East European Craton. In contrast, our model predicts thickness variations to be smaller than 50 km along the whole length of the cross section along northern Eurasia.

Petrological data suggest that the lithosphere beneath Siberia is at least 150-km thick (Pearson *et al.*, 1995). Priestley and McKenzie (2006), who combined their seismological model with pressure and temperature estimates from kimberlite data, estimate the lithospheric thickness in Siberia to be about 200 km, which is difficult to reconcile with the results of Artemieva and Mooney (2001). The modeling of Priestley and McKenzie (2006) also indicates that the lithosphere beneath the East European Craton may be slightly thicker than beneath Siberia, which agrees with our results.

Lerner-Lam and Jordan (1983) found that Rayleigh-wave data require the velocity structure beneath northern Eurasia to differ significantly from the upper mantle beneath western Pacific down to a depth of 400 km. Compositional heterogeneity is required to explain such anomalies below 200 km (Jordan, 1975, 1978, 1981a). Perturbations with respect to the global average in our model are indeed positive in the uppermost 400 km of the mantle but are as weak as 1-2% below 250 km.

The strong gradients observed near 200-km depth in our model may represent a boundary, perhaps the base of the continental lithosphere. An independent piece of evidence for the presence of

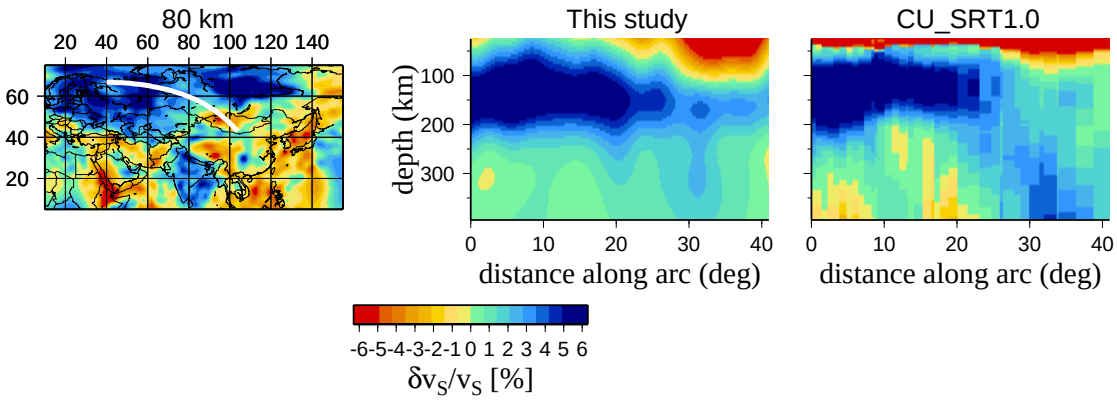

Figure 5.8: Same as Figure 5.7 but for central Eurasia. This cross section coincides with the profile 'Quartz' but extends about 1000 km further southeast. The sharp boundary at the base of the lithosphere is observed in the northwestern and central part of the cross section, and becomes less pronounced beneath the Altai.

such boundary comes from the analysis of compressional waves generated by chemical and nuclear explosions in the former Soviet Union. The measurements of P-wave travel times at frequencies of 1 to 2 Hz provide constraints on the velocity structure in regions poorly sampled by the regional-distance rays from earthquakes. Ryberg *et al.* (1996) obtained a two-dimensional velocity model along profile 'Quartz', which shows a discontinuity interpreted as the lithosphere-asthenosphere boundary at a depth of almost 200 km in the East European Craton and Western Siberia, and 150 km beneath Altai mountains. Similar discontinuity at about 200 km in the western part of the profile, which becomes shallower towards the mountains is also observed in the interpretation of Morozowa *et al.* (1999). Figure 5.8 shows cross sections through the shear-wave velocity models, which coincide with the profile Quartz but extend about 1000 km further southeast. Assuming that the depth of the sharpest gradient is an indication of the lithosphere-asthenosphere boundary, both models agree well with the results of Ryberg *et al.* (1996) in the western part of the profile showing the boundary at about 200 km. The thinning of the lithosphere occurs further west in CU_SRT1.0 compared to the model of Ryberg *et al.* (2006), while in our model, the thickness of the fast-velocity layer di-

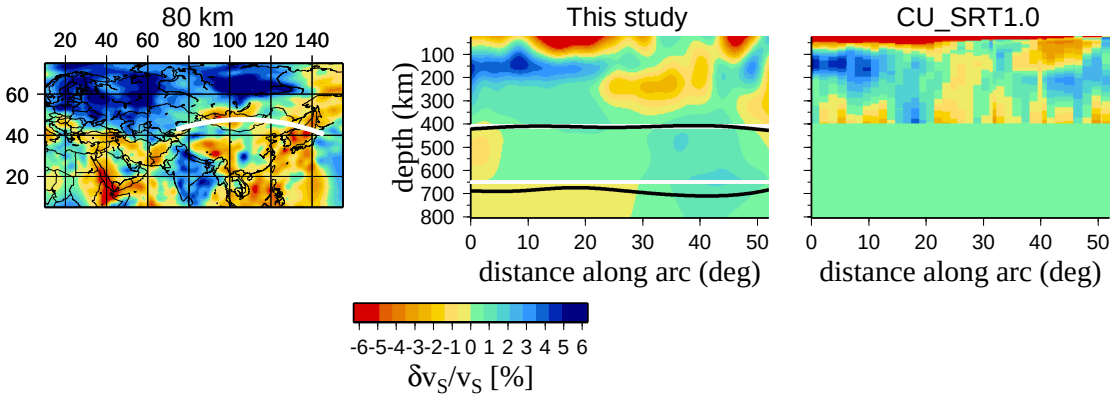

Figure 5.9: Same as figure 5.7, but for eastern Eurasia. Lithospheric slab beneath Japan appears to accumulate in the transition zone and depress the 650-km discontinuity. Note that topographies are plotted with the five-fold exaggeration. West of Japan, we observe another slab-like anomaly, which has been reported by van der Voo *et al.* (1999), and is thought to represent the subducting slab associated with the closing of the Mongol-Okhotsk Ocean.

minishes closer to the Altai. It is more difficult to estimate the lithospheric thickness beneath the mountain belt.

The upper mantle structure in Eurasia has also been studied by Grand and Helmberger (1985), who analyzed multiply-reflected shear waves, and found about 5% lower velocities in the upper 200 km of the mantle beneath fold belts in central Asia relative to the northern Eurasia. Our model S2.9EA, in agreement with the conclusions of Grand and Helmberger (1985), shows that significant differences beneath the mountain belts and cratons in northern Eurasia extend down to about 200 km, although the heterogeneity may be even higher than 5% (Figure 5.8). Defining the depth at which heterogeneity in this region becomes small in CU_SRT1.0 is difficult, because velocity anomalies below 300 km are as strong as in the lithosphere, and the structure is poorly resolved beneath 300 km depth.

5.3.3 Structure in regions of recent tectonic activity

The cross section through eastern Eurasia (Figure 5.9) traverses two pronounced slow velocity anomalies at shallow depths in the mantle. The easternmost anomaly is associated with the back-arc extension in the Sea of Japan. The sea is underlain by the fast velocity anomaly that represents the subducting Pacific lithosphere. The 650-km discontinuity in the subduction zone is depressed, which may indicate subhorizontal deflection or accumulation of the subducting slab in the transition zone, as suggested by Shearer and Masters (1992) and Gu *et al.* (2003).

The shallow negative anomaly in the western part of the cross section represents slow velocities within the tectonically deformed lithosphere beneath the Altai Mountains. The zone of higher velocities between the Altai and east Asia has been previously reported in the compressional-wave velocity model by van der Voo *et al.* (1999) and is thought to represent the subducting lithospheric slab associated with the closing of the Mongol-Okhotsk Ocean in the late Paleozoic or early Mesozoic. The fast-velocity anomaly continues down to the core-mantle boundary in the model presented by van der Voo *et al.* (1999), but it does not appear to extend below the transition zone in our model. While delineating fast velocity anomalies is important for understanding the character of the convection in the mantle, it is beyond the scope of this paper. The differences between models of compressional- and shear-wave velocities are discussed in detail by Masters *et al.* (2000), and the discrepancies between models obtained from high- versus low-frequency data have been investigated by Boschi and Dziewoński (1999).

The ability of our data to resolve regional-scale details of the structure in the upper mantle is demonstrated in Figure 5.10. We compare cross sections through our model and CU_SRT1.0 with the results of Kumar *et al.* (2006), who analyzed P and S receiver functions in Tibet. The

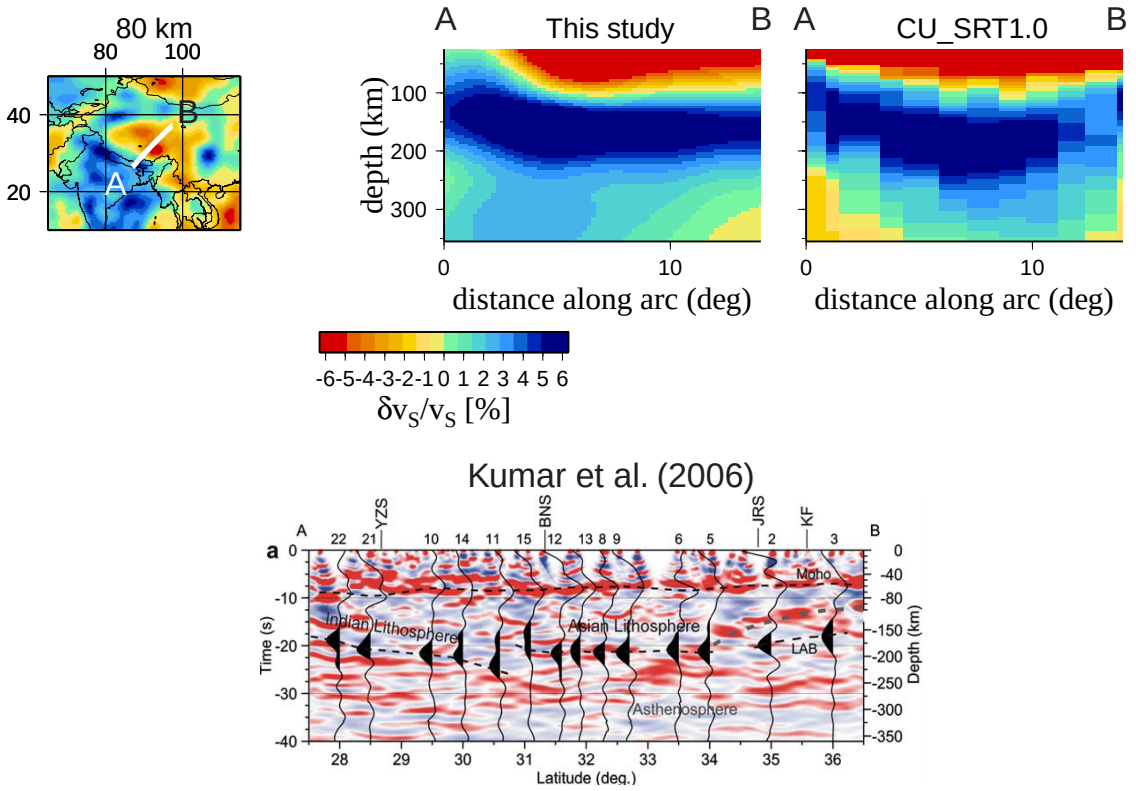

Figure 5.10: Top panels: Vertical cross sections through our new model S2.9EA and model CU_SRT1.0 of Shapiro and Ritzwoller (2002) in Tibet. Bottom panel: superposition of P and S receiver functions of Kind *et al.* (2002) and Kumar *et al.* (2006). Positive amplitudes of P receiver functions are plotted in red. Negative amplitudes of S receiver functions at the lithosphere-asthenosphere boundary are plotted in black. This boundary coincides with the zone of strong negative gradients observed in the tomographic models.

agreement between the depths of strong velocity gradients in tomographic models and the reflectors in receiver functions is striking. Kumar *et al.* (2006) interpreted the coherent, negative receiver functions between depths of 160 and 220 km as the lithosphere-asthenosphere boundary. In this depth range, sharp negative gradients are observed in our model and CU_SRT1.0. Both receiver functions and the gradients in tomographic models show that the boundary is inclined at a shallow angle in northern Tibet, and has an approximately constant depth of about 200 km beneath central Tibet. The fast shear-wave velocities of periods longer than 100 s in central and northern Tibet have also been found by Griot *et al.* (1998), and may indicate that the lithosphere beneath this regions

may have thickness typical for stable parts of continents. In southern Tibet, the boundary is inclined at a steep angle. Kumar *et al.* (2006) suggest that the thick lithosphere is inconsistent with the model of convective instability of the mantle lithosphere, and that the Tibetan Plateau is most likely to be formed by the subduction of the continental Indian lithosphere in southern Tibet and Asian lithosphere in northern Tibet.

In CU_SRT1.0, the negative gradients are observed about 50 km deeper than in S2.9EA. They are, however, nearly as sharp as in our model, and are also inclined at a steeper angle in the southern and shallower angle in the northern Tibet. The systematic difference in the depth of the strong gradient between S2.9EA and CU_SRC1.0 is significant, but we believe that our results are more likely to be correct, since they are consistent with the independent analysis of the receiver functions.

Strong negative anomalies in the uppermost 70-80 km beneath Tibet might represent low S_n velocities found, for example, by McNamara *et al.* (1995). The interpretation of the shallowest 100 km in Tibet in our model should be, however, carried out with caution. The crustal effects are removed in the inversion using the *a priori* model CRUST2.0 (Basin *et al.*, 2000), and our data should be sensitive only to the mantle heterogeneity. The velocity anomalies at crustal depths are, however, observed in S2.9EA because we implement a simple parameterization with the top of the mantle fixed at a constant depth of 24.4 km (more detailed discussion is presented in Section 4.2.7). We cannot rule out that the negative anomalies represent errors resulting from underestimated thickness or overestimated velocities in CRUST2.0. Regardless of imperfect parameterization and possible errors in the shallowest part of our model, the depth of strong positive gradients in central and northern Tibet is consistent with the depth of positive amplitudes of P and S receiver functions and of the positive gradients in CU_SRT1.0. The comparison with CU_SRT1.0 is important since the parame-

terization used in this model allows for the variations in the depth of the Moho, and crustal velocities and thickness are allowed to adjust to fit the measurements of short-period surface waves. The consistency of our model with the receiver functions and with CU_SRT1.0 suggests that our data are sufficient to resolve the velocity structure and discontinuity depths. In the southern part of the cross section, the crustal low-velocity layer becomes thinner in CU_SRT1.0, which is inconsistent with the interpretation of Kumar *et al.* (2006). The receiver functions become more complicated, and it is difficult to delineate the Moho discontinuity. In our model, shallow low-velocity anomalies vanish beneath the stable Indian lithosphere, indicating that crustal effects are removed efficiently in this part of the model.

Another region of recent tectonic activity in Eurasia is the Turkish-Iranian plateau. Maggi and Priestley (2005) imaged the upper mantle structure in this region using surface waveforms and found slow-velocity anomalies extending down to a 200-km depth (Figure 5.11). They conclude that low velocities in the upper mantle are consistent with a partial delamination of the lithosphere as a result of earlier continental collision and lithospheric thickening. Our model also shows slow-velocity anomalies beneath the Turkish plateau, which are, however, weaker and extend only to a depth of 100-150 km.

The ray path coverage of data used by Maggi and Priestley (2005) is good within the Turkish-Iranian Plateau, but not in the Mediterranean. Consequently, the east dipping subduction beneath the Hellenic Arc observed in S2.9EA, in the tectonic reconstruction of de Jonge *et al.* (1994), and the compressional-wave tomographic model of Spakman *et al.* (1993), is missing in their model. Furthermore, perturbations in the model of Maggi and Priestley vanish below 200 km depth, while our model shows a fast velocity anomaly underlying the Turkish plateau below 300 km. This anomaly

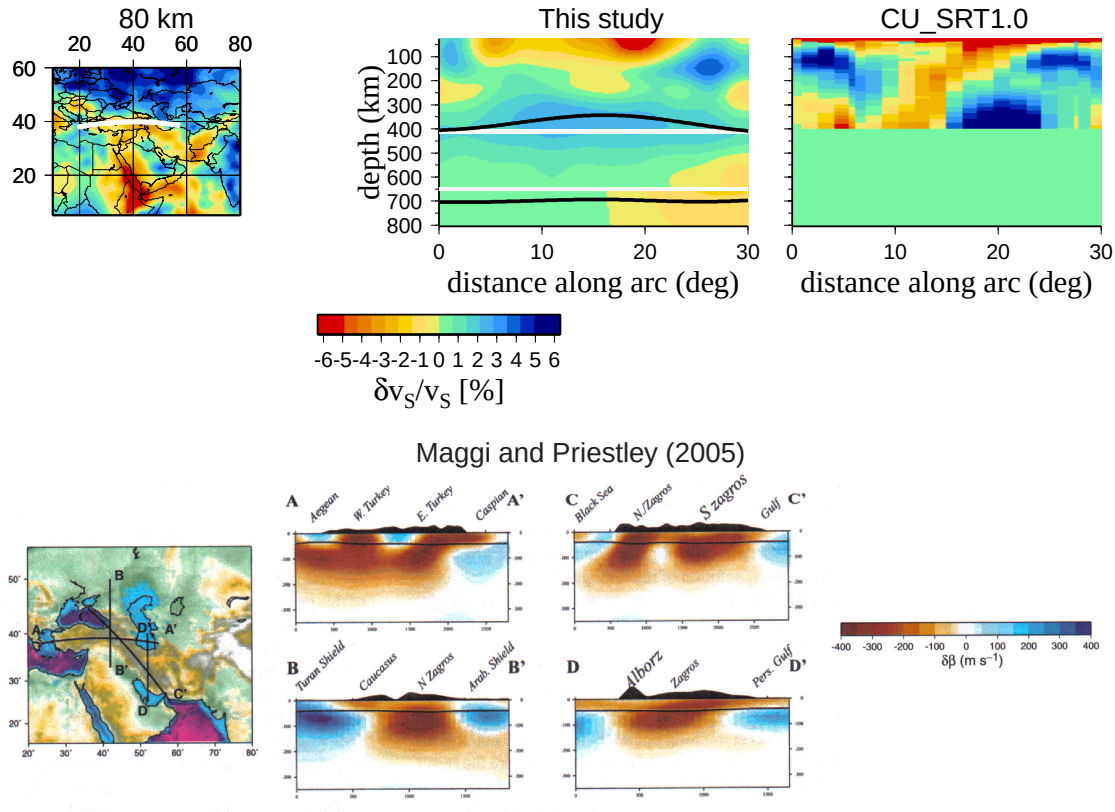

Figure 5.11: Top panels: same as Figure 5.7, but for the Turkish plateau. Bottom panels: vertical cross sections through the model of Maggi and Priestley (2005). The depth scale ranges from 0 to 350 km. The cross section A-A' is similar to, although shorter than, the cross sections shown in the upper panels. The low-velocity anomaly beneath Turkish plateau reported by Maggi and Priestley is weaker and does not extend as deep in our model. Our model, owing to larger horizontal and vertical extent, allows for the identification of slab-like features surrounding the slow-velocity anomaly, as well as a region of high velocities underlying this anomaly. The cross section B-B' is similar to that in Figure 5.12.

appears to be connected, not only to the lithospheric slab beneath the Hellenic Arc in the west, but also to the fast-velocity region beneath the Arabian platform in the southern part of the cross section in Figure 5.12. These fast-velocity anomalies may represent the northeast dipping subduction of the oceanic lithosphere that has been operating in this region since at least 150 m.y. ago (Dercourt *et al.*, 1986). In addition, the fast-velocity structure below 300 km in S2.9EA may represent the lithospheric material accumulating in the lower part of the upper mantle. Elevated topography of the exothermic 410-km discontinuity and depressed topography at the endothermic 650-km discon-

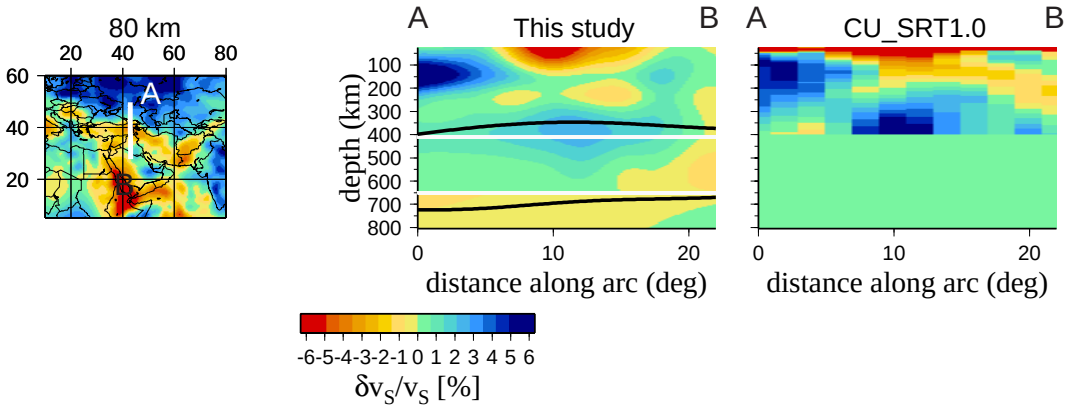

Figure 5.12: Same as figure 5.7, but for the eastern part of the Turkish plateau.

tinuity lend support to such an interpretation.

Similar to our model, the CU_SRT1.0 reveals a fast-velocity anomaly below 300 km beneath the eastern part of the Turkish plateau. In CU_SRT1.0, however, the anomaly is connected to the shallow fast-velocity anomalies underlying the Caspian Sea in the East (Figure 5.11) and Turan Craton north of the Caucasus Mountains (Figure 5.12). Although the episodes of the southwest dipping subduction associated with the continental collision cannot be ruled out in this region (Dercourt *et al.*, 1986), such a process is less likely to push a significant amount of the cold material into the transition zone than the north-east dipping subduction of the oceanic lithosphere.

Finally, it is important to note that the comparison of cross sections of our model with CU_SRT1.0 demonstrate the merits of using the spline rather than block parameterization. The average spacing between spline knots in our model is 2.9 degrees, whereas CU_SRT1.0 is parameterized in terms of 2-by-2-degree blocks. It is clear that the spline model can represent the regional structure as well as the block model although it involves fewer than half the number of basis functions per area.

5.3.4 Boundary at the base of the continental lithosphere

The fast-velocity layer in northern Eurasia appears to be thicker than 300 km in some global tomographic models (*e.g.*, Figures 4.11 and 4.12). In contrast, our global model, our model of Eurasia, as well as the results of Priestley and Debayle (2003) show a rapid decrease in the faster-than-average anomalies beneath cratons in the northern Eurasia at depths of about 175-225 km. Priestley and Debayle (2003) equate the fast-velocity layer beneath Siberia with the thermal lithosphere. In this section, we investigate the transition at the bottom of the lithosphere more closely. In addition to plotting the velocity anomalies relative to the global average, we also show and discuss the absolute velocities. This is important, because the decreasing anomalies in relative perturbations do not imply negative velocity gradients $\partial v_S / \partial depth$. In fact, the velocities in both the reference model REF and PREM increase with depth between 200 and 250 km.

In Figure 5.13, relative velocities in northern Eurasia are compared with the absolute velocities. It turns out that the decrease in positive perturbations in the regional model S2.9EA is so strong that the absolute velocities in the upper mantle beneath cratons decrease between 150 and 250 km. The negative velocity gradient is not an artifact of the regional inversion, since it is also observed in our global model. It provides an additional indication of a dramatic change in the velocity structure around the 200-km depth beneath cratons. Our long-period data are, however, not able to distinguish between the discontinuity and the zone of strong velocity gradients. One possible explanation for this abrupt decrease in absolute velocities is a compositional boundary between the continental lithosphere depleted in heavy components and the asthenosphere. A quantitative analysis would be necessary, however, to rule out a purely thermal origin of this boundary. Weak positive anomalies extending down to a depth of 400 km may represent a slightly colder-than-average, and hence more

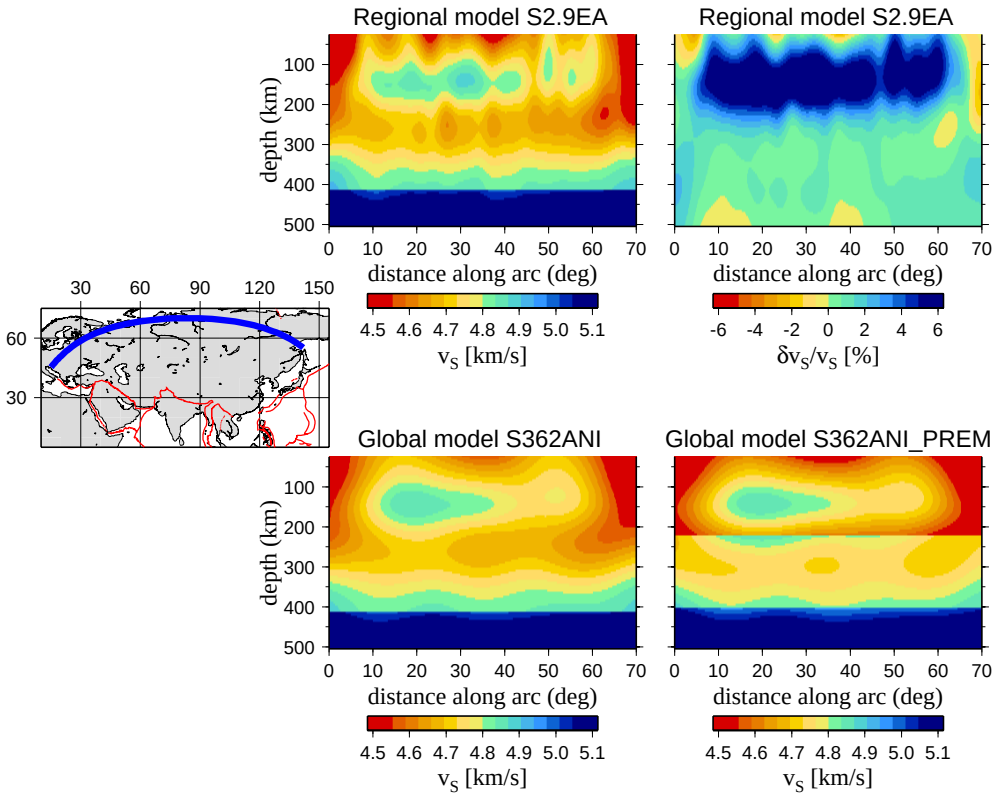

Figure 5.13: Vertical cross sections through the upper mantle in northern Eurasia calculated along the arc indicated with the blue line in the left panel. The red contours on the map delineate plate boundaries. Upper panels: absolute (center) and relative (right) velocities in the regional model S2.9EA, which has been derived using REF as a reference model. Lower panels: absolute velocities in our preferred global model S362ANI (center) calculated as a perturbation with respect to REF, and in a similar model S362ANI_PREM (right) calculated as a perturbation with respect to PREM. The absolute velocities are defined as $v_S = (v_{SH} + v_{SV})/2$. The perturbations are defined as $\delta v_S/v_S = (\delta v_{SH}/v_{SH} + \delta v_{SV}/v_{SV})/2$ and plotted with the global average removed.

viscous, asthenosphere, which might translate coherently with the lithosphere.

The velocities in the uppermost mantle cannot be resolved properly if PREM is used as a reference model. This is demonstrated by the comparison of our preferred global three-dimensional model S362ANI with S362ANI_PREM. The latter has been calculated as a perturbation with respect to PREM rather than REF; otherwise both models have been obtained using exactly the same technique and show nearly identical lateral velocity anomalies. The structure of the upper man-

tle in S362ANI_PREM, as in PREM, is characterized by the positive $\partial v_S/\partial depth$ discontinuity at 220 km. The inversion, however, forces the velocities to decrease with depth between 150 and 220 km and between 220 and 300 km. The increase in velocity at the 220-km discontinuity in PREM, therefore, appears, to be inconsistent with the data, which require the velocity to decrease between 150 and 250 km, regardless of which reference model is used in the inversion.

A global survey of the SS precursors (Gu *et al.*, 2001b) suggests the presence of a discontinuity or a zone of strong velocity gradients beneath Eurasia at a depth of about 220 km. The $S_{220}S$ seismogram predicted by PREM, however, does not match the observed stack in Siberia presented in the paper. Gu *et al.* (2001b) recognized that the discrepancy between observed and synthetic $S_{220}S$ waveforms may result, not only from the depth variations of the discontinuity, but may also represent a reversed polarity of the reflected waves. We prefer the latter interpretation, which is consistent with the presence of the negative velocity gradients in northern Eurasia in our models. It is important to note that the long-period data used by Gu *et al.* (2001b) are not capable of distinguishing between the discontinuity and a 50-km thick gradient zone. Since the difference between velocities at 195- and 245- km depths are as large in S2.9EA as in S362ANI_PREM (Figure 5.13), they are expected to produce $S_{220}S$ arrivals of roughly the same amplitude as PREM, which corroborates our interpretation.

Further evidence for the presence of the negative gradient or discontinuity is found in regional seismic studies from northern Eurasia. One-dimensional models of compressional-wave velocities of Mechie *et al.* (1993) show a negative discontinuity at 200-250 km with the local minimum velocity beneath this discontinuity. The negative discontinuity at 150-200 km along the seismic profile 'Quartz' has been considered by Ryberg *et al.* (1996) as the lithosphere-asthenosphere boundary

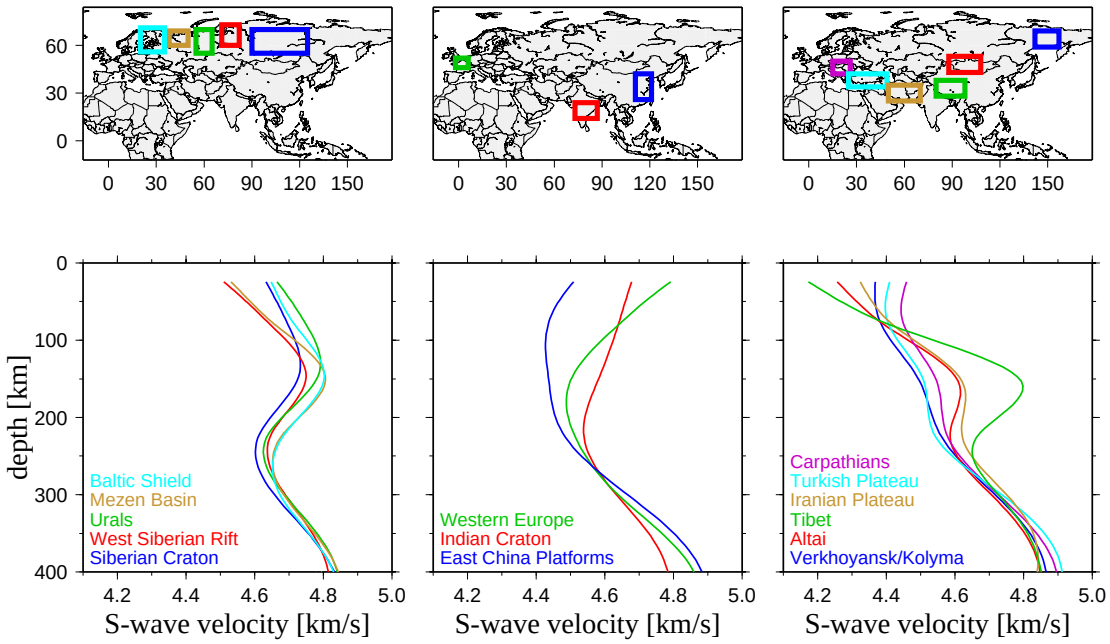

Figure 5.14: Vertical profiles of the Voigt average shear-wave velocity defined as $v_S = (v_{SH} + 2v_{SV})/3$. The velocities plotted in the lower panels represent averages calculated within rectangular regions shown in the upper panels. The names, geographical extent, and tectonic history of particular cratons and sedimentary basins can be found, for example, in Enkin *et al.* (1992), Yin and Harrison (1996), and Nikishin *et al.* (1996).

and a similar discontinuity is observed in the two-dimensional model of Morozova *et al.* (1999). Low-velocity zones in compressional-wave velocities at 200-250 km beneath seismic profile 'Kraton' are reported by Nielsen and Thybo (1999). Grand and Helmberger (1985) show that the shield model SNA of Grand and Helmberger (1984) with the strong negative gradient between 150 and 200 km fits the multiply-reflected shear waves in northern Eurasia.

To further investigate regional shear-wave velocity variations in Eurasia, we plot vertical profiles of Voigt averages calculated at different locations (Figure 5.14). The profiles beneath sedimentary basins and rift systems in northern Eurasia, as well as beneath the Ural orogen, show the same decrease in velocity between 150- and 250-km depths as the Siberian and East European Cratons.

This similarity indicates that the lithosphere beneath the entire northern Eurasia may have roughly the same thickness, regardless of differences in the crustal and shallow subcrustal velocity structure. Regional studies (*e.g.*, Priestley and Debayle, 2003) have shown that the seismic lithosphere may be about 200-km thick beneath Siberia, but a continental-scale model is necessary to demonstrate that the depth of this boundary is located at approximately constant depth over about 7000 km. A 180-240 km thick lithosphere beneath the entire northern Eurasia is also observed in the model CU_SRT1.0 of Shapiro and Ritzwoller (2002), as shown in Figure 5.7.

While the strong negative gradients at the base of the lithosphere in the northern part of Eurasia are confined to a relatively narrow depth range, they cannot be as easily identified in all stable parts of the continent. Beneath the Indian Craton, the velocity decreases monotonically with depth between the Moho and about 220-km depth. The gradient between the 150 and 250 km is similar to that observed in northern Eurasia, and the local minimum velocity occurs also at about 250 km. Therefore, we cannot rule out that the boundary beneath India is also located at about 200 km. The negative gradients beneath platforms in eastern China are observed only above 100-km depth. This profile is somewhat similar to the tectonic model of North America (Grand and Helmberger, 1984), which is thought to have a relatively thin lid compared to the stable part of the continents. The continental crust in Western Europe is underlain by the zone of negative velocity gradients, which decrease monotonically down to about 180 km. The estimation of the lithospheric thickness in this region is, therefore, difficult.

The negative velocity gradients at a depth of 200 km are also observed beneath some regions of recent tectonic activity in Eurasia. The profile beneath Tibet shows a very strong gradient, weaker gradients are observed beneath Altai and Iranian Plateau. In the Carpathians, Turkish Plateau, and

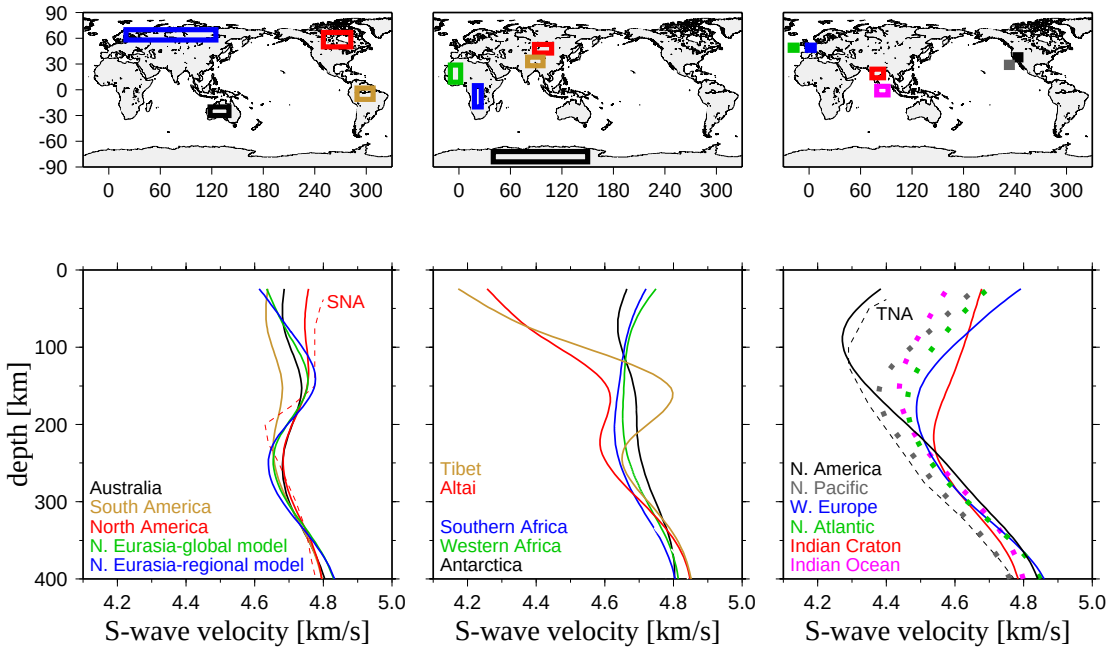

Figure 5.15: Similar to Figure 5.14, but for various tectonic settings both within and outside of the Eurasian continent. The dashed lines indicate models SNA and TNA of Grand and Helmberger (1984). The dark blue line in the bottom-left panel indicates the profile calculated in the regional model S2.9EA. Other profiles are calculated in the global model S362ANI. The solid lines in the bottom-right panel correspond to the continental regions and dotted lines correspond to the nearby oceanic regions.

the Verkhoyansk-Kolymian orogenic belts, the velocities slightly increase with depth at 200 km, but the depth range between 150 and 250 km is characterized by very weak gradients compared to the oceanic regions. The comparison of our model with the receiver functions of Kumar *et al.* (2006) shown in Figure 5.10 demonstrates that the zone of negative gradients in our model coincides with the lithosphere-asthenosphere boundary as suggested by those authors. Since the zones of negative velocity gradients or anomalously weak positive gradients in other tectonically deformed regions are located at approximately the same depth as in Tibet and stable parts of the continent, they may also represent the base of the continental lithosphere.

The zone of decreasing velocities with depth between 150 and 250 km is observed beneath

stable parts of other continents (Figure 5.15), although velocities do not decrease as rapidly as in Eurasia. The gradients in Eurasia are strong, but Grand and Helmberger (1984), for example, find even stronger gradients at the bottom of the lithosphere in North America. The model S362ANI shows nearly as strong gradients as S2.9EA, which indicates that they are not caused by allowing the regional model to be much rougher than in the global model.

The presence of the negative gradients between 150 and 250 km beneath Eurasia, North and South America, and Australia suggests that 175-225 km may be a typical depth of the base of the continental lithosphere. Narrow zones of negative gradients in this depth range are, however, not observed beneath Antarctica and Africa. The profile in Antarctica shows anomalously low positive gradients between 150 and 250 km, and velocities beneath African cratons have a minimum at 200-250 km. The velocity structure in Antarctica and Africa is, therefore, very different from that in oceanic regions, which show a pronounced minimum at about 150 km and strong positive gradients beneath this depth. We, therefore, cannot rule out the possibility that the base of the lithosphere beneath Africa and Antarctica is also at around 200-km depth.

It is likely that lithosphere-asthenosphere boundary is sharp in northern Eurasia, since it has been far from the disrupting flow in the oceanic mantle for a long time. In contrast, the velocity profiles beneath the Indian Craton and Western Europe appears to be of a transitional character; they are similar to the nearby oceanic mantle in the Indian and Atlantic oceans. It is, however, not clear why the continental lithosphere beneath old cratons on other continents is not separated from the asthenosphere by as sharp boundary as in Eurasia. Even more interestingly, the boundary appears to be sharper beneath some tectonically deformed regions in Eurasia, such as Tibet and Altai, than beneath cratons in Africa and Antarctica.

The strong positive velocity gradient in the uppermost 150 km beneath Eurasia mantle is not observed beneath other continents. Models of Shapiro and Ritzwoller (2002) and Nettles (2005) also show stronger positive anomalies at 150 km than at the Moho beneath Eurasia, but not beneath other continents. This indicates that the presence of positive gradients in the uppermost mantle in Eurasia does not result from neglecting the lateral variations in the sensitivity kernels and depth of the Moho in our inversion. At this point, the origin of the anomalous structure in Eurasia is unknown. It is, however, important to note that the gradients are much stronger in Mezen Basin and West Siberian Rift than in Baltic Shield and Siberian Craton.

5.4 Effect of crustal corrections

In the inversion for the regional model of Eurasia S2.9EA, we correct the waveform data for crustal effects using the new nonlinear method. In Chapter 4, we have shown that the strongest effects of using the new corrections on shear-wave velocities are observed in Eurasia. To investigate these effects in regional detail, we have developed a model S2.9EA_OLDCRCOR in the same way as S2.9EA, except that we have used the standard linear corrections. The differences between the two models at shallow depths down to 200 km are very small, as shown in Figure 5.16. The structures at shallow depths are constrained primarily by surface-wave data, which are corrected for crustal effects using the same method in both models. At a depth of 250 km, the sensitivity of mantle waves is significant compared to the intermediate-period surface waves, and the effects of crustal corrections become larger. The improved method yields weaker positive amplitudes beneath Tibet, central Asia, and East European Craton.

The positive anomalies at a depth of 300 km in our preferred model nearly vanish (Figure 5.17).

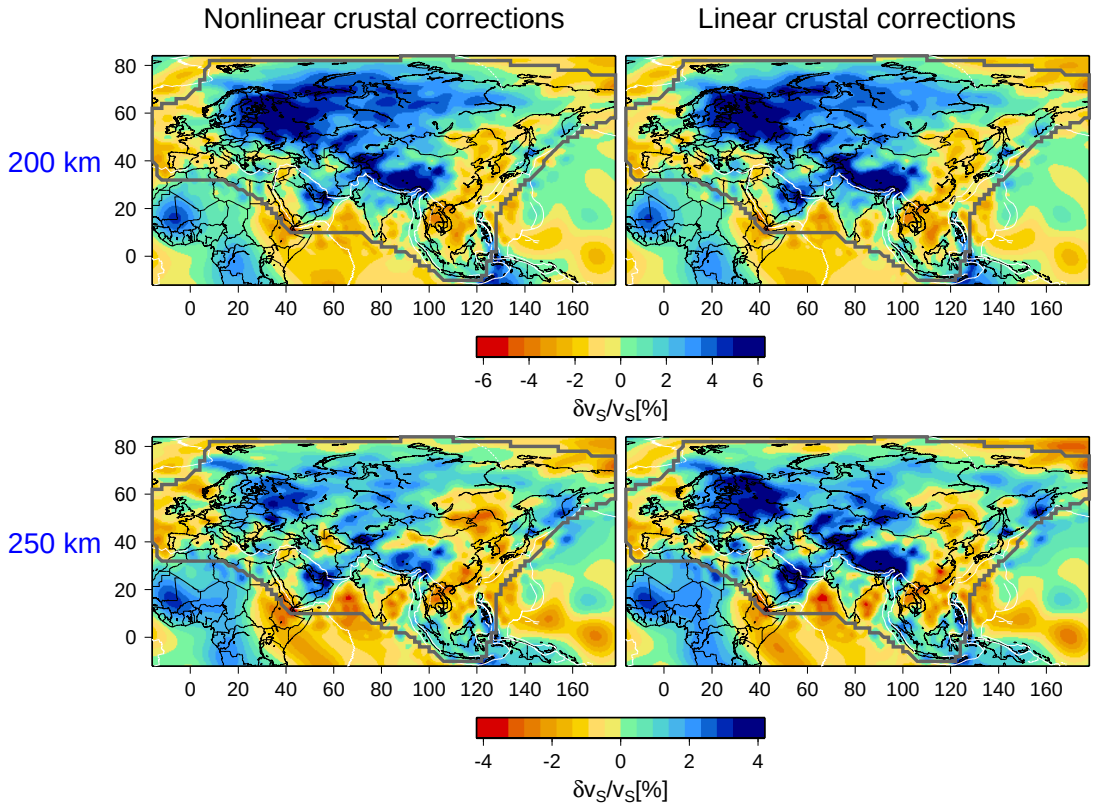

Figure 5.16: Effect of correcting the waveforms for perturbations in crustal structure using the new nonlinear method. Our new preferred model of Eurasia S2.9EA, which has been obtained using the nonlinear corrections, is plotted on the left. The model on the right, which has been obtained using the linear corrections of Woodhouse and Dziewoński (1984), overestimates amplitudes of fast-velocity anomalies beneath continents.

If the linear crustal corrections are used, however, the lithosphere beneath the East European Craton and central Asia appears to extend more than 300 km and about 350 km beneath Tibet and Altai. The anomalies beneath the mountain belts are likely to be affected by overtone data, for which the errors of the linear corrections are large in regions of thick crust (Figure 2.14).

Significant differences between the models are confined to the depth range of 200-400 km. We recognize that the model obtained using the linear approximation of Woodhouse and Dziewoński (1984) tends to overestimate lithospheric thickness. Nevertheless, it does not affect the pattern of lateral velocity variations considerably. Similar to our studies, Marone and Romanowicz (2006)

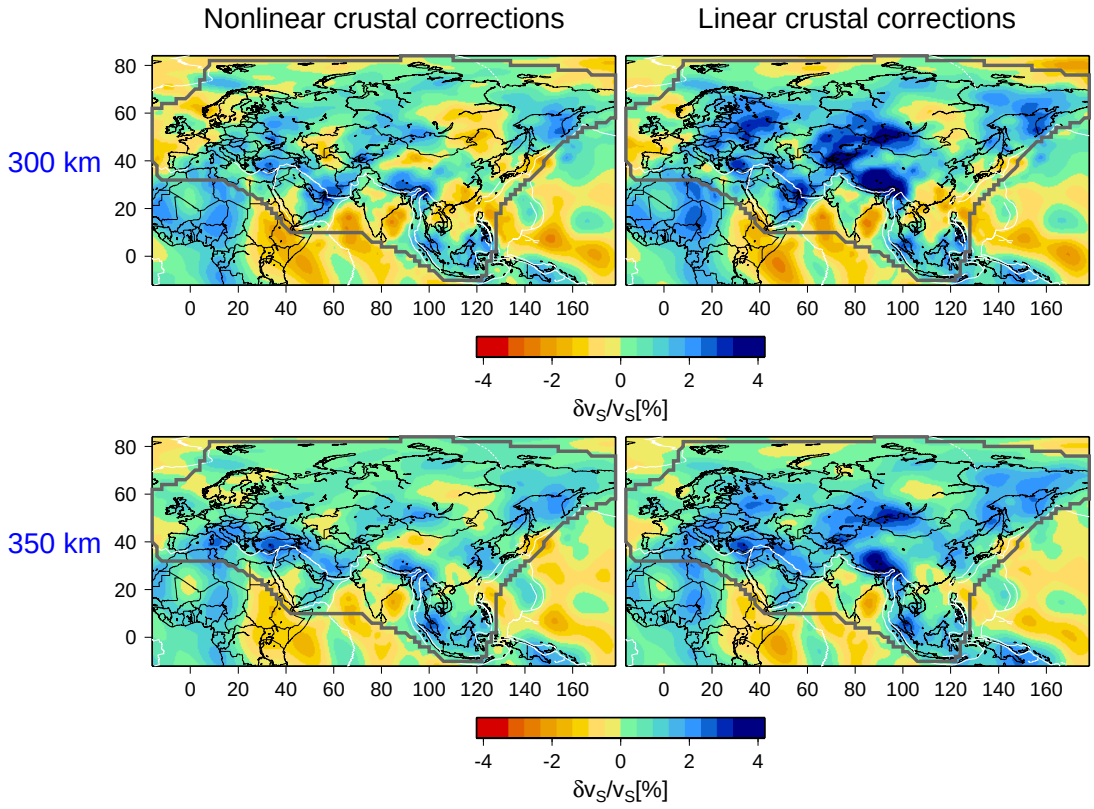

Figure 5.17: Same as Figure 5.16, but for larger depths. Strong fast-velocity anomalies beneath continents extend to larger depth if linear crustal corrections are used.

find that the linear crustal corrections yield continental lithosphere that is too thick beneath some stable parts of North America. However, they also report unexpected nonlinear crustal effects in the southern part of the continent, where deviations of the crustal structure from the global average are less significant.

5.5 Anisotropic variations

The presence of anisotropic variations in northern Eurasia has been reported by Gee and Jordan (1988), who found multiply reflected SH-waves to be faster than the predictions of the model EU2 (Lerner-Lam and Jordan, 1987) obtained from the measurements of Rayleigh waves. The latter was

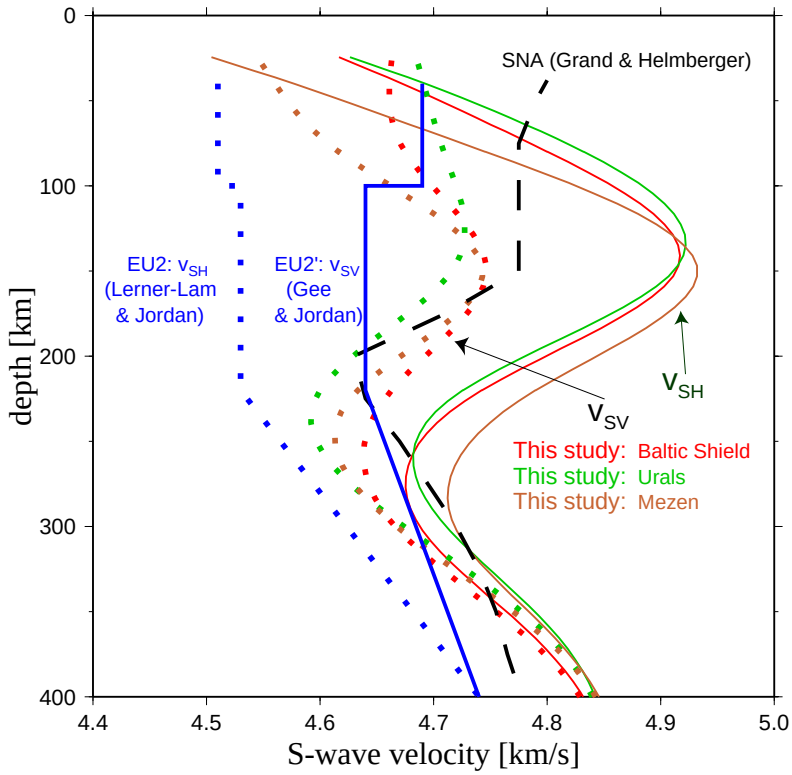

Figure 5.18: Velocities of the horizontally- and vertically- polarized shear waves in the upper mantle beneath Eurasia. Solid lines indicate v_{SH}, dotted lines indicate v_{SV}, and the solid black line indicates isotropic v_S in the shield model of North America SNA (Grand and Helmberger, 1984). EU2′ is the v_{SH} model of Gee and Jordan (1988), and EU2 is the v_{SV} model of Lerner-Lam and Jordan (1987). The red, green, and blown lines correspond to the velocities in our model S2.9EA at different locations in northern Eurasia.

7% slower than the shield model SNA (Grand and Helmerger, 1984) in the uppermost mantle, while the model EU2′ of Gee and Jordan obtained from the data sensitive to the horizontal velocities is only 2% slower than SNA (Figure 5.18).

Our model S2.9EA provides some new insight into the anisotropy and discrepancy between models EU2 and SNA reported by Gee and Jordan (1988). The difference between models EU2′ and EU2 below the depth of 100 km roughly agrees with the strength of anisotropy in S2.9EA. In the uppermost 100 km, however, Gee and Jordan (1988) find strong anisotropy, which is not observed in our model. The lack of anisotropy at shallow depths in our model may result from neglecting the

lateral variations in the Moho depth and sensitivity kernels. Stronger anisotropy in the continental lithosphere has been found by Nettles (2005), who accounted for these variations, and used the same surface-wave data as in this study.

We find shear-wave velocities at shallow depths beneath three different tectonic setting in northern Eurasia to be much lower than in SNA, and roughly similar to those in EU2 and EU2′. The velocities in SNA are likely to be lower, because of the difference in the structure beneath Eurasia and North America. At depths between 100 and 250 km, however, our model is even faster than SNA, and the models EU2 and EU2′ are too slow to fit our data. These models also fail to resolve the zone of negative $\partial v_S/\partial depth$ gradient between 150 and 250 km.

Lateral anisotropic variations in our model and in CU_SRT1.0 (Shapiro and Ritzwoller, 2002) are shown in Figure 5.19. In our model, northern Eurasia at the depth of 80 km is characterized by weak anisotropy, while tectonically active regions show stronger than average anisotropy. Since this pattern is anticorrelated with the isotropic variations, it is not clear whether the anisotropic variations are real or result from the velocity-anisotropy trade-offs. Shapiro and Ritzwoller (2002), who found a somewhat similar pattern of anisotropic heterogeneity in the uppermost mantle, estimate the uncertainty of these variations to be about 50%. Weak anisotropy with little lateral variations at 80-km depth in our model is inconsistent with the finding of Nettles (2005), and perhaps results from the simplified treatment of the crustal structure. At a depth of 150 km, the anisotropy becomes stronger and anticorrelated with the pattern at 80 km. In CU_SRT1.0, the anisotropy is constrained by the parameterization to decrease linearly with depth, and practically vanishes below 150 km.

The lateral anisotropic variations in our regional model of Eurasia are very similar to those in the global model (Figure 5.20). While anomalies of shorter wavelengths are observed in S2.9EA,

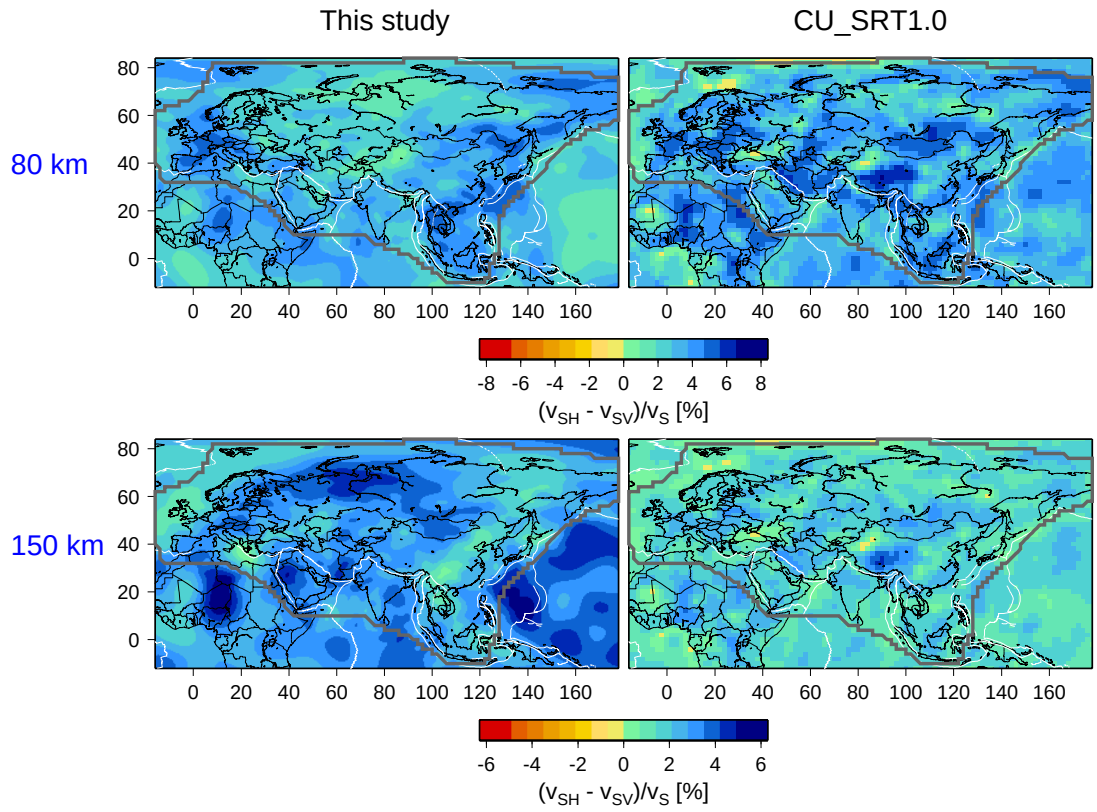

Figure 5.19: Lateral anisotropic variations in our model S2.9EA (left) and in CU_SRT1.0 (right; Shapiro and Ritzwoller, 2002). The anisotropic anomalies in S2.9EA at 80-km depth are anticorrelated with the isotropic anomalies, and show some similarity to those in CU_SRT1.0. At 150-km depth, the pattern of anisotropic anomalies in our model is somewhat anticorrelated with the pattern at 80 km.

the differences between the two models are not correlated with any tectonic features in Eurasia. Despite the differences, the regional isotropic variations remain almost unaffected by allowing for regional anisotropic variations in the inversion.

Anisotropic variations become very small at a depth of 300 km in both the global and regional model. However, at a depth of 250 km, they remain quite strong in Eurasia (Figure 5.21). The strongest positive anisotropy is observed beneath Tibet, and this +5% anomaly is difficult to explain. It may be that errors in the *a priori* crustal model are projected into larger depths, which are not well-constrained by the data. Such errors may involve, for example, significant anisotropic crustal

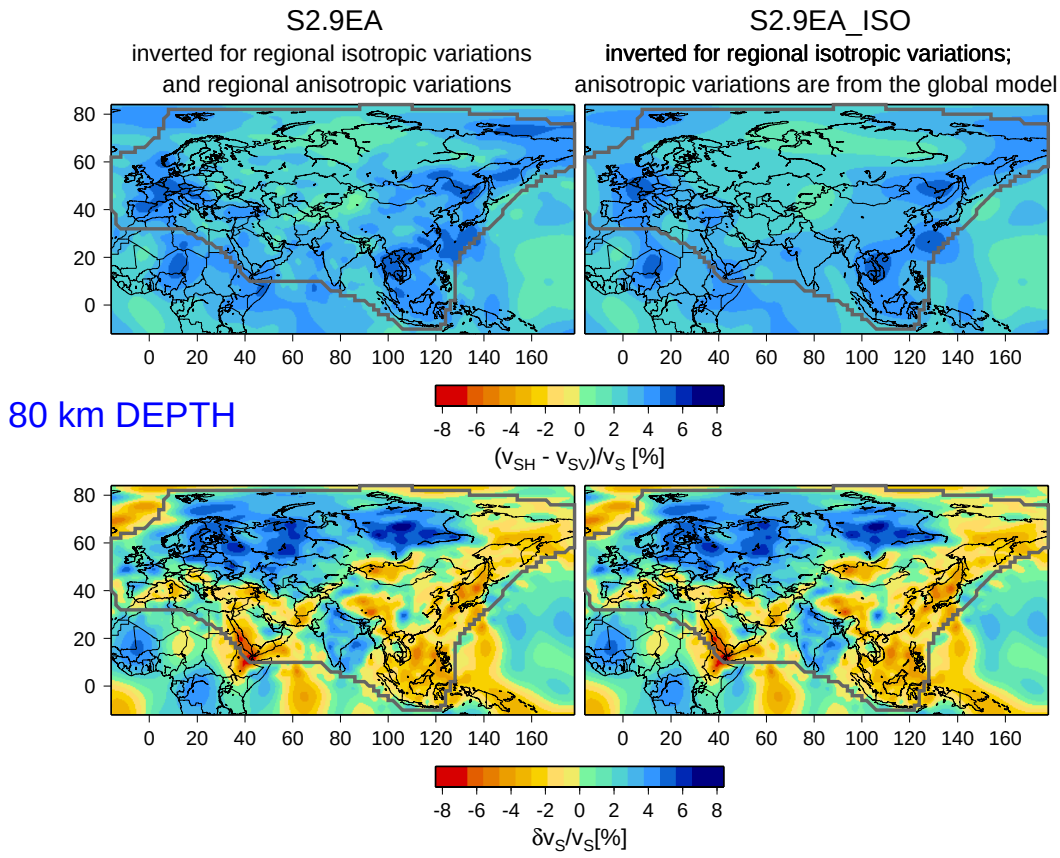

Figure 5.20: Lateral anisotropic (top) and isotropic (bottom) velocity variations in models S2.9EA and S2.9EA_ISO. The former is our preferred model, in which both regional isotropic and anisotropic variations have been determined. In model, S2.9EA_ISO, only isotropic regional variations have been determined while anisotropic variations are identical to those in the global model S362ANI. The regional isotropic variations remain almost unaffected by allowing for regional anisotropic variations in the inversion.

variations beneath Tibet reported by Shapiro *et al.* (2004), which are not incorporated in CRUST2.0.

East Asia shows strong negative anisotropy in our models at 250 km (Figure 5.21). While significant azimuthal anisotropy beneath Japan has been reported based on the measurements of shear-wave splitting (*e.g.*, Long and van der Hilst, 2005), it is difficult to explain why the maximum variations are observed beneath the Sino-Korean Platform. The anisotropic variations at 250 km are significantly stronger in the regional model than in the global model. Regardless of whether they represent real anisotropic variations or artifacts, it is clear that inverting for the regional anisotropic

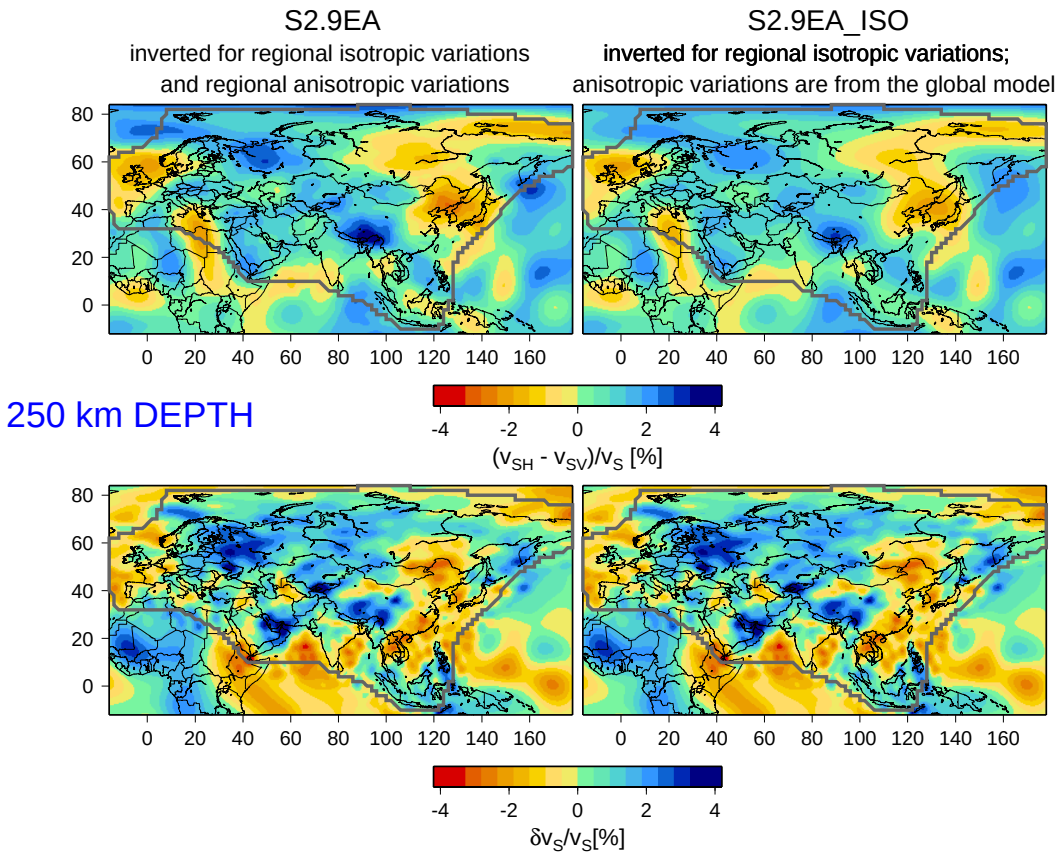

Figure 5.21: Same as Figure 5.20, but for a depth of 250 km and plotted with a different color scale. Despite the presence of strong anisotropic anomalies beneath Tibet and Sino-Korean Platform in S2.9EA, the isotropic velocity model is affected little by allowing for regional anisotropic variations.

variations does not appreciably affect the isotropic part of the model.

We conclude that the anisotropic variations in our model are probably not as robust as the isotropic variations. If the regional-scale anisotropic variations in Eurasian upper mantle exist, they may trade off with the isotropic variations. They may also be affected by the errors in the crustal structure imposed on our model. However, isotropic velocity variations are practically unaffected by allowing for regional anisotropic variations in the inversion.

Chapter 6

Discussion and future directions

In this work, we have demonstrated that progress in seismic tomography can be achieved by expanding data sets, as well as by improvements in the modeling technique such as accounting for radial anisotropy, development of more accurate method for crustal corrections, or implementation of a non-uniformly parameterized model. These new data and methods have been implemented in the computation of our new global and regional models. The new global and regional models facilitate understanding of the structure and dynamics of the Earth's mantle. In this chapter, we summarize what we have learned about the thickness of the continental lithosphere, and regional-scale lateral heterogeneity in Eurasia, and discuss their implications such as, global flow pattern in the asthenosphere, and the style of convection in the mantle. We emphasize that improvements obtained in this study are significant, and allow progress in understanding of the Earth's mantle.

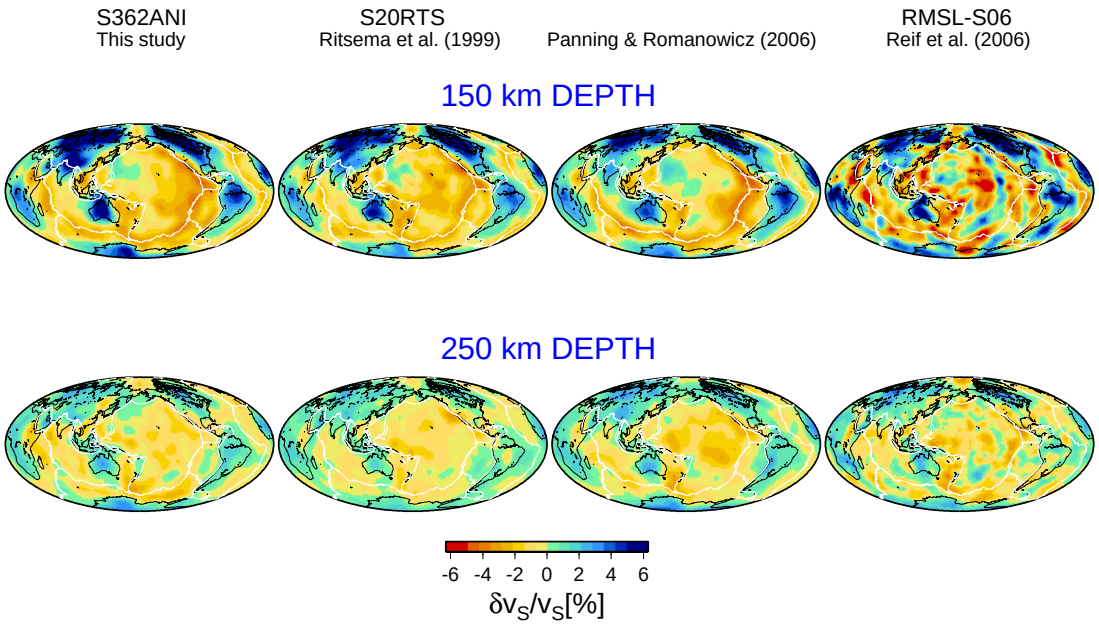

Figure 6.1: Isotropic shear-wave velocity perturbations at depths of 150 and 250 km in our model S362ANI, model S20RTS (Ritsema *et al.*, 1999), model of Panning and Romanowicz (2006), and model RMSL-S06 (Reif *et al.*, 2006). The decrease in positive anomalies between 150- and 250-km depths suggests moderate thickness of the continental lithosphere.

6.1 The continental lithosphere

Our global model S362ANI and the regional model of Eurasia S2.9EA both show fast-velocity anomalies beneath stable parts of continents extending down to a depth of about 200 km. This moderate thickness is consistent with some other global (*e.g.*, Ritsema *et al.*, 1999; Panning and Romanowicz, 2006) and regional (*e.g.*, Priestley and Debayle, 2002) models. Recent global models show very strong anomalies beneath continents at a depth of 150 km, which nearly vanish at a depth of 250 km (Figure 6.1). The decrease in the positive anomalies at the 200-km depth is so sharp that the absolute shear-wave velocity beneath cratons in Eurasia, as well as in North and South America, decreases between 150 and 250 km (Figure 5.15). We refer to the zone of the steepest negative $\partial v/\partial depth$ gradient as the base of the continental lithosphere. We speculate that the base

may represent a compositional boundary between the lithosphere depleted in basaltic components and the asthenosphere.

We find the lithosphere in Eurasia to be unique in two regards. First, the negative velocity gradients between 150 and 250 km are much stronger than beneath any other continent (Figure 5.15). Perhaps this indicates that the boundary between lithosphere and asthenosphere in Eurasia is sharper than beneath other continents, but the reason of such uniqueness is unclear. One possible explanation is that the interior of the largest continent is not as disturbed by the flow in the mantle as the continental boundaries or smaller continents. The second distinct feature of the lithosphere beneath Eurasia is the presence of positive $\partial v/\partial depth$ gradients above the 150 km depth, which are not observed beneath cratons in other continents (Figure 5.15). The origin of these gradients is also unknown.

Smooth parameterizations of our models do not resolve discontinuous jumps in velocity. Instead, discontinuities, if they exist, appear in the models as zones of strong velocity gradients. Therefore, the decrease in velocity between 150 and 250 km beneath continents may, in fact, represent a discontinuity underlain by a low-velocity zone. This would be inconsistent with the interpretations of the Lehmann discontinuity at the 220-km depth as a base of the low-velocity zone (Anderson, 1979). Our results also do not agree with the interpretation of the Lehmann discontinuity beneath continents reported in the global surveys of $S_{220}S$ reflections (Gu *et al.*, 2001b; Deuss and Woodhouse, 2002). The $S_{220}S$ waveforms provide higher vertical resolution than the surface-wave data used in this study, and therefore might detect a positive $\partial v/\partial depth$ discontinuity within the negative gradient zone. Such a complex velocity structure may be responsible for the inconsistency of our model with the $S_{220}S$ waveforms in some regions. In other regions, an alternative

explanation is possible. The $S_{220}S$ reflections in Eurasia stacked by Gu *et al.* (2001b) appear to have the opposite polarity than the PREM synthetics, and might be consistent with the negative velocity gradients observed in our models. Such an interpretation agrees with the negative discontinuity at about 200-km depth observed in some models obtained from high-frequency data in Eurasia (Ryberg *et al.*, 1996; Morozova *et al.*, 1999), and a zone of strong negative gradients in the model of Grand and Helmberger (1985) obtained from multiply-reflected shear waves. Further comparison of our models with the measurements of high-frequency reflected or converted waves should help to establish the character of this boundary. For example, in Figure 5.10, we presented a comparison of our model of Eurasia with the receiver functions of Kumar *et al.* (2006), which indicates that the locations of negative gradient beneath Tibet coincide with the sharp discontinuity reported by Kumar *et al.* (2006) as the base of the lithosphere.

It would be interesting to investigate how well our model of Eurasia fits the regional-distance travel-time data from the series of Peaceful Nuclear Explosions (PNE). Our three-dimensional ray tracing experiments (Kustowski *et al.*, 2003) show that the vertical velocity gradient in the global mantle model of Gu *et al.* (2001a) is inconsistent with the PNE data, and that this model does not fit the data better than PREM. Perhaps the new higher-resolution model of Eurasia with distinctly different vertical velocity gradients would be more consistent with the PNE data. In such case, the data could be used to further improve the resolution of the model.

Besides the layer of strong, fast-velocity anomalies in the uppermost 200 km of the mantle beneath continents, we find very weak positive anomalies beneath continents extending down to about 400 km, in agreement with the results of Ritsema (2004). The presence of the positive anomalies below 200 km suggests that thick continental roots may translate coherently with the continents.

Assuming that the boundary at about 200-km depth marks the top of the asthenosphere, the weak positive anomalies extending below this boundary may represent a colder-than-average, and therefore more viscous region, which might translate coherently with the lithosphere. Alternatively, the anomalies below 200 km in continental regions may be an artifact of an inversion, resulting either from smoothing constraints applied in the inversion, or systematic errors in the continental structure in the *a priori* crustal model.

6.2 Anisotropy in the uppermost mantle

The most abundant mineral in the uppermost mantle, olivine, is strongly anisotropic, and is thought to be preferentially oriented due to flow in the asthenosphere. Seismic waves are sensitive to anisotropy generated by such alignment, and models of seismic anisotropy are often used to infer deformation processes in the Earth's mantle. We find that the globally averaged shear-wave anisotropy is strongest at a depth of about 125 km, but it vanishes at the Moho (Figure 4.3). This is consistent with the results of Boschi and Ekström (2002) and Nettles (2005), but significantly different from PREM (Dziewoński and Anderson, 1981).

If the seismically-detected anisotropy indeed reflects the alignment of olivine crystals in the asthenosphere, the strongest anisotropy at 125 km suggests that the alignment is strongest at this depth. If this is the result of global-scale flow, the strength of the lateral anisotropic variations in anisotropy at this depth are expected to be at a minimum. This local minimum is indeed observed in our model S362ANI (Figure 4.27), as well as in the recent flow model of T. Becker (personal communication). The anisotropic properties observed and predicted by the two models agree well, but further comparisons are needed to determine the consistency of lateral anisotropic variations

between the two models.

We do not find evidence for the presence of $v_{SH} > v_{SV}$ anisotropy beneath the continental lithosphere reported by Gung *et al.* (2003), but we cannot rule out the existence of such anisotropy. In our inversions, anisotropy beneath continental regions strongly depends on regularization, and therefore, is not as robust as beneath oceans. Improved modeling of anisotropy beneath continents requires accounting for lateral variations in the sensitivity kernels, including variations in the Moho depth, as suggested by the comparison of our model with that of Nettles (2005).

6.3 Style of convection in the mantle

Although seismic tomography is the most powerful tool to study the structure of the mantle and dozens of velocity models have been produced, it is not yet clear whether the convection in the upper mantle is separated from the processes operating in the lower mantle. This problem is related, but not equivalent, to the question of the depth extent of lithospheric slabs. Some seismic tomography models (*e.g.*, Grand *et al.*, 1997; van der Hilst *et al.*, 1997) show fast-velocity anomalies beneath major subduction zones extending down to the mid-mantle or even to the lowermost mantle. Many scientists take this as an evidence for the whole-mantle convection. However, there are several lines of evidence indicating that it may be oversimplified or erroneous (for review, see Hamilton, 2002). From the seismologist's point of view, the most important issue is the poor sensitivity of teleseismic body waves to the structure of the upper mantle, and consequently, the models (*e.g.*, Grand *et al.*, 1997; van der Hilst *et al.*, 1997). For example, Boschi and Dziewoński (1999) show that, given the ray-path coverage of teleseismic body waves, it is possible to obtain the velocity model with fictitious narrow fast-velocity anomalies beneath subduction zones even from the synthetic input

data calculated without such structures.

On the other hand, lower-resolution whole-mantle models of shear-wave velocity, constrained by diverse data sets, suggest that the boundary between upper and lower mantle may inhibit penetration of the lithospheric slabs into the lower mantle. Fukao *et al.* (2001) point out that some slabs are deflected horizontally in the mantle transition zone. Gu *et al.* (2001a) report the change in the power spectrum at the 670-km discontinuity, which suggests a change in the flow pattern. Our model S362ANI with better data set than that used by Gu *et al.* (2001a), parameterization for anisotropy, topography of the transition zone discontinuities, and better one-dimensional reference model confirms this change in power spectrum at 670-km depth. It is also observed in other shear-wave velocity models, such as those of Ritsema *et al.* (1999, 2004) and Panning and Romanowicz (2006), as shown in Figure 6.2.

The presence of strong fast-velocity anomalies extending over thousands of kilometers beneath major subduction zones in the transition zone, but not in the uppermost lower mantle, indicates that slabs may accumulate in the transition zone (Figure 6.3). Ponding or horizontal deflection of slabs above the 650-km discontinuity is consistent with the presence of very deep earthquakes located away from the downgoing slabs, whose principal stress axes deflect horizontally from the slabs (Giardini and Woodhouse, 1984, 1986; Lekic, 2004).

Further evidence for the interaction of the lithospheric slabs with the upper-mantle boundary is provided by modeling of the topography of the transition zone discontinuities. The phase transition from γ-spinel to magnesiowustite and perovskite at 650-km depth is characterized by a negative Clapeyron slope (*e.g.*, Helffrich, 2000). Assuming that only thermal effects are responsible for the discontinuity topography, low temperature anomalies should lead to depressions in the 650-

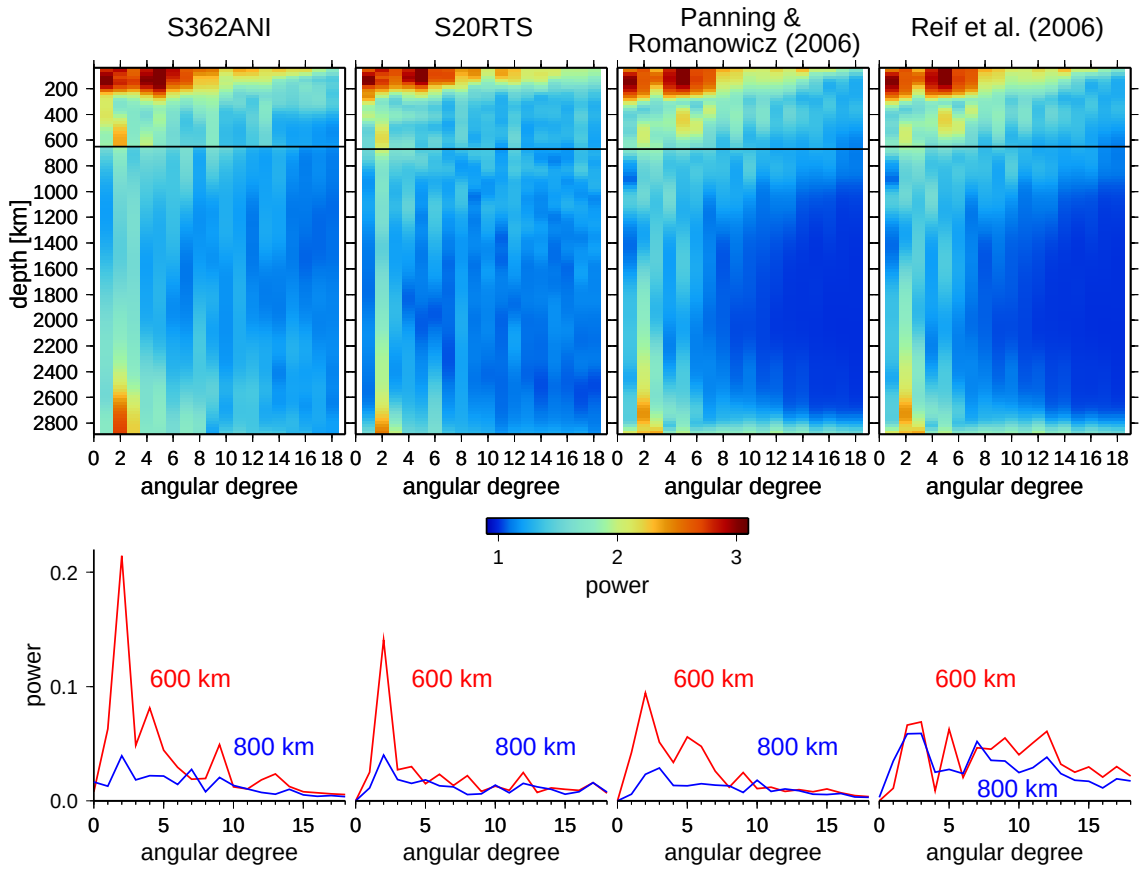

Figure 6.2: Power spectrum of shear-wave velocity heterogeneity in our model S362ANI, model S20RTS (Ritsema *et al.*, 1999), model of Panning and Romanowicz (2006), and model RMSL-S06 (Reif *et al.*, 2006). The first three models, which are well constrained in the transition zone by either body-wave waveforms or measurements of overtone phase velocities, show a significant change in the power spectrum between the upper and lower mantle indicated by the black line. In particular, a strong maximum at degree two is observed at the base of the transition zone, but not in the lower mantle. The model RMSL-S06 is poorly-constrained in the transition zone, and does not show the change at the upper-lower mantle boundary. In the upper panels we plot $log_{10}(10 + 1000 \cdot power)$. The change in the power spectrum between the upper and lower mantle is more pronounced when linear scale is used, as shown in the bottom panels.

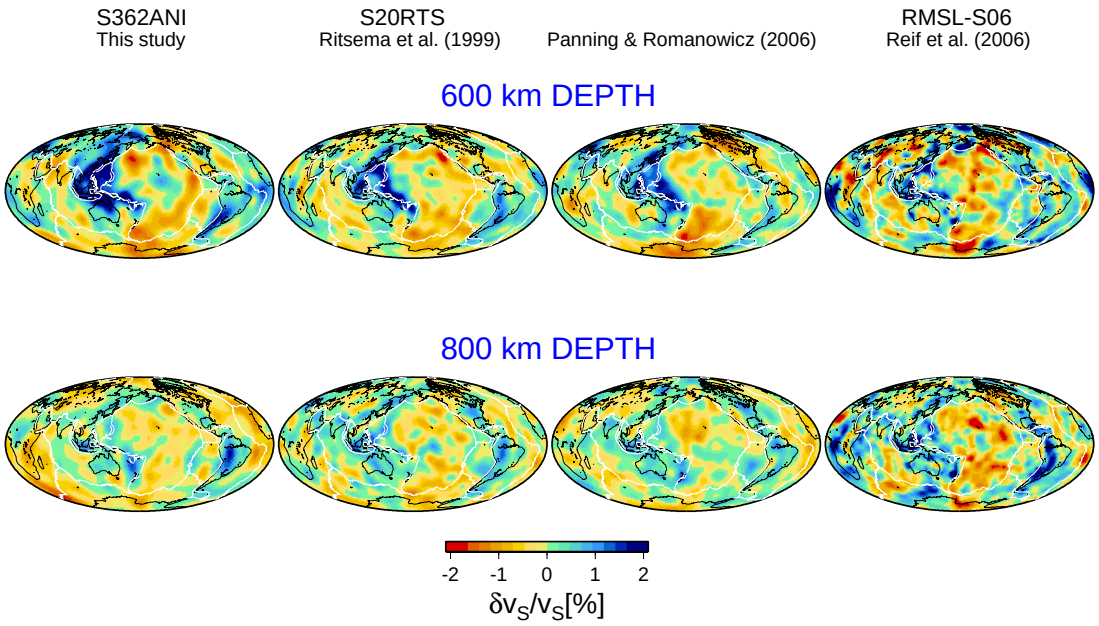

Figure 6.3: Isotropic shear-wave velocity perturbations in the transition zone and uppermost lower mantle in our new model S362ANI, model S20RTS (Ritsema *et al.*, 1999), model of Panning and Romanowicz (2006), and model RMSL-S06 (Reif *et al.*, 2006). Strong fast-velocity anomalies are observed beneath major subduction zones in the transition zone, but not in the uppermost lower mantle, which suggests that slabs may accumulate in the transition zone.

km discontinuity, which are indeed observed in regions of subduction (Figure 4.16). The positive Clapeyron slope at 410 km associated with the transition from olivine to β-spinel, on the other hand, should elevate the discontinuity near cold slabs. The 410-km discontinuity, however, is not elevated beneath the subduction zones. This lack of elevation in topography models may not be real. Flanagan and Shearer (1998) and Gu *et al.* (1998) suggest that the SS precursors used in their study are insensitive to the small-scale topography associated with the penetration of slabs across the 410-km discontinuity. The large Fresnel zone of SS precursors and the stacking procedure used to enhance the precursory signal average out the topography over 1000-1500 km. In contrast, the presence of large-scale depressions at 650 km indicates that slabs may be deflected horizontally at the bottom of the upper mantle and interact with the discontinuity over hundreds of kilometers, as

was first proposed by Shearer and Masters (1992).

The topography of the 410-km discontinuity is not only uncorrelated with, but also significantly weaker than, the topography at 650 km (Figure 4.16). Given that the Clapeyron slope at 410 km is steeper than at 650 km (*e.g.*, Helffrich, 2000), larger topography at 650 km requires either larger temperature variations, or that factors other than temperature, such as interaction of slabs with the viscous lower mantle, may regulate the discontinuity depth. In either case, stronger topography on the 650-km discontinuity favors the interaction of slabs with the discontinuity rather than uninhibited penetration of slabs into the lower mantle.

The shear-wave velocity models and the topography of the transition zone discontinuities suggest that the upper-lower mantle boundary inhibits flow, but they do not preclude some penetration. Tackley *et al.* (1993) showed that a flow model with partial barrier at the upper-lower mantle boundary generates slab accumulation and intermittent avalanches of the accumulated material into the lower mantle. Such model reproduces the power spectrum similar to those observed in tomographic models. Therefore, changes in power spectra should be used as a constraint in building geodynamic flow models.

6.4 Anisotropy in the transition zone and lower mantle

Although the presence of anisotropic variations in the uppermost 200 km of the mantle has been well-documented, it is not clear whether the mantle is also significantly anisotropic at larger depths. The presence of seismic anisotropy in the D$''$ region has been reported (for review, see Kendall, 2000). Both lattice- (Karato, 1998) and shape-preferred (Kendall and Silver, 1996) orientation have been proposed as a possible source of the anisotropy at the bottom of the mantle, and studies of

the properties of post-perovskite phase in the lowermost mantle indicate that it is highly anisotropic (*e.g.*, Murakami *et al.*, 2004; Oganov and Ono, 2004; Shim *et al.*, 2004). Recently, Panning and Romanowicz (2006) modeled anisotropic variations in the mantle using waveform inversion based on the nonlinear asymptotic coupling theory (Li and Romanowicz, 1996). They found that anisotropy in the transition zone and lower mantle is significant. Thus far, this has been the only attempt to model shear-wave anisotropic variations in the whole-mantle on the global scale, and in this work, we investigate whether their results can be reproduced by inversion of body-wave travel times and waveforms based upon the path-average approximation (Woodhouse and Dziewoński, 1984).

We find that allowing for radial anisotropy below the 200-km depth does not improve the fit of waveform data significantly (Figure 4.19). These data provide the most important constraints on the structure of the transition zone. We cannot rule out the presence of anisotropy in this region, however, anisotropy is not required by the waveform data.

There is evidence from regional studies that the lowermost mantle is significantly anisotropic (for review, see Kendall, 2000). When we invert for the whole-mantle anisotropic model, we find up to 2% anisotropic variations at the bottom of the mantle. The strength and the dominating degree-two pattern of these variations are comparable with those in the model of Panning and Romanowicz (2006; Figure 4.29). Allowing for radial anisotropy in the lowermost mantle significantly improves the data fit (Figure 4.19), but the synthetic test demonstrates strong trade-offs between isotropic and anisotropic velocity variations (Figure 4.20). These tests and the high correlation between the isotropic and anisotropic variations suggest that the anisotropy at the bottom of the mantle may be an artifact of the inversion. In order to improve constraints on the anisotropic structure of the transition zone and lower mantle, it would be useful to combine our data with the body-wave travel-time data

from the last decade and with the measurements of normal-mode splitting functions.

6.5 Robustness of the CMT solutions

A Centroid Moment Tensor (CMT) solution depends on a three-dimensional velocity model used in the source inversion. In sections 4.2.8 through 4.2.11, we have tested the sensitivity of the CMT solutions to the lateral anisotropic variations, reference model, and the method used to correct seismograms for crustal effects. We find that the CMT solutions for 219 earthquakes of $6.5 \leq M_w < 8.0$ and 10 great earthquakes with $M_w \geq 8$ are quite robust. Changing the reference model from PREM to REF significantly affects hypocentral depths. The differences in depth estimates are usually about 3 km and never exceed 8 km. Implementing an accurate, nonlinear method to calculate crustal corrections changes the depth estimates up to 5 km compared with the corrections based upon the linear approach. It also relocates some epicenters by up to 20 km, especially for earthquakes with ray paths in Asia. Accounting for lateral anisotropic variations has a systematic effect on the epicenters, in particular, along the circum-Pacific belt: the epicenters are shifted by about 4 km. The effect of anisotropy, crustal corrections, and the reference model on the earthquake magnitude is almost always smaller than 0.05. In the future, the robustness of the CMT solutions should also be tested for smaller events. In the case of $M_w < 6.5$ earthquakes, intermediate-period surface waves are used in the source inversion, and the effect of anisotropic, as well as isotropic, variations at shallow depths are expected be more significant than for the $M_w \geq 6.5$ earthquakes considered in this study.

6.6 Progress in seismic tomography

In this work, we have demonstrated that combining new data sets and improvements in modeling technique lead to better velocity models. Since progress in understanding properties and dynamics of the Earth's mantle benefits from refinement in tomographic models, it is important to emphasize the difference between our new model and older models.

We demonstrate that our combined data set of surface-wave measurements, waveforms, and body-wave travel times can independently constrain radial variations in five elastic parameters and the density in the upper mantle. Our new transversely isotropic reference model REF fits the waveform data as well as PREM (Dziewoński and Anderson, 1981), and can be useful in building a new generation of the three-dimensional upper-mantle models. Unlike PREM, the reference model REF is continuous at the 220-km depth. We show that when REF is used as a reference, negative velocity gradients $\partial v/\partial depth$ beneath continents at about 200-depth are observed, but they cannot be resolved when PREM is used as a reference (Figure 5.13).

We also show that radial variations in the parameter η are very similar to those in PREM (Figure 4.3). This parameter strongly affects synthetic seismograms. The P-SV body waveforms calculated assuming that $\eta = 1$ have average root-mean-square misfit higher by 0.1 than the seismograms obtained using the appropriate η profile. For Rayleigh waveforms, our preferred model lowers the average misfit by 0.04 compared to the model with η=1. The inversion for the depth-dependant compressional-wave velocity in REF is not as robust as that for the shear-wave velocity. It could be additionally constrained by the measurements of P_n waves in a future work. Our data do not provide sufficient information in the lower mantle, and therefore, REF is constrained to converge to PREM at 1320-km depth. In order to improve the reference model in the lower mantle, it would be

necessary to include the measurements of long-period free oscillations of the Earth.

In the analysis of surface-wave data, we neglect lateral variations of the sensitivity kernels and the Moho depth. We illustrate that these simplifications slightly overestimate isotropic velocity perturbations in the uppermost 100 km of the suboceanic mantle, and slightly underestimate isotropic perturbations within the continental lithosphere (Figure 4.30). The effects at larger depths are less significant. However, a model obtained using laterally-varying sensitivity kernels shows stronger anisotropic variations beneath continents than our model (Nettles, 2005), which demonstrates the importance of the more accurate approach for anisotropic models. Although accounting for lateral variations in the sensitivity kernels and the Moho depth is possible in the analysis of surface waves, it is computationally unfeasible for the waveform inversion. Our method for the crustal correction accounts for nonlinear effects on the normal-mode eigenfrequency (Section 2.4.3), but the sensitivity kernels for all data are determined using REF at every latitudes and longitudes. Marone and Romanowicz (2006) have developed an advanced technique, where the sensitivities are calculated using a reference model overlain by five different crustal types. It is, however, not clear whether more than one crustal structure is indeed needed in the computation of the sensitivity of long-period modes. On the other hand, we have demonstrated that the nonlinear crustal effects on the normal-mode eigenfrequency are significant, and should be taken into account in waveform inversions. Using our new nonlinear approach, we are able to find a sharp velocity gradient beneath some continents at the depth of about 200 km, which appears to be the base of the lithosphere; significantly thicker lithosphere is observed when a simple linear approximation is used to correct the waveforms.

Determination of the structure of the transition zone and uppermost lower mantle is crucial for understanding the style of convection in the mantle. It is, however, difficult, since this depth range

is not very well-constrained by often-used seismic data. The data are 10 times less sensitive at the bottom of the upper mantle than in the upper and mid-mantle (Figure 4.5). The velocities obtained in the transition zone are, therefore, more affected by the *a priori* regularization than at other depths. It is also unclear whether the path-average approximation used in this study to analyze overtones is sufficiently accurate. However, the comparison of different shear-wave velocity models (Figure 6.3) suggests that the structure in the transition zone is not strongly affected by the approximation as long as the overtone or body waveform data are included. Our model S362ANI, as well as models of Ritsema *et al.* (2004) and Panning and Romanowicz (2006), show a significant change in the heterogeneity spectrum at the upper-lower mantle boundary, suggesting a change in the flow pattern.

The inversion for the refined model of Eurasia (Chapter 5) shows that in regions of good data coverage, the measurements of 35-150-s surface waves can resolve upper-mantle structures as small as about 400 km. This empirical limit on surface-wave tomography is consistent with theoretical predictions of Yoshizawa and Kennett (2002), who analyzed the width of the region around the ray. On the other hand, our results suggest that the minimum resolvable length scale determined by Spetzler *et al.* (2002) based upon scattering theory is too conservative. At this point, expanding the data and improving ways of model parameterization and regularization are more likely to facilitate progress in seismic tomography than theoretical advances in modeling of the seismic wave propagation. However, incorporating more accurate techniques is important, and may eventually lead to improvements in the models. For example, lateral variations in attenuation significantly affect the sensitivity of surface waves to the velocity structure (C. Dalton, personal communication), and simultaneous inversion for the elastic and anelastic structure may be necessary to further improve

tomographic models of the mantle.

Appendix A

Model availability

The one-dimensional model REF, global three-dimensional models S362ANI, S362WMANI, S362ANI_PREM, and three-dimansional model of Eurasia S2.9EA are available from the author, who may be reached by email at kustowsk@seismology.harvard.edu. In the future, the models will also be available online at http://www.seismology.harvard.edu/~kustowsk.

References

Anderson, D. L., Elastic wave propagation in layered anisotropic media, *J. Geophys. Res.*, *66*, 2953–2963, 1961.

Anderson, D. L., The deep structure of continents, *J. Geophys. Res.*, *84*, 7555–7560, 1979.

Anderson, D. L., *Theory of the Earth*, Blackwell, Oxford, 1989.

Antolik, M., Y. J. Gu, G. Ekström, and A. M. Dziewonski, J362D28: a new joint model of compressional and shear velocity in the Earth's mantle, *Geophys. J. Int.*, *153*, 443–466, 2003.

Artemieva, I. M. and W. D. Mooney, Thermal thickness and evolution of Precambrian lithosphere: a global study, *J. Geophys. Res.*, *106*, 16,387–16,414, 2001.

Baig, A. M., Dahlen, F. A., and S.-H. Hung, Traveltimes of waves in random 3-D media, *Geophys. J. Int.*, *153*, 1–16, 2003.

Bassin, C., Laske, G., and G. Masters, The current limits of resolution for surface wave tomography in North America, *Eos Trans. AGU*, *81*, Fall Meet. Suppl., F897, 2000.

Berryman, J.G., Long-wave elastic anisotropy in transversely isotropic media, *Geophysics*, *44*, 896–917, 1979.

Bijwaard, H., Spakman, W., and E. R. Engdahl, Closing the gap between regional and global travel time tomography, *J. Geophys. Res.*, *103*, 30,055–30,078, 1998.

Bolton, H. F., Long Period Travel Times and the Structure of the Mantle, *Ph.D. thesis*, University of San Diego, 1996.

Bolton, H. F. and G. Masters, Travel times of P and S from global digital seismic networks; implications for the relative variation of P and S velocity in the mantle, *J. Geophys. Res.*, *106*, 13,527-13,540, 2001.

Boschi, L. and A. M. Dziewonski, Whole Earth tomography from delay times of P, PcP, PKP phases: lateral heterogeneities in the outer core, or radial anisotropy in the mantle?, *J. Geophys. Res.*, *105*, 13,675–13,696, 2000.

Boschi, L. and A. M. Dziewonski, High- and low-resolution images of the Earth's mantle: Implications of different approaches to tomographic modeling, *J. Geophys. Res.*, *104*, 25,567–25,594, 1999.

Boschi, L. and G. Ekström, New images of the Earth's upper mantle from measurements of surface wave phase velocity anomalies, *J. Geophys. Res.*, *107*, 10.1029/2000JB000059, 2002.

Boschi, L., Ekström G., and B. Kustowski, Multiple resolution surface wave tomography: the Mediterranean basin, *Geophys. J. Int.*, *157*, 293–304, 2004.

Conrad, C. P., Convective instability of thickening mantle lithosphere, *Geophys. J. Int.*, *143*, 52–70, 2000.

Dahlen, F. A. and J. Tromp, *Theoretical Global Seismology*, Princeton University Press, Princeton, New Jersey, 1998.

Dercourt, J., Zonenshain, L. P., Ricou, L.-E. et al., Geological evolution of the Tethys belt from the Atlantic to the Pamirs since the Lias, *Tectonophysics*, *123*, 241–315, 1986.

de Hoop, M. V. and R. D. van der Hilst, On sensitivity kernels for "wave-equation" transmission tomography, *Geophys. J. Int.*, *160*, 621–633, 2005.

de Jonge, M. R., Wortel, M. J. R., and W. Spakman, Regional scale tectonic evolution and the seismic velocity structure of the lithosphere and upper mantle: the Mediterranean region, *J. Geophys. Res.*, *99*, 12,091–12,108, 1994.

Deuss, A. and J. H. Woodhouse, A systematic search for mantle discontinuities using SS-precursors, *Geophys. Res. Lett.*, *29*, 10,1029/2002GL014768, 2002.

Dorman, J., Ewing, M., and J. Oliver, Study of the shear-velocity distribution in the upper mantle by Rayleigh waves, *Bull. Seismol. Soc. Am.*, *50*, 87–115, 1960.

Durek, J. J. and G. Ekström, A radial model of anelasticity consistent with long-period surface-wave attenuation, *Bull. Seismol. Soc. Am.*, *86*, 144–158, 1996.

Dziewonski, A. M., Upper mantle models from 'pure path' dispersion data, *J. Geophys. Res.*, *76*, 2,587–2,601, 1971.

Dziewonski, A. M., Mapping the lower mantle; determination of lateral heterogeneity in P velocity up to degree and order 6, *J. Geophys. Res.*, *89*, 5,929–5,952, 1984.

Dziewonski, A. M., and D. L. Anderson, Preliminary reference Earth model, *Phys. Earth Planet. Inter.*, *25*, 297–356, 1981.

Dziewonski, A. M., and F. Gilbert, The effect of small, aspherical perturbations on travel times and a re-examination of the corrections for ellipticity, *Geophys. J. R. Astr. Soc.*, *44*, 7–18, 1976.

Dziewonski, A. M. and J. H. Woodhouse, *Studies of the seismic source using normal-mode theory*, North-Holland Publ. Co., Amsterdam, Netherlands, 45–137, 1983.

Dziewonski, A. M. and J. H. Woodhouse, Global images of the Earth's interior, *Science*, *236*, 37–48, 1987.

Dziewonski, A. M. and J. H. Woodhouse, An experiment in systematic study of global seismicity: Centroid-moment tensor solutions for 201 moderate and large earthquakes of 1981, *J. Geophys. Res.*, *88*, 3247–3271, 1983.

Dziewonski, A. M. and R. L. Woodward, Acoustic imaging at the planetary scale, in Emert, H., and H.-P. Harjes, *eds.*, Acoustical Imaging, *19*, 785–797, Plenum Press, 1992.

Dziewonski, A. M., Chou, T.-A., and J. H. Woodhouse, Determination of earthquake source parameters from waveform data for studies of global and regional seismicity, *J. Geophys. Res.*, *86*, 2825–2852, 1981.

Dziewonski, A. M., Hager, B. H., and R. J. O'Connell, Large-scale heterogeneity in the lower mantle, *J. Geophys. Res.*, *82*, 239–255, 1977.

Ekström, G., Mapping the lithosphere and asthenosphere with surface waves: lateral structure and anisotropy, in *The history and dynamics of global plate motions*, AGU Geophysical Monograph 121, 239–255, 2000.

Ekström, G. and A. M. Dziewonski, The unique anisotropy of the Pacific upper mantle, *Nature*, *394*, 168–172, 1998.

Ekström, G., Tromp, J., and E. W. F. Larson, Measurements and global models of surface wave propagation, *J. Geophys. Res.*, *102*, 8,137–8,157, 1997.

Enkin, R. J., Yang, Z., Chen, Y., and V. Courtillot, Paleomagnetic constraints on the geodynamic history of the major blocks of China from the Permian to the present, *J. Geophys. Res.*, *97*, 13,953–13,989, 1992.

Flanagan, M. F. and P. M. Shearer, Global mapping of topography on transition zone velocity discontinuities by stacking *SS* precursors, *J. Geophys. Res.*, *103*, 2673–2692, 1998.

Fouch, M. S., Fisher, K. M., and M. E. Wysession, Lowermost mantle anisotropy beneath the Pacific: Imaging the source of the Hawaiian plume, *Earth Planet. Sci. Lett.*, *190*, 167–180, 2001.

Fukao, Y., Widiyantoro, S., and M. Obayashi, Stagnant slabs in the upper and lower mantle transition region, *Rev. Geophys.*, *39*, 291–323, 2001.

Gaherty, J. and T. H. Jordan, Lehmann discontinuity as the base of the anisotropic layer beneath continents, *Science*, *268*, 1468–1471, 1995.

Garnero, E. J., Helmberger, D. V., and L. J. Burdick, Preliminary observations from the use of US-soviet joint seismic program data to model upper mantle triplications beneath Asia, *Geophys. J. Int.*, *113*, 252–259, 1992.

Gee, L. S. and T. H. Jordan, Polarization anisotropy and fine-scale structure of the Eurasian upper mantle, *Geophys. Res. Lett.*, *15*, 824–827, 1988.

Giardini, D. and J. H. Woodhouse, Deep seismicity and modes of deformation in Tonga subduction zone, *Nature*, *307*, 505–509, 1984.

Giardini, D. and J. H. Woodhouse, Horizontal shear flow in the mantle beneath the Tonga arc, *Nature*, *319*, 551–555, 1986.

Godey, S., Deschamps, F., Trampert, J., and R. Snieder, Thermal and compositional anomalies beneath the North American continent, *J. Geophys. Res.*, *109*, 10.1029/2002JB002263, 2004.

Gorbatov, A., Fukao, Y., and S. Widiyantoro, Application of the three-dimensional ray-tracing technique to global *P*, *PP*, and P_{diff} traveltime tomography, *Geophys. J. Int.*, *146*, 583–593, 2001.

Grand, S. P. and D. V. Helmberger, Upper mantle shear structure of North America, *Geophys. J. R. Astr. Soc.*, *76*, 399–438, 1984.

Grand, S. P. and D. V. Helmberger, Upper mantle shear structure beneath Asia from multi-bounce S waves, *Phys. Earth Planet. Inter.*, *41*, 154–169, 1985.

Grand, S. P., van der Hilst, R. D., and S. Widiyantoro, Global seismic tomography: A snapshot of convection in the Earth, *GSA Today*, *7*, 1–7, 1997.

Griot, D.-A., Montagner J.-P., and P. Tapponnier, Phase velocity structure from Rayleigh and Love waves in Tibet and its neighboring region, *J. Geophys. Res.*, *103*, 21,215–21,232, 1998.

Gu, Y. J. and A. M. Dziewonski, Global de-correlation of the topography of transition zone discontinuities, *Earth Planet. Sci. Lett.*, *157*, 57–67, 1998.

Gu, Y. J. and A. M. Dziewonski, Global variability of transition zone thickness, *J. Geophys. Res.*, *107*, 10,1029/2001JB000489, 2002.

Gu, Y. J., Dziewonski, A. M. , Su, W., and G. Ekström, Models of the mantle shear velocity and discontinuities in the pattern of lateral heterogeneities, *J. Geophys. Res.*, *106*, 11,169–11,199, 2001a.

Gu, Y. J., Dziewonski, A. M., and G. Ekström, Preferential detection of the Lehmann discontinuity beneath continents, *Geophys. Res. Lett.*, *24*, 4655–4658, 2001b.

Gu, Y. J., Dziewonski, A. M., and G. Ekström, Simultaneous inversion for mantle shear velocity and topography of transition zone discontinuities, *Geophys. J. Int.*, *154*, 559–583, 2003.

Gung, Y., Panning, M., and B. Romanowicz, Global anisotropy and the thickness of continents, *Nature*, *442*, 707–711, 2003.

Harkrider, D. G. and D. L. Anderson, Computation of surface wave dispersion for multilayered anisotropic media, *Bull. Seismol. Soc. Am.*, *52*, 321–332, 1962.

Hamilton, W. B. The closed upper-mantle circulation of plate tectonics, in *Geodynamics Series*, AGU Geophysical Monograph, 30, 359–410, 2002.

Helffrich, G., Topography of the transition zone seismic discontinuities, *Rev. Geophys.*, *38*, 141–158, 2000.

Hess, H., Seismic anisotropy of the uppermost mantle under oceans, *Nature*, *203*, 629–631, 1964.

Jaupart, C. and J. C. Mareschal, The thermal structure and thickness of continental roots, *Lithos*, *48*, 93–114, 1999.

Jeffreys, H. and K. E. Bullen *Seismological Tables, British Association*, Gray-Milne Trust, London, 1940.

Jordan, T. H., The continental tectosphere, *Rev. Geophys. Space Phys.*, *13*, 1–12, 1975.

Jordan, T. H., Composition and development of the continental tectosphere, *Nature*, *274*, 544–548, 1978.

Jordan, T. H., Continents as a chemical boundary layer, *Phil. Trans. R. Soc. London A*, *301*, 359–373, 1981a.

Jordan, T. H., Global tectonic regionalization for seismological data analysis, *Bull. Seismol. Soc. Am.*, *71*, 1131–1141, 1981b.

Karato, S., On the Lehmann discontinuity, *Geophys. Res. Lett.*, *19*, 2255–2258, 1992.

Karato, S., Importance of anelasticity in the interpretation of seismic tomography, *Geophys. Res. Lett.*, *20*, 1,623–1,626, 1993.

Karato, S., Some remarks on the origin of seismic anisotropy in the D$''$ layer, *Earth Planets Space*, *50*, 1059–1028, 1998.

Kendall, J. M., Seismic anisotropy in boundary layers of the mantle, in Earth's Deep Interior, AGU Geophysical Monograph, 117, 133–159, 2000.

Kendall, J. M. and P. G. Silver, Constraints from seismic anisotropy on the nature of the lowermost mantle, *Nature*, *381*, 409–412, 1996.

Kennett, B. L. N., *The seismic wavefield, v1*, Cambridge University Press, Cambridge, 2001.

Kennett, B. L. N., Engdahl E. R., and R. Buland, Constraints on seismic velocities in the Earth from travel times, *Geophys. J. Int.*, *122*, 108-124, 1995.

Kind, R., Kosarev, G. L., Makayeva, L. I., and L. P. Vinnik, Observations of laterally inhomogeneous anisotropy in the continental lithosphere, *Nature*, *318*, 358-361, 1984.

Kind, R., Yuan, X., Saul, J., Nelson, D., Sobolev, S. V., Mechie, J., Zhao, W., Kosarev, G., Ni, J., Achauer, U., and M. Jiang, Seismic images of crust and upper mantle beneath Tibet: evidence for Eurasia plate subduction, *Science*, *298*, 1219-1221, 2002.

Kumar, P., Yuan, X., Kind, R., and J. Ni, Imaging the colliding Indian and Asian lithospheric plates beneath Tibet, *J. Geophys. Res.*, *111*, 10,1029/2005JB003930, 2006.

Kustowski, B., Ekström G. and A.M. Dziewoński, Travel Times in the Regional Distance Range: Results of 3-D Ray Tracing, *Eos Trans. AGU, 84*, Fall Meet. Suppl., S31E-0797, 2003.

Lancaster, P. and K. Salkauskas, *Curve and surface fitting – an introduction*, Academic Press, San Diego, California, 1986.

Larson, E. W. F., J. Tromp, and G. Ekström, Effects of slight anisotropy on surface waves, *Geophys. J. Int., 132*, 654–666, 1998.

Laske, G. and G. Masters, Constraints on global phase velocity maps by long-period polarization data, *J. Geophys. Res., 101*, 16,059–16,075, 1996.

Lay, T. and C. J. Young, The stability-stratified outermost core revisited, *Geophys. Res. Lett., 17*, 2001–2004, 1990.

Lay, T., Williams, Q., Garnero, E. J., Kellog, L., and M. E. Wysession, Seismic wave anisotropy in the D$''$ region and its implications, in *The Core-Mantle Boundary Region*, AGU Geophysical Monograph, 28, 219–318, 1998.

Lekic, V., Distribution of stresses in descending lithospheric slabs from a global survey of Harvard CMT solutions for subduction-zone earthquakes, *B. A. thesis*, Harvard University, 2004.

Lerner-Lam, A. L. and T. H. Jordan, How thick are the continents?, *J. Geophys. Res., 92*, 14,007–14,026, 1987.

Levshin, A. L., Yanovskaya, T. B., Lander, A. V., Bukchin, B. G., Barmin, M. P., Ratnikova, L. I., and E. N. Its, Recording, identification, and measurement of surface wave parameters, in *Seismic surface waves in a laterally inhomogeneous Earth*, Kluwer Academic Publisher, Dordrecht, 131-182, 1989.

Li, X.-D. and B. Romanowicz, Comparison of global waveform inversions with and without considering cross-branch modal coupling, *Geophys. J. Int., 121*, 695–709, 1995.

Li, X.-D. and B. Romanowicz, Global mantle shear velocity model developed using nonlinear asymptotic coupling theory, *J. Geophys. Res., 101*, 22,245–22,272, 1996.

Liu, X., The three-dimensional shear-wave velocity structure of Earth's lowermost mantle, *Ph.D. thesis*, Harvard University, 1997.

Liu, X.-F. and A. M. Dziewonski, Global analysis of shear wave velocity anomalies in the lowermost mantle, in *Geodynamics Series*, AGU Geophysical Monograph, 28, 21–36, 1998.

Long, M. D. and R. D. van der Hilst, Upper mantle anisotropy beneath Japan from shear wave splitting, *Phys. Earth Planet. Inter., 151*, 206–222, 2005.

Love, A.E.H., *A Treatise on the Theory of Elasticity*, 4th edition, Cambridge University Press, Cambridge, 1927.

Maggi, A. and K. Priestley, Surface waveform tomography of the Turkish-Iranian plateau, *Geophys. J. Int., 160*, 1068–1080, 2005.

Maggi, A., Debayle, E., Priestley, K., and G. Barruol, Azimuthal anisotropy of the Pacific region, *Earth Planet. Sci. Lett., 250*, 53-71, 2006.

Marone, F. and B. Romanowicz, Non-linear crustal corrections in high resolution regional waveform seismic tomography, *Geophys. J. Int.*, submitted, 2006.

Masters, G., Jordan, T. H., Silver, P. G., and F. Gilbert, Aspherical earth structure from fundamental spheroidal mode data, *Nature, 298*, 609–613, 1982.

Masters, G., Laske, G., and F. Gilbert, Autoregressive estimation of the splitting matrix of free-oscillation multiplets, *Geophys. J. Int., 141*, 25–42, 2000.

Masters, G., Laske, G., Bolton, H., and A. Dziewonski, The relative behavior of shear velocity, bulk sound speed, and compressional velocity in the mantle: Implications for chemical and thermal structure, in *Earth's Deep Interior*, AGU Geophysical Monograph, 117, 63–87, 2000.

Montagner, J.-P. and N. Jobert, Vectorial tomography; II. Application to the Indian Ocean, *Geophys. J.*, *94*, 309–344, 1988.

Montagner, J.-P. and T. Tanimoto, Global anisotropy in the upper mantle inferred from the regionalization of phase velocities, *J. Geophys. Res.*, *95*, 4797–4819, 1990.

McNamara, D. E., Owens, T. J., and W. R. Walter, Observations of regional phase propagation across the Tibetan Plateau, *J. Geophys. Res.*, *100*, 22,215–22,229, 1995.

Mechie, J., Egorkin, A. V., Fuchs, K. Ryberg, T., Solodilov, L., and F. Wenzel, P-wave mantle velocity structure beneath northern Eurasia from long-range recordings along the profile Quartz, *Phys. Earth Planet. Inter.*, *79*, 269–286, 1993.

Megnin, C. and B. Romanowicz, The three-dimensional shear velocity structure of the mantle from the inversion of body, surface and higher-mode waveforms, *Geophys. J. Int.*, *143*, 709–728, 2000.

Menke, W., *Geophysical data analysis: Discrete inverse theory*, Academic Press, 1989.

Montagner, J.-P., and D. L. Anderson, Petrological constraints on seismic anisotropy, *Phys. Earth Planet. Inter.*, *54*, 82–105, 1989.

Montelli, R., G. Nolet, Dahlen, F. A., Masters, G., Engdahl, E. R., and S.-H. Hung, Finite-frequency tomography reveals a variety of plumes in the mantle, *Science*, *303*, 338–343, 2004a.

Montelli, R., Nolet, G., Masters, G., Dahlen, F. A., and S.-H. Hung, Global *P* and *PP* traveltime tomography: rays versus waves, *Geophys. J. Int.*, *158*, 637–654, 2004b.

Mooney, W. D., G. Laske, and G. Masters, CRUST-5.1: A global crustal model at $5^\circ \times 5^\circ$, *J. Geophys. Res.*, *103*, 727–747, 1998.

Morozova, E. A., Morozov, I. B., and S. B. Smithson, Heterogeneity of the uppermost mantle beneath Russian Eurasia from the ultra-long-range profile QUARTZ, *J. Geophys. Res.*, *104*, 20,329–20,348, 1999.

Murakami, M. K., Hirose, K., Kawamura, K., Sata, N., and Y. Ohishi, Post-perovskite phase transition in $MgSiO_3$, *Science*, *304*, 855–858, 2004.

Nataf, H.-C. and Y. Ricard, 3SMAC: an *a priori* tomographic model of the upper mantle based on geophysical modeling, *Phys. Earth Planet. Inter.*, *95*, 101–122, 1996.

Nettles, M. K., Anisotropic velocity structure of the mantle beneath North America, *Ph.D. thesis*, Harvard University, 2005.

Nicolas, A. and N. Christensen, Formation of anisotropy in upper mantle peridotites: a review, in: Composition, Structure and Dynamics of the Lithosphere-Asthenosphere System, *Geodynamics Series*, AGU Geophysical Monograph, 16, 111–123, 1987.

Nielsen, L. and H. Thybo Seismic tomographic inversion of Russian PNE data along profile Kraton, *Geophys. Res. Lett.*, *26*, 3413–3416, 1999.

Nikishin, A. M., Ziegler P. A., Stephenson R. A. et al., Late Precambrian to Triassic history of the East European Craton: dynamics of sedimentary basin evolution, *Tectonophysics*, *268*, 23–63, 1996.

Nolet, G., Partitioned waveform inversion and two-dimensional structure under the Network of Autonomously Recording Seismographs, *J. Geophys. Res.*, *95*, 8499–8512, 1990.

Nolet, G. and F. A. Dahlen, Wavefront healing and the evolution of seismic delay times, *J. Geophys. Res.*, *105*, 19,043-19,054, 2000.

Oganov, A. R. and S. Sono, Theoretical and experimental evidence for a post-perovskite phase of $MgSiO_3$ in the Earth's D$''$ layer, *Nature*, *430*, 445–448, 2004.

Panning, M., Deep Earth Seismic Structure and Earthquake Source Processes from Long Period Waveform Modeling, *Ph.D. thesis*, University of California, Berkeley, 2004.

Panning, M. and B. Romanowicz, Inferences on flow at the base of Earth's mantle based on seismic anisotropy, *Science*, *303*, 351–353, 2004.

Panning, M. and B. Romanowicz, A three dimensional anisotropic model of shear velocity in the whole mantle, *Geophys. J. Int.*, submitted, 2006.

Pearson, D. G., Shirey, S. B., Carlson, R. W., Boyd, F. R., Pokhilenko, N. P., and N.Shimizm, Re-Os, Sm-Nd, and Rb-Sr isotope evidence for thick Archean lithospheric mantle beneath the Siberian craton modified by multistage metasomatism, *Geochemica et Cosmochimica Acta*, *59*, 959–977, 1995.

Priestley, K. and E. Debayle, Seismic evidence for a moderately thick lithosphere beneath the Siberian Platform, *Geophys. Res. Lett.*, *30*, 10,1029/2002GL015931, 2003.

Priestley, K. and D. McKenzie, The thermal structure of the lithosphere from shear wave velocities, *Geophys. J. Int.*, submitted, 2006.

Raitt, R. W., Shor, G. G., Francis, T. J. G., and G. B. Morris, Anisotropy of the Pacific upper mantle, *J. Geophys. Res.*, *74*, 3095–3109, 1969.

Reif, C., Masters, G., Shearer, P., and G. Laske, Shear and compressional velocity models of the mantle from cluster analysis of long-period waveforms, *Geophys. J. Int.*, submitted, 2006.

Resovsky, J. S., and M. H. Ritzwoller, New and refined constraints on three-dimensional Earth structure from normal modes below 3 mHz, *J. Geophys. Res.*, *103*, 783–810, 1998.

Ritsema, J., van Heijst, H.-J., and J. H. Woodhouse, Complex shear wave velocity structure imaged beneath Africa and Iceland, *Science*, *286*, 1925–1928, 1999.

Ritsema, J., van Heijst, H. J., and J. H. Woodhouse, Global transition zone tomography, *J. Geophys. Res.*, *109*, 10.1029/2003JB002610, 2004

Robertson, G. S. and J. H. Woodhouse, Ratio of relative S to P velocity heterogeneity in the lower mantle, *J. Geophys. Res.*, *101*, 20,041–20,052, 1996

Romanowicz, B., The upper mantle degree 2: Constraints and inferences from global mantle wave attenuation measurements, *J. Geophys. Res.*, *95*, 11,051–11,071, 1990.

Ryberg, T., Wenzel, F., Mechie, J., Egorkin, A., Fuchs, K., and L. Solodilov, Two-dimensional velocity structure beneath northern Eurasia derived from the super long-range seismic profile Quartz, *Bull. Seismol. Soc. Am.*, *85*, 857–867, 1996.

Shapiro, N. M. and M. H. Ritzwoller Monte-Carlo inversion for a global shear-velocity model of the crust and upper mantle, *Geophys. J. Int.*, *151*, 88-105, 2002.

Shapiro, S. S., Hager, B. H., and T. H. Jordan, Stability and dynamics of the continental tectosphere, *Lithos*, *48*, 115–133, 1999.

Shearer, P. M. and T. G. Masters, Global mapping of topography on the 660-km discontinuity, *Nature*, *355*, 791–795, 1992.

Shim, S.-H., Duffy, T. S., Jeanloz, R., and G. Shen, Stability and crystal structure of $MgSiO_3$ perovskite to the core-mantle boundary, *Geophys. Res. Lett.*, *31*, 10.1029/2004GL019639, 2004.

Silver, P. G. and W. W. Chan, Shear wave splitting and sub-continental mantle deformation, *J. Geophys. Res.*, *96*, 16,429–16,454, 1991.

Spakman, W., van der Lee, S., and R. D. van der Hilst, Travel-time tomography of the European-Mediterranean mantle down to 1400 km, *Phys. Earth Planet. Inter.*, *79*, 3–74, 1993.

Spetzler, J., Trampert, J., and R. Snieder, The effect of scattering in surface wave tomography, *Geophys. J. Int.*, *149*, 755–767, 2002.

Stevenson, D. J., Limits on lateral density and velocity variations in the Earth's outer core, *Geophys. J. R. Astr. Soc.*, *88*, 311–319, 1987.

Su, W.-J. and A. M. Dziewonski, Predominance of long-wavelength heterogeneity in the mantle, *Nature*, *352*, 121–126, 1991.

Su, W.-J. and A. M. Dziewonski, Simultaneous inversion for 3-D variations in shear and bulk velocity in the mantle, *Phys. Earth Planet. Inter.*, *100*, 135–156, 1997.

Su, W.-J., Woodward, R. L., and A. M. Dziewonski, Deep origin of mid-ocean ridge seismic velocity anomalies, *Nature*, *360*, 149–152, 1992.

Su, W.-J., Woodward, R. L., and A. M. Dziewonski, Degree-12 model of shear velocity heterogeneity in the mantle, *J. Geophys. Res.*, *99*, 6945–6980, 1994.

Tackley, P. J., Stevenson, D. J., Glatzmaier, G., and G. Schubert, Effects of an endothermic phase transition at 670 km depth in a spherical model of convection in the Earth's mantle, *Nature*, *361*, 699–704, 1993.

Takeuchi, H. and M. Saito, Seismic surface waves, in B. A. Bolt, *ed.*, Seismology: Surface Waves and Earth Oscillations, *Methods in Computational Physics*, *11*, 217–295, Academic Press, New York, 1972.

Thomsen, L., Weak elastic anisotropy, *Geophysics*, *51*, 1954–1966, 1986.

Toksöz, M. N. and D. L. Anderson Phase velocities of long-period surface waves and structure of the upper mantle, *J. Geophys. Res.*, *71*, 1649–1658, 1966.

Trampert, J. and J. Spetzler, Surface wave tomography; finite-frequency effects lost in the null space Geophysical Journal International, *Geophys. J. Int.*, *164*, 394–400, 2006.

Trampert, J. and J. H. Woodhouse, Global phase velocity maps of Love and Rayleigh waves between 40 and 150 seconds, *Geophys. J. Int.*, *122*, 675–690, 1995.

Trefethen, L. N. and D. Bau, *Numerical Linear Algebra*, Soc. for Ind. and Appl. Math., Philadelphia, Penn., 1997.

van der Hilst, R. D. and M. V. de Hoop, Banana-doughnut kernels and mantle tomography, *Geophys. J. Int.*, *163*, 956–961, 2005.

van der Hilst, R. D., Widiyantoro S., and E. R. Engdahl, Evidence for deep mantle circulation from global tomography, *Nature*, *386*, 578–584, 1997.

van der Lee, S. and G. Nolet, Upper mantle S velocity structure of North America, *J. Geophys. Res.*, *102*, 22,815–22,838, 1997.

van der Voo, R., Spakman W., and H. Bijwaard, Mezozoic subducted slabs under Siberia, *Nature*, *397*, 246–249, 1999.

van Heijst, H. J. and J. H. Woodhouse, Measuring surface-wave overtone phase velocities using a mode branch stripping technique, *Geophys. J. Int.*, *131*, 209–230, 1997.

Wang, Z. and F. A. Dahlen, Spherical-spline parameterization of three-dimensional Earth models, *Geophys. Res. Lett.*, *22*, 3,099–3,102, 1995.

Wang, Z., Tromp, J., and G. Ekström, Global and local surface-wave inversions: A spherical-spline parameterization, *Geophys. Res. Lett.*, *25*, 207–210, 1998.

Widiyantoro, S., Gorbatov, A., Kennett, B. L. N., and Y. Fukao, Improving global shear wave traveltime tomography using three-dimensional ray tracing and iterative inversion, *Geophys. J. Int.*, *141*, 747–758, 2000.

Woodhouse, J. H. A note on the calculation of travel times in a transversely isotropic Earth model, *Phys. Earth Planet. Inter.*, *25*, 357–359, 1981.

Woodhouse, J. H. The calculation of eigenfrequencies and eigenfunctions of the free oscillations of the Earth and the Sun, in D. J. Doornbos, *ed.*, *Seismological Algorithms*, 321-370, Academic Press, San Diego, CA, 1988.

Woodhouse, J. H. and A. M. Dziewonski, Mapping the upper mantle: Three-dimensional modeling of Earth structure by inversion of seismic waveforms, *J. Geophys. Res.*, *89*, 5953–5986, 1984.

Woodhouse, J. H. and A. M. Dziewonski, Seismic modelling of the Earth's large-scale three-dimensional structure, *Phil. Trans. R. Soc. London A*, *328*, 291–308, 1989.

Woodhouse, J. H. and T. P. Girnius, The calculation of dΔ/dp and of partial derivatives for travel-time inversion in transversely isotropic spherical earth models, *Seismic discrimination, semiannual technical summary report to the defense advanced research projects agency*, Massachusetts Institute of Technology, Lincoln Laboratory, Lexington, MA, 61-65,1982.

Yin, A. and T. M. Harrison, *The tectonic evolution of Asia*, Cambridge University Press, Cambridge, 1996.

Yoshizawa, K. and B. L. N. Kennett, Determination of the influence zone for surface wave paths, *Geophys. J. Int.*, *149*, 440–453, 2002.

Zhou, Y., Nolet, G., Dahlen, F. A., and G. Laske, Global upper-mantle structure from finite-frequency surface-wave tomography, *J. Geophys. Res.*, *111*, 10,1029/2005JB003677, 2006.